

Università degli Studi di Bologna

CENTRO DI RICERCA SUI SISTEMI ELETTRONICI
PER L'INGEGNERIA DELL'INFORMAZIONE E
DELLE TELECOMUNICAZIONI
"ERCOLE DE CASTRO" - ARCES

**Reduced-order Modelling,
Circuit-level Design and
SOI Fabrication of
Microelectromechanical Resonators**

Tesi di Dottorato di: LAURA DEL TIN

Relatore: Chiar. mo Prof. Ing. GIORGIO BACCARANI

Correlatore: Dott. Ing. ROBERTO GADDI

Coordinatore: Chiar. mo Prof. Ing. RICCARDO ROVATTI

Sigla del settore scientifico disciplinare: ING-INF/01

Marzo 2007

Università degli Studi di Bologna

FACOLTÀ DI INGEGNERIA

Dottorato di Ricerca in Tecnologie dell'Informazione

XIX ciclo (Anni accademici 2004-2006)

**Reduced-order Modelling,
Circuit-level Design and
SOI Fabrication of
Microelectromechanical Resonators**

Tesi di Dottorato di: LAURA DEL TIN

Relatore: Chiar. mo Prof. Ing. GIORGIO BACCARANI

Correlatore: Dott. Ing. ROBERTO GADDI

Coordinatore: Chiar. mo Prof. Ing. RICCARDO ROVATTI

Sigla del settore scientifico disciplinare: ING-INF/01

Marzo 2007

“Aber mehr laß mich davon nicht sagen. Die Worte tun dem geheimen Sinn nicht gut, es wird immer alles gleich ein wenig anders, wenn man es ausspricht, ein wenig verfälscht, ein wenig närrisch-ja, und auch das ist sehr gut und gefällt mir sehr, auch damit bin ich sehr einverstanden, daß das, was eines Menschen Schatz und Weisheit ist, dem andern immer wie Narrheit klingt.”

“Siddharta”, *H. Hesse*
1922

Contents

Abstract	1
1 Introduction	3
1.1 MEMS for RF Applications	3
1.2 MEMS compact modelling	6
1.3 Integrated resonators-switches fabrication	9
1.4 Thesis outline	9
2 RF MEMS active devices	11
2.1 Radio frequency MEMS devices	11
2.2 Microelectromechanical resonators	11
2.2.1 Working principle	12
2.2.2 Second order effects	21
2.2.3 Present status	24
2.2.4 Quality factor	27
2.2.5 Characteristic parameters and performance	34
2.2.6 Applications	37
2.2.7 Enabling technology	40
2.3 RF microswitch	44
2.3.1 Classification	44
2.3.2 Working principle	46
2.3.3 State of the art	49
2.3.4 Enabling technology	50
2.4 Integrated resonator-switch fabrication	51
2.4.1 Present state	52
3 Review of simulation methods for MEMS devices	55
3.1 Simulation requirements	56
3.2 Simulation approaches	57
3.2.1 Physical modelling: spatial discretization methods	57
3.2.2 Compact modelling	61

3.3	Conclusion	70
4	Theory and physical modelling of MEMS with electrostatic actuation	71
4.1	Mechanical domain	71
4.2	Electrical domain	74
4.3	Finite element modelling	75
4.3.1	Mechanical system	75
4.3.2	Electromechanical coupling	77
4.3.3	Electromechanical system matrices	79
4.3.4	Damping modelling	82
4.3.5	Contact force modelling	83
5	Model order reduction	85
5.1	Introduction and problem statement	85
5.2	Basics of system theory	87
5.2.1	System representation	87
5.2.2	System properties	87
5.3	Review of linear MOR methods	89
5.3.1	Eigensystem method	89
5.3.2	SVD-based methods	89
5.3.3	Moment matching based methods	91
5.3.4	Guyan reduction	96
5.3.5	Second-order systems	97
5.3.6	Methods summary	98
5.4	Extension of MOR linear techniques to RF MEMS active devices	100
5.4.1	Linearization	101
5.4.2	Modeling of nonlinearities as inputs	101
5.5	Model order reduction: practical implementation	102
5.5.1	MOR for ANSYS 2.0	103
5.5.2	Reduced model properties	105
6	Compact modelling	109
6.1	Models extraction	109
6.2	Model validation	111
6.2.1	Mechanical linearity	111
6.2.2	Electrostatic description	114
6.3	Simulation results	115
6.3.1	One port vertical beam resonator	116
6.3.2	Lateral beam	117
6.3.3	Free free beam resonator	118
6.3.4	Square resonator	121

6.3.5	Micromechanical filter	126
6.3.6	IRST capacitive switch	130
6.3.7	ST capacitive switch	133
6.4	Discussion	135
7	Integrated RF resonators and switches fabrication	137
7.1	Single processes	137
7.1.1	Switch process	137
7.1.2	Resonator process	139
7.2	Combined process-flow	141
7.2.1	Critical points	145
7.2.2	Effects on devices behaviour	148
7.3	Designed structures	149
7.3.1	Resonator design	150
7.4	Conclusions	152
8	Conclusions	153
	Publications	155

List of Figures

1.1	Block scheme of a dual-conversion heterodyne transceiver front-end. Colored blocks represent components off-chips in current implementations (from [7]).	5
1.2	Block scheme of a new receiver architecture, which make use of RF MEMS devices. Colored blocks are realized using micromechanical devices (from [16]).	6
2.1	Lumped model of a resonator.	13
2.2	Normalized displacement $ Y $ as a function of the frequency, for different values of the quality factor Q	14
2.3	Schematic model of a clamped-clamped beam resonator.	15
2.4	Micromechanical resonator equivalent circuits.	21
2.5	Effects of high order nonlinearities.	24
2.6	Clamped-clamped beam resonators from [51] (a) and [36] (b).	25
2.7	Free-Free vertical beam resonator from [51].	25
2.8	Longitudinal resonators: round geometries [51].	27
2.9	Quality factor of a flexural beam resonator, due to thermoelastic damping, as a function of the frequency. Different values of the beam width w are considered.	30
2.10	Damper schematic model.	32
2.11	Squeeze film coefficient normalized with respect to $\frac{p_0 A}{d}$	33
2.12	Series oscillator with a resonator tank.	38
2.13	Mechanically coupled resonators from [47] and [92].	40
2.14	Process flows for the fabrication of vertical and lateral resonating structure in polysilicon with surface micromachining technology.	42
2.15	Process flows for the fabrication of SCS resonators with bulk micromachining technology.	44
2.16	Switches configurations	46
2.17	Relays types: top view and cross section.	47
2.18	Switches examples from [112], [35] and [113].	50
2.19	Basic process steps for the fabrication of 2.19(a) ohmic and 2.19(b) capacitive switches. 51	51

2.20	IBM switch resonator combined process flow (from [119]).In (a) and (b) the top-view and the cross-sections of a switch and a resonators are shown, respectively. In (c) details on the metallization are given, while (d) and (e) report the steps necessary for the MEMS device release.	53
3.1	Design methodology diagram.	56
3.2	Relaxation scheme	59
3.3	Newton iteration scheme	60
3.4	Graphic representation of the approach adopted by different compact modelling techniques.	62
4.1	Convention for surface stresses of a cubic portion of a body.	72
4.2	Trans126 connects a node of the mechanical mesh (k) to a fixed node (j), representing the behaviour of a fixed electrode.	78
5.1	Error indicators computed for a clamped-clamped beam with electrostatic actuation at 1 and 10 MHz.	106
5.2	Block scheme, which illustrate a possible algorithm for fully-automatic model order reduction using computation of the error indicator in 5.32.	107
6.1	3D finite element model of a vertical free-free resonator.	110
6.2	Deflection of two beams with different length to a pressure load applied in the center of the beam.	112
6.3	Force vs. displacement relationships for the two adopted test structures, with and without the inclusion of mechanical nonlinearities.	113
6.4	Harmonic pre-stressed analysis simulation results obtained with ANSYS full model and compact model of different order extracted using MOR.	116
6.5	Dependency of the vertical beam resonance frequency from the applied bias voltage.117	
6.6	Harmonic and S-parameter analysis simulation results of a clamped-clamped beam resonator obtained in Cadence with a 15 d.o.f. reduced order model.	118
6.7	3D finite element model of a vertical free-free resonator.	119
6.8	Displacement and current amplitude for a one port vertical free-free beam resonator with and without a plane initial stress in the movable structure. Reduced order and full model simulation results are compared.	119
6.9	First resonant mode of a lateral free-free beam resonator.	120
6.10	Harmonic and S-parameter analysis simulation results of a free-free lateral beam resonator obtained in Cadence with a 15 d.o.f. reduced order model.	121
6.11	Square resonator mode shapes simulated with ANSYS.	121
6.12	Two-port single-ended (a), two-port differential (b) and one-port single-ended electrode configuration used for the square resonator in its Lamé (a-b) and extensional (c) modes.	122

6.13	Comparison between the full model and the reduced model simulation results. . .	123
6.14	Schematic circuits used for the simulations of the square resonator in a two-port single-ended (a) and differential (b) electrode configuration.	124
6.15	Circuit level simulation of the square resonator in its Lamé mode with a single-ended (a) and differential (b) electrode configuration.	124
6.16	Motional and displacement components of the current at the terminal v_{top} for the single-ended (S) and the differential (D) configurations.	125
6.17	Circuit level simulation of the square resonator in its extensional mode.	125
6.18	Micromechanical filter mode shapes, normalized to unity.	126
6.19	Typical measurement setup of a micromechanical filter.	127
6.20	Low- and high-velocity coupling filter transmission parameter for different values of the termination resistance.	128
6.21	Displacement at the center of the filter input and output beam, when a small signal sinusoidal voltage applied to the device input terminal and for increasing values of the termination resistances.	129
6.22	Currents at the filters terminals, when a small signal sinusoidal voltage is applied to the device input terminal. Increasing values of termination resistance have been considered.	129
6.23	Simulated S_{21} parameter for a micromechanical correctly terminated filter in presence of parasitic capacitance at device terminals terminals.	130
6.24	Finite element model of the IRST switch. Only one quarter of the geometry has been considered.	130
6.25	Grouping of the external node of the switch armatureswitchconductors for capacitance calculation. Nodes with the same color belong to the same conductor. The bottom area represents the conductor surface.	131
6.26	Transient (a) and steady-state harmonic response (b) of a capacitive switch to a periodic square wave and sinusoidal signal. Experimental data are compared with compact model simulation results.	132
6.27	Finite element model of the ST switch. Only one quarter of the geometry has been considered.	133
6.28	Static pull-in behaviour of the ST switch. Full model sequential coupling results are compared with a 15 d.o.f. reduced order model results.	134
6.29	Dynamic pull-in behaviour of the ST switch in low and high damping conditions for increasing value of the applied voltage.	134
6.30	Dynamic pull-in (a) and pull-out (b) behaviour of the ST switch for a more realistic stiffness of the structure.	135
7.1	Schematic cross section of the IRST switch process.	138
7.2	Combined process-flow steps (a-g).	142
7.2	(continued) Combined process-flow steps (h-o).	143

7.3	Measured 3D profile of the photoresist surface for a $3\mu\text{m}$ resist thickness spin-coated on a substrate with trenches.	146
7.4	Cross section of the wavy area of the photoresist profile.	146
7.5	Topography of the spin-coated photoresist layer on a wafer with trenches.	147
7.6	Aspect of the resist surface after oxygen plasma etching, for an RF power of 50W 7.6(a) and 30W 7.6(b).	147
7.7	Block scheme of the designed duplexer with integrated channel selection.	149
7.8	Masks layout of the designed duplexer with integrated channel selection (a) and detail on the switch underpass lines.	150
7.9	Quality factor vs. frequency dependency for various values of the resonator width w , in case of 7.9(a) support damping and 7.9(b) thermoelastic damping. Squares and crosses represent the values corresponding to the designed clamped-clamped and free-free beam resonators, respectively.	151

List of Tables

2.1	Scaling laws of some physical forces, which can be present in microdevices, at constant voltage.	12
2.2	Thermoelastic damping coefficients for single-crystal silicon	29
2.3	Frequency scaling laws of different resonator parameters, at constant gap and voltage and assuming that the resonator dimensions scale as f^{-1} [70].	35
2.4	Comparison of realized microresonators properties.	37
2.5	Comparison between the characteristic properties of the material of interest for microresonators implementation.	41
3.1	Through/across variables couples for different energy domains	64
3.2	Electromechanical analogies for lumped transitional systems.	66
3.3	Comparison between the main properties of the previously described simulation approaches	70
4.1	ANSYS electromechanical coupling methods.	77
5.1	SVD based approximation methods	90
5.2	Comparison between the Arnoldi and the Lanczos process	95
5.3	Comparison between the presented methods for linear model order reduction	99
6.1	Geometrical dimensions of the various types of beam used in the simulations.	112
6.2	Linear and cubic stiffness coefficient extracted for different beam dimensions.	114
6.3	Comparison of the maximum displacement of beams with different geometrical parameters obtained using ANSYS sequential solver and TRANS126 elements. Different values of the applied voltage are considered.	115
6.4	Computational time for a vertical clamped-clamped beam model extraction.	117
6.5	Device dimensions and material properties.	122
6.6	Computational time comparison.	123
6.7	Computational time for the extraction and simulation of a switch compact model.	132
7.1	IRST switch process: detailed process flow [185,186].	139
7.2	IMTEK resonator process: detailed process flow [188].	140

- 7.3 Combined switch process: detailed process flow. The starting wafer is an SOI wafer with a $10\mu\text{m}$ thick device layer and a resistivity $> 3000\Omega\text{cm}$, both for the device layer and the substrate. 144
- 7.4 Geometrical dimensions (in μm) of the designed beams. L_r and W_r are the length and the width of the resonator beam, respectively, while L_s and W_s are the length and the width of the supporting beams in the free-free design. W_e is the width of the resonators electrodes. 151
-

Abstract

This thesis deals with two important research aspects concerning radio frequency (RF) microresonators and switches. First, a new approach for compact modeling and simulation of these devices is presented. Then, a combined process flow for their simultaneous fabrication on a SOI substrate is proposed.

Compact models for microresonators and switches are extracted by applying mathematical model order reduction (MOR) to the devices finite element (FE) description in ANSYS[®]. The behaviour of these devices includes forms of nonlinearities. However, an approximation in the creation of the FE model is introduced, which enables the use of linear model order reduction.

Microresonators are modeled with the introduction of transducer elements, which allow for direct coupling of the electrical and mechanical domain. The coupled system element matrices are linearized around an operating point and reduced. The resulting macromodel is valid for small signal analysis around the bias point, such as harmonic pre-stressed analysis. This is extremely useful for characterizing the frequency response of resonators.

Compact modelling of switches preserves the nonlinearity of the device behaviour. Nonlinear reduced order models are obtained by reducing the number of nonlinearities in the system and handling them as input to the system. In this way, the system can be reduced using linear MOR techniques and nonlinearities are introduced directly in the reduced order model. The reduction of the number of system nonlinearities implies the approximation of all distributed forces in the model with lumped forces.

Both for microresonators and switches, a procedure for matrices extraction has been developed so that reduced order models include the effects of electrical and mechanical pre-stress. The extraction process is fast and can be done automatically from ANSYS binary files.

The method has been applied for the simulation of several devices both at devices and circuit level. Simulation results have been compared with full model simulations, and, when available, experimental data. Reduced order models have proven to conserve the accuracy of finite element method and to give a good description of the overall device behaviour, despite the introduced approximations. In addition, simulation is very fast, both at device and circuit level.

A combined process-flow for the integrated fabrication of microresonators and switches has been defined. For this purpose, two processes that are optimized for the independent fabrication of these devices are merged. The major advantage of this process is the possibility to create on-chip circuit blocks that include both microresonators and switches. An application is, for example, a

switched filter bank for wireless transceiver. The process for microresonators fabrication is characterized by the use of silicon on insulator (SOI) wafers and on a deep reactive ion etching (DRIE) step for the creation of the vibrating structures in single-crystal silicon and the use of a sacrificial oxide layer for the definition of resonator to electrode distance. The fabrication of switches is characterized by the use of two different conductive layers for the definition of the actuation electrodes and by the use of a photoresist as a sacrificial layer for the creation of the suspended structure. Both processes have a gold electroplating step, for the creation of the resonators electrodes, transmission lines and suspended structures.

The combined process flow is designed such that it conserves the basic properties of the original processes. Neither the performance of the resonators nor the performance of the switches results affected by the simultaneous fabrication. Moreover, common fabrication steps are shared, which allows for cheaper and faster fabrication.

Chapter 1

Introduction

This thesis deals with compact modelling and simulation of microelectromechanical resonators for radio frequency (RF) applications and their integrated fabrication with RF switching devices. Compact modelling makes use of model order reduction and leads to models, which can be translated in hardware description language (HDL) for circuit level simulation. The compact modelling technique has been then extended to address also RF MEMS switches. Using the developed tools, two typologies of microresonators have been designed and the possibility of their combined fabrication with RF MEMS switches has been studied.

1.1 MEMS for RF Applications

After the introduction of silicon as a mechanical material in 1982 [1], the use of microelectromechanical system (MEMS) has spread in several applications fields. Some of the most successful MEMS-based devices are accelerometers for the automotive industry [2], ink-jet printheads, and devices for information storage, such as the IBM millipede [3].

MEMS technology is based on technological processes originally derived from the integrated circuit technology, which have been extended to cover the requirements of the different application fields. The result is a very flexible technology, offering a wide range of processes and fabrication materials, yet maintaining the advantages intrinsic to micromachining technology [4]. MEMS technology comprises both surface and bulk micromachining processes, which, eventually combined with the use of layers of sacrificial materials, allows for the realization of 3D and suspended structure. Apart from standard silicon-based materials, such as silicon, polysilicon and silicon dioxide, a large number metals can be used, including copper, gold, aluminum, titanium. Fabrication using micromachining techniques offers easy dimensional downscaling, high design flexibility, batch fabrication, and thus low dispersion of device properties, and cost reduction [5]. In addition, the possibility exists to monolithically integrate MEMS devices with CMOS circuitry.

A rather new but extremely promising application field for MEMS devices is wireless radio frequency telecommunication. Micromechanical components are suitable for signal processing and

routing in a wide frequency range [5]. Taking advantage of the resonance modes which characterize the frequency behaviour of mechanical structures, micromechanical devices can be used to perform frequency selection and generation operations. Bistable structures can also be realized to be employed for switching operations [6].

The small dimensions of MEMS devices enable various actuation principles. These include magnetostatic effects, piezoelectric effects, thermoelectric effects and electrostatic effects. One of the more commonly adopted actuation forces is electrostatic force.

The use of electrostatic forces in MEMS devices, for the excitation and the sensing of their movement, offer several advantages, such as design flexibility, freedom in the choice of fabrication material, temperature stability etc. However, the most important aspect of capacitive sensing and actuation is that it leads virtually to no power consumption.

On-chip fabrication, size reduction and low power consumption make MEMS devices very attractive for wireless transceivers. In the last place, the eligibility of these devices to be used in wireless transceivers depends on their signal processing performance. Wireless communication systems have to serve a large number of users simultaneously, which requires several communication channels with narrow bandwidth to be resolved. Consequently, transceiver functionality relies on the availability of devices with high frequency selectivity and stability. These properties are quantified in terms of device quality factor [7].

The quality factor of a system is a parameter which is a measure of the energy loss in the system. Devices with a high quality factor are characterized by low energy dissipation. For a resonating system, low energy dissipation results in sharp resonance peaks of its frequency behaviour. In signal processing, this is fundamental since it results in low signal attenuation and thus better noise performance as well as higher frequency selectivity [7].

Conventional transceiver front-end architectures employ a great number of off-chip mechanical or electrical components. Fig. 1.1 shows a classical transceiver architecture (a dual-conversion heterodyne transceiver) [7]. This operates a two-stage translation of the spectrum of the input signal at low frequency, so that this can be processed in baseband, instead of at RF frequencies [8]. This enables the selection and processing of small signals also in presence of strong interference. However, it requires numerous filtering and mixing operations both at RF and intermediate frequency (IF). Low-loss and low-noise devices for frequency selection and generation are thus required. These functionalities are at present realized using off-chip components, which are represented in Fig. 1.1 by colored blocks.

Nowadays, filtering operation in portable cellular system are realized using surface acoustic wave (SAW) devices, while frequency generation still relies on bulk acoustic wave (BAW) devices, such as quartz crystals [9, 10]. SAW devices are micromachined mechanical devices based on the piezoelectric excitation and detection of surface wave on the free surface of homogeneous piezoelectric materials. SAW Filters can be realized with center frequencies in the 50MHz-2GHz range and offer high quality factor (2000-4000) and low signal attenuation [11]. Their size is rather small, however, they cannot be realized on-chip.

BAW devices are the evolution of quartz crystals [12]. They are composed by a piece of piezoelec-

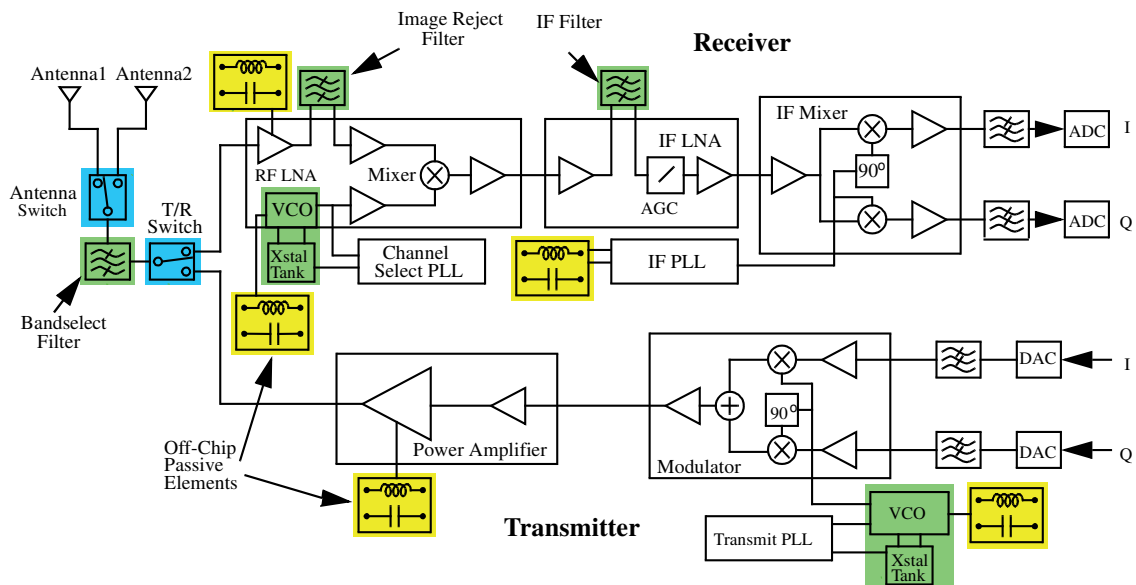


Figure 1.1: Block scheme of a dual-conversion heterodyne transceiver front-end. Colored blocks represent components off-chips in current implementations (from [7]).

tric material, in which longitudinal acoustic wave are excited using piezoelectricity. Such devices are very popular for their very high quality factor (around 100000 at 100MHz) and temperature stability [13]. However, due to technological limits, they can be used only under 500MHz. Moreover, they are bulky devices.

In basestations, also dielectric and transmission line resonators and filters are employed, which can guarantee good performance, but are again large off-chip devices [14, 15].

Off-chip devices need to interface with other electronics at board level, which is a major drawback for what concerns the area occupied by the overall system as well as its cost and its performance. RF MEMS devices are likely to overcome these problems. Micromechanical resonators and filters have proven to achieve quality factors competing with the one of SAW devices (if not defeating) and can be fabricated on-chip with CMOS control circuitry. Moreover, MEMS technology allows to realize micromechanical devices with different characteristic and functionalities on the same substrate and hence with small area occupation. Considering the small power consumption of MEMS devices, it can be concluded that MEMS components can actually be used as building blocks for the creation of new transceiver front-end architecture with enhanced functions and reconfigurability. An example is presented in Fig. 1.2, where all the colored blocks represent RF MEMS components [16]. With respect of Fig. 1.1, not only all off-chip components are replaced, but also some CMOS components. Moreover, micromechanical components allow to merge the function previously realized by multiple blocks into only one block and to realize a switched filter bank for multiple channels selection.

The promising characteristics of RF MEMS in terms of performance, cost and size attracted the attention of the scientific community and the telecommunication market. According to [17], in 2009 the RF MEMS market will exceed the one billion dollars, with commercial mobile application as

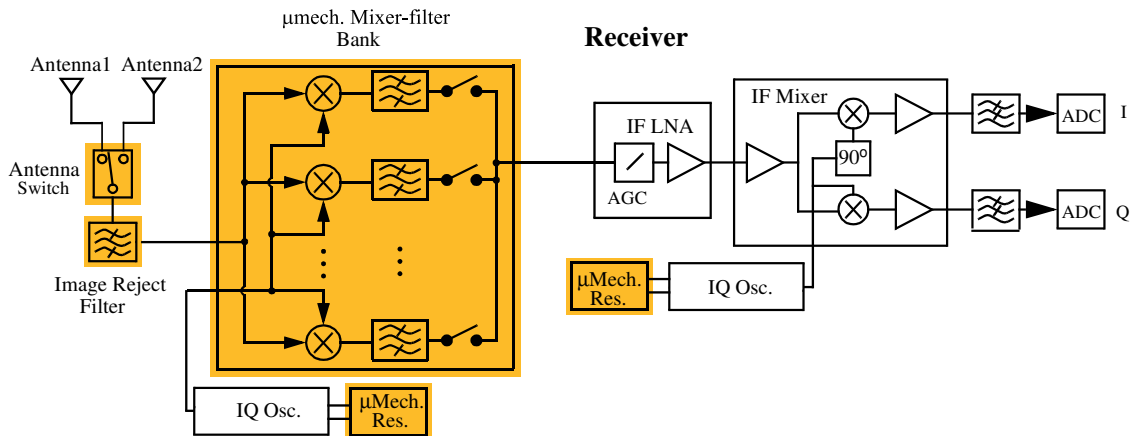


Figure 1.2: Block scheme of a new receiver architecture, which make use of RF MEMS devices. Colored blocks are realized using micromechanical devices (from [16]).

first target.

The use of MEMS devices for commercial products still requires some developments. From a device perspective, some device characteristic parameters have still to be tuned in order to satisfy application specific requirements. This is for example the case for power handling of microresonators [18] and actuation voltage for switches [6].

Fabrication issues are primarily concerned with the development of CMOS compatible fabrication processing and packaging techniques. Successful realization of CMOS and different kinds of RF MEMS devices on a same substrate is a key point for taking full advantage of the new technology. The attention of the scientific community has been particularly focused on the fabrication of a specific kind of MEMS device on a CMOS substrate. Examples of integrated RF MEMS-CMOS structures have been already demonstrated using different approaches [19–26].

Packaging of radio frequency movable devices is also a difficult and important task. Packaging materials and strategy have to be carefully chosen, since they influence the electrical and mechanical behaviour of the device, as well as its reliability and lifetime [27].

1.2 MEMS compact modelling

As for any new emerging technology, the advance in MEMS fabrication goes together with the development of new tools, which could support the device design phase. Modeling and simulation is at the basis of the prediction of the device behaviour and optimization of its performance. Modeling of MEMS devices is a very complex task. Their behaviour involves multiple coupled energy domains. The electrical and the mechanical domains are the main ones, but also the fluidic and thermal domain may be of interest. In addition, the devices have most of the time a three-dimensional and geometrically complex structure. As a consequence, MEMS modelling is always a trade-off between accuracy and computational complexity [28].

An accurate device model can be achieved using the so called physical modelling. The partial

differential equation governing the device behaviour can be discretized on the device domain. The resulting system of ordinary differential equations gives a representation of the device. Several commercial tools are already available for device physical modelling and simulation, which make use of different discretization and solution techniques [28]. However, proceeding this way, the afore-mentioned complexity factors lead to device physical models with a large number of degrees of freedom: 10-100 thousands of equations to solve represent a standard problem.

The complexity of the simulation analysis adds to the complexity of the model. MEMS characterization often requires computationally expensive analysis such as transient analysis. Moreover, the derived models are often nonlinear. The primary source of nonlinearity is the electrostatic force, which couples the electrical and mechanical energy domains. Simulation of nonlinear models makes use of iterative time consuming algorithms.

The use of RF MEMS for signal processing and their tight link with external electronics requires simulation to be performed at circuit level. In order to correctly predict the device behaviour, simulation of the complete circuit in which the device is included has to be performed.

Modern computers are capable of handling very large and complex problems. However, a reduction of the problem complexity becomes mandatory when the number of d.o.f. of the single device or of the complete circuit to simulate drastically increases. This is easily the case for future highly reconfigurable transceivers for wireless applications. These might in fact include several micromechanical components together with RF CMOS circuitry. The size of the problem to solve will therefore explode. The availability of lower order models is extremely convenient for optimization purposes, since a large part of the optimization techniques makes use of an iterative algorithm and thus requires multiple solutions of the problems to be performed.

A possibility for simulation complexity reduction of MEMS devices is compact modelling. Compact modelling developed within the framework of a hierarchical design and simulation, which is based on the study of the behaviour of complex systems at different levels of complexity and accuracy. The term compact modelling addresses all the techniques that can be used to extract reduced order models of complex devices. Reduced order models are characterized by a higher degree of approximation with respect to physical models, but they allow fast simulation of complex systems. The concept of compact modelling is not new. The huge development of very large scale integrated systems (VLSI), for example, would have probably not been possible without the availability of compact models of single transistors to be employed for the simulation of the complete system and the use of a hierarchical design approach.

Various compact modelling approaches have been proposed and various tools are available for simulations at different levels. The first approaches introduced were borrowed from the IC or the mechanical world. These include for example analytical modelling, semi-empirical modelling, extraction of equivalent circuit models, structural analysis and mode superposition methods. A great part of these approaches starts from the PDE governing the device behaviour and reduce them to a low dimensional ODE system introducing strong simplifications of the starting equations or using a coarse discretization of the problem. The reduction process is in these cases strongly based on the knowledge of the device behaviour and on intuition.

A second class of compact modelling techniques, which is emerging in the last years, is mathematical model order reduction (MOR). These techniques were developed in the framework of control theory and have been only lately applied to the complexity reduction of MEMS simulations [29]. However, their potential in these fields is extremely promising. Mathematical MOR is not directly concerned with the creation of a device model. Starting point for the extraction of a device reduced order model is already its description with a (large) ODE system, which is typically derived using physical modelling techniques. MOR application allows the extraction of lower order ODE system that reproduces the input/output behaviour with good accuracy. Unlike the approaches previously introduced, the method is thus solely based on the mathematical properties of the original system and is therefore formal, robust and in great part automatic [29]. Little knowledge of the reduction mechanism is required from the user. These properties render the use of mathematical model order reduction more and more popular in the study of MEMS devices [29–32], even if tools for MOR are still scarcely available in the public domain.

MOR techniques have been originally developed for large order linear systems. Their extension to nonlinear systems is not trivial. It represents a major issue for the application of this technique to RF MEMS, due to the nonlinearity of the coupling between the electrical and mechanical domains that is characteristic for these devices. Nonlinear MOR techniques are currently under study, but, at present, they often lead to loss of the possibility of extraction of a reduced order model in an automatic fashion [33].

In this work, model order reduction has been applied to the modelling of RF MEMS by performing a complexity reduction at different stages of the device modelling and simulation. First, an assumption about the device behaviour and/or operating conditions is made, which renders the device physical model suitable to be reduced with linear model order reduction. Then linear MOR is applied to extract a reduced order model from the original one. The resulting compact modelling process is therefore hierarchical: one step deals with the creation of the large dimensional model, based on the knowledge of the device behaviour, and the second one with its reduction. In this way, the modelling step can be specialized to improve the description of various devices, while the reduction step is device independent and conserves the properties of mathematical reduction.

The approach has proven successful for compact modelling of both microresonators and switches. In order to fill the gap between MOR mathematical theory and its practical application to the design and simulation of these devices, two procedures have been developed. These enable proper modelling of these devices, using the commercial finite element simulation tool ANSYS[®], and the correct creation and extraction of the system element matrices representing the original model. Such matrices are reduced automatically using the tool MOR for ANSYS [34], which has been extended to handle the new type of problem. Reduced order models have been translated into the HDL language VerilogA and their use in circuit simulation has been demonstrated.

1.3 Integrated resonators-switches fabrication

The materials adopted for the fabrication of RF MEMS devices strongly depends on its function. Vibrating devices have to be fabricated with high stiffness materials, in order to achieve high resonance frequencies with relatively big structures. The mechanical resonance frequency of a structure is in fact directly proportional to the structure stiffness and inversely proportional to its dimensions. Switching devices instead should be realized with low stiffness material, since this influences the voltage values needed to achieve their toggling. Moreover, switches are generally planar devices while, for resonators, structures with high aspect ratio are often preferable. This results in specific fabrication processes, which are generally specialized for the optimized fabrication of only one type of devices, either resonators or switches. However, for the on-chip creation of circuit blocks including both devices, such as the switched filter bank in Fig. 1.2, a combined fabrication of microresonators and switches is advantageous in terms of performance, size and costs [7].

As for the RF MEMS-CMOS integration, the realization of vibrating and switching devices, both with optimized performance, on a same substrate can give rise to compatibility issues. Typical problems encountered are different thermal budget for the materials present on the wafer, high topography of the substrate, which cause planarity problems, and protection of one type of devices while processing the other type. While various approaches have been proposed in literature for the integration of CMOS and MEMS devices, little can be found about combined microresonators-switch fabrication.

A combined process flow for microresonators and switches fabrication on a silicon on insulator substrate has been developed by merging the process flows, which had been previously developed and used for an optimized fabrication of microswitches [35] and microresonators [36]. In the case considered, a simultaneous fabrication of switch and resonator appears to be the optimal choice, since it allows to minimize the number of masks and process steps needed for the combined process, thus reducing costs and fabrication time. The process flow presents a few critical steps, which have been handled in order to guarantee the minimum loss of optimality with respect to the original single fabrication processes.

1.4 Thesis outline

The material in this thesis is organized as follows. In chapter 2, an introduction on RF MEMS resonators and switches is proposed. This includes the working principle of these devices, the parameters which are important in device design optimization, the possible applications of the devices in the telecommunication field and an overview of the device fabrication technology.

In chapter 3, a short description of the principle approaches used for physical and compact modelling of electrostatically actuated MEMS devices is presented. These methods essentially represent the state of the art for MEMS modelling and simulation, with respect to the approach of this thesis.

Chapter 4 presents the governing equations for the considered electromechanical problem and derive the form of the ODE system to which model order reduction will be applied.

In chapter 5, various approaches for linear and nonlinear model order reduction are reviewed and the different choices for the compact modelling of microresonators and switches are presented.

The introduced compact modelling approach is applied to the simulation of vibrating and switching devices both at device and system level. Simulation results are presented in chapter 6.

Finally, chapter 7 deals with the design choices for the fabrication of SOI microresonators and with the development of a combined microresonators/microswitches process flow.

Chapter 2

RF MEMS active devices

This chapter gives an introduction on microelectromechanical active devices for radio frequency application, that is microresonators and microswitches. The working principle of both devices is described, together with the main applications and the parameters, which are important to characterize their performance. Some realization examples are then presented and the technology used for their fabrication.

2.1 Radio frequency MEMS devices

RF MEMS are generally classified according to their functionality in passive components, that is inductors and tunable capacitors, and active components, including microresonators and switches. In this thesis, only active devices will be considered.

2.2 Microelectromechanical resonators

A *resonator* is any device that, under particular excitation conditions, exhibits a natural vibratory response [37]. Using this definition, it can be said that a micromechanical resonator is a device, which bases its functionality on the mechanical resonance of one of its component structures.

Microresonators have been used for several applications. Their first use was for sensing purpose, such as chemical [38], vapor [39] and pressure sensors. In radio-frequency applications, microresonators are essentially used for their capabilities as electromechanical transducers. The conversion between electrical and mechanical energy can be done using different transduction principles, corresponding to different method for excitation and detection of the mechanical vibration. One can distinguish:

- piezoelectric electric effect,
 - thermo-mechanical expansion,
 - magnetostatic effect,
-

- electrostatic effect,

for conversion from electrical and mechanical, and:

- piezoelectric electric effect,
- piezoelectric resistive effect,
- magnetostatic effect,
- electrostatic effect,

for the reverse conversion. The majority of resonators presented until now uses for both the energy conversions the electrostatic effect, with capacitive excitation and sensing. This is mainly due to the fact that piezoelectric and magnetic actuation and/or detection usually requires special material, which are not available in standard IC foundry. Electrostatic forces instead occur between any couple of conductive materials. In addition, due to the scaling laws of physical fields with device dimensions, electrostatic forces are dominant with respect to magnetic forces (see Table 2.1). Assuming constant voltage, if L_c is the typical device length, magnetic forces scale with L_c^2 , while electrostatic forces do not scale. Forces due to thermal expansion and piezoelectric effects scale as magnetic forces. Their relative importance depends from the specific material properties, through the coefficient of thermal expansion α and the piezoelectric coefficient d . Moreover, capacitive actuation and sensing generally results in lower design complexity, compared to the other transduction methods, and are rather insensitive to changes in temperature, which is required in order for the device to have stable performance in different working environments. Lately, piezoelectric resistive resonators have also been presented [40].

2.2.1 Working principle

First order analysis

Equations describing mechanical and electric behaviour of a resonator are necessary design dependent. For a first understanding of microresonator behaviour an idealized model can be considered. Any device is basically constituted by a movable mechanical structure, surrounded by one or more electrodes. Here, the movement of the structure will be reduced to a one-dimensional

Table 2.1: Scaling laws of some physical forces, which can be present in microdevices, at constant voltage.

Physical forces	Generalized expression	Scaling law
Mechanical force	$L_c^2 \sigma$	L_c^2
Thermal expansion force	$\alpha L_c^2 \Delta T$	L_c^2
Piezoelectric force	$d L_c^2 \sigma$	L_c^2
Electrostatic force	$L_c^2 E^2$	1
Magnetic force	$L_c^2 B^2, B L_c$	L_c^2

damped rigid motion. Moreover, only one electrode will be considered, which forms with the movable structure a variable parallel plate capacitor. The device can be schematically described with the one-dimensional lumped model in Fig. 2.1, which is applicable to the simplified description of any electrostatically actuated MEMS device. The structure is represented by a mass/spring system while the electrostatic interaction is represented by a variable capacitor $C(y)$. Damping phenomena are included in the model by the addition of a damper.

When a voltage V is applied between the suspended structure and the actuation electrode, electrostatic forces pull the structure towards the actuation electrode. The structure movement causes a variation of the capacitance between the actuation electrode and the structure itself. The equilibrium of the forces acting on the movable structure is given by d'Alembert equation [41]:

$$m\ddot{y} = F_m + F_e + F_{damp} \quad (2.1)$$

where F_m is the elastic force exerted by the spring k_m , F_e is the electrostatic force between the plates of the capacitor and F_{damp} represents the damping force. Gravity effects are neglected because their entity is much smaller than the entity of the other forces into play. With the sign convention of Fig. 2.1, assuming a linear spring force and that for $y = 0$ the spring is in rest condition, the elastic force is given by:

$$F_m = -k_m y.$$

For the damping force a simple viscous model is considered, in which the force is proportional to the velocity of the structure:

$$F_{damp} = c\dot{y}.$$

Substituting the expression of the forces in (2.1), we find the equation of motion:

$$m\ddot{y} + c\dot{y} + k_m y = F_e(y, t) \quad (2.2)$$

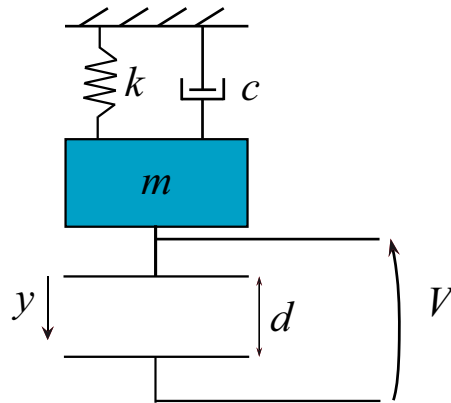


Figure 2.1: Lumped model of a resonator.

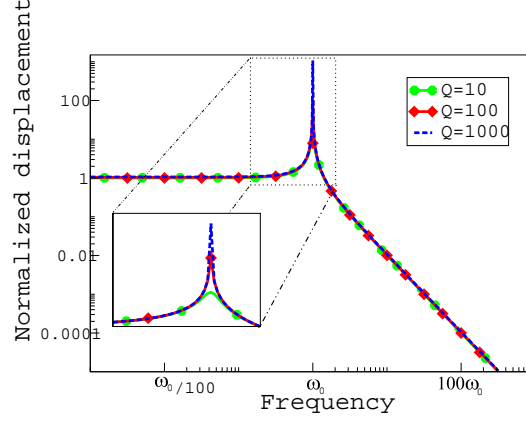


Figure 2.2: Normalized displacement $|Y|$ as a function of the frequency, for different values of the quality factor Q .

that is simply the equation of a damped harmonic resonator with forcing term $F_e(y, t)$, which depends explicitly on the displacement y and on time, both through V and y . Neglecting the dependency of the electrostatic force on the displacement, this simple equation allows a preliminary study of the device behaviour. Assuming that the displacement varies periodically with a certain angular frequency ω , setting the forcing term to zero and solving for ω , the mechanical resonance angular frequency of the system is found. In the undamped and damped case, this is respectively given by:

$$\omega_0 = \sqrt{\frac{k_m}{m}}$$

$$\omega_{0,damped} = \omega_0 \sqrt{1 - \zeta^2},$$

having introduced the damping ratio $\zeta = \frac{c}{2m\omega_0}$. Thus, dissipation phenomena lead to a decrease of the system resonance frequency.

The frequency behaviour of the device displacement can be described by taking the Laplace transform $\mathcal{L}(x)$ of both sides of equation (2.2). Assuming $Y = \mathcal{L}(y)$, $F = \mathcal{L}(f)$ and $s = j\omega$, it is [41]:

$$Y = \frac{F}{s^2 m + s\gamma + k_m}.$$

The displacement amplitude for a certain excitation frequency is then given by:

$$|Y| = \frac{F}{k_m \sqrt{\left(1 - \frac{\omega^2}{\omega_0^2}\right)^2 + \left(\frac{\omega}{Q\omega_0}\right)^2}}$$

where $Q = \omega_0 m / c = 1/2\zeta$. From the plot in Fig. 2.2, it can be seen that for frequency of the excitation force lower than ω_0 the amplitude of the displacement is simply given by F/k_m , while when the excitation frequency is close to ω_0 this amplitude increases. At resonance, the low frequency value of the displacement is amplified by a factor Q . Q is the *quality factor* of the system, which gives a description of the device overall damping behaviour in the frequency domain. The higher is the quality factor, the sharpest is the resonance peak.

Modal shape and dynamic bending behaviour

The modal shapes and dynamic bending behaviour of a device can be derived from its constitutive equations, together with proper values to assign to the lumped model parameters of Fig. 2.1. Here, the procedure will be presented for a clamped-clamped beam resonator, but it can be extended with small modification to any other device.

A simple model of clamped-clamped beam resonator is shown in Fig 2.3. The one-dimensional differential equation of motion governing the deflection $y(x, t)$ of the beam at its location x (with x extending from 0 to the length L_r of the beam), in presence of an axial tensile load S and a transverse driving load $F(x, t)$ is

$$\frac{EI}{1 - \nu^2} \frac{\partial^4 y(x, t)}{\partial x^4} - S \frac{\partial^2 y(x, t)}{\partial x^2} + \rho W_r h \frac{\partial^2 y(x, t)}{\partial t^2} + c \frac{\partial y(x, t)}{\partial t} = F(x, t) \quad (2.3)$$

with boundary conditions

$$\begin{aligned} \frac{\partial y}{\partial x} \Big|_{x=0} &= 0 & \frac{\partial y}{\partial x} \Big|_{x=L_r} &= 0 \\ y \Big|_{x=0} &= 0 & y \Big|_{x=L_r} &= 0 \end{aligned}$$

where E , ν , I , ρ , c , W_r and h are respectively Young modulus, Poisson ratio, second moment of inertia, density, viscous drag parameter, width and thickness of the beam [42]. Such an equation neglects the effects of shear displacement and rotary inertia. Assuming a driving load of the type:

$$F(x, t) = f(x)e^{j\omega t}$$

the steady state solution to equation (2.3) may be expressed as an infinite series of the orthogonal modal shape functions ϕ_n [43]:

$$y(x, t) = \sum_{n=1}^{\infty} y_n(t) \phi_n(x). \quad (2.4)$$

Neglecting axial forces, the general solution for the beam modal shape functions are

$$\phi_n(x) = A \cdot \sin \lambda_n x + B \cdot \cos \lambda_n x + C \cdot \sinh \lambda_n x + D \cdot \cosh \lambda_n x, n \in [1, \infty[$$

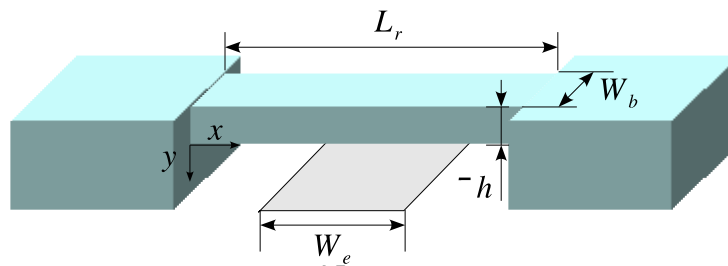


Figure 2.3: Schematic model of a clamped-clamped beam resonator.

where

$$\lambda_n^4 = \frac{\rho h W_r \omega^2}{EI}.$$

For the given boundary conditions:

$$\phi_n = u_n [\sin \lambda_n x - \sinh \lambda_n x + \xi_n (\cos \lambda_n x - \cosh \lambda_n x)] \quad (2.5)$$

where $\xi_n = \frac{\sinh \lambda_n L_r - \sin \lambda_n L_r}{\cosh \lambda_n L_r - \cos \lambda_n L_r}$ and u_n is a scaling factor, generally chosen so that:

$$\max_{x \in [0, L_r]} \phi_n(x) = 1$$

The mechanical resonance frequencies are defined by the equation:

$$f_n = \lambda_n^2 \sqrt{\frac{EI}{\rho h W_r}} \quad (2.6)$$

with

$$\cos \lambda_n L_r \cosh \lambda_n L_r = 1.$$

Inserting $I = (W_r h^3 / 12)$ and $\lambda_1 L_r = 4.703$ in (2.6) gives for the fundamental frequency:

$$f_1 = 1.03 \sqrt{\frac{E}{\rho}} \left(\frac{h}{L_r^2} \right) \quad (2.7)$$

From the computation of the values of λ_n , it can be noticed that the spacing between resonance frequencies is not constant, but increases with the mode number n . In real structures and operating conditions, the resonance frequency of the device differs from the nominal one. The expression (2.7) in fact ignores the effects of damping and nonlinear loading of the structure, which will be considered in 2.2.2.

If we substituted the expression (2.4) of $y(x, t)$ in (2.3) we obtain:

$$\sum_{n=1}^{\infty} \frac{EI}{1 - \nu^2} \lambda_n^4 y_n(t) \phi_n(x) + \rho W_r h \frac{dy_n^2(t)}{dt^2} \phi_n(x) + c \frac{dy_n(t)}{dt} \phi_n(x) = F(x, t)$$

If both sides of the equation are multiplied by ϕ_i and integrated over the beam length, considering that for the orthogonality of the mode shape functions it is:

$$\int_0^{L_r} \phi_i(x) \phi_j(x) dx = 0 \quad \forall i \neq j$$

an infinite set of decoupled equation independent from x is obtained, which gives the time-dependent deflection of the beam in principal coordinates [43]. For the mode n , it is:

$$m_n^{eq} \ddot{y}_n + \gamma \dot{y}_n + k_n^{eq} y = f(t) \quad (2.8)$$

where m_n^{eq} , k_n^{eq} , γ and f are respectively the equivalent beam mass, the equivalent beam bending stiffness, a damping coefficient and a position independent force. These quantities are given by:

$$m_n^{eq} = \rho S \int_0^{L_r} \phi_n^2(x) dx \quad (2.9)$$

$$k_n^{eq} = \frac{EI}{1 - \nu^2} \lambda_n^4 \int_0^{L_r} \phi_n^2(x) dx = \omega_n^2 m_n^{eq} \quad (2.10)$$

$$\gamma = c \int_0^{L_r} \phi_n^2(x) dx \quad (2.11)$$

$$f_n(t) = \int_0^{L_r} F(x, t) \phi_n(x) dx. \quad (2.12)$$

The equivalent mass and spring values of the beam describe the inertia and elastic behaviour of the beam when it is excited in its n -mode. In particular, with the normalization choice made, the equivalent mass corresponds to the mass of a material point that moving at the velocity of the location $x = L_r/2$ of the beam would have a kinetic energy equal to the peak kinetic energy of the beam. An equivalent mass can be defined at any location of the beam as [44]:

$$m_n^{eq}(x) = \frac{\rho S \int_0^{L_r} \phi_n^2(x) dx}{\phi_n^2(x)}.$$

The equivalent spring constant at the location x is then derive by multiplying $m_n^{eq}(x)$ for ω_n^2 . Computing the integral in (2.10) for the first mode, it is: $m_n^{eq} \approx 0.37 \rho S L_r$. Hence, less than one half of the physical mass of the beam participates to the movement.

The generalized load $f_n(t)$ is a measure for the efficiency of the excitation of a particular mode. A high value of f_n results in a large contribution of the mode n to the overall device response. A proper choice of the load allows to excite some modes and suppress some others [45]. With a symmetric excitation for example, only symmetric modes give contribution to the expression of the beam dynamic deflection.

Capacitive excitation

Let now consider the electrostatic force. The voltage applied between the beam and the electrode is usually composed by an AC voltage signal v_i at a certain angular frequency ω , superimposed to a large DC voltage V_{bias} . With this voltage configuration, the energy stored in the system is [45]:

$$E = \frac{1}{2} C (V_{bias}^2 + 2v_i V_{bias} + v_i^2), \quad (2.13)$$

where C is the capacitance between the beam and the electrode. Assuming that the direction of the electric field is perpendicular to the x -axis along the entire length of the beam, the driving force for unit length of the resonator is [45]:

$$F(x, t) = \frac{1}{2} \frac{\epsilon W_r}{(d - y(x, t))^2} (V_{bias}^2 + 2V_{bias}v_i + v_i^2) \quad (2.14)$$

where d is the transduction gap. The total force is found integrating (2.14) over the width W_e of the actuation electrode.

The dc-bias V_{bias} effectively acts to create and amplify force components at the frequency of the AC excitation voltage $v_i(t)$. The force applied to the resonator is in fact composed by three terms. The first term is a DC force that statically bends the beam, but has little effects on its signal processing function. The second term is a force at the frequency of the input signal, with amplitude proportional to the DC-bias voltage V_{bias} . When this frequency is close to the resonance frequency of the beam, this force drives the beam into resonance, creating a time-varying capacitance between the electrode and the beam. The third term would be instead capable to excite the beam vibration for a frequency of the input signal equal to half the resonance frequency of the beam. Far from this frequency, the displacement driven by this force component is not Q-amplified. If V_{bias} is large compared to v_i , as in typical microresonators operating conditions, the quadratic term can be neglected [46]. Assuming $v_i \ll V_{bias}$, the AC driving load reduced to

$$F(x, t) \approx \frac{\epsilon W_r V_{bias} v_i}{(d - y(x, t))^2}. \quad (2.15)$$

The deflection y has a static component, $y_{stat}(x)$, caused by the static term in (2.14), together with a harmonic component, $y_i(x, t)$, which can be decomposed as in (2.4). Without any further assumption the substitution of the expression of $F(x, t)$ in (2.12) leads to a nonlinear equation in the modal displacement y_n , which can be solved only numerically.

If the voltage signal is much lower than the DC voltage, then it can also be assumed that $y_i(x, t) \ll y_{stat}(x)$ at any instant in time [45]. In this case, it is:

$$f_n(t) = \epsilon W_r V_{bias} v_i \int_{W_e} \frac{\phi_n(x) dx}{(d - y_{stat}(x))^2}. \quad (2.16)$$

Let us now consider the current $i(t)$ flowing through the variable capacitance. If y_i is written in the form $y_i(x, t) = \tilde{y}_n(t)\phi_n(x)$, as in (2.4), with the n th mode excited by the electrostatic force, such a current is given by:

$$i(t) = \frac{dCV}{dt} = C \frac{dV}{dt} + V \frac{dC}{dt} \simeq C_0 \frac{dv_i}{dt} + V_{bias} \frac{dC}{dt} \quad (2.17)$$

with

$$C_0 = \epsilon W_r \int_{W_e} \frac{dx}{d - y_{stat}(x)} \quad (2.18)$$

$$\frac{dC}{dt} = \frac{dC(y(t))}{dt} = \left(\epsilon W_r \int_{W_e} \frac{\phi_n(x) dx}{[d - y_{stat}(x)]^2} \right) \frac{d\tilde{y}_n}{dt} \quad (2.19)$$

where the integrals are taken on the width of the electrode. Defining a new variable, the *electromechanical transduction factor* η , given by:

$$\eta = V_{bias} \frac{dC}{dy} = \epsilon W_r V_{bias} \int_{W_e} \frac{\phi_n(x) dx}{[d - y_{stat}(x)]^2} \quad (2.20)$$

the current can be also written as

$$i(t) = C_0 \frac{dv_i}{dt} + \eta \frac{d\tilde{y}_n(t)}{dt} = i_{ac} + i_{motional} \quad (2.21)$$

The first term in (2.21) is the AC current in the capacitor C_0 , while the second term, known as *motional current*, arises from the time-dependency of the capacitance. With the further assumption that $y_{stat} \ll d$ and that $\phi_n(x) \approx \phi_n(L_r/2)$ for all the x in the integration interval of equation (2.20), the above definitions can be simplified to

$$C_0 = \frac{\epsilon W_r W_e}{d} \quad (2.22)$$

$$\frac{dC}{dy} = \frac{\epsilon W_r W_e}{d^2}.$$

and the electromechanical transduction factor becomes: $\frac{\epsilon V_{bias} W_r W_e}{d^2}$.

Close to the resonance frequency ω_n , the displacement $\tilde{y}_n(t)$ can be written as:

$$\tilde{y}_n(t) = \frac{Q f_n(t)}{k_n^{eq}}.$$

The total force acting on the beam can be expressed in function of η simply as:

$$f_n(t) = \eta v_i. \quad (2.23)$$

Thus, it is:

$$\tilde{y}_n(t) = \eta \frac{Q}{k_n^{eq}} v_i(t) \quad (2.24)$$

$$\frac{d\tilde{y}_n(t)}{dt} = \eta \frac{Q}{k_n^{eq}} \frac{dv_i(t)}{dt}.$$

These equations can be interpreted as follows. The application of an AC voltage between the beam and the actuation electrode results in the electrostatic force (2.23), which causes the beam to vibrate according to the equation (2.8). Electrical energy is thus converted into mechanical energy. On the other side, the movement of the beam generates a new term in the current through the device, the motional current, which allows the sensing of the beam vibration and thus the inverse conversion. When the frequency of the applied signal is equal to the beam mechanical resonance frequency, the beam displacement is amplified by a factor Q and thus also the motional current results amplified by this factor. The electromechanical transduction factor gives a measure of the efficiency of the energy transformation in both directions. Note that a rigorous treatment would lead to the introduction of a stiffness effective coefficient which differ from k_n^{eq} , due to the nonlinear dependency of the excitation load from the beam dynamic deflection, here neglected. An exact expression for the coefficient can be found in [47].

Due to the capacitive actuation mechanism, no DC current flows in the device and thus the power consumption is theoretically zero. This is true for all electrostatic actuated MEMS devices.

Electric equivalent circuit

The simplified equations describing the resonator behaviour can be simply translated into an electrical equivalent circuit. By using equations (2.21) and (2.23), equation (2.8) can be rewritten as [41]:

$$\frac{m^{eq}}{\eta^2} \frac{di_{motional}}{dt} + \frac{\gamma}{\eta^2} i_{motional} + \frac{k^{eq}}{\eta^2} \int i_{motional} dt = v_i$$

where the subscripts indicating the excited mode have been dropped for simplicity. It is then easy to recognize the equation of a series RLC circuit that relates the motional current to the AC voltage, with motional parameters given by:

$$R_m = \frac{\gamma}{\eta^2} = \frac{\sqrt{k^{eq}m^{eq}}}{Q\eta^2} \quad (2.25)$$

$$C_m = \frac{\eta^2}{k^{eq}} \quad (2.26)$$

$$L_m = \frac{m^{eq}}{\eta^2} \quad (2.27)$$

R_m is the so called *motional resistance* of the resonator and fixes the entity of the motional current in the device. The complete electrical equivalent circuit of the resonator is shown in Fig. 2.4(a), where a second branch has been added in parallel to the motional one in order to represent the AC-current path.

The representation derived is the current analogue of equation (2.8) and is not unique [41]. A

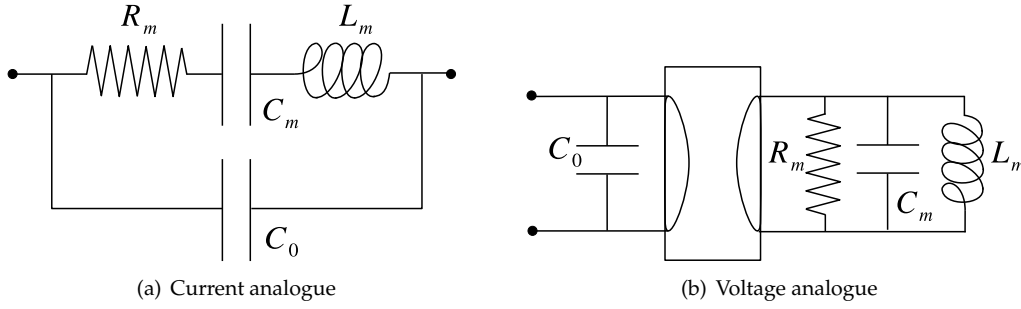


Figure 2.4: Micromechanical resonator equivalent circuits.

voltage analogue can be similarly derived by setting in (2.8):

$$\frac{dy}{dt} = u_{vel}, \quad (2.28)$$

$$f = i_{force}.$$

The resulting equation is:

$$C_m \frac{du_{vel}}{dt} + \frac{1}{R_m} u_{vel} + \frac{1}{L_m} \int u_{vel} dt = i_{force} \quad (2.29)$$

where

$$R_m = \frac{1}{\gamma} \quad C_m = m^{eq} \quad L_m = \frac{1}{k^{eq}}.$$

This is the equation of a parallel LRC resonator. Current and voltage in the circuit are only equivalent quantities. The relation between mechanical and real current and voltage:

$$i_{motional} = \eta u_{vel} \quad v_i = \frac{i_{force}}{\eta}$$

which are the equations of a gyrator. The resulting total circuit is shown in Fig. 2.4(b).

2.2.2 Second order effects

In the previous section, a simplified description of the behaviour of a microresonator has been given, based on the assumption that the device deflections are very small and therefore the mechanical stiffness of the structure is linear and the electrostatic forces can be linearized. In this section, these two approximations are revisited. However, in order to keep the calculations simple, a lumped device model as in Fig. 2.1 is still used.

Spring softening

Let us assume that the microresonator behaves as a rigid body. In this case, electrostatic forces can be written as:

$$F_e = \frac{\epsilon S V^2}{2(d-y)^2}.$$

where $S = W_r W_e$ is the coupling area between the resonator and the actuation electrode. If we develop such an expression in Taylor series of y around $y = 0$ till the third order, we have [48]:

$$F = \frac{\epsilon S V^2}{2d} \left(1 + \frac{2y}{d} + \frac{3y^2}{d^2} + \frac{4y^3}{d^3} + \mathcal{O}(y^4) \right) = F_0 + k_e x + k_{e1} x^2 + k_{e2} x^3 + \mathcal{O}(y^4) \quad (2.30)$$

Together with the constant force F_0 , a linear spring term and two nonlinear spring terms appear. The linear spring term is generally referred to as *electrical stiffness* and it is responsible for the dependency of the resonance frequency of the device from the applied bias voltage. This phenomenon will be here described, while higher order nonlinearities will be considered together with mechanical nonlinearities.

The movements of the beam towards the y positive direction causes an increase in the elastic force in the opposite direction, but also an increase of the electrostatic force, which is directed in the positive y direction. Such an increase can be interpreted as a reduction in the stiffness of the structure. The effect can be expressed mathematically using the expression (2.30) of the electrostatic force, in which the nonlinear terms are neglected. By setting the first order expansion of the force in (2.2) and grouping the terms in y on the left hand side, the equation of motion reads:

$$m\ddot{y} + \gamma\dot{y} + (k_m - k_e)y = \frac{\epsilon S}{d}.$$

The electrical stiffness $k_e = \epsilon S V^2 / d^2 > 0$ subtracts to the mechanical stiffness thus lowering the total stiffness of the structure. Consequently, its resonance frequency, which is proportional to the square root of the total stiffness, is decreased and depends on the applied voltages. If we assume the same voltage configuration as in the previous section, then k_e is proportional to the applied bias voltage V_{bias} . The phenomenon, known as *spring softening*, can be used for a fine tuning of the resonance frequency of the device.

Mechanical nonlinearity

Up to here, the relation between structure stiffness and displacement has been assumed linear as well as the behaviour of the material. Nevertheless, in the general case, this assumption does not hold, and the elastic force has to be written as:

$$F_{el} = -k_m y - k_{m1} y^2 - k_{m2} y^3 + \mathcal{O}(y^4) \quad (2.31)$$

where k_m is the usual linear spring stiffness and k_{m1} and k_{m2} are the first and second order corrections, respectively. The importance of higher terms contributions for electrostatic and elastic force

calculation increases with the vibration amplitude, and it is therefore dependent on the applied voltages.

Considering the nonlinear expressions for the elastic and the electrostatic force, the lumped equation of the resonator becomes:

$$m\ddot{y} + \gamma\dot{y} + ky + k_1y^2 + k_2y^3 = F. \quad (2.32)$$

with $k = k_m - k_e$ and $k_i = k_{m_i} - k_{e_i}$. The presence of nonlinear terms causes the angular vibration frequency of the resonator to differ from its linear value ω_0 and to depend on the oscillation amplitude. Equation (2.32) can be solved for the undamped unforced case by carrying out a perturbation analysis [48]. Introducing a perturbation parameter ε , a solution of the equation is searched in the form:

$$y = y_0 + \varepsilon y_1 + \varepsilon^2 y_2.$$

The new angular frequency of the resonator is then written as: $\tilde{\omega}_0 = \omega_0 + \varepsilon\omega_1 + \varepsilon^2\omega_2$. Calculations yield to the displacement and the angular frequency of the system. For what concerns the displacement:

- the first component y_0 has only one term, periodic with frequency $\tilde{\omega}_0$ and a certain amplitude X_0 ;
- the second component y_1 adds two corrections to y_0 : a constant term and a harmonic term with frequency equal to $2\tilde{\omega}_0$;
- the last component considered also adds two terms: an additional term with frequency $\tilde{\omega}_0$ and one with frequency $3\tilde{\omega}_0$.

If we consider that y_0 is actually the desired signal, the term at frequency $\tilde{\omega}_0$ in y_2 causes noise and interference in the signal band and it is thus detrimental in communication systems.

The angular frequency of the structure $\tilde{\omega}$ is given by [48]:

$$\tilde{\omega} = \omega_0 + \kappa X_0^2 \quad (2.33)$$

where

$$\kappa = \frac{3k_2}{8k}\omega_0 - \frac{5k_1^2}{12k^2}\omega_0.$$

Fig. 2.5 show the effects of the expression (2.33) of the resonance frequency on the behaviour of the system. Increasing values of the resonator quality factor and thus of the vibration amplitude X_0 , have been plotted. Depending on the signs of k_1 and k_2 , the resonance peak shift towards higher or lower frequency. If the mechanical spring constants dominates the structure get stiffer and the peak moves towards higher frequencies, while if the electrical spring constants dominates the shift is towards lower frequencies. The prevalence of one or the other nonlinear force components depends mainly on the applied voltage, on the entity of the transduction gap and on the structure stiffness and geometry. At high excitation levels, the amplitude-frequency relation

shows hysteresis. The bifurcation point corresponds to the point where the slope of the curve becomes infinite. After bifurcation, the amplitude-frequency curve is no longer a single valued function. The value of the vibration amplitude of the curve at bifurcation sets the maximum value of vibration amplitude before hysteresis and can be used to estimate the limit for linear operation of the device [48]. The bifurcation point and the critical vibration amplitude are given by:

$$y_b = \sqrt{\frac{\omega_0}{\sqrt{3}Q|\kappa|}} \quad y_c = \sqrt{\frac{4\omega_0}{3\sqrt{3}Q|\kappa|}}$$

High-Q devices results therefore more sensitive to nonlinearities. The critical vibration amplitude fixes also the maximum energy, which can be stored in the resonator, given by:

$$E_{max} = \frac{1}{2}ky_{max}^2 = \frac{1}{2}ky_c^2. \quad (2.34)$$

2.2.3 Present status

Micro resonator designs can be basically classified with respect to the type of capacitive coupling used, the kind of resonant modes excited and the shape of the resonating and anchoring structures.

In the previous treatment, a parallel plate transducer has been assumed, but resonators based on interdigitated transducers have also been realized [46, 49]. If this kind of transduction is used, the movement of the mechanical structure causes a variation in the area of the coupling capacitance, so that the voltage-displacement relation is actually linear. Moreover, increasing the number and/or the dimensions of the transducers combs, the electromechanical transduction factor can be improved without adding technological complexity to the device realization. On the other side, comb-resonators are relatively large and consequently are not suitable for high-frequency applications. In the last years, the attention is thus focused on resonators with parallel transduction. These can be grouped into flexural and longitudinal mode resonators.

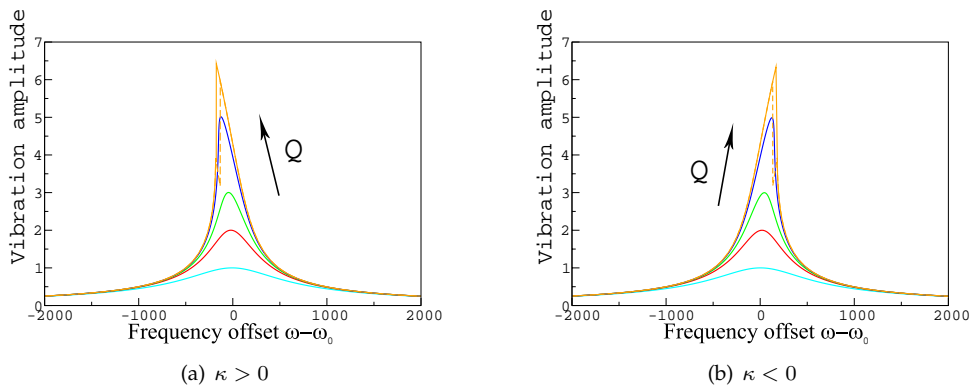


Figure 2.5: Effects of high order nonlinearities.

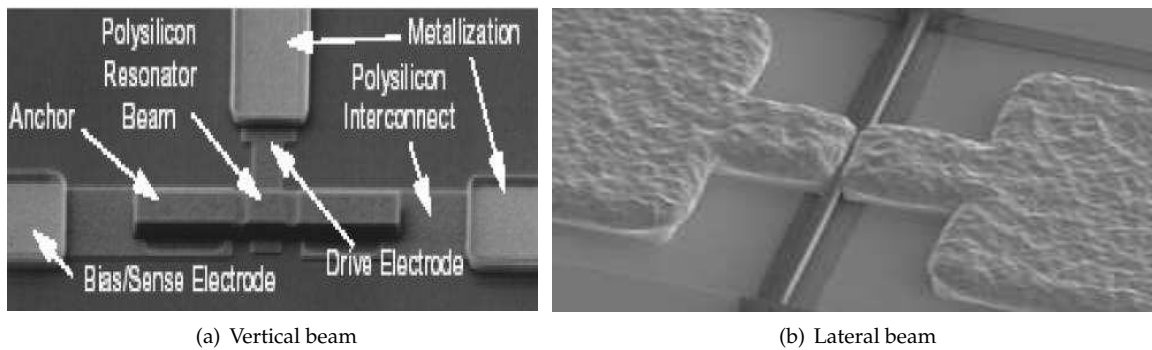


Figure 2.6: Clamped-clamped beam resonators from [51] (a) and [36] (b).

Flexural mode resonators

The simplest and more common flexural mode microresonators are realized using clamped-clamped or clamped-free beam structures. Several micromachining technologies are available to realize such devices, with different materials, in-plane or out of plane transversal vibration of the beam and a wide range of dimensions.

In Fig. 2.6, the two most adopted configurations are shown. Figure 2.6(a) shows a clamped-clamped vertical beam resonator. The device presents a beam anchored at both ends and suspended over an electrode. Both beam and electrode can be separately polarized. From an electrical point of view, the device is a one-port device, since it has only one electrode that is used both for excitation and for sensing. The main advantage of this topology is the ease of fabrication. The device can be realized with standard surface micromachining processing. Drawbacks are topography induced frequency uncertainties, reduced geometrical flexibility and large dissipation in the anchors [50]. Moreover, fabrication complexity issues often constrain vertical-mode devices to be one-port devices. The device in figure 2.6(b) differs from the previous one in the direction of vibration that is in-plane [52] and is a two-port device. This topology enables the realization of two different electrodes, one for excitation and one for sensing of the beam vibration, without lowering the capacitive coupling between each electrode and the beam, nor introducing a big capacitive coupling between the electrodes. This electrical configuration virtually allows the

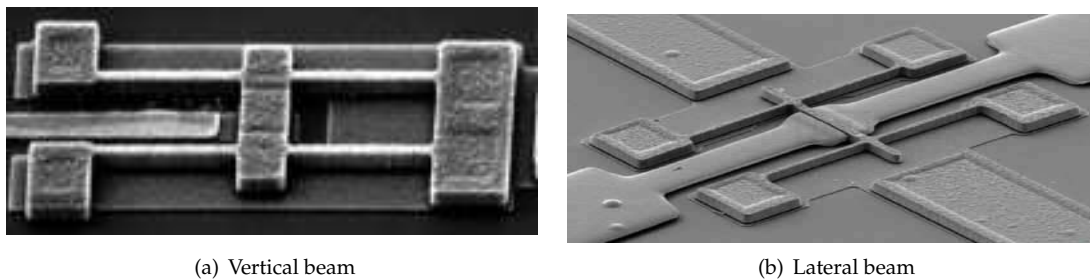


Figure 2.7: Free-Free vertical beam resonator from [51].

elimination of the AC current components at the output electrode.

Fig. 2.7 shows other examples of beam resonators that present non intrusive supports for reducing energy dissipation in the anchors, enabling the achievement of higher Q factors [53]. The resonating beam is in fact held in its fundamental mode nodes by four supporting beams designed so as to isolate the resonating beam from the rigid anchors, as if it was suspended without supports (the so call *free-free beam*).

The frequency of a beam flexural mode is inversely proportional to the square of the beam length. In order to achieve ultra high frequency (UHF), device dimensions have therefore to be reduced. This leads however to lower power handling, lower area for actuation and sensing, technology issues and increased susceptibility to environmental effects, such as contamination or thermal fluctuation [5]. For frequency higher than 10MHz, other geometries or higher frequency modes are preferable. In [54] for example, a high frequency flexural resonator is realized using an annular design.

Longitudinal resonators

Realization of UHF micro resonators with better performance, for what concerns power handling and phase noise, can be attained using alternative geometries operated in longitudinal modes. In this case, the structure is subjected to bulk acoustic waves, expanding and contracting with respect to the original shape along one or more directions. The resonance frequency of bulk acoustic modes is generally given by:

$$f_n = a_n \frac{1}{l_c} \sqrt{\frac{E}{(1 - \nu^2)\rho}} \quad (2.35)$$

where a_n is a factor depending on the resonant mode and the device shape, l_c is the device characteristic length along the direction of propagation of the acoustic wave (for example, the length of a beam shaped device or the radius of a disk shaped device), and the quantity:

$$\sqrt{\frac{E}{(1 - \nu^2)\rho}}$$

is the material acoustic velocity. It can thus be seen that this kind of vibration modes allows to achieve high resonance frequencies, while retaining larger dimensions with respect to flexural modes. Moreover, in in-plane vibrating devices, multiple electrodes can be easily realized. The device can therefore be operated with different electrode configurations.

Various shapes and resonant modes have been explored. In [55], the simple beam geometry has been maintained. In [56], a square single crystal silicon resonator is presented, with T-type anchors at its edges to minimize energy leakage to the substrate. The device exhibits both the Lamé-mode, in which its square edges bend in anti-phase preserving the plate volume, and a square extensional mode, in which the plate expands and contracts preserving the original shape. The two modes can be separately excited by four electrodes positioned along its sides. Anti-symmetrical

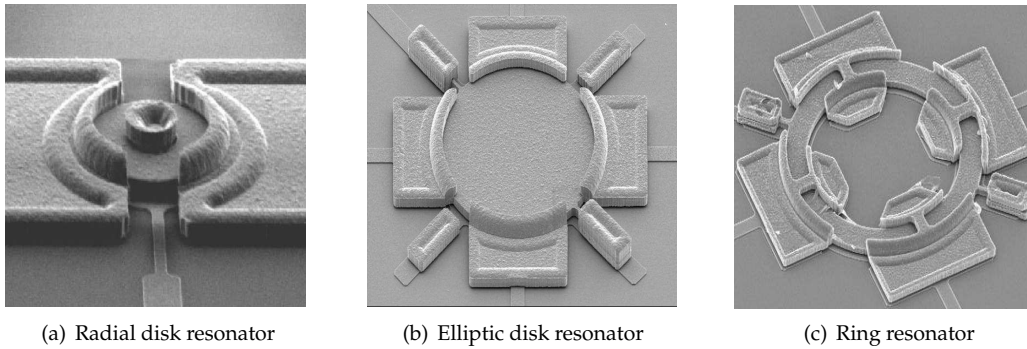


Figure 2.8: Longitudinal resonators: round geometries [51].

and symmetrical excitations lead respectively to the former and the latter mode. Other geometrical shapes frequently used are the disk and the ring, with different possible modes to be excited, such as the radial contour mode and the elliptic mode. Examples of this kind of devices are shown Fig. 2.8.

2.2.4 Quality factor

The quality factor of a system is defined by the ratio:

$$Q = \frac{2\pi W}{\Delta W}$$

where W is the total energy stored in the system and ΔW the energy dissipated in each time cycle. The smaller are the dissipative effects in the system the higher is its quality factor.

The dissipation mechanisms, which characterize the mechanical behaviour of a resonator define its mechanical quality factor or *unloaded* quality factor. This depends on different loss mechanisms, which can be classified into [57]:

- surface losses, which include losses in the surrounding fluid due to acoustic radiation or viscous damping and losses due to surface defects;
- intrinsic losses, which include all the losses inside the material, such as the ones due to thermoelastic damping, viscosity of the material, defects, impurities etc.;
- losses in the supports.

The importance of the different damping mechanisms in microresonators depends of their fabrication material, their design and their operating conditions.

The insertion of the resonator into an external electric circuit generally leads to other sources of dissipation. The quality factor of the overall circuit, referred to as *loaded* quality factor, results thus lower. Each source of energy loss can be described by a corresponding quality factor Q_i and

the total quality factor Q_{tot} can then be calculated as:

$$Q_{tot}^{-1} = \sum_i \frac{1}{Q_i}$$

since the total dissipated energy is simply the sum of the energy dissipated by each mechanism [58]. The device overall Q_{tot} cannot exceed the value of the smallest Q_i . Therefore, in the device design phase, the various energy losses have to be valued in order to find the limiting factor and possibly improve it with appropriate design choices. If the quality factor is not affected by design parameters, they can be chosen according to other optimization criteria.

Intrinsic losses are mainly dependent on the device material properties. The main source of intrinsic losses for the materials typically used in microresonator fabrication is thermoelastic damping, due to change of entropy caused by heat flow between regions of the microresonator, which have a different stress state.

Losses in the support are due to the transmission of vibration energy from the resonator into the support, energy that will be in large part dissipated. The phenomenon can be reduced with special shaping of the supports, even if this could lead to a complicate design and increasing dimensions of the resonator.

Surface losses are strongly influenced by the device operating conditions. If the device is operated in vacuum, losses due to surface defects are prevalent, otherwise damping phenomena dominates. Surface defects and thus the respective energy dissipation can be reduced only enhancing the surfacing properties with modification of the fabrication techniques. Gas damping phenomena depend on the shape and dimension of the region in which the gas movement is confined.

Among damping phenomena, gas damping is the most significant source of energy dissipation for devices not operated under vacuum. Resonators, as well as most of electrostatically actuated micromechanical devices, present a fixed electrode and a mechanical structure moving approximately parallel to it. In order to maximize the electromechanical interaction, this structure has a large area and is at a very small distance from the electrode. In these conditions, the so called *squeeze-film damping* is the dominant gas damping phenomenon.

Thermoelastic damping

Stress inhomogeneity inside a vibrating structure creates temperature fluctuations and therefore heat flow in the structure from hot to cold regions. The heat current increases the entropy of the structure and hence causes energy dissipation. The phenomenon is known as *thermoelastic damping* and is present in all structures under inhomogeneous stress conditions, independently from their material. The energy dissipated can be interpreted in two ways: as the rate of dissipation of the mechanical vibration energy due to the phase difference between the stress and the corresponding strain in the structure or as a rate of heat generation.

The effect of thermoelastic damping on the quality factor of a vibrating structure were first studied by Zener [59], who computed the energy dissipated in a vibrating thin beam using both the

purely thermal and the mechanical interpretation of thermoelastic damping. He calculated the thermal relaxation time associated with different thermal modes for the beam under flexure and showed that, for this geometry, only a few of these modes are sufficient to describe thermoelastic effects. The thermal relaxation time of the first mode is given by:

$$\tau_z = \frac{W_b^2}{\pi^2 \chi} \quad (2.36)$$

where χ is the thermal diffusivity of the solid and W_b is the width of the beam in the direction of vibration [59]. This dimension gives the distance between the regions of the beam subjected to compression and the ones subjected to tension and defines therefore the length of the thermal path. The thermoelastic quality factor is then given by:

$$Q_{TED}^{-1} = \frac{E\alpha^2 T_0}{C_p} \frac{\omega \tau_z}{1 + (\omega \tau_z)^2} \quad (2.37)$$

where E is the Young modulus of the material, α its thermal expansion coefficient, C_p its heat capacity per unit volume at constant pressure, T_0 is the equilibrium temperature, that is the ambient temperature, and ω_0 is the angular frequency of vibration of the beam. Typical values of these parameters for single-crystal silicon are given in Table 2.2. Zener expression is valid only for vibration frequencies which are lower than the inverse of the relaxation time τ_z , but can have an error up to 20% for higher frequencies. The theory has been extended by solving the thermoelastic equation for a thin beam and the following expression for Q_{TED} was obtained [60]:

$$Q_{TED}^{-1} = \frac{E\alpha^2 T_0}{C_p} \left(\frac{6}{\xi^2} - \frac{6}{\xi^3} \frac{\sinh \xi + \sin \xi}{\cosh \xi + \cos \xi} \right) \quad (2.38)$$

with:

$$\xi = W_b \sqrt{\frac{\omega_0}{2\chi}}$$

Using this equation, the quality factor for a single-crystal silicon thin beam has been plotted in Fig. 2.9, for different values of the beam width W_b . ξ can be also written so to underline its relation with the beam dimensions as:

$$\xi \propto \sqrt{\frac{W_b^3}{L_r^2}}$$

Table 2.2: Thermoelastic damping coefficients for single-crystal silicon

Coefficients	Value
α	$2.6 \cdot 10^{-6} \text{K}^{-1}$
C_p	$0.7 \cdot 10^3 \text{J K}^{-1} \text{kg}^{-1}$
χ	$0.8 \cdot 10^{-4} \text{m}^2 \text{s}^{-1}$

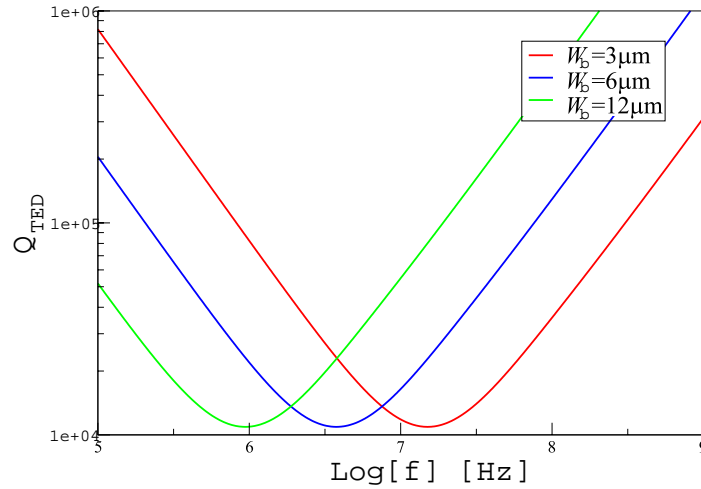


Figure 2.9: Quality factor of a flexural beam resonator, due to thermoelastic damping, as a function of the frequency. Different values of the beam width w are considered.

where L_r is the length of the beam.

Thermoelastic damping can be seen as an interaction of the vibration modes with the surrounding bath of thermally excited elastic modes, or phonons. In this view, the above equation is valid only if phonons are in diffusive regime, so that the temperature field is well-defined [60].

Thermoelastic damping for longitudinal vibration modes follows the same principle. However, the distance between regions of compression and regions of tension, and thus between hot and cold regions, does not depend on the dimensions of the structure, but it is equal to half of the wavelength λ of the acoustic wave, along the propagation direction. Since the thermal relaxation time is proportional to λ^2/χ , for acoustic modes it is inversely proportional to the square of the resonance frequency. A relaxation peak still characterizes the thermoelastic behaviour of the structure, but with a characteristic thermal relaxation time which depends only on the acoustic velocity of the longitudinal waves, and thus on the mechanical properties of the material and their variation with temperature.

Support damping

The main source of support damping is the transmission and subsequent dissipation of elastic vibration energy in the device support, through its anchors. In a typical clamped-clamped beam resonator, the vibration of the beam generates forces in the anchors, which act as external forces on the substrate and give rise to acoustic waves in it.

Rigorous calculation of the energy dissipation in the substrate per oscillating cycle requires the solution of the two-dimensional theory of elasticity in the substrate, which has to be modeled as an infinitely large elastic body. This has been done in [61] for cantilever and beam structures in their n mode of vibration by computing reaction moments and forces at the anchors and the

respective energy losses. The following dependence has been found:

$$Q_{support,n} = a_n \left(\frac{L_r}{h_r} \right)^3 \quad (2.39)$$

where a_n is a factor ranging from 0.1 to some units, which depends on the mode of vibration and the clamping of the structure. With the increase of the resonance frequency, and thus the shrinking of the beam length, this loss mechanism becomes important in clamped-clamped and clamped-free beam structures. It is therefore advisable to use different designs, which allow for compensation of the reaction forces and moments at the anchors. Alternatively, a suspension, which isolates the beam from the substrate, can be added [58].

In [62, 63] an alternative computational model is presented for the simulation of waves propagation in the substrate of MEMS vibrating devices. At this purpose, the finite element model of the MEMS device is coupled with a model of the substrate derived using a modified Fourier transform method. Simulation has been used for studying the sensitivity of the quality factor to different substrates and design factors for a clamped-clamped beam. It has been observed that the quality factor increases with an increase of the elastic modulus and/or the thickness of the substrate, but with an influence of the elastic modulus 20 times bigger than the one of the thickness. Small decrease of the Q factor is instead observed for longer length of the anchors and higher electrode-beam gaps.

Squeeze-film damping

The behaviour of a fluid surrounding a movable microstructure is described by the Navier Stokes equation, together with the continuity equation and proper boundary conditions. If we consider the typical parallel plate configuration encountered in MEMS devices, shown in Fig. 2.10, it is generally possible to assume that [64]:

- the vertical distance between the plates is much smaller than lateral dimensions, that is $h \ll l, w$;
- the gas flow in the gap is laminar and primary viscous, which implies a low Reynolds number: $Re \ll 1$;
- the gas undergoes an isothermal process so that the density of the gas can be replaced by its pressure;
- the relative displacement z of the plates is small compared with their initial distance h : $z \ll h$.

If we further assume that the gas acts as a continuum, the pressure distribution in the gap between the plates can be described by the Reynolds equation for compressible fluids:

$$6 \left[\nabla(\rho dv) + 2 \frac{\partial(\rho d)}{\partial t} \right] = \nabla \left(\frac{d^3}{\eta} p(\nabla p) \right) \quad (2.40)$$

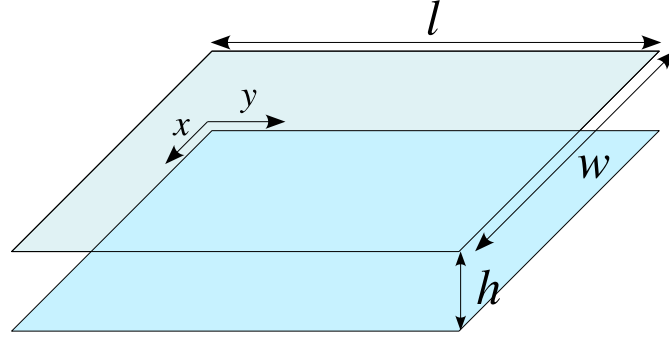


Figure 2.10: Damper schematic model.

where ρ is the density of the gas, v its velocity, η its viscosity and p is the pressure. Furthermore, it is usually assumed that the pressure p is constant across the gap and is subjected to small variations with respect of the ambient value p_0 . In this case, if the plates are on the xy -plane as in Fig. 2.10, equation (2.40) can be linearized around p_0 and reduced to the 2 dimensional equation:

$$\frac{\partial}{\partial x} \left(d^3 p \frac{\partial p}{\partial x} \right) + \frac{\partial}{\partial y} \left(d^3 p \frac{\partial p}{\partial y} \right) = 12\eta \frac{\partial(pd)}{\partial t}. \quad (2.41)$$

Such an equation has been solved for rectangular plates assuming harmonic vibration of the plates and that the pressure variations vanish at the plates borders [65]. Integrating the pressure over the area of the plates is then possible to find the force that the gas exerts on them. Such a force has a damping and a spring component. At low frequency of vibration, force and displacement are out of phase, and the gas pressure is simply proportional to the velocity of the plate. The gas squeezed by the moving plates has enough time to flow away from the gap and thus we have viscous damping. At high frequency instead, the force and displacement are in phase. The gas is trapped into the gap and behaves as a spring, with low dissipation. The force components, as a function of the angular frequency of the plates are given by the infinite series expansions [65]:

$$F_{damp}/z = \frac{64\sigma p_0 A}{\pi^6 d} \sum_{m,n \text{ odd}} \frac{m^2 + c^2 n^2}{(mn)^2 [(m^2 + c^2 n^2)^2 + \sigma^2/\pi^4]} \quad (2.42)$$

$$F_{spring}/z = \frac{64\sigma p_0 A}{\pi^8 d} \sum_{m,n \text{ odd}} \frac{1}{(mn)^2 [(m^2 + c^2 n^2)^2 + \sigma^2/\pi^4]} \quad (2.43)$$

$$(2.44)$$

where A is the area of the plate, $c = w/l$ is the ratio between its width and its length and σ is the *squeeze film number* given by:

$$\sigma = \frac{12\eta\omega^2}{p_a d^2} \omega. \quad (2.45)$$

This number is a measure of the relative importance of spring and damping force components. A cut-off angular frequency ω_c is found for $\sigma = 1$, when these have the same entity:

$$\omega_c = \frac{p_a d^2}{12\eta w^2}$$

The behaviour of the force components as a function of the squeeze film number is shown in Fig. 2.11. For angular frequency much lower than ω_c , the damping component only can be considered, while for much higher angular frequency only the spring component is important. Close to the cut off frequency, both components must be considered.

For very narrow gap and very low pressure, the gas cannot be treated as a continuum anymore. Introducing the Knudsen number K_n :

$$K_n = \frac{\lambda}{d} = \frac{p_0 \lambda_0}{pd}$$

where λ is the molecular mean free path of the gas, related to the local pressure p , the gas flow can be divided into four regimes [57]:

- continuum flow when $K_n < 0.01$;
- slip flow when $K_n \in [0.01, 0.1]$;
- transitional flow when $K_n \in [0.1, 10]$;
- free molecular flow when $K_n > 10$.

Slip flow effects can be included in equation (2.41) by replacing the real viscosity η with an effective viscosity η_{eff} which is a function of the Knudsen number. Various models for η_{eff} can be found in literature. One of the most used model, due to its good accuracy ($\pm 5\%$) and wide range of validity ($K_n \in [0, 880]$) is the model of Veijola [66], based on an empirical expression for the

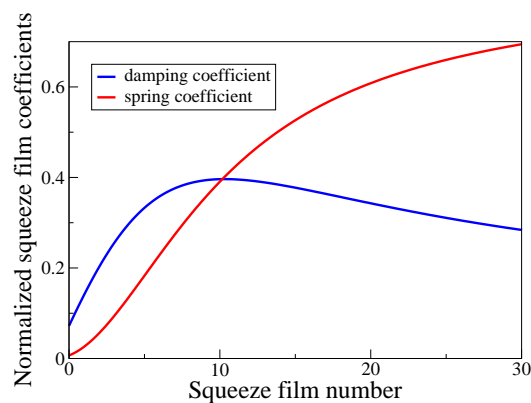


Figure 2.11: Squeeze film coefficient normalized with respect to $\frac{p_0 A}{d}$.

solution of the linearized Boltzmann equation for a diffusely reflecting surface. This reads:

$$\eta_{eff} = \frac{\eta}{1 + 9.638K_n^{1.159}}.$$

Corrections have also been introduced for other effects such as the inertial effects and boundary effects for structure with lateral dimensions comparable with the gas film thickness.

When the Reynolds number is close to unity, the inertia of the gas comes into play. Assuming a continuous flow, the frequency at which this happens is given by [67]:

$$f_c = \frac{\eta}{2\pi\rho d^2}.$$

The effects of inertia, for small velocity and continuous flow can be included in the model assuming a frequency dependency of the flow rate coefficient [67].

If the height of the gas film is comparable with the plate lateral dimensions, the damping models usually underestimate the damping force, since the open boundary effects at the borders of the plates are not correctly described by the used boundary conditions. The effects of the gas escaping from the gap can be included adopting a surface-elongation model [68]. The flow at the borders can be modeled assuming that the flow channel continues outside the plates. The problem is still solved with trivial boundary conditions, but these are applied to fictitious dimensions.

Models are also available, which describe squeeze-film damping in presence of perforations holes in the structure. In this case, it is generally assumed that there is no net flow under the moving plate, but all the gas escapes from the holes. The problem is thus reduced to a flow problem in proximity of a single hole [69].

2.2.5 Characteristic parameters and performance

The design of a micro resonator aims at realizing a device with the following properties:

- desired resonance frequency,
- frequency stability to temperature variation and in time,
- high Q-factor,
- low motional resistance,
- low phase noise,
- high power handling,
- linear behaviour in a wide region around the operating point.

All these properties are influenced by geometrical and materials parameters, as well as by the operating conditions. Process technology at disposal defines compatible materials and design rules to ensure devices feasibility and to reduce process-induced parameters scattering. Measurement

Table 2.3: Frequency scaling laws of different resonator parameters, at constant gap and voltage and assuming that the resonator dimensions scale as f^{-1} [70].

Parameter	Scaling factor
Equivalent stiffness	f^{-1}
Equivalent mass	f^{-3}
Quality factor Q	f^{-1}
Static coupling capacitance C_0	f^{-2}
Electromechanical transduction factor η	f^{-2}
Motional resistance R_m	f^3
Figure of merit $i_{motional}/i_{ac}$	f^{-2}
Maximum stored energy E_{max}	f^{-2}

capabilities and parameters, such as applied voltage and pressure conditions, have a big influence on device characterization and performance.

The frequency range addressable with micromechanical resonator is very large. As seen for the simple clamped-clamped beam device, the nominal resonance frequency of a mechanical structure depends essentially on the material properties (Young modulus, Poisson ratio, density and initial stress) and geometrical shape and dimensions.

Ideally, for meeting the requirements of communication systems, the resonance frequency has to be stable with temperature and time. The temperature frequency coefficient is basically fixed by the elastic coefficient of the movable structure. Typical values for MEMS materials are much higher than the one offered by off-chip material such as quartz [71]. For single-crystal silicon for example, the temperature frequency coefficient is given by -28ppm/K , versus the 1ppm/K of quartz crystals [70]. This requires the adoption of techniques for frequency temperature stabilization. One possibility is tuning the resonant frequency by changing the applied bias voltage or through an external tuning circuit. Alternatively, temperature compensation structures can be introduced in the resonator layout [72–74]. Making use of these solutions, resonators are expected to retain quartz temperature stability [5].

Long-term stability involves both material and surface stability. Materials such single crystal silicon are very stable and suitable for the application. Microdevices are on the other side sensitive to surface effects, with different measure depending on their shape and their volume-surface ratio. In order to ensure a long-term stability and lifetime, vacuum encapsulation is generally required [71]. This is also a key requirement for the achievement of a device high quality factor, since it enables to reduce the effects of squeeze-film damping.

In order to match the device with outside circuitry, typically around 50Ω , its impedance should not be far from this value. The device motional resistance should therefore be reasonably small. This quantity influences also the level of the output signal and thus the device noise performance. A low motional resistance requires high electromechanical coupling, which can be achieved by increasing the area of the electrodes, increasing the bias voltage or, more effectively, by minimizing the gap between moving structure and electrode. The motional resistance is proportional

to the first two parameters and inversely proportional to the fourth power of the transduction gap. The electrode area is influenced by the choice of the resonating structure shape and can thus be maximize by proper design. Yet, this is generally not enough to significantly lower the motional resistance value. The transduction gap is a fabrication parameter and its lower limit is necessarily bound. The high motional resistance of microresonators is thus still a primary issue. Recently, microresonators with solid gap have been introduced, which should allow to improve the electromechanical coupling by substituting the air dielectric layer, with a solid layer with higher dielectric constant [75, 76]. However, the real advantages of such an approach are still to be demonstrated [77]. Another possibility, which has already proven to give good results, is the use of multiple mechanically coupled resonators [78, 79], vibrating in phase.

The lower device dynamic limit is set by mechanical noise. A resonator is fully characterized by two variables, displacement and velocity, each characterized by a thermal noise $1/2k_bT$, where T is the temperature of the system and k_b the Boltzmann constant. The total mechanical noise is therefore given by k_bT . Assuming that this noise is the only noise source, the signal to noise ratio is related to the maximum power that the resonator can handle at every cycle P_{out} by the expression [70]:

$$\frac{S}{N} \propto \frac{P_{out}}{k_bT} \left(\frac{2Q\Delta\omega}{\omega_0} \right).$$

Since P_{out} is given by:

$$P_{out} = \frac{E_{max}\omega_0}{Q}$$

with E_{max} maximum energy stored in the resonator given by (2.34), the signal to noise ratio is proportional to E_{max} . If the device is operated outside of the linear regime, which generally means in large-displacement conditions, other noise sources add to the mechanical noise. In order to avoid degradation of the phase-noise, the maximum vibration amplitude has to be kept under a certain value. On the other hand, this limits the energy stored in the device and its power handling capabilities, also affecting the phase noise. In real applications, the signal to noise ratio calculation is more complex, since microresonators interface with external components that contribute to it. For achieving a device with good overall performance, all the presented factors need ideally to be simultaneously optimized, as a function of the design parameters. Table 2.3 reports the dependency of some of the device parameter of interest from the resonance frequency, assuming a constant gap¹ (indicated with d) and actuation voltage and that the resonator dimensions scale as f^{-1} . It can be noticed how the increase of the resonance frequency leads to a fast increase of the motional resistance R_m . The ratio between motional and AC current, also called *figure of merit*, instead decreases, as well as the maximum energy that can be stored in the device. With the movement of microresonator applications towards very high frequency, optimization of the device performance becomes therefore more and more difficult.

¹The value of the gaps achievable with nowadays technology are in fact close the physical minimum.

Table 2.4: Comparison of realized microresonators properties.

Shape	Mode type	$L_c[\mu\text{m}]$	$f_0[\text{MHz}]$	$Q[K]$	$R_m[\text{k}\Omega]$	$V_{bias}[V]$	Others
Beam	flexural (CC) [80]	44	14	1.5	1000	100	$-12.5\text{pmm}/\text{C}^*$
	flexural (FF) [81]	13	90	7.45	167	76	
	acoustic [55]	180	12	180	1500	100	
	acoustic [82]	20	213	28.7	6.3	100	
Modified beam	acoustic [83]	40	5.5	57	5.5	3	$-26.7\text{pmm}/\text{C}^*$
Square	extensional [84]	320	13	130	4.47	100	$I_{max} = 160\mu\text{A}$
Disk	radial [85]	20	1560^\dagger	2.6	2441	10.5	$y_{max} = 0.41\text{\AA}$
	elliptic [53]	30	143	45	91.2	17	$v_i = 1.26\text{V}$
Ring	radial [86]	23.6	1200^\dagger	15	274	10	$-11.2\text{pmm}/\text{C}^c$
	elliptic [87]	44	1200^\ddagger	3.7	560	20	

* $\Delta f/f_0$ † in the 3rd resonance mode‡ in the 4th resonance mode

Performance

The performance of microresonators varies depending of the adopted design, the frequency range of interest, and the operating conditions. The main characteristics of different kind of resonators reported in literature have been collected in Table 2.4.

It can be seen that a wide range of frequency can be obtained, with an upper limit fixed up to now at around 1GHz. The typical value for the mechanical quality factor of devices tested in vacuum conditions is several tenths of thousands, which is an order of magnitude difficult to reach with other kinds of on-chip resonators, both electrical and mechanical. On the other side, even for very high value of the bias voltage, the motional resistance of single resonators does not go below the tenths of $\text{k}\Omega$. Such a high value poses phase-noise and power handling issues. As previously mentioned, the problem has been addresses with the use of mechanically coupled resonators, vibrating in phase. In [78], a 500Ω motional frequency 70MHz microresonator has been demonstrated, obtained by coupling 7 flexural mode square-resonators at their corners. Despite of the coupling, a high-quality factor (9000) was also maintained.

From the reported data, the temperature frequency stability of the resonators seems a less relevant problem. Still little information is instead available about reliability and long-term stability of these devices.

2.2.6 Applications

The high quality factor that microelectromechanical resonators can attain makes them suitable for several communication technology applications. Due to their small size and low power consumption, they can be used in large numbers in order to realize different functionalities. Here only the principal microresonators applications are presented.

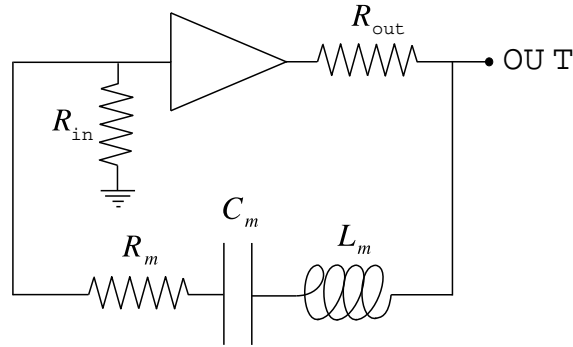


Figure 2.12: Series oscillator with a resonator tank.

Local oscillator

A first natural application for high-Q resonators is the realization of local oscillators. The implementation of an oscillator using a microresonator is strictly dependent on the resonator electrical equivalent parameters. The design of an oscillator always requires particular attention in order to preserve the quality factor of the high-Q element. The loading of the resonator by the sustaining electronics, and thus the degradation of its quality factor, must be minimized. This consideration generally causes a series resonant architecture of the oscillator to be preferable over a parallel one [46].

In the series resonant architecture, schematically represented in Fig. 2.12, the input impedance of the amplifier is in series with the resonator motional resistance. The effective quality factor of the oscillator is thus given by:

$$Q_l = \frac{\omega L_m}{R_m + R_{in} + R_{out}} = \frac{Q}{1 + ((R_{in} + R_{out})/R_m)},$$

where R_{in} and R_{out} are the input and output resistance of the amplifier and $Q = \omega L_m/R_m$ is the unloaded quality factor of the resonator [46]. Since generally the motional resistance is very large, it is $R_m \gg R_i + R_o$ and thus this architecture offers minimum Q-loading. This is generally not the case for a parallel architecture, which would be convenient for low values of the motional resistance [46].

In order to maximize the stability performance of the oscillator and its bandwidth capability, a very simple design of the sustaining amplifier is preferable. A transresistance amplifier is often adopted. Its loop gain should be larger than one for oscillation to build up, which implies that the transresistance R_{amp} should be larger of the total resistance which consumes power in the oscillation loop. As the oscillation amplitude increases, nonlinearities in the amplifier or in the resonator tank either reduce R_{amp} or raise the total resistance, respectively, until the loop gain is equal to one [88]. The amplitude of the oscillation becomes thus stable and a steady-state oscillation is achieved.

For this kind of application, the resonator tank is required to have high long and short term

frequency stability and low phase noise, both close and far to the carrier [5].

Micromechanical filters

A single resonator cannot be used as a filter because it does not provide sufficient out-of-band rejection. However, a filter can be realized by coupling a certain number of resonators [89]. The typical filter characteristic can be approximated using a system with a high-order transfer function. The higher is the number of coupled resonators the better the frequency selectivity of the filter, but at the expenses of a degradation of the insertion loss.

Micromechanical resonators offer different coupling techniques [89]. One can distinguish between:

- Mechanical coupled filters: This kind of filters is generally constituted by resonators with equal stiffness coupled by mechanical elements, such as beams, with a different stiffness. When the two resonators vibrate in phase at their resonance frequency f_r , the coupling spring is not excited. If they vibrate out of phase, the spring is instead excited and the resonance frequency of the complete structure shifts of a certain value Δf , which depends on the ratio between the stiffness of the coupling element and the effective stiffness of the resonator at its coupling point. Placement of coupling elements at low-velocity, and thus high stiffness, points results in filters with narrow bandwidth. A special class of these filters is filters that are coupled through the supports. At the clamping points, the effective stiffness of the resonators is in fact maximal. This could represent a possible solution for very high frequency filters, in which, due to the small dimensions of the resonators, coupling elements are difficult to realize.
- Electrically coupled filters: Microresonators can also be coupled electrically, using passive capacitors or active elements, such as buffers [90]. Capacitive coupling is obtained by the addition of grounded capacitive elements between adjacent resonators [91]. The interaction of each capacitor with the RLC resonator equivalent circuit adds a resonance mode to the system. Electrostatic coupling can actually be achieved also without a physical coupling element. If the resonators are closely placed, electrostatic forces arise between the resonating structures themselves, which give rise to a higher order system.
- Electrical cascading: If resonators with different resonance frequencies are cascaded, with buffers or amplifier in between them, the loading effect is eliminated and the resulting transfer function, which is the product of the transfer function of the single resonators, has several pairs of conjugate poles.

In Fig. 2.13, typical realizations of a mechanically coupled micromechanical resonators are shown.

Micromechanical mixer-filter

The square law transfer function of capacitive electromechanical transducers allows to perform mixing operation. Let us rewrite the expression of the electrostatic force acting on a beam resonator, when a voltage v_i is applied to its actuation electrode and a voltage v_r is applied on the resonator itself. If C is the capacitance between the electrode and the beam and y is its direction of movement, then:

$$F = \frac{1}{2} \frac{\partial C}{\partial y} (v_i^2 - 2v_i v_r + v_r^2).$$

Each of the terms of this equation is capable of mixing, if proper input voltages are chosen. In particular, if we assume that [93]:

$$\begin{aligned} v_i &= V_i \cos \omega_i t \\ v_r &= V_r \cos \omega_r t \end{aligned}$$

then the electrostatic force will have components of the kind:

$$F_{mix} = \frac{1}{2} \frac{\partial C_1}{\partial y} V_i V_r \cos(\omega_i \pm \omega_r),$$

which represent a mixing of the voltage signals v_i and v_r . A filtering operation can at this point be introduced to retrieve the desired mixing product. If we consider instead of a simple beam a micromechanical filter as in Fig. 2.5(a) with pass band centered at $\omega_i - \omega_r$ (that means that $\omega_i - \omega_r$ is the resonance frequency of the constituting resonators) and input and output structure electrically decoupled, this force component is Q amplified, while components at other frequencies are filtered. The second beam of the filter simply vibrates at $\omega_i - \omega_r$ so that the electromechanical capacitive transduction at the output electrode gives rise to an electrical signal at that frequency. Both mixing and filtering operation can thus be achieved with only one device. An example is presented in [93].

2.2.7 Enabling technology

Various kinds of microresonators have been implemented using both surface and bulk micromachining techniques, or a combination of the two. The choice between these techniques is mainly

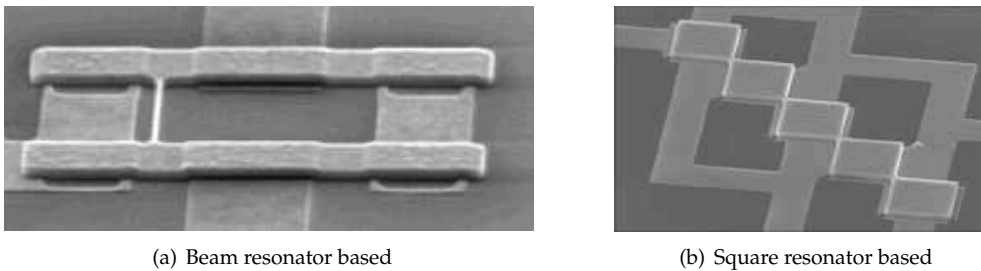


Figure 2.13: Mechanically coupled resonators from [47] and [92].

dictated by the structural material of the resonators, which is also one of the most important technological parameter.

In order to realize high frequency and low losses microresonators, silicon-based material are generally adopted. Silicon offers a high Young modulus, at least compared to the typical values of metals, low intrinsic losses, high temperature stability and, with the addition of a doping step, low resistance. In addition, several technological processes are already available for its manipulation: typical IC doping processes can be used for its doping and advanced etching and deposition techniques are available.

The materials most commonly used in the last 10 years are single-crystal silicon (SCS) and polycrystalline silicon. Due to its crystalline structure, SCS has superior properties: the internal friction is lower than for polysilicon and some crystallographic directions (110) offer lower Poisson ratio and a higher Young modulus, which allow to achieve resonance frequency 20% higher than isotropic polysilicon. On the other side, the use of SCS as a structural material requires the adoption of bulk micromachining, which limits the position of the device anchors and electrodes: anchors can only be realized as an attachment to the silicon side walls, and the electrodes have to be positioned laterally to the resonating structure [4]. Only in-plane resonators can thus be fabricated and, in order to maximize the electrodes area, structures with a high aspect ratio have to be realized. Polysilicon instead can be deposited and patterned using standard surface micromachining techniques, which simplifies fabrication and enhances design flexibility.

Other materials that have been used for the realization of microresonators are Silicon Carbide, poly-silicon-germanium (poly – $\text{Si}_{0.35}\text{Ge}_{0.65}$) and diamond like carbon. In Table 2.5 the main properties of interest for the realization of microresonators with these materials are reported. It can be noticed that these materials are very promising for the realization of bulk acoustic wave resonators, due to their very high acoustic velocity. Their fabrication technology is still in an early stage of the development.

Common issue of a microresonator fabrication process is the realization of thin, ideally sub-micron, transduction gaps and the compatibility with the fabrication processes of other kinds of MEMS and CMOS devices. The variety of technological processes presented can be roughly divided into three groups: polysilicon only processes, silicon only processes and merged processes.

Polysilicon process

A first possibility for the fabrication of a resonator in polysilicon makes used of a conventional surface micromachining process to create both the vertical vibrating polysilicon structures and

Table 2.5: Comparison between the characteristic properties of the material of interest for microresonators implementation.

Property	Poly-Si	SCS (110)	SiC	Diamond like carbon
Density [kg/m^3]	2300	2330	3300	3500
Young modulus [GPa]	150	168	448	1200
Acoustic velocity [m/s]	8.075	8.514	11.652	18.516

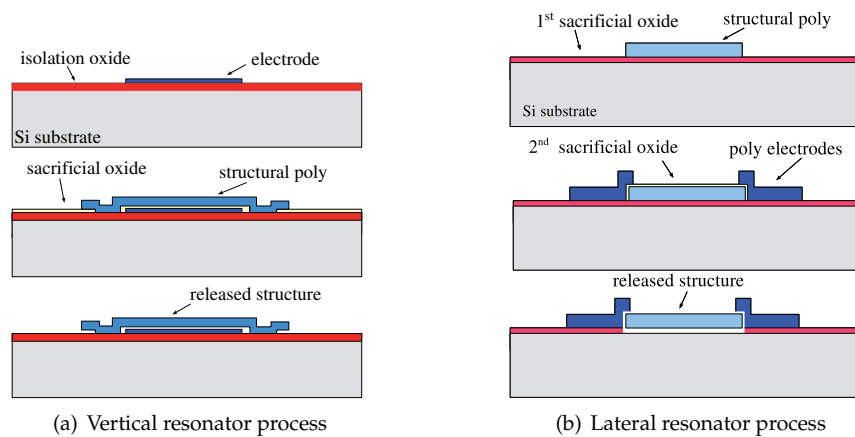


Figure 2.14: Process flows for the fabrication of vertical and lateral resonating structure in polysilicon with surface micromachining technology.

the underlying electrode. In this case, as shown in the process flow of Fig. 2.14(a), the thickness of the gap between the electrode and the resonating structure is defined using a sacrificial oxide layer, which can be easily deposited with thicknesses in the sub-micron range. This layer is etched using either a HF wet etch or a dry etch step. One problem with the use of polysilicon is that often it cannot be used in conjunction with metallization [4]. In order to avoid metal contamination of the machines used for plasma deposition of oxide and polysilicon, metal can be deposited on the wafer only after all oxide/polysilicon deposition steps. The thin polysilicon electrodes present therefore a very high resistance, which leads to a degradation of the loaded quality factor of the device. This problem can be overcome by turning to an in-plane resonators design, in which thick electrodes can be realized. Very-thin vertical resonator-electrode gaps were first achieved using e-beam lithography followed by high-density plasma etching and then making use of a sacrificial layer. A process flow as in Fig. 2.14(b) is in this case used. Additional polysilicon depositions can be added to create more complex structures. If deposition of the electrodes follows all the LPCVD deposition steps, electrodes can be also realized with metal electroplating, as in [94]. Note that in Fig. 2.14, a thick oxide layer is always first deposited on the wafer in order to isolate different devices on the same substrate and reduce losses in the substrate. At this aim, for RF devices, the use of a high resistivity substrate is also advisable.

Due to the high temperature required by polysilicon deposition and contamination problems, polysilicon processes are not post-CMOS compatible. A pre-CMOS fabrication is theoretically possible, but complicated by the high aspect ratio of the structures present on the wafer, which may create planarity and resolution issues in the CMOS photolithography steps.

SCS process

Single-crystal silicon processes are generally realized with bulk micromachining technology, using a combination of anisotropic and isotropic etching steps, silicon on insulator (SOI) based or

bonded wafer based processes. In SOI based processes, the device layer of the wafer serves as a structural layer for the resonator. The resonator shape is defined through an anisotropic deep reactive ion etching (DRIE) of the device layer, which reaches the oxide buried layer. The structure is then released by wet-etch of the buried oxide. The basic process steps are shown in Fig. 2.15. Two main possibilities for the definition of the resonator to electrode gap and the creation of the electrode are available. In the first approach, presented in [80], the electrodes are also realized in SCS. The gap between the resonator structure and the electrode is simply realized via a DRIE step. The same fabrication steps can also be performed on a silicon substrate. The release of the structure is then obtained by substituting the last oxide etch with an isotropic silicon etch, as shown in Fig. 2.15(b) [95,96]. With this technology, the minimum achievable thickness for the gap depends on the photolithographic resolution and the aspect ratio of the anisotropic process. Sub-micron gaps are thus difficult to achieve, especially if high structures have to be realized. The device layer has first to be doped to guarantee low resistivity of both the electrodes and the device structure. Alternatively, the structures can be covered with a metallization as in the SCREAM process [97]. A second approach is based on the use of a sacrificial oxide to define the gap and requires the subsequent deposition of the electrode structures, as shown in Fig. 2.15(a). These have been fabricated using metal-electroplating [36] or polysilicon deposition [98].

Vertical resonating structures have been realized also bonding two pre-processed wafers, as shown in Fig. 2.15(c). At this aim, a silicon wafer is etched so to create the shape of the structure and trenches, which will result in the gap between resonator and electrode. The gap value is thus fixed by the depth of a silicon etch step. A second wafer, typically with high resistivity such as glass, is pre-processed in order to define the electrodes. Afterwards the wafers are bonded and the resonating structure is released by etching its carrying wafer from the back. An example of a process involving the bonding of two wafers is presented in [99]. The process is quite complex and poses some limitation on design flexibility. On the other end, the electrodes can be realized on a isolating wafer, thus greatly reducing losses and parasitic capacitance towards the substrate for both the devices and the interconnections.

SCS processes are more suitable for integration with CMOS. If electroplating of the electrodes is used, the process is low-temperature and thus post-CMOS compatible [36] [95].

Combined SCS-poly process

High aspect ratio single-crystal and polysilicon isolated structure can be realized at the same time on a single wafer using the so called *HARPSS* process, presented in [100]. This is based on the anisotropic deep-reactive ion etch of trenches in a silicon substrate, which are then covered with a thin oxide layer and refilled with polysilicon. A deep dry-etch step followed by a dry isotropic etch allows then to release polysilicon and/or silicon structures and to open large air gaps. The silicon structures are under-etched by the isotropic etching step, so that the use of SOI wafers is not needed. Using this technique $20\mu\text{m}$ high beam resonators have been realized, with a transduction gap of 80nm [101]. A trench refilling technique has also been reported for the deep sub-micron dry-etch of transducers gap in silicon structure fabricated on a SOI wafer [102].

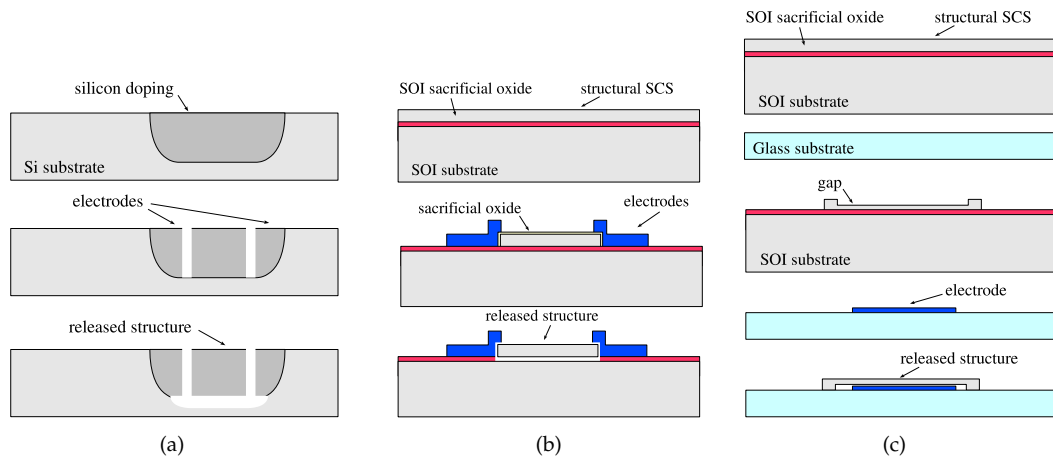


Figure 2.15: Process flows for the fabrication of SCS resonators with bulk micromachining technology.

Before the final etch, the wafer surface has a good planarity due to the trench refilling step. The process is thus ideally compatible with a pre-CMOS fabrication.

2.3 RF microswitch

A switch is a device that allows to make or break an electric circuit, thus creating an interface between devices in a system. Such a functionality provides the capability for redirecting signals and enhancing the flexibility and expansibility of a circuit [103].

Micromechanical switches were the first and more extensively studied MEMS devices, with the first realization presented as early as 1979 [104]. As other switching devices, RF MEMS switches have two stable states and the toggling between them is achieved through the mechanical displacement of a movable structure, also called armature. This movement is used to achieve a short circuit or an open circuit in a transmission line. The displacement can be induced using different actuation mechanisms. As for microresonator, electrostatic, electrothermal and piezoelectric actuation can be in principle employed. Electrostatic actuation is generally preferred, since it offers low power consumption, easy design and integration with planar and micro-strip transmission lines, simple fabrication and high compatibility with the standard IC processes and materials [105].

2.3.1 Classification

Switches can be categorized according to different characteristics. Depending on the configuration in which they are inserted in a circuit, switches are divided in series and shunt switches. In the series configuration, shown in Fig. 2.16(a), the switch is inserted in series between two sections of a transmission line. If the switch is open, the two lines are disconnected. When the switch is closed instead, it creates a contact between them.

In the shunt configuration in Fig. 2.16(b) the switch is inserted between the two transmission lines and ground. When the switch is open, the input and output lines are simply connected, and the signal can pass through them. If the switch is closed instead, the transmission line is shorted to ground, through the switch. Input and output lines are thus disconnected.

From a functional point of view, two couples of electrodes can be identified: the actuation electrodes, which carry the DC actuation signal, and the input and output switch electrodes, for the RF signal. If the actuation and the RF signal are physically decoupled, the device is called relay, while when these are on the same control lines, the device is said to be a switch [106]. Switches have therefore usually only two terminals, while relays have 4 or minimum 3, if a common ground configuration is adopted. The switch configuration requires biasing element to decouple actuation and RF signal and thus require more complex control circuitry. On the other end, fabrication is simpler than for relays, for which an extra conductive and isolation layer is generally needed. Based on the position of the switch armature with respect to the transmission line, broad side and in-line switches can be distinguished. In the first type, the switch armature has its unconstrained edges perpendicular to the direction of the transmission line. In the in-line switch instead, this is parallel to the transmission line and it is typically part of it.

Finally, switches can be classified, according to the characteristic of their contact, in *metal contacting* or ohmic switches and in *capacitive coupling* switches. Ohmic switches use a metal-to-metal direct contact to create an ohmic contact between two electrodes. In capacitive switches, a dielectric film is used in between the metal surfaces. Typically, ohmic switches are used in a series configuration and capacitive switches in a shunt configuration, but the choice is application dependent. Ohmic switches are suitable to be used both for low frequency and for high frequency applications [107]. The contact material should guarantee high conductivity, fabrication, environment and packaging compatibility, a long lifetime and no stiction. A good choice is gold based materials [105]. However, a long metal-to-metal contact lifetime is difficult to achieve. Capacitive switches can be used only for high frequency applications. Limitations in the frequency working range are on the other side compensated by a generally longer lifetime, due to the metal-dielectric contact [105]. However, due to the roughness of the dielectric surface, the quality of such a contact can be low.

Based on the introduced criteria and additionally on the kind of transmission line adopted, various configurations can be identified. Here two of the most common configurations will be described more in details: a series ohmic relay and a capacitive shunt relay, both broadside and implemented assuming coplanar wave guide (CPW) transmission lines.

A schematic representation of the series ohmic relay is shown in Fig. 2.17(a). A metal bridge, which constitutes the relay armature, is suspended above the input and output signal line of the coplanar wave guide, with a certain overlap area. When a proper actuation voltage is applied between the V_{act} and V_{bridge} terminals, the bridge collapses on the signal lines shorting them together. A series ohmic switch is electrically characterized by its up-state capacitance C_u and its contact series resistance R_s . The bridge membrane can be connected through a high resistance to the ground line of the CPW. In this way, the correct functionality of the switch can be obtained

using only three terminals. Note that the switch is designed so that the actuation lines do not get into contact with the suspended membrane, when this collapses.

A capacitive shunt relay has a thin dielectric layer over one of the two metallic contact surfaces, typically the bottom electrode, and its switching leads to a significant variation of the capacitance between the two surfaces. A schematic representation is given in Fig. 2.17(b). In this case, the metal bridge is suspended over a continuous signal line of the CPW, covered with a dielectric layer. In the up state, a low capacitance C_u between the bridge and the line causes their coupling to be low and the signal can pass through the CPW unperturbed. In the down state, the capacitance increases and so does the coupling between the switch bridge and signal line, thus reducing the impedance that the RF signal see towards ground. The ratio between the capacitance in the up state and in the down state is very important for the correct functionality of such a switch. If ω is the frequency of the signal carried by the input line, the impedance between the signal and the ground lines when the switch is in its up state, given by $(C_u\omega)^{-1}$ should be very high, ideally infinite. In the down state instead, the impedance $(C_d\omega)^{-1}$ has to be low, so that the signal is deviated towards ground. This implies that, in order to accomplish to its function, both in the up and down state a high ratio C_d/C_u is needed, but also implies that capacitive switches are more suited to be employed at high frequencies.

2.3.2 Working principle

The actuation behaviour of a switch can be introduced using a lumped model similar to the one adopted for illustrating the behaviour of microresonators. The armature of the switch can be considered as the rigid armature of a capacitor, connected to a spring with a certain stiffness k_m , and suspended above a second fixed capacitor armature, representing the actuation electrode, which in rest conditions is at a certain distance d . In metal contact switches, stop dimples set the minimum distance t_c between the two armatures. In capacitive switches, the armature can instead reach the actuation electrode, which is covered with a dielectric layer of thickness t_d .

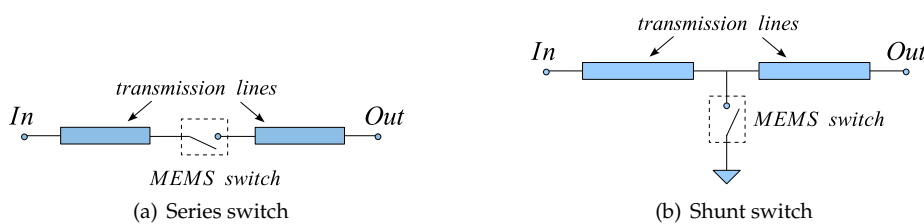


Figure 2.16: Switches configurations

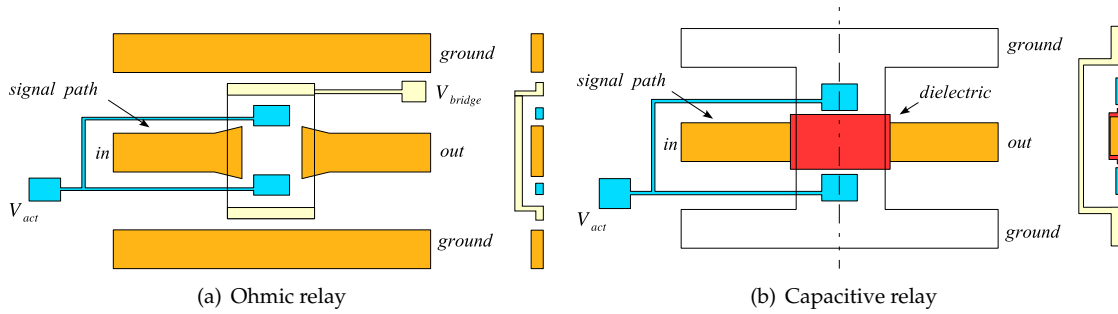


Figure 2.17: Relays types: top view and cross section.

Static behaviour

When a bias voltage is applied between the armature and the actuation electrode, electrostatic forces arise, which cause the armature to move towards the electrode, till the equilibrium between the electrostatic and the elastic forces is reached. In static conditions, this happens when the displacement y satisfies the equation:

$$-k_m y + \frac{1}{2} \epsilon_0 \frac{V^2}{(d-y)^2} = 0 \quad (2.46)$$

where a metal contact switch has been considered. However, due to the nonlinearity of the electrostatic forces, with the increase of the voltage a point is reached in which the elastic forces cannot balance anymore the electrostatic forces and the switch configuration is unstable. For applied voltages above this value, called *pull-in voltage*, the armature collapse towards the electrode and the switch toggles from the up to the down state. The expression of the *pull-in* voltage can be derived by imposing that the derivative of the voltage with respect to the displacement is zero. This happens for $y_p = d/3$, which leads to the following expression of the pull-in voltage:

$$V_p = \sqrt{\frac{8k_m d^3}{27\epsilon_0 S}}, \quad (2.47)$$

where S is the area of the switch armature.

Once the transition has happened, the voltage can be reduced, while still maintaining the switch in its down position. The applied voltage should be such to ensure a good contact force between the switch armature and the electrode to be contacted. When the voltage is lowered under the value for which electrostatic and the elastic force acting on the switch in the down position are equal, the switch is recall in its up position by a pull-up force given by $-k_m(d - t_c)$. This value of the voltage is called pull-out voltage and is lower of the pull-in voltage. Hence, the static characteristic of MEMS switches shows hysteresis.

In capacitive switches, the electrostatic force acting on the switch armature is given by:

$$F_e = \frac{\epsilon_0 S V^2}{2 \left[\frac{t_d}{\epsilon_r} + (d - y) \right]^2},$$

where ϵ_r its relative dielectric constant. The resulting pull-in voltage is given by:

$$V_p = \sqrt{\frac{8k_m}{27\epsilon_0 S} \left(d + \frac{t_d}{\epsilon_r} \right)^3}. \quad (2.48)$$

Dynamic analysis

The dynamic equation describing the behaviour of a switch is the d'Alambert equation of motion (2.1). The typical values of switches resonance frequencies are between 30 and 100 kHz. When an AC actuation voltage is applied with a frequency, which is much lower than the switch resonance frequency, the switch shows a quasi-static behaviour: its armature moves nearly in phase with the AC waveform. If the amplitude of the waveform exceeds the pull-in voltage, the switch toggles. When the frequency of the applied signal is much greater than the switch resonance frequency, the armature does not follow the instantaneous waveform, but its root mean square (RMS) [108]. This makes the switch very linear with respect to signals with high frequencies. No mixing and intermodulation occur between two signals with different frequencies incident on the switch. If the RMS voltage exceeds the pull-in voltage, a RF induced switching occurs.

In dynamic low damping conditions, the voltage needed to actuate the switch is lower than in the static case. The collapse of the switch armature on the actuation electrode happens already for a displacement $y_p^{dyn} = d/2$ and the dynamic pull-in voltage is given by:

$$V_p^{dyn} = \frac{1}{2} \sqrt{\frac{k_m d^3}{\epsilon_0 S}} \approx 0.92 V_p. \quad (2.49)$$

In microswitches, the main phenomenon contributing to the damping force is squeeze-film damping. For the typical value of the switch stiffness and damping coefficient, the device quality factor is ranging from 0.2 to 5 [103]. In such conditions, dynamic and static pull-in voltage cannot be distinguished anymore.

A simple expression of the device switching time can be computed neglecting the damping force and assuming that the electrical force maintains during the transition the value corresponding to $y = 0$. In this case, the switching time becomes [109]:

$$t_s = 3.67 \frac{V_p}{V \omega_0} \quad (2.50)$$

where V is the applied bias voltage and ω_0 the resonance frequency of the device. This expression of the switching time have been demonstrated accurate for $Q > 1$ and $V > V_p$. Typical values of the switching time are in the 2-50 μ s range.

As for microresonators, MEMS switches do not require DC current for operation. Hence, they have low power consumption. The power dissipated to toggle the switch with a certain frequency f_s is approximately given by:

$$P_s \sim \frac{1}{2} C_d V^2 f_s$$

with C_d and V switch down capacitance and actuation voltage [108].

Second order effects

If the switch undergoes large displacements, mechanical nonlinearity can become important. In this case, higher order spring coefficients have to be considered, which render the structure stiffer. Consequently, the switch pull-in voltage increases. With the assumption that:

$$F_{el} = k_m y - k_{m_2} y^3,$$

the pull-in displacement can be found by solving the third order equation [110]:

$$2k_m(y-d) + 2k_{m_2}(y-d)^3 + 3k_{m_2}y(y-d)^2 + k_m y = 0. \quad (2.51)$$

Rewriting the solution y_p^{nl} of such a system as $y_p^{nl} = rd$, the new static pull-in voltage is given by the relation:

$$V_p^{nl} = \sqrt{2 \frac{r^2 d^3}{\epsilon_0 S} (k_m(1-r) + k_{m_2}(1-r)^3)}. \quad (2.52)$$

2.3.3 State of the art

Combining the different possibilities in term of circuit configuration, kind of contact and position with respect to the waveguide, a great variety of switches have been designed and fabricated. Nearly all the switches are based on an out of plane movement, even if some lateral switches have been demonstrated with a good dynamical behaviour [111].

The most employed configurations are broadside capacitive shunt switches and ohmic serial relays, both broadside and in-line. The first one make generally used of a membrane, as in Fig. 2.18(a), or a plate supported and anchored through beams structures as in Fig. 2.18(b) and 2.18(c). Various shapes have been used for the supporting beams, in order to achieve the desired stiffness: straight beams, L-shaped beams and meanders are the most adopted solutions. Large dimensions suspended structures generally presents regularly distributed perforation holes. These are required for a complete release of the structure and are also useful to reduce the effect of squeeze-film damping.

Ohmic serial in-line relay have been realized using cantilevers beams, or more complex simply supported structures, designed in order to offer a large actuation area. In broadside ohmic relays, the actuation electrodes can be placed in different positions with respect to the signal line. In [35], for example, an interdigitated solution is presented.

It is then worthy to mention the so called toggle-switches, introduced in [114], which have an additional electrode to induce a faster switch pull-out.

2.3.4 Enabling technology

Most of RF MEMS switches are fabricated using surface micromachining, even if bulk micromachining and bonding techniques have also been used [115, 116].

The simplest surface micromachining process requires a minimum of 4 masks for both metal contact and capacitive switches. The respective fabrication processes are illustrated in Fig. 2.19. In both cases, for the deposition and patterning of the electrodes and the transmission lines, as well as for the armature, a high conductivity material is needed. The armature is deposited on top of a sacrificial layer that is removed at the end of the process to release the armature from the substrate. For capacitive switches, the definition of a thin oxide layer is further necessary. More complex processes offer more design flexibility.

A big variety of materials has been used for realizing the different layers. For the switch armatures and the transmission lines, low resistivity metals are generally preferred, such as gold, copper and aluminum. These can be sputtered or evaporated, using lift off of wet etching for their patterning, or can be electroplated on a previously deposited seed layer. For relatively high thickness of the metal, electroplating is generally adopted. The choice of the deposition parameters is very important, since it influences the roughness of the metal surfaces, which has a direct impact on the quality of the contact, and the stress in the material. Such a stress, not only modifies the stiffness of the layer, but can also lead to a deformation of the released armature that can compromise completely its functionality.

Various materials can also be used as sacrificial layers. These include oxides (SiO_2 , Si_3N_4 , etc.), metals (Au, Al, etc.), and polymers (photoresist, polymethacrylate etc.) [108]. Both oxides and metals require removal techniques, which are selective with respect to other material with similar compositions already present on the wafer. Moreover, oxide deposition is a conformal process, which means that the deposited oxide layer, and thus the structures grown on top of it, will reproduce the topography of the substrate. For metals, reaching the required sacrificial layer thickness with adequate homogeneity could represent a problem. Polymers are often an easier, as well as

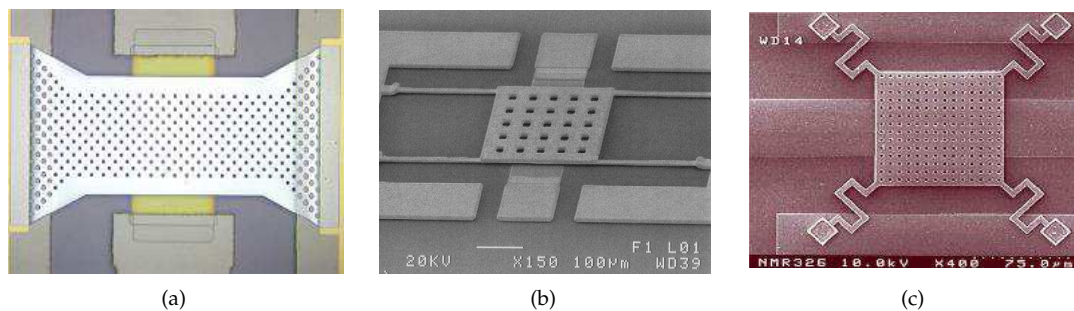


Figure 2.18: Switches examples from [112], [35] and [113].

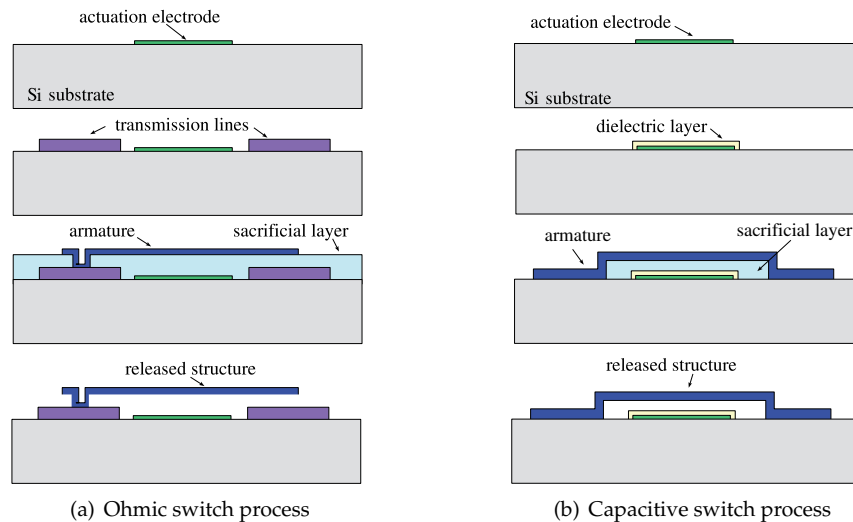


Figure 2.19: Basic process steps for the fabrication of 2.19(a) ohmic and 2.19(b) capacitive switches.

inexpensive, solution. Photoresist can be deposited on the wafer by spinning, planarizing the wafer surface with good uniformity, provided that the ratio between its thickness and the one of the underlying structures is not too small. If the condition is not satisfied, other deposition techniques can be used, such as electrodeposition [117] or spray-coating [118]. Removal of the photoresist or other polymer-based materials can be done by either wet or dry etching, with very high selectivity with respect to other materials. Wet etch simply make use of the solvent normally used for the stripping of the photoresist, while dry etch generally adopts an oxygen plasma. Two specific requirements that the fabrication of MEMS switches in general poses are:

- the realization of stress-free suspended structure;
- the uniform deposition on the wafer of high planarity sacrificial layer.

2.4 Integrated resonator-switch fabrication

In order to obtain the maximum advantages from the use of RF MEMS devices in telecommunication systems, microresonators, switches and passive components have to be integrated on a same substrate. In general, a typical switch fabrication process is also suitable for the realization of variable MEMS capacitors and suspended inductors. Microresonators and switches processes are instead highly dissimilar. The same compatibility issues arising for the integration of MEMS with CMOS circuitry appear therefore for the fabrication of microresonators and switches on a same substrate. The main incompatibility sources are [4]:

- topography: Switches are essentially planar devices, while microresonators are devices with a high aspect ratio;

- thermal budget: The constitutive materials of the two kind of devices, typically silicon-based materials for microresonators and metals for switches, have different thermal budgets;
- protection: Each device has to be protected during the fabrication of the others. These could be problematic when common materials are processed.

In order to avoid planarity issues during switches fabrication, one could think to fabricate the resonators after the switches. However, also low-temperature (CMOS-compatible) resonator fabrication processes generally have a too high thermal budget for metal-based switches, due to the oxidation step used as a masking layer for the DRIE etch steps and eventually for the creation of the resonators sacrificial layer. Low-temperature oxide is generally deposited at a temperature of around 400°C. Such a temperature can induce phase transitions between metal layers and between metal and semiconductor layers and it create stress and deformation in the suspended metal layers. Contamination is also an issue.

On the other end, switches post-fabrication on a resonators substrate is complicated by planarity issues. An exception is when the HARPSS process is used. In this case, before the release of the resonating structure, the trenches are filled with polysilicon, and the wafer surface does not present a high topography. Yet, switches have to be adequately protected during the release of the resonators.

A simultaneous realization of switches and resonators could give better results of the consecutive fabrication, enhancing the integrated design possibility and reducing its overall area. By sharing some of the process steps, also costs reduction could be achieved. However, much interlaced processes might require the introduction of several passivation layers.

2.4.1 Present state

While several approaches have been presented for the integration of different MEMS component with CMOS circuitry, little can be found in literature about the integration of different kinds of MEMS components. To the knowledge of the author, up to now, only one combined switch-resonator process has been presented, developed by IBM [119]. The simplified process flow is illustrated in Fig. 2.20. The process is based on copper interconnect technology, and in particular on the Damascene process [120]. This uses stacked levels composed of a layer of dielectric, deposited by plasma-enhanced chemical vapor deposition (PECVD), and a layer of copper, deposited using sputtering or a combination of sputtering and electroplating. For the fabrication of each level, a dielectric film is patterned and covered with thick copper. This is then removed everywhere apart from the trenches in the dielectric, using chemical mechanical polishing (CMP). A first level is fabricated for creating a device ground plane (M1 in Fig. 2.20(c)), followed by a thick passivation layer (V1 in Fig. 2.20(c)). In the second level, the bottom contacts of the MEMS devices are realized (M2 in Fig. 2.20(c)). Then an organic sacrificial layer is deposited, indicated with G1 in Fig. 2.20(c), and planarized using a dielectric layer (V2 in Fig. 2.20(c)). Two more levels are fabricated, which will form the device top contacts and the upper conductor level for

the switches (M3 in Fig. 2.20(c)). For resonators instead, apart for the upper contact, no metal is deposited in the area above the sacrificial layer, in order not to lower the Young modulus of the resonating structure. A last metal level is created for contacting purposes. The process is finally completed with a two steps release of the MEMS devices. First a DRIE anisotropic etch step is used to each the oxides down until the sacrificial layer, effectively defining the dimensions of the free-standing structures. Then, the sacrificial oxide is removed.

The described process allows to fabricate vertically moving devices made out of copper, dielectric, or a combination of the two. In [119], the fabrication of a cantilever beam resonator and a series switch are reported, but little information is given on the technological constrains, such as the minimum gap dimension. From the presented process flow, the limits posed on the device design by the fabrication process appear quite strong. In particular, without additional steps, the same gap dimension and moving structure vertical dimension has to be used for both resonators and switches.

A new process for the combined fabrication of micromechanical resonators and switches will be proposed in chapter 7.

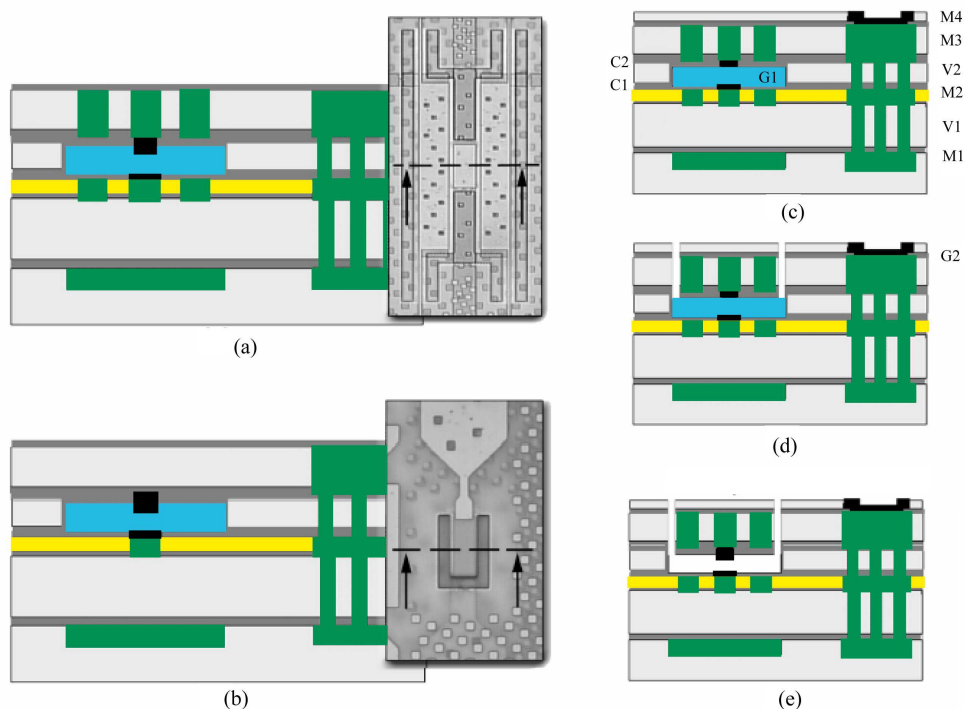


Figure 2.20: IBM switch resonator combined process flow (from [119]). In (a) and (b) the top-view and the cross-sections of a switch and a resonators are shown, respectively. In (c) details on the metalization are given, while (d) and (e) report the steps necessary for the MEMS device release.

Chapter 3

Review of simulation methods for MEMS devices

Micromachining technologies for fabrication of MEMS devices have seen a rapid development over the last 20 years. This has been followed by the development of computational tools for efficient and effective design of these devices in order both to assist the creation of new kinds of devices and to optimize the performance of the ones already tested. Device design and modelling is done at different levels, and consequently makes use of different tools. MEMS devices characterization requires the following steps [28]:

- process modelling and optimization tools,
- physical simulation,
- extraction of behavioural macromodels,
- device optimization tools,
- insertion of behavioural macromodels into system-level simulation tools,
- system performance optimization.

A bottom-up design methodology performs design optimization at the lowest level of the hierarchy and then tries to encapsulate device behaviour in a fixed macromodel for system design (see Fig.3.1). In contrast, top-down design methodology is based on the implementation of parametric behavioural macromodels that allow to perform design optimization at system level. In this way, the high level system specifications are used to obtain the desired subsystem performance (so called structured design approach). System and sub-system design specifications are in both cases the link between layers of the design hierarchy. In order to reduce the time required to complete such development cycle, depicted in Fig. 3.1, many efforts have been put in the development of computational tools for each step. The major task still to be addressed for MEMS optimization appears to be a good information exchange between the physical and system level.

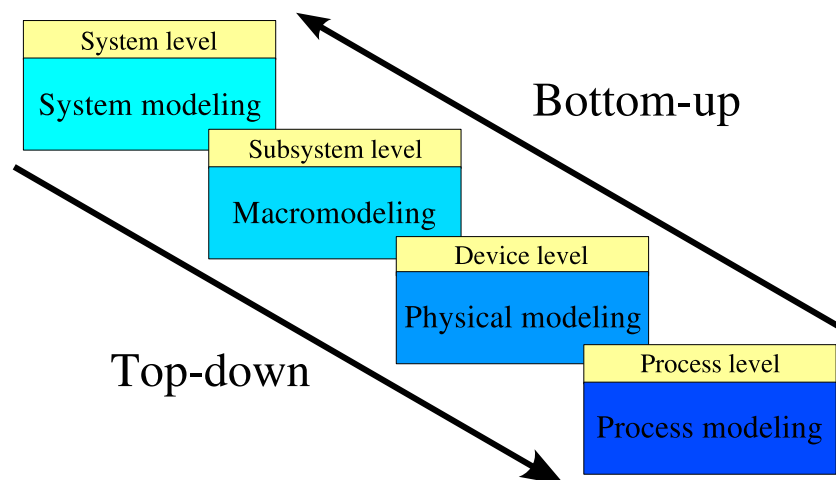


Figure 3.1: Design methodology diagram.

This should be performed through macromodels, which can greatly improve the overall process. Some commercial simulators already offer the possibility to automatically proceed bottom-up along the hierarchy [121,122], but there is still space for improvement.

In the following paragraphs, the modelling requirements and the strategies adopted at device and circuit level for the simulation of MEMS devices in the last years will be considered with respect to the simulation of RF active devices. Modeling of the fabrication processes will not be treated.

3.1 Simulation requirements

Simulation of microelectromechanical structures requires the description of all energy domains involved in their behaviour and the coupling between them. The device geometry (either created or derived from simulation of the fabrication process using a process flow and mask description) is in most of the cases complex and a three-dimensional simulation domain needs to be considered. Moreover, computationally expensive dynamic simulations are often needed in order to characterize the device behaviour. This makes simulation of MEMS devices computationally very complex.

Device nature and operating conditions define the phenomena, effects, and parameters, which are important for the creation of an accurate model. Frequency selective devices for RF application are characterized by their frequency response to a harmonic signal with small amplitude, superimposed to a bias voltage. In order to do this, the mechanical and electrostatic forces need to be described, together with their coupling. This introduces a first source of nonlinearity in the problem. Depending on the device dimension and operating conditions, it might be necessary to take into account also geometrical nonlinearities, which for this kind of devices often arise even at small applied signal. In order to exactly compute the device resonance frequency, quality fac-

tor and its overall dynamic performance, damping phenomena should be included in the model. Dissipation of energy through the device anchors towards the substrate is very difficult to model and is therefore generally estimated only analytically. When the device is not operated in vacuum, the effects of squeeze-film damping occurring in the air film between the resonant structure and its actuation electrode need to be taken into account. The squeeze-film damping governing equation, the Reynolds equation, is intrinsically nonlinear and dissipative, requiring therefore the knowledge of both velocities and displacements. In vacuum conditions, the dominant damping effect is generally thermoelastic damping. Despite of the sources of nonlinearity, the entity of the voltages applied to microresonators is generally chosen so that the device behaviour is actually linear and can be described with good approximation by a set of linearized equations.

RF switches are mainly characterized by their pull-in voltage and the time-dependent response to an applied large amplitude signal, such as a square wave, as well as intermodulation analysis. Also for this class of devices, the main phenomena to model are mechanical and electrostatic forces and squeeze film damping that is the dominant dissipation mechanism. Unlike microresonators, switches are intrinsically nonlinear devices. Nonlinear electromechanical coupling and squeeze-film damping need to be described as such. The importance of geometrical nonlinearity is strictly dependent on the dimensions of the device considered.

Both classes of devices need to be electrically characterized for prototype testing and interfacing with external electronic circuitry. They are in fact basically used for the manipulation of electrical signals. Outputs of the simulation should therefore be both mechanical and electrical quantities.

3.2 Simulation approaches

The various approaches presented for modelling MEMS devices can be divided in physical modelling, for the simulation at device level, and compact modelling, for simulation at circuit level. The choice of the complexity of the model is always a trade-off between accuracy and analysis speed.

Physical modelling is characterized by high accuracy and computational complexity and it is generally used for device level design optimization in a bottom-up modelling approach but also for design verification in a top-down modelling approach as well as post-fabrication verification for both cases.

Compact modelling focuses on the extraction of low complexity macromodels for design optimization, both at device and system level. The modelling accuracy achieved with macromodels is generally lower than for physical modelling techniques, but the simulation time is drastically reduced.

3.2.1 Physical modelling: spatial discretization methods

Physical simulation, also referred to as 3-D modelling and simulation (M&S) normally involves numerical methods, such as the Finite Element Method (FEM), the Finite Volume Method (FVM),

the Boundary Element Method (BEM), or a combination of them. These methods are based on a spatial or superficial discretization of the partial differential (PDE) or integral equations that describe the single-energy domains. Discretization leads to the solution of a system of ordinary differential equations (ODE). In particular finite element methods divide the spatial domain into a great number of elements, defined by a subdomain and a certain number n of points, called nodes. The solution of the original PDE system over the entire spatial domain is then approximated with a linear combination of highly localized interpolation functions, called basis functions, each defined only in a single element. Indicating with $\mathbf{x} \in \mathbf{R}^h$ the vector of physical unknowns quantities of the problem (for example in the electromechanical case the displacement in three direction and the electric potential), with $u(\mathbf{x})$ the desired solution and with φ_i a set of independent interpolation functions, this is expressed mathematically by:

$$u(\mathbf{x}) \simeq \sum_{i=1}^{n \times h} \xi_i(t) \varphi_i(\mathbf{x}) \quad (3.1)$$

where n is the number of discretization points used and $\boldsymbol{\xi} \in \mathbf{R}^{n \times h}$ is a vector of time dependent parameters, which represent the actual unknowns of the finite element formulation of the initial problem. Each entry of $\boldsymbol{\xi}$ represents the value of one of the physical unknowns of the problem at a certain node. Once the basis functions are chosen, the Galerkin method is applied to convert the solution of the original PDE system into the solution of a system of ODE [123]. In order to achieve a good simulation accuracy, a fine discretization is needed and a high dimensional system is thus obtained.

First issue encountered in the simulation of a three-dimensional MEMS structure with discretization methods is that not only interior quantities, but also quantities at its exterior, like electric fields [124], need to be computed. This poses mainly two problems: the creation of an adequate mesh and the truncation of the semi-infinite problem domain. A possible solution to these problems, adopted for example by the commercial simulation tool Coventor[©] [121], is to apply BEM to solve numerically the surface-integral formulation of the Laplace equation. The method is based on the assumption that the conductors are ideal, embedded in piece-wise constant dielectric and that potential boundary condition are provided. The conductors surfaces are divided into small panels, each assumed to be uniformly charged, and the potential at the center of each panel is related to the sum of contribution to that potential from the charge distribution on all panels. In this way, the problem is reduced to a dense linear system and the mesh of the exterior of the domain is replaced by a surface mesh, thus eliminating truncation problems.

Other tools, such as ANSYS[©], adopt a FE description of each element domain, but offer special elements for modelling the open boundary conditions [125].

The efficiency of coupled simulations can be improved using the fastest solvers available for each domain, provided an effective coupling between these domains. For this purpose, different approaches can be followed. For the generic coupling between m energy domains, each discretized

with n_i d.o.f., the problem can be expressed formally with the residual equations:

$$f_i(\mathbf{x}_1, \dots, \mathbf{x}_i, \dots, \mathbf{x}_m) = 0, i \in [1, m] \quad (3.2)$$

where $\mathbf{x}_i \in \mathbf{R}^i$ is the vector of the unknowns of the domain i . If structural deformation occurs, the equilibrium equation of each energy domain can be written with reference to the original unstressed and undeformed structure, or with respect to the last computed deformed configuration. The first technique is defined as Lagrangian approach, the second as update Lagrangian. The methods presented in the following paragraphs are specialized for the modelling of electromechanical coupling and are based on the use of either sequential or full coupling techniques, with different possibilities for the description of the two energy domains.

Independently from the solution strategy adopted, numerical simulation of MEMS devices still requires long computational times, especially for dynamic analysis. Moreover, the high complexity of the device model generated using numerical techniques does not always give a terminal description of the device behaviour. Their direct insertion at a higher hierarchical level for circuit simulation is therefore unpractical. Yet, combined simulation of MEMS device and electronic circuit can be performed coupling a physical and a circuit level simulator, as presented in [126].

Some commercial software, such as ANSYS, offer special lumped circuit and transducer elements. The first kind of elements is used for simulating a FEM model together with some simple external circuitry, such as voltage/current generator and passive components. The transducer elements allow for the direct coupling between physical domains. Detailed information on the elements available in ANSYS for the description of electromechanical coupling will be given in chapter 4.

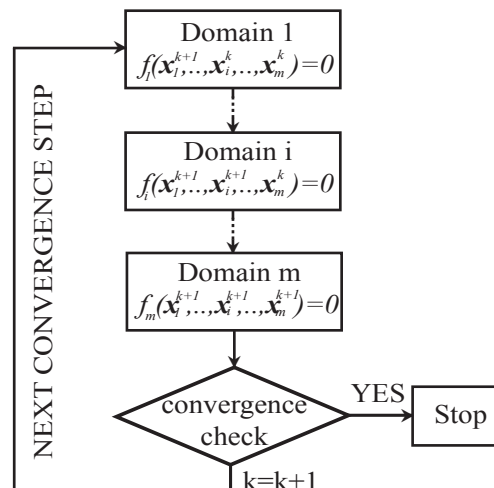


Figure 3.2: Relaxation scheme

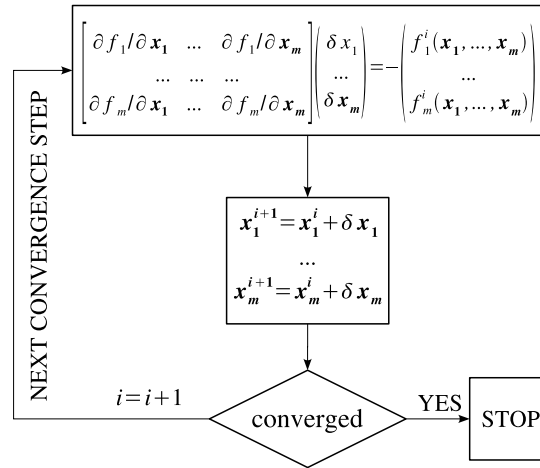


Figure 3.3: Newton iteration scheme

Relaxation method

Coupled-domain simulations have been addressed mainly with the Gauss-Seidel relaxation method. The relaxation method makes use of single energy domain solvers that are called in sequence. Each solver updates the value of its associated variables, and passes the results to the following one, until convergence is achieved. Each residual equation in (3.2) is thus practically solved by a domain-specific tool (black-box approach). The implementation of the coupling algorithm is therefore very simple and can easily include several coupled domains.

For the electromechanical case, the relaxation scheme adopts a semi-Lagrangian approach. The electrostatic charge distribution is computed for the deformed configuration of the structure and used to compute the electrostatic forces acting on the undeformed geometry. Morphing or remeshing of the electrostatic domain (or the surface in case of BEM) is therefore needed for each iteration step, with an increase of the simulation computational cost. This step can be eliminated by adopting a full-Lagrangian approach, in which also electrostatic forces are computed according to the Lagrangian description on the undeformed geometry [127]. In any case, the nonlinearity of the coupling between electric and mechanical domain greatly reduce the rate of convergence of the algorithm, especially close to instability points of the state space [124]. With the relaxation scheme, the computational cost for the solution of coupled-domain simulations, including forms of nonlinearity and dissipative effects, becomes rapidly very high.

Newton scheme

An alternative to the relaxation scheme is the simultaneous solution of the electrical and mechanical domains, using an iterative Newton-like method. In this case, the coupled system Jacobian is computed for a certain initial configuration, and at each iteration step, the following residual

equations are solved:

$$\frac{\partial f_i}{\partial \mathbf{x}_i} (\mathbf{x}_i^{k+1} - \mathbf{x}_i^k) = -f_i (\mathbf{x}_1, \dots, \mathbf{x}_i^k, \dots, \mathbf{x}_m), i = 1, \dots, m \quad (3.3)$$

where k is the iteration index. The algorithm requires more implementation effort with respect to the relaxation scheme and does not allow a black-box approach. The inclusion of other energy domains, such as fluidic domain for the description of damping phenomena, is therefore not straightforward. On the other side, the strong-coupled nature of this approach improves the convergence of the algorithm in all the state space. The computation of a consistent Jacobian system matrix can be un-trivial, especially for a conventional semi-Lagrangian approach. In particular, the mechanical to electrical coupling term is generally approximated using finite difference [128]. Moreover, at each iteration the geometry of the structures needs to be updated. A self-consistent computation of the Jacobian matrix can be obtained using variational calculus to derive the equilibrium equations of the electromechanical problem from its energy [129]. The Jacobian matrix, including off diagonal coupling terms, is then found by linearizing the equilibrium equation around the equilibrium point. Alternatively, both issues are solved by the use of a full-Lagrangian scheme, which offers a more robust and accurate solution of the electromechanical problem [130]. A multilevel Newton scheme has also been presented, which combines the robust convergence of the Newton algorithm with the black-box properties of the relaxation one [131].

3.2.2 Compact modelling

With the term compact modelling, all the technique used for the extraction of low complexity device macromodels are generally indicated. Macromodels are required to:

- give an accurate description of device behaviour, both static and dynamic, by including all the energy domains that are important for its description and their coupling;
- give a terminal description of the device, in order to be easily integrated in a circuit simulator for simulation together with electronic circuitry;
- be a valuable tool for effective and efficient device design. For this purpose, an analytical model is preferable, which allows to predict or rapidly evaluate the dependence of the device behaviour from each design parameter (parametric model);
- allow for fast simulation;
- have a simple but general form.

Various approaches have been presented for the extraction of macromodels that satisfy the above requirements. These have been classified into the following groups, according to their theoretical basis:

- semi-analytical modelling, based on an approximated analysis of the of the device governing equation, so as to generate a model either in a circuit or low-order ODE system form;

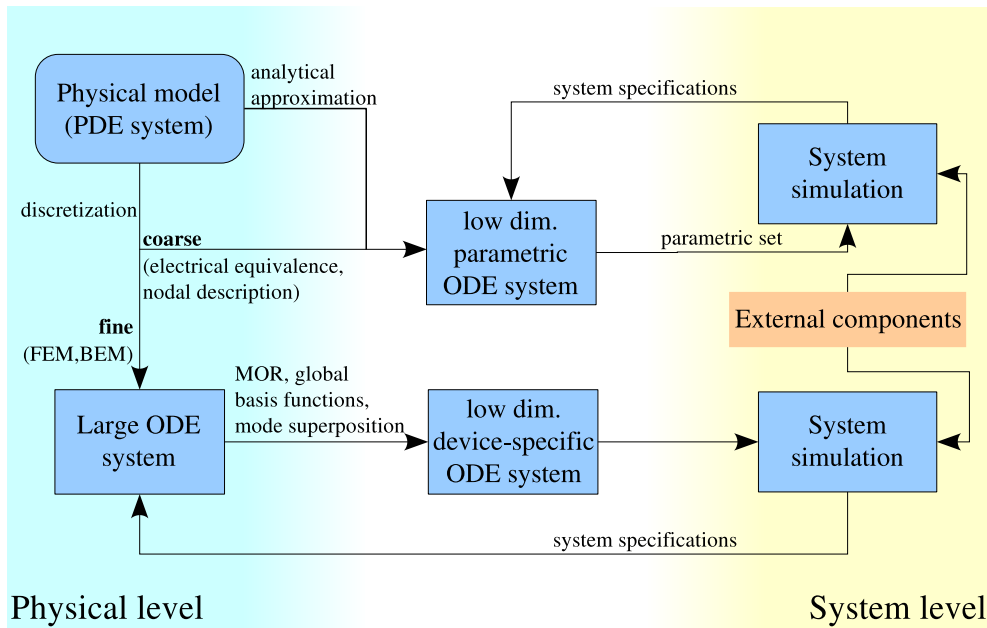


Figure 3.4: Graphic representation of the approach adopted by different compact modelling techniques.

- mixed-level hierarchical analysis, based on the partition of the device geometry/physical properties into basic elements, which can then be described by a macromodel and used to compose the original device;
- electrical equivalence, based on the use of electrical equivalent circuits to describe the device dynamic equations;
- global basis function methods, based on the use of the Galerkin method with global basis functions to derive a discretized form of the real continuous problem;
- model order reduction techniques that make use of mathematical techniques to reduce the complexity of the ODE system of equations describing the problem.

The path followed by these methods, from physical level to system level simulation, can be schematized as in Fig. 3.4. The first three show several analogies: they all start from the device governing partial differential equations, which are eventually decomposed and described with one or more parameterized schematic blocks. These blocks can be used at system level for a structured custom design, following the top-down design flow diagram of Fig. 3.1. The last two instead start from a device physical model and its FE discretization and by applying numerical techniques derive a macromodel that is in great extent device-specific. Hence, they can be employed in circuit level simulation and used to explore the design space, but they are only suitable for device optimization at circuit level if the extraction of compact models is very fast.

Semi-Analytical modelling

One possibility for the creation of macromodels is to start from analytical formulations. This requires:

1. Reducing the structure of interest to a simpler one;
2. Modeling the idealized problem analytically, either by solving its governing differential equations or by approximating the solution with energy methods.
3. Alternatively:
 - (a) Identifying a set of non-dimensional numerical parameters that can be varied in the analytical solution.
 - (b) Perform a numerical solution of the original structure and use the results to assign a value to the parameters, so as to ensure agreement between the numerical and analytical solution.

or:

- (b) Use experimental data to define the parameters, so that the analytical solution is in agreement with the measured behaviour.

Ideally, the parameters should be an explicit function of the device parameters, or at least maintain a physical meaning. This method has been widely used to extract static and dynamic models, both linear and nonlinear [109]. It can in fact be applied to any kind of devices. On the other side, there is no standard method to generate these macromodels, so there is no possibility to do it in an automatic way or to control its a priori accuracy. The quality of the model depends completely on the skill of the user.

Mixed-level hierarchical analysis

The biggest part of suspended MEMS devices can be modeled with the use of a limited set of atomic elements, such as beams, plates, anchors and electrostatic gaps. Hierarchical analysis is based on the extraction of a lumped schematic-based behavioural model for each of these elements and a subsequent modular design composition in generalized Kirchhoffian networks by interconnecting such models. The methodology is analogous and compatible with VLSI design. The network concept can in fact be generalized to any physical domain, providing that the system to be described does fulfill the following requirements:

- Networks should consist of elements connected with links;
 - Any physical domain should be characterized by a flow quantity (through variable) and a difference quantity (across variable);
 - A link has two extreme nodes with no loss in through quantities and the same values of across quantities between them;
-

- The relation between through and across quantities should be given implicitly or explicitly as a function of the terminal quantities and eventually internal states;
- Through and across quantities should satisfy the Kirchhoffs current (KCV) and voltage (KVL) laws, that is the sum of all through quantities entering a node is zero and the oriented sum of all across quantities along a closed path is zero.

Although the lumped models can be derived with different techniques, they all capture the mechanical or electrostatic behaviour of each device part and give a parametric description of its geometry. The reduced complexity and their schematic representation via mixed-signal hardware description language enable their use at system level in order to evaluate design performance. To ensure the interoperability between different modules, interactions between them have to be incorporated in each module in a self-consistent and comprehensive way. At this purpose, all the modules have to use the same definition of across and through variables and uniform conventions have to be adopted for physical quantities and potential and flux directions. Forces are chosen as through variables, so that Kirchhoffs law at the nodes automatically ensures that the forces acting on the mechanical system are in dynamic equilibrium at each instant in time. Either position, displacement or velocity can be chosen as across variables, satisfying the Kirchhoff current law. In the case of MEMS devices, displacement is generally preferred as it is of direct interest and it allows easy modelling of the device dynamics. Table 3.1 reports the typical through/across variable pairs for various energy domains. Another issue is then the proper definition of a local and a global reference coordinate system for all device elements.

The main library developed for the circuit-level representation of MEMS devices based on hierarchical device composition through generalized Kirchhoffian networks are Coventor ARCHITECT, NODAS (developed at the Carnegie Mellon University) and SUGAR (from Berkeley University of California). The first two are implemented in analog hardware description language, the third in MATLAB. They usually differ for what concerns the representation styles, the design frameworks the availability of specific models, especially for second order effects such as viscous damping or electrostatic actuation, and the capability of handling particular design steps, such as layout extraction.

The central element of each library is a flexible beam, which can be composed of 1 or more beam elements. Each beam element has only 2 nodes and forces and displacements can be applied only

Table 3.1: Through/across variables couples for different energy domains

Physical domain	Through quantity	Across quantity
electrical	current	voltage
mechanical translational	force	velocity/displacement
mechanical rotational	torque	angular velocity/displacement
pneumatic	volume flow	pressure
thermal	heat flow	temperature

to them. Torsion, expansion and bending are considered independent, with the first two assumed to be linear along the neutral axis while the bending is approximated at the second order. Based on these assumptions, each beam element has 12 d.o.f., three rotational and three translational for each node. Its behavioural description is based on matrix structural analysis [132], which lumps the structure distributed behaviour into the limited number of terminal nodes and describes the physics of the problem in matrix form. In the linear case, they can be computed solving a 12-dimensional second order ODE system with mass and stiffness matrices function of the geometry and the material properties of the beam element. Extensions are then available to model also the nonlinear case. Once computed, the system matrices of each element are assembled to create an ODE system that represents the entire structure. A similar approach is used to model rigid plates, defined by mass, center of mass and moment of inertia. Electrostatic air-gaps are modeled by computing the capacitance between two conductive plates as a function of their relative position, based on a simplified consideration of the electrostatic field between them. ARCHITECT furnishes a library of electromechanical components able to model also optical MEMS [133]. The model is implemented in MASTTM for simulation in the circuit simulator SABERTM. In addition, layout extraction from the macromodel for verification and masks fabrication is supported. NODAS uses VerilogA-AMS language, which is supported by several circuit simulators, and offers a tool for the automatic extraction of the layout from the macromodel schematic. SUGAR includes also numerical tools for dealing with ill-conditioned problems and for applying moment matching model order reduction via the Lanczos process to structures that cannot be modeled with atomic elements [134]. Another possibility in this sense is substructuring, available in some commercial FE simulator, such as ANSYS. Both will be presented in more detail in chapter 5.

Another approach for the derivation of the single element lumped models is developed in AutoMM [135]. AutoMM is an environment for design of MEMS devices, offering automatic generation of parameterized macromodels for atomic elements. These macromodels are derived by simulating the behaviour of each element over the desired operation space, modelling simulation data with multi-variable polynomial curve fitting and using the derived coefficients to express the element dynamic equation of motion. For each component in which the original device is divided, a lumped representation is adopted, so that single energy domain 3D finite element simulations are sufficient to extract its behaviour.

Some of the tools presented above include schematic components for the description of damping. In addition, a mixed-level simulation of squeeze-film damping in microstructures has been proposed by Wachutka [136]. A netlist is extracted from a FE model of the device and used for discretization of the device behaviour. A finite network model is then obtained, which describes in the generalized Kirchhoffian network theory squeeze film damping.

Compact modelling based on mixed-level hierarchical analysis offers the possibility to rapidly perform iterative multi-domain coupled simulation at circuit level. The simulation accuracy is generally around some percentage points, but it is usually degrading when mechanical nonlinear effects are to be considered. The methodology can then easily be extended to the modelling of new physical phenomena. Nevertheless, when the structure to model has a very heterogeneous

geometry, the partitioning process can be difficult or lead to a large number of elements. Moreover, when structural analysis is applied to derive the behavioural models of atomic elements, such models can be used for dynamical analysis only if the frequency components of the forcing input signals are much lower than the resonant frequency of the structure described by the model. Although this is generally true for RF switches, it clearly does not hold for microresonators.

Equivalent circuit models

Macromodels can be built by interconnecting a set of lumped electrical network elements, based on analogies in the mathematical description of various physical domains. These formal similarities of the integrodifferential equations governing the behaviour of various energy domains can be exploited for representing the properties of energy transducers through a lumped-element electrical equivalent circuit. If a set of analogies between physical quantities is established, all the equations governing the original system can be represented by the equation of an electrical circuit [137]. As for mixed-level hierarchical analysis, equivalent circuit representation makes use of the properties of Kirchhoffian networks and generally implies the decomposition of the system in functional blocks. Yet, the two approaches have been grouped separately, because of the different representation of the final macromodels.

Transducer energy ports are defined by a pair of conjugate dynamic variables, efforts and flows, which are respectively the across and through variables. Their product is the power through the port. Each component is characterized by a state variable and flow variables are defined by the time derivative of the corresponding state variable. The set of analogies between electrical and mechanical lumped components of a system undergoing a translation is listed in Table 3.2.

The approach has been applied for the approximation of the original problem both with a lumped-parameter and with a distributed system. The circuit simulator APLACTM offers a library of parametric circuit blocks, each describing a different structure/physical effect, which allows to perform nonlinear, static and dynamic simulation of various MEMS structures [138]. Each block offers different levels of accuracy. At the lower level, phenomena are generally described by analytical approximation of their governing PDE, while model parameters are in the form of lumped parameters [139]. At higher level, the finite-difference technique is used to introduce a coarse discretization of the PDE, and model parameters are given by material or geometrical properties

Table 3.2: Electromechanical analogies for lumped transitional systems.

Mechanical quantities	Electrical quantities
Force F	Voltage V
Velocity $v(x)$	Current $i(q)$
Displacement x	Charge q
Mass m	Inductance L
Compliance k^{-1}	Capacitance C
Viscous resistance c	Resistance R

of the part represented by the block. This means that a mechanical beam will be in the first case treated as a spring, with a given stiffness, eventually nonlinear, while in the second case the Euler beam equation for a certain set of geometrical and material parameters will be discretized and solved. This offers a certain level of flexibility to the designer.

Providing a single representation of a device operating in multiple physical domains, the electrical circuit approach is very convenient. Moreover, powerful mathematical techniques and network analysis programs are available for solving the derived problems. The major issues in creating circuit lumped-element macromodels are the definition of the parameter values for each component, and the partitioning of the continuum device into discrete parts, suitable to be represented by lumped elements. Lumped-element parameters have often to be obtained from a combination of analytical formulas and numerical simulations, but for well-understood phenomena they can be derived effectively and ensure a good simulation accuracy. The partitioning problem is not trivial, since mechanical structures usually cannot be mapped into a network topology. For both steps, a general approach cannot be identified and the designer's expertise is required.

Global basis functions methods

The finite element formulation of an electromechanical problem can be used as a starting point for the extraction of macromodels. With the introduction of an appropriate set of global basis functions, the behaviour of a device can be described by equations with the same form as the one solved in standard finite element simulations, but with much fewer d.o.f. The deformation state of the structures is not anymore given by n nodal displacements but by a linear combination of m global basis functions, with $m \ll n$, weighted by time dependent amplitude coefficients, also known as generalized coordinates, which become the unknowns to be found [140]. The method has been widely used and various basis functions have been tested. Once the basis functions are chosen, the problem is reduced to the expression of the device governing equations in terms of the amplitude coefficients and the solution of an m -dimensional ODE system. This is equivalent to the projection of the original system describing the device behaviour on the subspace defined by the global functions. Many of the ODE coefficients can be pre-computed, while the ones derived from the nonlinear energy terms are evaluated during the simulation of the macromodel or approximated by analytical functions of the generalized coordinates on the basis of full-model physical level simulations.

In [141] and [142], singular value decomposition (SVD) has been used to generate the global basis functions from data extracted from a set of full dynamic finite elements simulations. The spatial distribution of the state variables is sampled at N instants in time during this simulation and stored in N vectors, called snapshots. An N -dimensional orthogonal basis is then found that minimizes the least square of the distance between simulated states and the representation of these states with basis functions. This condition can be satisfied by computing the SVD of the matrix, which has the N snapshot vectors as columns. This approach is mathematically equivalent to the Karhunen-Loève approach. The extracted N -dimensional macromodels have two nonlinear terms that describe electrostatic and damping effects. These have to be evaluated at each time

step, during the ODE numerical integration.

Other techniques, such as the generalized Hebbian algorithm have been presented to extract global basis function by a series of snapshots [143]. Linear elastic undamped normal modes of the undeflected device have been often chosen as basis functions to approximate the solution of an electromechanical problem discretized using finite element methods. Modal representation is very efficient since it requires only one equation per mode and involved conductor to describe the entire system. With this choice, equation (3.1) describes a coordinate transformation from finite element coordinates to modal coordinates. The device governing equations are generally derived from Lagrange equations, after expressing the internal (elastostatic and kinetic) and external (electrostatic) energy of the system in terms of modal amplitudes and calculating the gradients symbolically. Assuming that the device undergoes small displacement, the basis chosen results in diagonal mass and stiffness matrices, which can be pre-computed. The nonlinear energy terms, instead, are generally expressed as analytical functions of the modal coordinate. In [140], a single static full finite element simulation is used to determine the number of modal functions needed to capture the device behaviour and their expected amplitude. This information is then used to construct the electrostatic energy term. A 3D full model electrostatic simulation is run for values of the modal amplitude that span the operating range of the device, in order to compute the capacitance/deformation curve. The results are fitted with a rational fraction of multivariate polynomials using a nonlinear function fitting scheme. In order to model also large-displacement behaviour of the device, the strain energy is derive by fitting data from a set of full finite element simulations [144]. A similar procedure is proposed in [145]. In this case, the force-displacement function and the modal strain energy are still derived from a series of FE simulations, but a polynomial multi-variable fit is used. In order to reduce the complexity of the fitting step, dominant and relevant modes are first characterized. Both the procedures in [140] and [145] can be partially automated and extended to include other conservative energy domains. Other algorithms have also been proposed for the approximation of dissipative energy terms [146,147].

Dedicated methods have been demonstrated for actuated microbeams, still using the linear undamped mode shapes of the device as basis functions in the Galerkin procedure [148]. Younis proposed two expressions of the nonlinear electrostatic term as a function of modal coordinates, each including all nonlinearities up to the fifth order, obtained via mathematical manipulation [148].

Macromodels obtained via global basis functions methods have been demonstrated to reproduce results obtained with full physical level simulation with an accuracy of some percentage points and a reduction of the simulation computational complexity. Moreover, macromodels are flexible in handling different input functions and scaling of device dimensions and parameters. Basis function methods can thus be used, at device level, to speed up multiple simulations of a single device, in order to explore the design space or at system level, to perform circuit simulation of complex circuits with many coupled devices. On the other side, the macromodel is not parametric and its extraction requires, in most cases, an initial computational overhead, thus precluding its use in an iterative procedure. For an accurate simulation of nonlinear dynamical systems, a careful choice of the states used for the generation of the basis functions and the energy terms is

required.

Global basis functions method can be considered a subclass of model order reduction techniques. As will be presented in chapter 5, both methods are based on the computation of a certain low-dimensional subspace and the projection of the system onto it. However, it has been chosen to treat these techniques separately, since they strongly differ in the way such a subspace is computed. In global basis function methods, this requires a simulation and fitting procedure strongly influenced by a high number of user dependent parameters, while for model order reduction technique the procedure is purely mathematical and can be performed in an almost automatic fashion.

Model order reduction modelling

With the term model order reduction (MOR) all the numerical techniques for the approximation of large scale ODE systems are generally addressed. For linear problems, these techniques have already been demonstrated in several engineering fields [34]. For what concerns MEMS, they have been applied to the study of thermal, electrothermal and purely mechanical devices, with a tremendous speed up of the simulation time and very high accuracy [30,31]. The main linear model order reduction techniques will be presented in the next chapter.

MOR application to electromechanical and squeeze film damping problems is not straightforward, due to the nonlinear nature of the coupling between the energy domains. Nevertheless, various approaches have been suggested for the modelling of electromechanical coupling. In [149], the electromechanical problem has first been linearized and then solved using linear model order reduction techniques. These techniques have then also been extended to the truly nonlinear case [150–153].

Compact models extracted with model order reduction usually present higher simulation accuracy than macromodels extracted with other techniques. In the linear case, the extraction process can be performed fully automatically and, for some methods, the accuracy of the model can also be predicted on forehand, without the need of model validation by physical level simulation. In the nonlinear case, instead, the solution of the problem is neither general nor automatic [33,154]. As for global basis functions methods, the extracted macromodels are device-specific. Every time a change in a design parameter is performed, a new reduced order model needs to be extracted. The extraction of macromodels, on the other hand, is generally fast and the shortening of the simulation so high that it is anyway possible to consider application of MOR in a design optimization iterative loop. Despite of the great potential offered by model order reduction techniques for compact modelling and the progress witnessed in the last year in the development of efficient algorithms, there is still a lack of available software in the public domain [32].

Table 3.3: Comparison between the main properties of the previously described simulation approaches

Simulation approaches	Accuracy	Computational complexity	System level integration	Parameterized analysis	Automatic extraction
Physical simulation	++++	++++	No	Yes	/
Semi-analytical models	+	+	Yes	Not always	No
Modified nodal analysis	++	+	Yes	Yes	No
Electric equivalence	++	+	Yes	Not always	No
Global function methods	+++	+*	Yes	No	Yes
MOR techniques	+++	+*	Yes	No	Yes

*but initial overhead for model extraction

3.3 Conclusion

In this chapter, the requirements and issues encountered in the simulation of MEMS devices at physical and system level have been presented. Particular attention has been posed on the main aspects of interest for the simulation of radio frequency microresonators and switches. The qualities of the various methods in fulfilling the requisites for a design optimization oriented simulation of these devices are summarized in Table 3.3. It is quite evident that, till now, none of the presented approaches enables both fast and accurate simulation, if not giving up some of the flexibility of the model. The great number of available approaches on the other hand gives the designer the possibility of gradually tuning its design towards the optimum, by choosing more than one compact modelling approach at different stages of the design. In the design methodology diagram of Fig. 3.1, the subsystem level stage can be divided into smaller design steps that make use of tools with increasing accuracy. In this view, a first device layout could be obtained using modified nodal analysis or electric equivalence, which allow tuning of the device geometry through parametric analysis. This could then be tested at system level using more accurate compact models, such as global function methods and MOR techniques. With respect to global function methods, MOR techniques allow for a faster and easier extraction of the models, so that they can also be used inside an iterative optimization cycle. The obtained simulation accuracy with these methods is generally the highest achievable with a compact model.

The application of model order reduction for the extraction of compact models has been explored already several years ago, but automatic tools and procedures for its effective application in device design by non-competent users are still lacking.

Chapter 4

Theory and physical modelling of MEMS with electrostatic actuation

In this chapter, the equations governing the behaviour of microelectromechanical devices are introduced. The modelling of these devices using the finite element tool ANSYS is then presented. The mechanical and electrical domains are separately described and the coupling possibilities available in ANSYS are discussed. Damping is introduced in the finite element model in a simplified form. Finally, the model adopted for contact forces is presented.

4.1 Mechanical domain

Physical modelling of structural mechanics problems is based on the theory of elasticity. The devices considered in this thesis are made of *elastic* material, that is a material in which deformations produced by external forces disappear with the removal of the forces. Materials will be considered homogeneous.

When external forces are applied to a body, internal forces are produced in the body. If we consider a cross section of the body, the force per unit area acting on this surface is called *stress*. The stress component perpendicular to the surface is called *normal stress* and is generally indicated with σ . The components acting in the plane of the surface are called *shear stresses* and are indicated with τ [42]. Let us now consider a Cartesian coordinate system and a small cubic element inside the body, around a certain point P, with sides parallel to the coordinate axes. Using the convention in Fig. 4.1, the direction of each normal stress component is identified by its subscript, while for shearing stresses the two subscripts identify the plane on which the stress component lays. In order to describe the stresses acting on the external surfaces of the element, only the three components of normal stress $\sigma_x, \sigma_y, \sigma_z$ and three components of shearing stress are needed. The equilibrium of the element leads to the relations:

$$\tau_{xy} = \tau_{yx} \quad \tau_{xz} = \tau_{zx} \quad \tau_{yz} = \tau_{zy}.$$

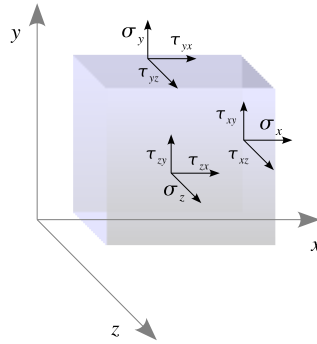


Figure 4.1: Convention for surface stresses of a cubic portion of a body.

These six quantities are called components of stress at the point P, and they are usually arranged in a matrix as:

$$[\sigma] = \begin{bmatrix} \sigma_x & \tau_{xy} & \tau_{xz} \\ \tau_{xy} & \sigma_y & \tau_{yz} \\ \tau_{xz} & \tau_{yz} & \sigma_z \end{bmatrix}$$

This matrix is also called *Cauchy stress tensor* [42].

A second effect of the application of external forces is the deformation of the body. This can be resolved into the three components of the displacement of each point of the body along the coordinate axes that will be indicated as u_x , u_y and u_z . The unit elongation of the distance between two points of the body due to deformation, along their connecting direction, is called *strain* and indicated with ε . The variation of the angle between two planes in the body, due to deformation, is instead called *shearing strain* and indicated with γ . Small strains can be written as a function of the above displacements as:

$$\begin{aligned} \varepsilon_x &= \frac{\partial u_x}{\partial x} & \varepsilon_y &= \frac{\partial u_y}{\partial y} & \varepsilon_z &= \frac{\partial u_z}{\partial z} \\ \gamma_{xy} &= \frac{1}{2} \left(\frac{\partial u_x}{\partial y} + \frac{\partial u_y}{\partial x} \right) & \gamma_{xz} &= \frac{1}{2} \left(\frac{\partial u_x}{\partial z} + \frac{\partial u_z}{\partial x} \right) & \gamma_{yz} &= \frac{1}{2} \left(\frac{\partial u_y}{\partial z} + \frac{\partial u_z}{\partial y} \right) \end{aligned} \quad (4.1)$$

where the same convention of the components of stress has been adopted in the use of the subscripts. The knowledge of three strains in perpendicular directions and three shearing strains related to the same directions allows to calculate the deformation of the body in any direction. The above quantities are called *components of strain* and generally arranged in the matrix:

$$[\varepsilon] = \begin{bmatrix} \varepsilon_x & \gamma_{xy} & \gamma_{xz} \\ \gamma_{xy} & \varepsilon_y & \gamma_{yz} \\ \gamma_{xz} & \gamma_{yz} & \varepsilon_z \end{bmatrix}$$

In the linear case, both stress and strain tensors are symmetric and their components are often arranged in vectors as:

$$\boldsymbol{\varepsilon} = (\varepsilon_x \quad \varepsilon_y \quad \varepsilon_z \quad \gamma_{xy} \quad \gamma_{xz} \quad \gamma_{yz})^T \quad \boldsymbol{\sigma} = (\sigma_x \quad \sigma_y \quad \sigma_z \quad \tau_{xy} \quad \tau_{xz} \quad \tau_{yz})^T.$$

Moreover, for small deformations, a linear relation between components of stress and components of strain can be assumed. In this case, the following relations hold:

$$\begin{aligned} \varepsilon_x &= \frac{1}{E} [\sigma_x - \nu(\sigma_y + \sigma_z)] \\ \varepsilon_y &= \frac{1}{E} [\sigma_y - \nu(\sigma_x + \sigma_z)] \\ \varepsilon_z &= \frac{1}{E} [\sigma_z - \nu(\sigma_x + \sigma_y)] \end{aligned} \quad (4.2)$$

where E and ν are characteristic properties of the material, called respectively *modulus of elasticity* or Young modulus and *Poisson ratio*. Shear stress and shearing strain are instead linked by the relation:

$$\gamma_{ij} = \frac{2(1+\nu)\tau_{ij}}{E} = \frac{\tau_{ij}}{G} \quad (4.3)$$

where G is called *modulus of rigidity* of the material. Introducing the *elasticity matrix*:

$$\mathbf{D} = \frac{E}{(1+\nu)(1-2\nu)} \begin{bmatrix} 1-\nu & \nu & \nu & 0 & 0 & 0 \\ \nu & 1-\nu & \nu & 0 & 0 & 0 \\ \nu & \nu & 1-\nu & 0 & 0 & 0 \\ 0 & 0 & 0 & \frac{1-\nu}{2} & 0 & 0 \\ 0 & 0 & 0 & 0 & \frac{1-\nu}{2} & 0 \\ 0 & 0 & 0 & 0 & 0 & \frac{1-\nu}{2} \end{bmatrix},$$

the above equations can be rewritten in the form:

$$\boldsymbol{\sigma} = \mathbf{D}\boldsymbol{\varepsilon}. \quad (4.4)$$

This takes the name of *generalized Hooke's law* [42].

The equilibrium of a structure subjected to body forces described by the load vector $\mathbf{f} = [f_x \quad f_y \quad f_z]^T$ is described by the partial differential equations:

$$\begin{aligned} \frac{\partial \sigma_x}{\partial x} + \frac{\partial \tau_{xy}}{\partial y} + \frac{\partial \tau_{xz}}{\partial z} + f_x &= 0 \\ \frac{\partial \sigma_y}{\partial y} + \frac{\partial \tau_{xy}}{\partial x} + \frac{\partial \tau_{yz}}{\partial z} + f_y &= 0 \\ \frac{\partial \sigma_z}{\partial z} + \frac{\partial \tau_{xz}}{\partial x} + \frac{\partial \tau_{yz}}{\partial y} + f_z &= 0 \end{aligned}$$

which can be expressed in a more compact form as:

$$-\nabla \cdot [\boldsymbol{\sigma}] = \mathbf{f}. \quad (4.5)$$

This equation together with equation (4.4), the strain-displacement relations (4.1) and appropriate boundary conditions defines completely the static problem [42]. For dynamic problems, the inertia force of the structure adds to the body forces on the right hand side of (4.5). This will have the form:

$$\mathbf{f}_i = \rho \frac{\partial^2 \mathbf{u}}{\partial t^2},$$

where ρ is the density of the material of which the structure is made of.

The above equations rely on the assumptions that both linear strain-displacement and stress-strain relations hold. However, this is not always the case. The main sources of nonlinearities are:

- material nonlinearities, such as plasticity, creep, etc.;
- geometrical nonlinearities, such as large strain, small strain but large displacements or rotation and structural instability.

The study of non elastic material requires to abandon the simple linear stress-strain relation for more complex constitutive relations. Geometrical nonlinearities arise when a structure is subjected to substantial shape variation, displacement or rotation. Their modelling requires the use of strain-displacement relations in the form:

$$\begin{aligned} \varepsilon_x &= \frac{\partial u_x}{\partial x} + \frac{1}{2} \left[\left(\frac{\partial u_x}{\partial x} \right)^2 + \left(\frac{\partial u_y}{\partial x} \right)^2 + \left(\frac{\partial u_z}{\partial x} \right)^2 \right] \\ \gamma_{xy} &= \frac{1}{2} \left[\frac{\partial u_x}{\partial y} + \frac{\partial u_y}{\partial x} + \left(\frac{\partial u_x}{\partial x} \cdot \frac{\partial u_x}{\partial y} + \frac{\partial u_y}{\partial x} \cdot \frac{\partial u_y}{\partial y} + \frac{\partial u_z}{\partial x} \cdot \frac{\partial u_z}{\partial y} \right) \right] \end{aligned} \quad (4.6)$$

with other components obtained with proper subscripts permutations. This formulation defines the so called *Greens strain tensor*, which is valid in the general case [155].

4.2 Electrical domain

In the general case, electromagnetic fields are described by the Maxwell equations [156]:

$$\begin{aligned} \nabla \times \mathbf{E} &= -\frac{\partial \mathbf{B}}{\partial t} \\ \nabla \times \mathbf{H} &= \mathbf{J} + \frac{\partial \mathbf{D}}{\partial t} \\ \nabla \cdot \mathbf{D} &= \rho_e \\ \nabla \cdot \mathbf{B} &= 0 \end{aligned} \quad (4.7)$$

where \mathbf{E} is the electric field, \mathbf{B} the magnetic induction, \mathbf{H} the magnetic field, \mathbf{D} the electric displacement, ρ_e the charge density and \mathbf{J} the surface current density due to free charges. This system of equations needs to be solved together with the constitutive relations:

$$\begin{aligned} \mathbf{J} &= \sigma_e \mathbf{E} \\ \mathbf{B} &= \mu \mathbf{H} \\ \mathbf{D} &= \epsilon \mathbf{E} \end{aligned} \quad (4.8)$$

where σ_e , μ and ϵ are respectively the electrical conductivity, permeability and permittivity of the material, the continuity equation:

$$\nabla \cdot \mathbf{J} = -\frac{\partial \rho_e}{\partial t} \quad (4.9)$$

and appropriate boundary conditions [156].

In the study of electrostatically driven MEMS devices, not all the terms of equations (4.7) are important. For what concerns microresonators and microswitches, it can be assumed that the wavelength of the electromagnetic wave is much larger of the device typical dimensions L_c . Under this condition, propagation effects can be neglected and the electromagnetic problem reduces to a sequence of stationary states. The time derivatives in (4.7) can thus be neglected and the electrical and magnetic problems are decoupled. In absence of static currents and external magnetic fields, the problem is electrostatic and governed by the equation [157]:

$$\nabla \cdot (\epsilon \mathbf{E}) = \rho_e \quad (4.10)$$

in vacuum and in the device dielectrics, while in conductors the electrokinetic equation holds:

$$\nabla \cdot (\sigma_e \mathbf{E}) = 0. \quad (4.11)$$

Conductors are equipotential and no electrical computation is required inside them.

In order to take into account the effects of the finite conductivity of the conductors in circuit level simulations, the distributed resistance of the materials is replaced with an external resistor.

4.3 Finite element modelling

4.3.1 Mechanical system

The finite element formulation of the PDE equations, describing a structural mechanics problem, has the following form:

$$\mathbf{M}\ddot{\mathbf{u}} + \mathbf{E}\dot{\mathbf{u}} + \mathbf{K}_m\mathbf{u} = \mathbf{F} \quad (4.12)$$

where \mathbf{M} , \mathbf{E} and \mathbf{K}_m are, respectively, the mass, damping and mechanical stiffness element matrices, \mathbf{u} is the vector of displacement d.o.f., and \mathbf{F} is the vector of applied nodal forces. When the structure undergoes small displacement and small strain, its behaviour can be assumed linear and system matrices are constant. The stiffness matrix depends linearly on the Young modulus of the modeled material, while nonlinear dependency arise for the Poisson ratio and the elements geometrical dimensions. The mass matrix depends linearly on the density of the material. The form of the damping matrix, describing dissipation phenomena, will be considered separately.

Nonlinear stiffness matrix

If mechanical nonlinearities occur, the above formulation of the mechanical problem is not valid anymore. Flexural resonators and switches nonlinear behaviour is dominated by geometrical nonlinearities, while in bulk acoustic wave resonators material effects are generally more important [158]. Material nonlinearities can be considered without a complete reformulation of the problem, while geometrical nonlinearities require major reorganization [155]. In this section, material nonlinearities are not taken into account.

In the case of geometrical nonlinearity, the nonlinear relation between displacement and strain has to be considered and the stiffness matrix \mathbf{K}_m becomes a function of the displacement of the structure. In the most general case of geometrical nonlinearity, \mathbf{K}_m can be considered as the sum of three matrices: a constant small-displacement matrix \mathbf{K}_0 , a large deformation matrix \mathbf{K}_L , which describes the effects of the structure geometry change with deformation and an initial stress or stress stiffening matrix \mathbf{K}_σ , which takes into account variations in stiffness due to deformations and initial stresses [155]. The solution of the problem requires an iterative approach in which, at each iteration, \mathbf{K}_L and \mathbf{K}_σ are recomputed with updated values of strains and stresses.

ANSYS distinguishes 4 cases of geometrical nonlinearities:

- Stress stiffening: stiffening of the structure due to its state of stress. It is important for thin structures in which the bending stiffness is small compared to the axial stiffness and couples in-plane and transverse displacements. This effect is taken into account calculating \mathbf{K}_σ , under the assumption that strains and rotations are small.
- Large rotation: the structure undergoes a large rotation, but does not change shape. We have therefore rigid motion and strains can be approximated with a linearized expression.
- Large strains: shape changes are taken into account, together with arbitrary displacement and deflection. Strains are not assumed infinitesimal anymore. It is the more general case of nonlinearity.

In the study of micromechanical resonators, the properties of the structures and the entity of the displacement involved generally allow to neglect, in first approximation, the effects of large deformations. It is instead important to consider stress stiffening effects. Fabrication induced stresses are in fact often present in microdevices and can alter significantly their behaviour. A nonlinear small deformation analysis performed with ANSYS allows to compute the stress stiffening matrix \mathbf{K}_σ for static loading as:

$$\mathbf{K}_\sigma = \int_V \mathbf{G}^T [\sigma] \mathbf{G} dV \quad (4.13)$$

where \mathbf{G} is a matrix of derivatives of shape functions, $[\sigma]$ the Cauchy stress tensor and the integral is taken on the volume of the structure. In a small-signal analysis around that bias point, \mathbf{K}_σ can then be kept constant, as long as stress variations are small compared to the initial value.

For switches, the same considerations as for microresonators hold. Also for this kind of devices, it is important to consider the effect of initial stress in the material, which can cause variations

Table 4.1: ANSYS electromechanical coupling methods.

Method	Description	Coupling	Supported analysis	Convergence
Multifield solver	Solver	weak	static/ transient	Slow
TRANS109	2D element	strong	static/ transient	Slow
TRANS126	1D element	strong	pre-stressed modal/ harmonic	Fast and robust

of the pull-in voltage and of the device dynamic behaviour. In first approximation, the effects of geometrical nonlinearities are remarkable only for devices in which the thickness of the structure is smaller than its maximum displacement, fixed in this case by the switch transduction gap [110].

4.3.2 Electromechanical coupling

The calculation of the electrostatic forces acting between pairs of conductors at different potentials requires the solution of equation (4.10). In a finite element frame, this means to discretize equation (4.10) in a portion of space surrounding the conductors so as to obtain a linear ODE system. However, the problem is complicated by the coupling between electrical and mechanical domains. As introduced in chapter 3, various methods have been developed for electromechanical coupling modelling. ANSYS itself offers various possibilities at different levels of complexity. These are presented in Table 4.1 in decreasing order of accuracy. The multifield solver makes use of sequential coupling for modelling coupling between energy domains. The mechanical and electrical parts of the model have to be modeled and separately meshed. A special flag is used to identify interface areas on which force and displacement transfer between the two domains take place. The two domains are then solved iteratively. An update of the electrostatic mesh follows each mechanical iteration. The electrostatic problem is recomputed with the new mesh and the electrostatic forces updated and transferred to the mechanical domain. This loop is repeated till convergence is reached. The main problems observed with this method are the low convergence rate and complexity in the creation of the FE mesh. Due to the high number of d.o.f. resulting from the finite element discretization of both the mechanical and electrical domain, solution of the coupled problem is already for static simulation computation very expensive and, in many cases, close to instability regions convergence cannot be reached. Especially for the electrostatic domain, with the increasing geometrical complexity of the mechanical structure, the creation of an electrical mesh that surrounds it can be not trivial. Moreover, open space boundary conditions are required. They can be modeled using infinite element [122] or considering a wide region of space around the device.

In order to obtain a finite element model, which can be used for the extraction of a device compact model, a strong (or direct) coupling between energy domains is needed. Finite element matrices have to contain all the degrees of freedom (d.o.f.) necessary for the description of the problem.

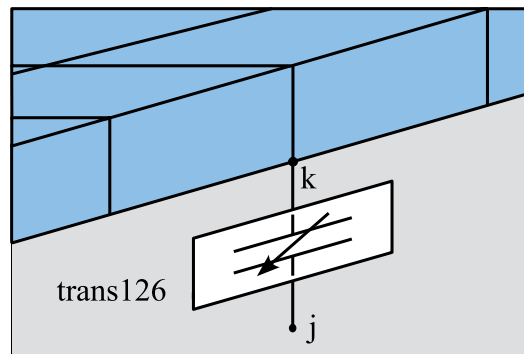


Figure 4.2: Trans126 connects a node of the mechanical mesh (k) to a fixed node (j), representing the behaviour of a fixed electrode.

The two strong electromechanical coupling methods available in ANSYS rely on the modelling the electrical part of the problem with special elements, which have both mechanical and electrical d.o.f. By using these elements, a single finite element system is assembled and electrical and mechanical d.o.f. are solved simultaneously. When highly nonlinear problems have to be solved, strong coupling improves convergence.

In this thesis, the TRANS126 elements are used [159]. These elements represent variable capacitive transducers with displacement and voltage as across quantities and electrostatic force and current as through quantities. They model capacitance variations between pairs of conductors moving along a preferential direction. Each element has two nodes with one displacement and one voltage degree of freedom. The elements are placed in such a way that they connect the nodes of the mechanical finite element model between which electrostatic forces act, thus replacing the 3D mesh of air gaps. Fixed electrodes do not have to be included in the model, because they can be described by the boundary conditions at TRANS126 mechanical nodes. An example of placement of this element between a 3D mechanical mesh and a fixed electrode is shown in Fig. 4.2. The capacitance between the nodes is a function of the distance between them, which is computed as the difference of the respective nodal displacement along a chosen coordinate direction, also referred to as stroke. Such a direction should coincide with the preferential direction of movement of the node when the mechanical structure deforms. Only devices whose capacitance variation is locally described with good approximation as a function of a uni-directional displacement can thus be modeled. This condition is satisfied by a large part of RF MEMS devices.

The relation stroke-capacitance is assigned to the elements by the user. Different possibilities are available, depending on the device to model. If the capacitive effects can be accurately described using a parallel-plate capacitor approximation, the capacitance is simply assumed to be inversely proportional to the stroke. In this case, an ANSYS macro, called EMTGEN macro, allows to automatically layer one TRANS126 element for each node of the mechanical structure facing the electrode and assign the correct area to the element capacitance. If fringing effects are important, the capacitance can be expressed as a series of powers of the stroke or the capacitance-stroke curve can be extracted from electrostatic simulations and assigned as points.

The electrostatic force acting between the nodes of a TRANS126 element is computed according to energy principles. Let $C_{kj} = C(u_i^k - u_i^j)$ be the capacitance between nodes k and j for a certain value of the distance $d = u_i^k - u_i^j$ along the coordinate direction u_i . The force is directed along u_i and its module is given by [37, 159]:

$$f_i^k = -f_i^j = -\frac{1}{2} \frac{\partial C_{kj}}{\partial u_i^k} (v_k - v_j)^2 \quad (4.14)$$

where v_k and v_j are the voltages at the nodes k and j , respectively. The current flowing in the element is computed as the charge time derivative:

$$i_k = \frac{d}{dt} [C_{kj} (v_k - v_j)] \quad (4.15)$$

According to the assumption that conductors are equipotential, all the nodes of the TRANS126 elements connected to a certain conductor are subjected to the same voltage boundary conditions. The total current flowing in the conductor is simply given by the sum of the currents at those nodes.

The use of TRANS126 elements introduces an approximation of the electrostatic forces. However, with a proper choice of the capacitance-stroke relation, the resulting error is small, as it will be demonstrated in chapter 6. In addition to enabling the use of the model for compact modelling purposes, TRANS126 elements enable a huge reduction of the complexity of the problem. The electrostatic mesh is eliminated from the model and convergence is greatly enhanced with respect to the sequential solver.

TRANS109 elements are a 2 dimensional version of TRANS126 elements [160]. They have triangular shape and 2 displacements and 1 voltage d.o.f. for each node. They are useful for simulating structures such as comb drivers and optical MEMS, in which capacitance between the device parts is generally a function of a two-directional displacement. Their use is on the other end limited to 2 dimensional simulation and static or transient analysis and convergence of the solution might be an issue.

4.3.3 Electromechanical system matrices

The modelling of electromechanical coupling using TRANS126 elements leads to system matrices containing both mechanical and electrical d.o.f. Due to the nonlinearity in the electrostatic forces, such a system is derived as follow. Assuming that the state variables u and v vary around a bias point $(\mathbf{u}_0, \mathbf{v}_0)$:

$$\mathbf{u} = \mathbf{u}_0 + \delta\mathbf{u}(t) \quad \mathbf{v} = \mathbf{v}_0 + \delta\mathbf{v}(t)$$

the expressions of the force (4.14) and the current (4.15) can be linearized at the first order approximation:

$$f_k = f_{0k} + \mathbf{K}^{uu,k} \delta \mathbf{u} + \mathbf{K}^{uv,k} \delta \mathbf{v} \quad (4.16)$$

$$i_k = i_{0k} - \mathbf{E}^{vu,k} \dot{\delta \mathbf{u}} - \mathbf{E}^{vv,k} \dot{\delta \mathbf{v}} \quad (4.17)$$

where the superscript k denotes the k -row of the matrices \mathbf{K}^{uu} , \mathbf{K}^{uv} , \mathbf{E}^{vv} and \mathbf{E}^{vu} . These are sparse matrices with non zero entries given by:

$$\begin{aligned} K_{kj}^{uu} &= -\frac{\partial f_k}{\partial u_i^j} = -\frac{1}{2} \frac{\partial^2 C_{kj}}{\partial u_i^j \partial u_i^k} \Big|_{u_0} (v_k - v_j)^2 \Big|_{v_0} \\ K_{kj}^{uv} &= -\frac{\partial f_k}{\partial v_j} = -\frac{\partial C_{kj}}{\partial u_i^k} \Big|_{u_0} \frac{\partial (v_k - v_j)^2}{\partial v_j} \Big|_{v_0} \\ E_{kj}^{vu} &= \frac{\partial i_k}{\partial \dot{u}_i^j} = \frac{\partial C_{kj}}{\partial u_i^j} \Big|_{u_0} (v_k - v_j) \Big|_{v_0} \\ E_{kj}^{vv} &= \frac{\partial i_k}{\partial \dot{v}_j} = C_{kj} \Big|_{v_0}. \end{aligned} \quad (4.18)$$

The subscripts k and j run on the TRANS126 element nodes, while i is used to indicate the axis of the coordinate system, global or local, along which each TRANS126 element lies. The linear ODE system describing the electromechanical problem for small-signal analysis is given by:

$$\begin{aligned} &\begin{pmatrix} \mathbf{M} & 0 \\ 0 & 0 \end{pmatrix} \begin{pmatrix} \ddot{\delta \mathbf{u}} \\ \ddot{\delta \mathbf{v}} \end{pmatrix} + \begin{pmatrix} \mathbf{E} & 0 \\ \mathbf{E}^{vu} & \mathbf{E}^{vv} \end{pmatrix} \begin{pmatrix} \dot{\delta \mathbf{u}} \\ \dot{\delta \mathbf{v}} \end{pmatrix} + \\ &+ \begin{pmatrix} \mathbf{K}_m - \mathbf{K}^{uu} & -\mathbf{K}^{uv} \\ 0 & 0 \end{pmatrix} \begin{pmatrix} \delta \mathbf{u} \\ \delta \mathbf{v} \end{pmatrix} = \begin{pmatrix} 0 \\ \mathbf{i} \end{pmatrix} \end{aligned} \quad (4.19)$$

It can be noticed that \mathbf{K}^{uu} , also known as electrical stiffness, lowers \mathbf{K}_m , thus reducing the stiffness of the structure. This is the basis of the electrostatic spring-softening effect observed in MEMS devices.

General case

The system in the form (4.19) is the starting point for the solution of a static or transient analysis using the *Newton-Raphson method* [122]. This iterative procedure, commonly used for the solution of nonlinear systems of equations, is presented in Algorithm 1. The process uses the Jacobian matrix of the system, also called *tangent stiffness matrix* and the so called *vector of restoring force*. Starting from a tentative solution, which in time dependent problems generally corresponds to the converged solution of the previous iteration step, these quantities are used in order to compute,

in a finite number of iteration steps, the equilibrium solution. Convergence is assumed to be reached, when the norm of the vector of restoring force, which is a measure of how much the system is out of equilibrium, is below a certain tolerance.

Algorithm 1 *Newton-Raphson algorithm: given the nonlinear system of equation: $\mathbf{A}(\mathbf{x}) = 0$ and a starting point x_0 :*

1. $i=0$
Do
 2. Compute the Jacobian matrix of $\bar{\mathbf{A}}(\mathbf{x}_i) = \bar{\mathbf{A}}_i$ and the vector of restoring force: $\mathbf{F}_i^r = \mathbf{A}(\mathbf{x}_i)$;
 3. Solve: $\bar{\mathbf{A}}_i \Delta \mathbf{x}_i = -\mathbf{F}_i^r$;
 4. Compute $\mathbf{x}_{i+1} = \mathbf{x}_i + \Delta \mathbf{x}_i$ and \mathbf{F}_{i+1}^r ;
 5. if $\|\mathbf{F}_{i+1}^r\| \leq \text{tol}$ **exit**;
 6. Go back to point 2 with $i = i + 1$.
-

For the static case, the linearized stiffness matrix:

$$\begin{pmatrix} \mathbf{K}_m - \mathbf{K}^{uu} & -\mathbf{K}^{uv} \\ 0 & 0 \end{pmatrix}$$

is used as tangent stiffness matrix in the Newton-Raphson process, while \mathbf{f}_0 is the vector of restoring force. For transient analysis, the system (4.19) is rewritten in a form in which the derivatives of the state variables are eliminated from the unknowns of the problem by using a time integration method. Next, the Newton-Raphson process is applied. The mass matrix does not contribute to the tangent stiffness matrix of the nonlinear problem because it is linear, while the damping matrix does. The vector of restoring force is then constituted by both \mathbf{f}_0 and \mathbf{i}_0 .

For the applications of interest, all voltage d.o.f. are assumed to be constrained to a known value. This implies a voltage-controlled implementation of the device model but it does not limit the modelling capabilities. In this case, the tangent stiffness matrix is a function of the displacement only. With Dirichlet boundary conditions $\delta \mathbf{v} = \tilde{\mathbf{v}}(t)$ applied to voltage d.o.f., the system (4.19) reduces to:

$$\mathbf{M} \delta \ddot{\mathbf{u}}(t) + \mathbf{E} \delta \dot{\mathbf{u}}(t) + \mathbf{K} \delta \mathbf{u}(t) = \mathbf{B} \tilde{\mathbf{v}}(t) \quad (4.20)$$

where $\mathbf{K} = \mathbf{K}_m - \mathbf{K}^{uu}$ and the matrix \mathbf{K}^{uv} has been replaced with the symbol \mathbf{B} . On the right hand side the constrained voltages appear as input functions. Their action is distributed on the system d.o.f. through the scattering matrix \mathbf{B} . After solving (4.20), the currents can be derived as a function of first derivatives of the computed displacements and the applied voltages:

$$\mathbf{i} = \mathbf{E}^{vu} \dot{\mathbf{u}} + \mathbf{E}^{uu} \dot{\tilde{\mathbf{v}}}. \quad (4.21)$$

Harmonic pre-stressed analysis

The harmonic analysis of an electromechanical system can be simply performed using the linearized system (4.19), or, for constrained voltage d.o.f., the system (4.20) together with (4.21). Harmonic analysis is in fact for definition linear. However, the nonlinearity of the system requires the previous computation of the operating point with a nonlinear static analysis, using the Newton-Raphson algorithm. Harmonic analysis is then performed for the desired angular frequency ω with the system linearized around the operating point $(\mathbf{u}_0, \mathbf{v}_0)$. This kind of two steps analysis is generally referred to as *harmonic pre-stressed analysis*.

Harmonic analysis assumes that both forcing terms and state variables vary sinusoidally in time with a certain angular frequency ω . Introducing complex notation and expanding derivatives, the final system is obtained:

$$[-\omega^2 \mathbf{M} + i\omega \mathbf{E} + \mathbf{K}] (\mathbf{u}_r + i\mathbf{u}_i) = \mathbf{B} (\tilde{\mathbf{v}}_r + i\tilde{\mathbf{v}}_i) \quad (4.22)$$

where the subscripts r and i indicate respectively the real and imaginary part of the considered quantity.

Note that the definition of the \mathbf{K}^{uv} renders this kind of analysis intrinsically wrong when the difference between the bias voltages applied at the nodes of a TRANS126 element is zero. In this case, all the entries of the matrix would be zero and the applied voltage signal $\delta \mathbf{v} = \tilde{\mathbf{v}}(t)$ would have no influence on the system. As introduced in chapter 2, microresonators are typically operated with a small signal voltage superimposed to a large bias voltage and hence their harmonic behaviour can be correctly characterized using harmonic pre-stressed analysis. For this purpose, the complex linear system (4.22) needs to be solved for each frequency of interest. This can be very time consuming when large frequency ranges or fine frequency discretization is used. This is generally the case for high Q devices, such as microresonators.

4.3.4 Damping modelling

In the previous chapter, the various phenomena that contribute to energy dissipation in micromechanical devices have been presented. Damping modelling requires first to define the major damping source between these mechanisms for the device under study, and then to model it. For microswitches, the first step is quite simple. For the dynamic, the dimensions and the operating conditions of these devices, the main damping mechanism is squeeze film damping. In microresonators, instead, various damping phenomena are important and each of them is prevalent over the others only in a certain area of the design parameter space. Slightly changing the device parameters might cause the dominant damping mechanism to change, requiring a completely different damping model. On the other hand, the introduction of a dissipation source in the model is extremely important because it is the only way to obtain a faithful description of device mechanical and electrical behaviour.

An approximated description of damping phenomena, common to civil and mechanical engi-

neers, has been adopted, that is, *Rayleigh mode preserving damping*. The system damping matrix E is computed as a linear combination of mass and stiffness matrices:

$$\mathbf{E} = \alpha\mathbf{M} + \beta\mathbf{K} \quad (4.23)$$

where α and β are constant coefficients. With this choice of the damping matrix, modes do not couple and have the same shape than in the undamped case [161].

Rayleigh damping has generally little theoretical background, but enables a great simplification of the problem and can anyway lead to reasonably accurate results, with a proper choice of the damping coefficients. For this purpose, there are several possibilities, depending on the problem under study:

- Fitting of experimental data: if experimental data of the dynamical behaviour of the device under study (or a similar devices) are available, the damping coefficients can be extracted by fitting of the experimental curve. For microswitches, dynamical measurements are not always available, while they are very common for microresonator;
- Physical simulation: in certain damping conditions, it is possible to extract the damping parameters from physical level simulations. ANSYS, for example, offer the possibility to approximately compute modal Rayleigh coefficients in case of squeeze film damping. This is done on the basis of a 2D simulation of the pressure distribution on the structure, when this vibrates in a particular mode [162]. The effects of holes through the structure can also be included. This can be useful especially for the simulation of microswitches.
- Analytical models: analytical damping models can be used to extract an approximate value of a device dynamic property, and the damping parameters can then be chosen in order to reproduce it. One simple example is the estimation of the quality factor of the resonator using analytical formulas, followed by an appropriate choice of the damping parameters. For switches, the method is not straightforward due to the lack of analytical expression of dynamical parameters.

In the simulations of this thesis, the first and the last approach have been applied to obtain meaningful values of the resonator damping parameters, while only the first one has been applied for switches.

It is worth noting that accurate compact models for squeeze-film damping are available in literature [67, 136]. Damping can thus be introduced also at circuit level, simply adopting the same description language and conventions of these damping models in the creation of the electromechanical reduced model.

4.3.5 Contact force modelling

The modelling of microswitches requires also the description of the reaction force exerted by the switch stop surface on the switch when they get into contact. This force has a nonlinear dependency from the switch position.

TRANS126 elements have integrated the capability to model such a force. This is done by modelling the contact plane as a spring with very large stiffness. For a distance d between the nodes of the elements which is lower than a certain value $gapmin$, the movable nodes are subjected to a force that acts to push them apart with entity given by:

$$F_{cont} = K_n |d - gapmin|, \quad (4.24)$$

where K_n is the stiffness of the contact. This model has been used for the introduction of the contact forces in switches compact models, at circuit level.

Chapter 5

Model order reduction

In this chapter, an introduction on model order reduction and an overview of the relevant MOR methods will be presented. The devices under study are, after spatial discretization, described by a second order nonlinear ODE system. However, linear model order reduction techniques have been adopted for their modelling. The main methods for model order reduction of linear systems are therefore first reviewed. Since the theoretical basis of these methods comes from control theory, a brief introduction of some concepts of control theory is necessary.

The extension of linear model order reduction techniques to the modelling of electromechanical system is then discussed.

5.1 Introduction and problem statement

The need of approximating large systems of equations describing a certain physical phenomenon with a simpler dynamic model arises from limited computational time and storage capability in either simulation or control problems [29].

Model order reduction techniques address the approximation of first or second order dynamic ODE systems. These are derived either by direct modelling of the physical problem of interest or by discretization of a set of partial differential equations. An n dimensional time-invariant m -input p -output second order system is described by the equations:

$$\mathbf{M}\ddot{\mathbf{x}}(t) + \mathbf{E}\dot{\mathbf{x}}(t) + \mathbf{K}\mathbf{x}(t) = \mathbf{B}\mathbf{q}(t) \quad (5.1)$$

$$\mathbf{y}(t) = \mathbf{C}\mathbf{x}(t) + \mathbf{D}\mathbf{u}(t)$$

with suitable initial conditions. The vector $\mathbf{x}(t) \in \mathbb{R}^n$ is the vector of state variables, while $\mathbf{q}(t) \in \mathbb{R}^m$ and $\mathbf{y}(t) \in \mathbb{R}^p$ are the input and output vectors, respectively. The matrices \mathbf{M} , \mathbf{K} , $\mathbf{E} \in \mathbb{R}^{n \times n}$ are respectively the mass, stiffness and damping system matrices. The matrix $\mathbf{B} \in \mathbb{R}^{n \times m}$, called scattering or input matrix, distributes the action of the inputs on the system d.o.f. and the output matrices \mathbf{C} and $\mathbf{D} \in \mathbb{R}^{n \times p}$ allow to extract from the state vector the desired d.o.f. and

eventually combine them linearly with the input functions¹. Generally the numbers of the inputs of the system and of the output quantities of interest are much lower than the number of system d.o.f., that is $n \ll m, p$. Any second order system in the form (5.2) can be transformed in the $2n$ -dimensional first order system:

$$\begin{bmatrix} \mathbf{I} & \mathbf{0} \\ \mathbf{0} & \mathbf{M} \end{bmatrix} \begin{bmatrix} \dot{\mathbf{x}}(t) \\ \ddot{\mathbf{x}}(t) \end{bmatrix} = \begin{bmatrix} \mathbf{0} & \mathbf{I} \\ -\mathbf{K} & -\mathbf{E} \end{bmatrix} \begin{bmatrix} \mathbf{x}(t) \\ \dot{\mathbf{x}}(t) \end{bmatrix} + \begin{bmatrix} \mathbf{0} \\ -\mathbf{B} \end{bmatrix} \begin{bmatrix} \mathbf{x}(t) \\ \dot{\mathbf{x}}(t) \end{bmatrix} \quad (5.2)$$

$$\mathbf{y}(t) = \begin{bmatrix} \mathbf{C} & \mathbf{0} \end{bmatrix} \begin{bmatrix} \mathbf{x}(t) \\ \dot{\mathbf{x}}(t) \end{bmatrix} + \mathbf{D}\mathbf{u}(t).$$

A lot of attention has therefore been focused on the study of first order systems.

Model order reduction aims at finding a system with dimension $r \ll n$, which approximates the input/output behaviour of the original system at any instant in time, while respecting these conditions [29]:

- the procedure to build the reduced order system has to be computationally efficient and stable;
- the reduced order system has to preserve properties of the original system such as stability and passivity;
- the approximation error has to be small and limited by a global error bound.

When a large system has to be approximated, also storage and reduced model computational speed issues arise.

All the main model order reduction methods for linear systems are *projection* methods. This means that the reduced order system is found by projecting the original system on a lower dimension subspace. This is mathematically equivalent to a base transformation, followed by *truncation*. The model reduction problem is thus reduced to finding appropriate subspaces, which can lead to a good approximation of the original system. These subspaces depend on the system matrices and eventually on the input and the output matrices. Linear model order reduction methods differ for the choice of the subspaces. According to the classification in [29], these methods are divided into eigensystem methods, methods based on singular value decomposition (SVD) and moment matching based methods.

¹In the general case the system outputs could also depend on the state vector first derivatives.

5.2 Basics of system theory

5.2.1 System representation

The state equation of a first order linear system is generally written in the form [32]:

$$\dot{\mathbf{x}}(t) = \mathbf{A}\mathbf{x} + \mathbf{B}\mathbf{q}(t) \quad (5.3)$$

$$\mathbf{y}(t) = \mathbf{C}\mathbf{x} + \mathbf{D}\mathbf{u}(t)$$

where $\mathbf{A} \in \mathbb{R}^{n \times n}$ is the system matrix. These equations give an internal description of the system in the time domain. The system can be equivalently described in the frequency domain using the Laplace transform, defined by:

$$\mathcal{L}[f(t)] = \int_0^{\infty} f(t)e^{-st} dt, \quad s \in \mathbb{C}. \quad (5.4)$$

Applying the Laplace transform to (5.3), with zero initial conditions, we obtain the frequency domain representation of the system:

$$s\mathbf{X}(s) = \mathbf{A}\mathbf{X}(s) + \mathbf{B}\mathbf{U}(s) \quad (5.5)$$

$$\mathbf{Y}(s) = \mathbf{C}\mathbf{X}(s) + \mathbf{D}\mathbf{U}(s)$$

where $\mathbf{X}(s)$, $\mathbf{Y}(s)$, $\mathbf{U}(s)$ are the Laplace transform of the state vector, the output vector and the input vector, respectively. The system transfer function, which gives the direct relation between the Laplace transform of the inputs and the outputs of the system, can be found by eliminating $\mathbf{X}(s)$ in (5.5). For a first order system it is:

$$\mathbf{H}(s) = \frac{\mathbf{Y}(s)}{\mathbf{X}(s)} = \mathbf{C}(s\mathbf{I} - \mathbf{A})^{-1}\mathbf{B} + \mathbf{D}. \quad (5.6)$$

Proceeding in the same way for a second order system in the form (5.2), we have instead:

$$\mathbf{H}(s) = \mathbf{C}(s^2\mathbf{M} + s\mathbf{E} + \mathbf{K})^{-1}\mathbf{B} + \mathbf{D}. \quad (5.7)$$

For both systems, the transfer function is a $p \times m$ matrix-valued rational function, with entries of the form:

$$H(s)_{ij} = \frac{b_0 + b_1s + \dots + b_{n-1}s^{n-1}}{1 + a_1s + \dots + a_ns^n}. \quad (5.8)$$

5.2.2 System properties

Various properties can be defined for system (5.3). The system is said to be [29, 32]:

- *stable*, if the system evolution $\mathbf{x}(t)$ from any initial state without applied loads (free re-

response) remains bounded as $t \rightarrow \infty$. This condition is satisfied if all eigenvalues of the system matrix \mathbf{A} have negative real part;

- *passive*, if the system does not create energy;
- *controllable*, if, for any initial state \mathbf{x}_0 and any final state \mathbf{x}_1 , there exists an input $\mathbf{u}(t)$ that transfers \mathbf{x}_0 in \mathbf{x}_1 in a finite time;
- *observable* if, given the system final state and its input and output history in a finite time interval $[t_0, t_1]$, it is possible to uniquely derive its initial state $\mathbf{x}(t_0)$;
- a *minimal realization* of its transfer function $\mathbf{H}(s)$ if its system matrix has minimal dimension. In this case, there are no states, which are not controllable or observable.

Controllability and observability of a system are mathematically described by the so called infinite controllability and observability grammians, \mathcal{P} and \mathcal{Q} , which, for a stable system, are defined respectively by [29]:

$$\mathcal{P} = \int_0^{\infty} e^{\mathbf{A}t} \mathbf{B} \mathbf{B}^T e^{\mathbf{A}^T t} dt \quad (5.9)$$

$$\mathcal{Q} = \int_0^{\infty} e^{\mathbf{A}^T t} \mathbf{C}^T \mathbf{C} e^{\mathbf{A}t} dt \quad (5.10)$$

If the infinite controllability and observability grammians have full rank (i.e. are not singular) the system is completely controllable and observable. These grammians allow to determine the degree of controllability and observability of the states of a system. In fact, the states which are more difficult to control and to observe are the ones with a big component or completely belonging to the span of the eigenvectors of \mathcal{P} and \mathcal{Q} , which corresponds to small eigenvalues [163]. The ability to classify the system states according to their degree of controllability and observability is very important for model order reduction. States of a system with a low degree of controllability and observability are in fact of low importance for the given inputs and outputs. The two grammians are positive definite matrices and can be found by solving the so called Lyapunov equations, given by:

$$\mathbf{A} \mathcal{P} + \mathcal{P} \mathbf{A}^T = -\mathbf{B} \mathbf{B}^T \quad (5.11)$$

$$\mathbf{A}^T \mathcal{Q} + \mathcal{Q} \mathbf{A} = -\mathbf{C}^T \mathbf{C}$$

Stable methods to solve such equations are available [164]. The positive square roots of the eigenvalues of the matrix $\mathcal{P} \mathcal{Q}$ are called *Hankel singular values*.

5.3 Review of linear MOR methods

5.3.1 Eigensystem method

Let us consider the transfer function of a linear stable system:

$$\mathbf{H}(s) = \mathbf{C}(s\mathbf{I} - \mathbf{A})^{-1}\mathbf{B} + \mathbf{D}$$

If the matrix \mathbf{A} is diagonalizable:

$$\mathbf{A} = \mathbf{S}\mathbf{\Lambda}\mathbf{S}^{-1} = \mathbf{S} \cdot \text{diag}(\lambda_1, \lambda_2, \dots, \lambda_n) \cdot \mathbf{S}^{-1}$$

with $\Re(\lambda_n) \leq \Re(\lambda_{n-1}) \leq \Re(\lambda_1) < 0$, then the system transfer function can be expressed in the *pole-residue representation*:

$$H_{ij}(s) = \rho_{\infty,ij} + \sum_{k=1}^n \frac{\kappa_{ij,k}}{s + \lambda_k}$$

where the eigenvalues of the system matrices are the *poles* of the transfer function and $\kappa_{ij,k}$ are the *residues* [32]. By analyzing this expression, it can be seen that only a few poles around the regions of frequency of interest are necessary for a good approximation of the transfer function. These are called *dominant poles*. A reduced order model of the system can thus be extracted by projecting the original system on the space spanned by the matrix \mathbf{S} and then truncating it so that only the dominant poles are retained. Several techniques have been developed to evaluate the effective importance of the different poles on the input/output behaviour of the system (the so called modal dominance analysis) [165].

Since diagonalization of the system matrix requires $\mathcal{O}(n^3)$ operation, this approach cannot be applied to large systems. Partial eigendecomposition is instead used. This is the base of the modal superposition method, which approximates the system transfer function by computing only the first eigenvalues of the system and the respective eigenvectors [166]. Such a choice, however, does not ensure that the dominant poles of the system are correctly represented in the reduced system.

5.3.2 SVD-based methods

Given a matrix $\mathbf{A} \in \mathbb{R}^{n \times m}$, its *singular value decomposition* is defined as:

$$\mathbf{A} = \mathbf{U}\mathbf{\Sigma}\mathbf{V}^T, \quad \mathbf{\Sigma} = \text{diag}(\sigma_1, \dots, \sigma_n) \in \mathbb{R}^{n \times m}, \quad (5.12)$$

where $\sigma_1 \geq \dots \geq \sigma_n \geq 0$ are the singular values of \mathbf{A} , positive square roots of the eigenvalues of $\mathbf{A}\mathbf{A}^T$, and the columns of \mathbf{U} and \mathbf{V} are called the left and right singular vectors of \mathbf{A} , respectively. These are the eigenvectors of $\mathbf{A}\mathbf{A}^T$ and $\mathbf{A}^T\mathbf{A}$. This decomposition is applied in different ways in the reduction procedure of dynamic systems, as summarized in Table 5.1. For linear systems, the main SVD-based methods are approximation by balanced truncation, singular perturbation and Hankel-norm approximation. Application of SVD to nonlinear system is called *proper orthogonal*

Singular value decomposition	
Non linear	Linear
Proper orthogonal decomposition (POD)	Balanced truncation Singular perturbation Hankel-norm approximation

Table 5.1: SVD based approximation methods

decomposition.

Balanced truncation

A reduced model of a system may be obtained by eliminating from the original system or from an equivalent representation the state variables that are difficult both to control and to observe. However, it is not always true that the states of a system with a low degree of controllability have simultaneously a low degree of observability. In order to solve this issue, a transformation can be applied that brings the system in a balanced representation in which each state has the same degree of controllability and observability [163]. When the system is in a balanced representation, the infinite controllability and observability grammians of the system are diagonal and equal. From a mathematical point of view, the concept of balancing consists therefore on a simultaneous diagonalization of \mathcal{P} and \mathcal{Q} . If the system is in a balanced representation and the state variables corresponding to small Hankel singular values are truncated, a reduce order system is obtained, which preserves the stability of the original system and has a bounded approximation error. This procedure is at the basis of model order reduction by balanced truncation. If S is a system in balanced representation with grammians $\mathcal{P} = \mathcal{Q} = \text{diag}(\sigma_1, \dots, \sigma_n)$ with $\sigma_1 > \sigma_2 > \dots > \sigma_n$ matrices and state vector can be partitioned as:

$$\mathbf{A} = \begin{bmatrix} \mathbf{A}_{11} & \mathbf{A}_{12} \\ \mathbf{A}_{21} & \mathbf{A}_{22} \end{bmatrix}, \mathbf{B} = \begin{bmatrix} \mathbf{B}_1 \\ \mathbf{B}_2 \end{bmatrix}, \mathbf{C} = \begin{bmatrix} \mathbf{C}_1 & \mathbf{C}_2 \end{bmatrix}, \mathbf{x} = \begin{bmatrix} \mathbf{x}_1 \\ \mathbf{x}_2 \end{bmatrix}. \quad (5.13)$$

The system defined by the matrices $\mathbf{A}_{11} \in \mathbb{R}^{r \times r}$, $\mathbf{B}_1 \in \mathbb{R}^{r \times m}$ and $\mathbf{C}_1 \in \mathbb{R}^{p \times r}$ is a reduced order system obtained by balanced truncation. If $\mathbf{H}(s)$ and $\mathbf{H}_r^{BTA}(s)$ are the transfer functions of the original and of the r -dimensional reduced order system, respectively, the following relation is satisfied:

$$\|\mathbf{H}(s) - \mathbf{H}_r^{BTA}(s)\|_\infty \leq 2(\sigma_{r+1} + \dots + \sigma_n) \quad (5.14)$$

where the norm $\|\cdot\|_\infty$ selects the maximum of its arguments [167]. This equation expresses a trade-off between the accuracy of the approximation and the complexity of the approximant. It provides therefore a criterion for choosing the order of the reduced order model, according to the desired accuracy. The maximum error generally occurs in the approximation of the low frequency behaviour of the system.

From a numerical point of view, due to the rapid decay of the singular values of the grammians as

well as the Hankel singular value, diagonalization can become inefficient and ill-conditioned. It is therefore important to avoid matrices inversion. Stable algorithms for the simultaneous balancing and truncation of the original system are based on computation and the SVD of the grammians [29]. The extraction of reduced order models is therefore computationally expensive, especially for large systems. If n is the dimension of the original system $\mathcal{O}(n^3)$ operations and $\mathcal{O}(n^2)$ storages are required.

Singular perturbation approximation

In some cases, it is important that the transfer function of the approximated system matches the one of the full system at zero frequency. In order to satisfy this condition, the balanced representation of the original system can be divided into a fast and a slow component, and the latter can be chosen as dominant component. This can be done by partitioning the system as in (5.13), and then truncating as follows:

$$\begin{aligned}\dot{\mathbf{x}}_1 &= (\mathbf{A}_{11} - \mathbf{A}_{12}\mathbf{A}_{22}^{-1}\mathbf{A}_{21})\mathbf{x}_1 + (\mathbf{B}_1 - \mathbf{A}_{12}\mathbf{A}_{22}^{-1}\mathbf{B}_2)\mathbf{u} \\ \dot{\mathbf{y}}_1 &= (\mathbf{C}_1 - \mathbf{C}_2\mathbf{A}_{22}^{-1}\mathbf{A}_{21})\mathbf{x}_1 - \mathbf{C}_2\mathbf{A}_{22}^{-1}\mathbf{B}_2\mathbf{u}\end{aligned}\tag{5.15}$$

The numerical techniques used to derive this reduced order model and the model properties are the same as for balanced truncation [164]. The computational cost is instead higher.

Hankel-norm approximation

A balanced state-space representation of a system can also be derived by minimizing a certain criterion. Model order reduction based on the Hankel norm approximation aims at finding an approximation of the original system, which is optimal with respect to the Hankel norm, defined as the maximum Hankel singular value of a system. This means that the Hankel norm of the error:

$$\|\mathbf{H}(s) - \mathbf{H}_r^{HNA}(s)\|_{\mathcal{H}}$$

has to be minimized. Algorithms for the construction of a reduced order system, which satisfies this condition, can be found in [29]. The error bound of a reduced order system obtained with this method is half of the one achievable with the use of balanced truncation. The computational cost of model extraction is quite high.

5.3.3 Moment matching based methods

Moment matching model order reduction is based on the approximation of the transfer function (5.8) of the original n -dimensional system with a rational function with a lower degree. This is done by matching some terms of the Taylor expansion of $\mathbf{H}(s)$ around a certain expansion point

s_0 [32]:

$$\mathbf{H}(s) = \sum_{i=0}^{\infty} \mathbf{m}_i (s - s_0)^i. \quad (5.16)$$

where $\mathbf{m}_i = \mathbf{C} \tilde{\mathbf{A}}^i \mathbf{R}$, $\tilde{\mathbf{A}} = (\mathbf{I} - s_0 \mathbf{A})^{-1}$, $\mathbf{R} = \tilde{\mathbf{A}} \mathbf{B}$ and $\tilde{\mathbf{A}}$ is assumed to be not singular. This is equivalent to matching the coefficients \mathbf{m}_i of the Taylor expansion, called moments of the system. For simplicity, in the following, a single-input single-output (SISO) system will be considered. For this kind of system, the transfer function is scalar and the input and output matrices are vectors, which will be indicated as \mathbf{b} and \mathbf{c} , respectively. However, the methods can be extended to the more general multi input multi-output (MIMO) case [166].

The maximum number of moments of the original system that can be matched with an r -dimensional approximant is equal to $2r$. Reduced systems, which match $2r$ moments are called *Padé approximant*, while if less moments are matched, the term *Padé type approximant* is used.

Moment matching can be done explicitly by developing $H(s)$ until the moment $2r$ and then computing the coefficient $\{a_1, \dots, a_r\}$, $\{b_0, \dots, b_r\}$ of the rational function $H_r(s)$:

$$H_r(s) = \frac{b_0 + b_1 s + \dots + b_{k-1} s^r}{1 + a_1 s + \dots + a_k s^r} \quad (5.17)$$

by solving the $2r$ conditions expressed by:

$$m_0 + m_1(s - s_0) + \dots + m_{2r}(s - s_0)^{2r} = H_r(s). \quad (5.18)$$

However, such a procedure is numerically unstable due to round-off errors [32]. Implicit methods are therefore generally applied.

Implicit moment matching model order reduction is based on Krylov subspaces. The right/left r -dimensional Krylov subspaces of matrix \mathbf{A} and vector \mathbf{v} are defined as:

$$\mathcal{K}_r^R = \text{span} \{ \mathbf{v}, \mathbf{A}\mathbf{v}, \dots, \mathbf{A}^{r-1}\mathbf{v} \} \quad (5.19)$$

$$\mathcal{K}_r^L = \text{span} \{ \mathbf{v}^T, \mathbf{v}^T \mathbf{A}, \dots, \mathbf{v}^T \mathbf{A}^{r-1} \} \quad (5.20)$$

The moments of a linear system can be computed as the inner product of the right Krylov subspace generated by the matrix $\tilde{\mathbf{A}}$ and the vector $\mathbf{r} = \tilde{\mathbf{A}} \mathbf{b}$ and the left Krylov subspace of matrix $\tilde{\mathbf{A}}$ and vector \mathbf{c} . However, direct computation of Krylov subspaces are not indicated since the Krylov vectors rapidly become linearly dependent. Padé or Padé type approximants of the original system can be implicitly found by computing an orthonormal basis of the Krylov subspaces and projecting of the original system onto it. For this purpose, the Lanczos and the Arnoldi process are used, which are based on iterative and numerically more reliable algorithms [168].

A link between Krylov subspace techniques and SVD methods can be established, noting that, in the language of control theory, the right and left Krylov subspaces correspond to the reachability and the controllability subspaces of the matrix \mathbf{A} , respectively. Moreover, Krylov subspaces offer a method to approximate the eigenvalues of a matrix. If \mathbf{V} is a basis of the right Krylov

subspace $\mathcal{K}_r^R(\mathbf{A}, \mathbf{v})$ and \mathbf{A} is symmetric, it is proved that the eigenvalues of $\mathbf{V}^T \mathbf{A} \mathbf{V}$ converge to the eigenvalues of \mathbf{A} [29].

Lanczos process

The Lanczos process is based on the computation of a pair of biorthogonal basis $\mathbf{W}_r, \mathbf{V}_r \in \mathbb{R}^{n \times r}$ for the subspaces $\mathcal{K}_r^R(\tilde{\mathbf{A}}, \mathbf{r})$ and $\mathcal{K}_r^L(\tilde{\mathbf{A}}, \mathbf{c})$ so that:

$$\mathbf{W}_r^T \mathbf{V}_r = \mathbf{I}_r$$

where $\mathbf{I}_r \in \mathbb{R}^{r \times r}$ is the identity matrix. A reduced order approximation of the original system can be found by applying the Petrov-Galerkin projection, defined by:

$$\mathbf{A}_r = \mathbf{W}_r^T \mathbf{A}, \mathbf{b}_r = \mathbf{W}_r^T \mathbf{b}, \mathbf{c}_r = \mathbf{c} \mathbf{V}_r. \quad (5.21)$$

The system matrix of the reduced system is tridiagonal and can be considered an oblique projection of the original system on $\mathcal{K}_k^r(\tilde{\mathbf{A}}, \mathbf{b})$ while remaining perpendicular to $\mathcal{K}_k^l(\tilde{\mathbf{A}}, \mathbf{c})$ [32].

Algorithm 2 *Lanczos algorithm: given the system matrix $\mathbf{A} \in \mathbb{R}^{n \times n}$ and two starting vectors $\mathbf{b}, \mathbf{c} \in \mathbb{R}^n$*

1. Set $\tilde{\mathbf{v}}_1 = \mathbf{b}, \tilde{\mathbf{w}}_1 = \mathbf{c}$;
For $i=1, \dots, r$ do:
2. Compute $v_i = \|\tilde{\mathbf{v}}_i\|, w_i = \|\tilde{\mathbf{w}}_i\|$;
3. Set $\mathbf{v}_i = \tilde{\mathbf{v}}_i/v_i, \mathbf{w}_i = \tilde{\mathbf{w}}_i/w_i$;
4. Set $\delta_i = \mathbf{w}_i^T \mathbf{v}_i$;
5. Set $\alpha_i = \mathbf{w}_i^T \mathbf{A} \mathbf{v}_i / \delta_i$;
6. Set $\beta_i = (\delta_i / \delta_{i-1}) v_i$;
7. Set $\gamma_i = (\delta_i / \delta_{i-1}) w_i$;
8. Set $\tilde{\mathbf{v}}_{i+1} = \mathbf{A} \mathbf{v}_i - \tilde{\mathbf{v}}_i \alpha_i - \tilde{\mathbf{v}}_i \beta_i$ and $\tilde{\mathbf{w}}_{i+1} = \mathbf{A}^T \mathbf{w}_i - \mathbf{w}_i \alpha_i - \mathbf{w}_i \gamma_i$;
End for

It can be demonstrated that the reduced system matches the first $2r$ moments of the original system and it is invariant to system representation [168]. The $2r$ unknowns of the Taylor expansion of the transfer function of the reduced system are in fact all fixed by the implicit matching of $2r$ moments. Both the system input and output matrices are used for the derivation of the reduced model, thus optimizing it. Due to the oblique projection, preservation of model stability is not

guaranteed. The algorithm of the Lanczos process, reported in Algorithm 2, is iterative and reasonably fast, also for large values of r . At each step two new vectors are produced, each perpendicular to the previously generated vectors and only matrix-vector multiplications are needed. The computational cost is $\mathcal{O}(rn)$ for sparse matrices and $\mathcal{O}(rn^2)$ for dense systems. Major drawback of the algorithm is that it can lose stability and it stops prematurely if δ_i becomes zero, as it could occur due to the finite precision arithmetic.

The algorithm can be extended to multi-input multi-output systems by repeating the algorithm 2 for all the columns of the input and the output matrices (*matrix Padé via Lanczos*).

Arnoldi process

The Arnoldi process produces only a orthonormal basis \mathbf{V}_r of the right Krylov subspace $\mathcal{K}_r^R(\tilde{\mathbf{A}}, \mathbf{r})$ and the matrix [168]:

$$\mathbf{A}_r = \mathbf{V}_r^T \mathbf{A} \mathbf{V}_r, \quad a_{r,ij} = 0 \forall (i, j) : |i - j| > 1. \quad (5.22)$$

This is the system matrix of the reduced order system obtained by the Galerkin (orthogonal) projection of the original system onto $\mathcal{K}_r^R(\tilde{\mathbf{A}}, \mathbf{r})$. The reduced system is a Padé type approximant of the original system and implicitly matches its first r moments. This implies that the reduced model is not invariant with respect to the representation: r of the $2r$ unknowns are in fact chosen arbitrary. The reduced accuracy in terms of moment matched, with respect to the Lanczos process, is due to the fact that the output vector is not used in the derivation of the reduced order model. A modified version of the Lanczos process, called *two-sides Arnoldi*, has been proposed, which applies the Arnoldi process to generate a basis for both the right and left Krylov subspaces, respectively $\mathcal{K}^R(\tilde{\mathbf{A}}, \mathbf{r})$ and $\mathcal{K}^L(\tilde{\mathbf{A}}, \mathbf{c})$. The two matrices thus obtained are then used for oblique projection of the system. In this case $2r$ moments are matched and the resulting transfer function is unique, but at the expenses of computational complexity and numerical stability.

Algorithm 3 *Arnoldi algorithm: given the system matrix $\mathbf{A} \in \mathbb{R}^{n \times n}$ and the starting vector $\mathbf{b} \in \mathbb{R}^n$*

1. Set $\tilde{\mathbf{v}}_1 = \mathbf{b}$;
For $i=1, \dots, r$ do:
 2. Compute $v_{i,i-1} = \|\tilde{\mathbf{v}}_i\|$;
if $v_{i,i-1} = 0$ STOP
 3. Set $\mathbf{v}_i = \tilde{\mathbf{v}}_i / v_{i,i-1}$;
 4. Set $\tilde{\mathbf{v}}_{i+1} = \mathbf{A} \mathbf{v}_i$
 5. For $j=1, \dots, i$ do:
 - Set $v_{j,i} = \mathbf{v}_j^T \tilde{\mathbf{v}}_{i+1}$ and $\tilde{\mathbf{v}}_{i+1} = \tilde{\mathbf{v}}_{i+1} - v_{j,i} \mathbf{v}_j$
 - End for
 - End for
-

As for the Lanczos process, the Arnoldi process does not preserve, in the general case, the stability and passivity properties of the system. However, if the original system is stable, passive and has a symmetric system matrix, these properties are preserved in the reduced system. Moreover, due to its simplicity, several modifications of the Arnoldi algorithm have been presented, which, with some extra computational effort, preserve the properties of the original system [31].

The Arnoldi process automatically produces a full output reduced order system. Its extension to a multi-input system, called *Block Arnoldi*, is therefore simpler than the matrix Padé via Lanczos approach [169]. The Arnoldi algorithm, described by Algorithm 3, is iterative. At each step, a new vector of the Krylov subspace basis is computed and the modified Gram-Schmidt orthogonalization process is applied so that this is perpendicular to all previously computed vectors. When the vectors become linearly dependent, the Krylov subspace is called *exhausted* and the algorithm stops. As in the Lanczos process, only matrix-vector multiplications are needed, but in this case the computational complexity is higher, since the orthogonalization process involves more vectors. $\mathcal{O}(r^2n)$ operations are required for sparse matrices and $\mathcal{O}(rn^2)$ for dense systems. The characteristics of the Arnoldi and the Lanczos are summarized in Table 5.2.

Krylov subspace methods concluding remarks

Due to their iterative nature, the algorithms for model order reduction via moment matching are simple, numerically reliable and efficient. Both algorithms involve only matrix-vector multiplications and have therefore a maximum computational complexity of $\mathcal{O}(rn^2)$ (for dense system), which is lower than the one achievable with methods involving factorization. In addition, the use of an iterative algorithm has the advantage that, once an r -dimensional model is available, also all the models with lower order are available by submatrices extraction. Hence, downsizing of the model does not require any additional calculation.

The reduction in computational complexity comes at the expenses of the mathematical optimality. In fact, moment matching techniques lead intrinsically to local approximation of the original system: its transfer function is approximated with good accuracy only around the expansion point s_0 . Moreover, for Krylov-subspace methods, a global error estimate is not available and the prop-

	Arnoldi	Lanczos
Moments matched	r	$2r$
Invariance properties	No	Yes
Computational complexity	$\mathcal{O}(r^2n)$ for sparse matrix $\mathcal{O}(rn^2)$ for dense matrices	$\mathcal{O}(rn)$ for sparse matrix $\mathcal{O}(rn^2)$ for dense matrices
Numerical stability	Yes	No
System properties preservation	Possible	No
Output approximated	Complete output	Specific Output
Extension to MIMO system	Easy	Complex

Table 5.2: Comparison between the Arnoldi and the Lanczos process

erties of the system such as stability and passivity are in the general case not preserved in the reduced model. The degree of approximation over the complex plane can be improved using a multi-point expansion [170]. In this case, the transfer function is expanded around several points and a reduced order model with transfer function that matches the first moments at all expansions points is found.

5.3.4 Guyan reduction

Guyan reduction, also known as substructuring, is a reduction method based on projection, which is commonly adopted in mechanical engineering and it is available in some commercial software. It was originally developed for the steady-state ODE system derived from the study of structural problems and has then been extended to dynamic undamped problem [171].

Guyan reduction is based on partitioning the system internal degrees of freedom into two parts. The d.o.f. that are subjected to the action of the input vector or outputs of the system are grouped in a vector of *master nodes* \mathbf{x}_e . The remaining d.o.f. define a second vector \mathbf{x}_i . The system matrices are then partitioned accordingly. Using the notation in (5.2), for a static system, we will have:

$$\begin{bmatrix} \mathbf{K}_{ee} & \mathbf{K}_{ei} \\ \mathbf{K}_{ie} & \mathbf{K}_{ii} \end{bmatrix} \begin{bmatrix} \mathbf{x}_e \\ \mathbf{x}_i \end{bmatrix} = \begin{bmatrix} \mathbf{F}_e \\ \mathbf{F}_i \end{bmatrix} \quad (5.23)$$

where the input term \mathbf{q} has been incorporated in the input matrix to create the load vector: $\mathbf{F} = \mathbf{B}\mathbf{q}$. Since the load vector \mathbf{F}_i has to be zero, the two equations yield:

$$\mathbf{F}_e = (\mathbf{K}_{ee} - \mathbf{K}_{ei}\mathbf{K}_{ee}^{-1}\mathbf{K}_{ie})\mathbf{x}_e,$$

and therefore the reduced stiffness matrix is given by:

$$\mathbf{K}_r = \mathbf{K}_{ee} - \mathbf{K}_{ei}\mathbf{K}_{ee}^{-1}\mathbf{K}_{ie}.$$

The procedure is equivalent to the coordinate transformation $\mathbf{x} = \mathbf{V}\mathbf{x}_e$, where the transformation matrix \mathbf{V} is given by:

$$\mathbf{V} = [\mathbf{I}_e \quad -\mathbf{K}_{ii}^{-1}\mathbf{K}_{ie}]^T.$$

Until here, the reduction problem is exact. In order to handle also dynamic problems, however, an approximation is introduced. The reduced mass matrix is computed using the same transformation. With this choice, the potential and kinetic energy of the reduced model have a similar form, but combinations of the stiffness and mass element appear [171]. In case of Rayleigh damping, a damping matrix can be simply computed by combination of the reduced stiffness and damping matrices.

The performance of Guyan reduction is generally poor if compared with other linear model order reduction methods, except for the stationary case. Reduced order models are generally unnecessarily large for the achieved accuracy [30, 31]. The extraction process takes in fact into account

only the properties of the stiffness matrix.

On the other side, the degrees of freedom of the system are preserved during the reduction: the unknowns of the reduced model correspond to physical quantities. This can be convenient for the coupling of reduced order models, since their master degrees of freedom are automatically the external terminals of the reduced system.

5.3.5 Second-order systems

Second order system can be reduced by transforming them to the first order system (5.3), and then applying the methods described for these kinds of problems. This approach is called *linearization*. However, the reduction of second order systems by linearization ignores the physical meaning of the original matrices and gives a reduced order model in a first order form. It is instead desirable for the reduced system to preserve the form of the original system. Approaches, which deal directly with the system (5.2) have therefore been introduced, especially in the framework of Krylov subspaces methods [166, 172]. In the following, we will consider the extension to the second order case of these methods only. An overview of other methods is presented in [32].

As previously introduced, the transfer function of the system (5.2), with zero initial conditions, is given by:

$$\mathbf{H}(s) = \mathbf{D} + \mathbf{C}(s^2\mathbf{M} + s\mathbf{E} + \mathbf{K})^{-1}\mathbf{B}.$$

Undamped system

If the system is undamped, i.e. $\mathbf{E} = 0$, the transfer function (5.7) can be formally written as the transfer function of a first order system [173]. In fact, the Taylor expansion of the transfer function of the system, around a certain expansion point s_0^2 , can be written as:

$$\mathbf{H}(s) = \sum_{i=0}^{\infty} \mathbf{m}_i (s - s_0^2)^i. \quad (5.24)$$

assuming that the moments \mathbf{m}_i are:

$$\mathbf{m}_i = \mathbf{C} \left(- [s_0^2\mathbf{M} + \mathbf{K}]^{-1} \mathbf{M} \right)^i [s_0^2\mathbf{M} + \mathbf{K}]^{-1} \mathbf{B}.$$

These are the moments of the first order system:

$$\dot{\mathbf{x}} = \tilde{\mathbf{A}}\mathbf{x} + \mathbf{R}\mathbf{q}$$

with $\tilde{\mathbf{A}} = - [s_0^2\mathbf{M} + \mathbf{K}]^{-1} \mathbf{M}$ and $\mathbf{R} = \tilde{\mathbf{A}}\mathbf{B}$ around the expansion point $s = -s_0^2$. The procedure used for these systems can then be extended to second order systems. Assuming for simplicity that $s_0 = 0$ the Arnoldi or the Lanczos processes can be applied for the computation of a basis for the Krylov subspaces $\mathcal{K}_r^R(\mathbf{K}^{-1}\mathbf{M}, \mathbf{K}^{-1}\mathbf{B})$ and $\mathcal{K}_r^L(\mathbf{K}^{-1}\mathbf{M}, \mathbf{C})$. If the Arnoldi process is used, the

reduced system matrices are obtained by the orthogonal projection:

$$\begin{aligned} \mathbf{M}_r &= \mathbf{V}^T \mathbf{M} \mathbf{V} & \mathbf{K}_r &= \mathbf{V}^T \mathbf{K} \mathbf{V} \\ \mathbf{B}_r &= \mathbf{V}^T \mathbf{B} & \mathbf{C}_r &= \mathbf{C} \mathbf{V} \end{aligned} \quad (5.25)$$

and the matching properties of the method are conserved [31].

It is worth noting that, starting from a second order system in the form (5.2), Krylov subspace methods require the knowledge of \mathbf{K}^{-1} . For high dimensional systems, the explicit calculation of the inverse of \mathbf{K} is computationally not affordable. Its computation is therefore replaced by the solution of a linear system of equations. For the Arnoldi algorithm for example, this means to solve the system:

$$\mathbf{K} \mathbf{v}_1 = \mathbf{B}$$

and at the iteration step i :

$$\mathbf{K} \mathbf{v}_{i+1} = \mathbf{v}_i,$$

where $s_0 = 0$ has been assumed. For sparse matrices, as the one derived from the application of finite element methods, various linear solvers are available, which allow to solve such a system efficiently [34].

Damped system

Structure preserving model order reduction of damped second order system is more complex, except when the damping matrix has a particular form [174]. In case of Rayleigh damping, it can be demonstrated that the damping matrix can be neglected during the reduction process and it can be computed afterwards, as a linear combination of the reduced stiffness and mass matrices [31]. If $\mathbf{E} = \alpha \mathbf{M} + \beta \mathbf{K}$, this means that:

$$\mathbf{E}_r = \alpha \mathbf{M}_r + \beta \mathbf{K}_r. \quad (5.26)$$

A second-order structure preserving Krylov-subspace method (called SOAR) has also been presented, which takes the damping matrix into account [175].

5.3.6 Methods summary

In this section, the methods presented and their properties will be summarized. In addition, their application to the second order ODE system derived from the discretization of an electromechanical problem is valued on the base of their properties. The most important features of each method are reported in Table 5.3.

SVD methods are mathematically optimal, since they provide a global error and preserve the properties of the original system. The error bound can be used to estimate the difference in response between the original system and its reduced model. Hence, the choice of the order of the reduced model, which allows to achieve the desired accuracy can be done on mathematical

basis. However, the high computational complexity renders these methods unpractical for large systems, such the ones considered. Moreover, their extension to second order systems generally requires linearization.

Guyan reduction is developed for second order systems and has the advantage to preserve the interface d.o.f. of the system. This is convenient for the integration of the reduced models at system level, when at the interface between the models distributed quantities have to be exchanged. This is for example the case of the temperature field for models representing the thermal behaviour of contiguous areas of a device. For electromechanical models, preservation of the physical d.o.f. is not particularly important since reduced order models communicate only through a small number of electrical quantities.

Due to their numerical efficiency, Krylov subspace methods are the most suited for the study of large ODE systems. A Krylov subspace method has therefore been adopted in this thesis. In particular, due to its simplicity and numerical stability, the Arnoldi process has been used. The accuracy and extraction speed experienced using this algorithm are already so high that, in the opinion of the author, it is not convenient to sacrifice stability adopting the Lanczos process.

The local approximation resulting from the use of a moment matching method does not seem to limit the modelling accuracy for RF devices. With a proper choice of the expansion point, discussed in 5.5.2, a good description of the devices' behaviour has always been observed. In addition, various techniques have been proposed for choosing the order of the reduced models. These are presented in 5.5.2.

Table 5.3: Comparison between the presented methods for linear model order reduction

Methods	Advantages	Disadvantages
SVD based methods (Balance truncation, Hankel norm approximation and Singular perturbation)	- global error estimate - preserve system properties - fully automatic method	- High computational complexity $\mathcal{O}(n^3)$ - not easy to extend to structure preserving second order reduction
Guyan reduction	- exact in the stationary case - preserve physical d.o.f.	- requires large reduced models for good accuracy
Krylov based methods (Arnoldi and Lanczos process)	- Low computational complexity $\mathcal{O}(r^2n)$ - reliable, iterative and simple implementation - easy to extend to structure preserving second order reduction	- no global error esteem - properties of the system generally not preserved - local approximation (in the frequency domain)

5.4 Extension of MOR linear techniques to RF MEMS active devices

The previously presented techniques are valid for first or second order linear ODE system. Their application to RF MEMS devices requires the development of a procedure to handle nonlinearities.

Several approaches have been developed for the application of model order reduction techniques to various types of nonlinear systems. An overview of these methods can be found in [33]. Some of them act on the system directly in its original form, others require a previous approximation of the system. For weak nonlinearities, such the one introduced by electromechanical coupling, the original system is often first expanded in Taylor series around a certain expansion point and then reduced [176]. Nevertheless, nonlinear model order reduction is still an open problem: automatic and generalized methods are not available, also due to the wide range of possible systems.

Here, we present the approaches that have been chosen to deal with the nonlinearities arising in the modelling of microresonators and microswitches. In particular, considering the different behaviour of these two kinds of devices, two different approaches have been chosen. In order to present these methods, the general form for the electromechanical system is first defined and the source of nonlinearities identified.

Nonlinear electromechanical system

The general system derived from the spatial discretization of an electromechanical problem has the form:

$$\mathbf{M}\ddot{\mathbf{u}} + \mathbf{K}_m(\mathbf{u})\mathbf{u} = \mathbf{B}\mathbf{q}(t) + \mathbf{F}(\mathbf{u}, \mathbf{v}(t)). \quad (5.27)$$

Since damping phenomena are approximated using Rayleigh damping, the mechanical damping matrix does not take part to the reduction process. Hence, an undamped system is considered. In addition, as in 4.3.3, voltages are assumed to be constrained.

In the general case, the stiffness matrix is nonlinear since its entries dependent on the nodal displacements \mathbf{u} . The system load vector has been divided into a linear part, described by the input matrix \mathbf{B} and the time dependent input function \mathbf{q} , and a nonlinear part, $\mathbf{F}(\mathbf{u}, \mathbf{v}(t))$. $\mathbf{F}(\mathbf{u}, \mathbf{v}(t))$ represents the electrostatic force and, for switches, contact forces. Consequently, it is a nonlinear function of the nodal displacements and the applied voltages \mathbf{v} . However, only the dependency $\mathbf{F}(\mathbf{u})$ introduces nonlinearities in the system. In fact, nonlinear inputs are not a real source of nonlinearities for the system.

It is worth noting that an accurate modelling of damping phenomena would introduce a third source of nonlinearity in the system, which here is not considered.

5.4.1 Linearization

The simplest approach to reduce the system (5.27) is to linearize it around a certain operation point $(\mathbf{u}_0, \mathbf{v}_0)$. If the applied voltages can be written as

$$\mathbf{v} = \mathbf{v}_0 + \delta\mathbf{v}(t), \quad \delta\mathbf{v} \ll \mathbf{v}_0$$

it can be assumed that the state vector undergoes small variations around the bias point:

$$\mathbf{u} = \mathbf{u}_0 + \delta\mathbf{u}(t), \quad \delta\mathbf{u} \ll \mathbf{u}_0.$$

In this condition, we can assume with good approximation that $\mathbf{K}(\mathbf{u}) = \mathbf{K}(\mathbf{u}_0)$ and the load vector can be linearized. In this way, the system (4.20) is obtained, which can be reduced using linear model order reduction methods.

Linearization can be applied to the modelling of micromechanical resonators, since these devices are generally operated under small signal condition. For this purpose, a procedure has been developed for the correct extraction of system (4.20) from ANSYS binary files. This will be introduced in the next section. A more detailed explanation of the use and limit of linearization for the simulation of microresonators is instead presented in chapter 6, together with simulation results. The application of linearization to the modelling of RF switches is unfeasible since these devices are always operated in large signal conditions. An extension of this approach, the *trajectory piecewise-linear method*, could be adopted, which uses a weighted linear combination of models linearized around different operating points to create a reduced order model [177]. The operating points are usually chosen on a trajectory that represents the response of the system to a training input. This should be typical for the system. Each single linearized model is reduced using linear MOR technique. However, the subspace used for the projection is the union of the subspaces of all the linearized systems. In this way, a correspondence between the states of the individual models is obtained, but the dimensions of the reduced order models grow with the number of expansion points. Moreover, the choice of the expansion points can be critical for the accuracy of the reduced model.

5.4.2 Modeling of nonlinearities as inputs

The extraction of a nonlinear reduced order model of system (5.27) using linear model order reduction techniques can be done by regarding nonlinearities as inputs.

Let us isolate the nonlinearities in (5.27) by moving them in a new input function \mathbf{f} . The system can be rewritten as:

$$\mathbf{M}\ddot{\mathbf{u}} + \mathbf{K}\mathbf{u} = \mathbf{B}\mathbf{q}(t) + \mathbf{F}\mathbf{f}(\mathbf{u}, t). \quad (5.28)$$

If the nonlinearities are confined in the input function, the system can be reduced using linear model order reduction technique. The only complication is that, after the reduction, the argument of \mathbf{f} has to be recovered by the projection $\mathbf{u} = \mathbf{V}\mathbf{u}_r$. The reduced order nonlinear system will have

the form:

$$\mathbf{M}_r \ddot{\mathbf{u}}_r + \mathbf{E}_r \dot{\mathbf{u}}_r + \mathbf{K}_r \mathbf{u}_r = \tilde{\mathbf{B}}_r \tilde{\mathbf{q}}. \quad (5.29)$$

with $\tilde{\mathbf{B}} = [\mathbf{B}_r \quad \mathbf{V}^T \mathbf{F}]$ and $\tilde{\mathbf{q}} = [\mathbf{q}(t) \quad \mathbf{f}(\mathbf{V}\mathbf{u}_r, t)]^T$. The solution of the system (5.29) is computationally advantageous with respect to the solution of (5.27) only if the evaluation of the function $\mathbf{f}(\mathbf{V}\mathbf{x}_r, t)$ is fast [31]. This implies that the number of nonlinear equations of the system should be small or possible to reduce to a small number. This requirement is also important for an efficient extraction of the model, since the time needed for the extraction of the model depends linearly on the number of inputs of the system.

Neglecting mechanical nonlinearities, the system (5.27) is already in the desired form. However, in order to value the efficiency of the method it is necessary to consider the number of nonlinear equations of the original model. In theory, each node of the FE model that is subjected to electrostatic or contact forces introduces one nonlinear capacitance-stroke dependency. Consequently, the total of nonlinear equations in the model is far to be small. Nevertheless, one can introduce an approximation, which enables to reduce this number. The distributed electrostatic and contact forces can be replaced by a limited number of lumped forces, which act on some nodes spread over the surface of the mechanical model. In this way, the number of nonlinear equations is drastically reduced. With the introduction of this approximation on the forces, the reduction approach described by (5.29) can be applied to switches modelling, enabling the extraction of nonlinear reduced order models.

The right hand side of (5.27), that is the purely mechanical device model, is reduced using Krylov subspaces via the Arnoldi algorithm and the electrostatic and contact forces are reintroduced in the reduced model.

Contribution of the electrostatic forces to the load vector $\mathbf{F}\mathbf{f}(\mathbf{V}\mathbf{x}_r, t)$ can be computed at different levels of approximation, i.e. using simple analytical formulas or accurate FE electrostatic simulation. Contact forces have been described using the expression (4.24).

The approach is flexible and very easy to implement. In addition, the extraction and simulation (both static and dynamic) of the reduced model have proven to be fast and to give an accurate description of switches behaviour. More details about the approximation introduced on the electrostatic forces and the computation of the load vector are given in the chapter 6, together with simulation results.

5.5 Model order reduction: practical implementation

The application of MOR to the ANSYS system element matrices is performed with the command line tool MOR for ANSYS [178]. This has been originally developed for thermal and purely mechanical problems. Its extension to electromechanical problems required the development of a new approach for the extraction of the correct stiffness matrix for pre-stressed analysis and of the matrices needed for calculation of current outputs. The approach led to the implementation of a new version of the software, MOR for ANSYS 2.0, which is based on the extraction of the matrices

produced by ANSYS for harmonic analysis, and not for static analysis as in the previous version. After creation of the FE model, a first static nonlinear analysis is performed in ANSYS for the computation of the bias point and of the linearized tangent stiffness matrix, for a certain bias voltage and initial stress. In the purely mechanical case, this step is needed only if initial stress has to be taken into account. The complex matrix of the system (4.22), sometimes referred to as super-stiffness matrix, is calculated for two values of angular frequency and stored in ANSYS binary files. The total stiffness and mass matrices can then be extracted separately from its real part. Damping is included later in the model according to (5.26).

MOR for ANSYS 2.0 allows to read directly the computed matrices from ANSYS binary files, to reduce them and to compute the required output matrices.

5.5.1 MOR for ANSYS 2.0

The tool MOR for ANSYS 2.0 is basically constituted of two independent modules. The first reads system matrices from ANSYS binary files, assemble them in the form:

$$\mathbf{M}\ddot{\mathbf{u}} + \mathbf{E}\dot{\mathbf{u}} + \mathbf{K}\mathbf{u} = \mathbf{B}\mathbf{q} \quad (5.30)$$

and computes the output matrices using information given by the user through an input file.

The second module applies model order reduction to the above system and writes the reduced system into text files in Matrix Market Format. Variations with respect to the previous version concern only the first module.

Extraction and output matrix calculation

MOR for ANSYS 2.0 reads information necessary to assemble the system in form (5.30) from ANSYS binary FULL file. This file is generated using ANSYS partial solver, which enables to assemble system element matrices for the desired analysis without solving them and it therefore computationally fast. The FULL file contains all the information about the system: the system element matrices, Dirichlet boundary conditions, equation constrains and the load vector. The speed of the reading operation has been optimized taking into account that the element matrices are sparse. The load vector directly gives the matrix-vector product $\mathbf{B}\mathbf{q}$ and thus describes the distribution of all loads applied on the system d.o.f. In order to obtain the \mathbf{B} matrix, and thus being able to modify the inputs singularly, it is necessary to repeat the partial solution for each input of interest.

MOR for ANSYS 2.0 reads the super-stiffness matrices and the load vectors generated for harmonic pre-stressed analysis for two different values of the angular frequency and automatically extracts the mass and stiffness matrices. Since the entries of the two matrices generally have different orders of magnitude, the values of the angular frequency should be chosen so that $\omega^2\mathbf{M}$ has the same order of magnitude of \mathbf{K} and numerical errors are minimized.

Output degrees of freedom of interest for micromechanical resonators are the displacement of

special points of the resonator, such as the position of the device node subjected to maximum displacement during vibration, and the electric quantities at each device terminal. With the chosen modelling approach, voltages are known, while the currents in TRANS126 elements have to be calculated using equation (4.15) and computed values of displacement and voltage derivatives. The current at each device terminal will then be the sum of the currents flowing in the elements, which constitute that terminal. Distinguishing between displacement y_u and current y_i outputs, the equations for the system outputs become:

$$\begin{pmatrix} y_u \\ y_i \end{pmatrix} = \begin{pmatrix} \mathbf{C} & 0 \\ 0 & 0 \end{pmatrix} \begin{pmatrix} \mathbf{u} \\ \tilde{\mathbf{v}} \end{pmatrix} + \begin{pmatrix} 0 & 0 \\ \mathbf{D}_u & \mathbf{D}_v \end{pmatrix} \begin{pmatrix} \dot{\mathbf{u}} \\ \dot{\tilde{\mathbf{v}}} \end{pmatrix}. \quad (5.31)$$

The matrices \mathbf{D}_u and \mathbf{D}_v have to be derived from \mathbf{E}_{vv} and \mathbf{E}_{vu} in (4.19). The application of Dirichlet boundary conditions to the voltage degrees of freedom leads to the elimination of the entries of these matrices. The additional creation of the FULL file for the unconstrained system is therefore needed. The user has then to create two input files. One has to contain, for each mechanical output, the node number and the degrees of freedom of interest for that node. MOR for ANSYS 2.0 uses this information for computing the displacement output matrix \mathbf{C} of the original system. The second file contains, for each device terminal, the numbers of the nodes of the TRANS126 elements connected to it. These numbers are used in \mathbf{E}_{vv} for retrieving the displacements of interest for current computation and in \mathbf{E}_{vu} for selecting the rows which corresponds to d.o.f. of TRANS126 nodes belonging to the same device terminal. The matrices \mathbf{D}_u and \mathbf{D}_v are then created.

The output matrices \mathbf{C} and \mathbf{D}_u are reduced in the second module, while matrix \mathbf{D}_v is ready to be written in a text file.

Reduction

MOR for ANSYS (both versions) implements implicit moment matching model order reduction via the Arnoldi algorithm or the block Arnoldi algorithm, for multi-input systems. Second order systems can be reduced using either conversion to a first order system or structure preserving model order reduction, either neglecting the damping matrix or via the SOAR algorithm. As previously mentioned, the algorithm requires the solution of a large first order system at each iteration step. For this purpose, various linear solvers are available and the module is implemented so that the reduction algorithm is actually independent from the solver used. This is achieved using a virtual function mechanism [178].

Once a base \mathbf{V} for the appropriate Krylov subspace is computed, the system (5.30) and the output matrices \mathbf{C} and \mathbf{D}_u are projected onto it, thus obtaining the reduced order system. This is then written into text files in Matrix Market format.

The user has to choose the reduced order model properties, that is the order of the reduced model and one or more expansion points. Apart for the choice of these values, the whole process is completely automatic.

5.5.2 Reduced model properties

The lack of a global error bound and the local nature of Krylov subspace leave to the user two important choices: the number of the d.o.f. of the reduced order model to use in order to achieve the desired modelling accuracy and the expansion point for the transfer function of the original model.

Model dimension

If a single full model simulation of the device under study is available, the choice of the dimension of the reduced order model is trivial. The full model simulation results have to be compared with the results obtained with reduced order models of increasing order till the error introduced by the latter is under the desired value, in all the time or frequency range of interest. It is worth underlining again that, due to the fact that the Arnoldi algorithm is iterative, once a reduced model of order k is available, also all the reduced models of order $p < k$ are directly available, so that this process is very fast and simple. On the other end, for very large systems, it would be desirable to avoid a full model solution.

In [179], three methods have been suggested to compute error indicators, which allow to estimate the error of a reduced model extracted with Krylov subspace techniques for thermal models, without the solution of the original full model. These are:

- convergence of the relative error;
- convergence of the Hankel singular values;
- sequential model order reduction.

The first indicator allows to estimate the error of a reduced order model, either in the time or frequency domain, by observing the difference in the results produced by reduced order models of contiguous order. Assuming a SISO system, the relative frequency response error is defined as:

$$E_r(s) = \frac{|H(s) - H_r(s)|}{|H(s)|},$$

where $H(s)$ and $H_r(s)$ are the transfer function of the original and the reduced model. A relative frequency response error indicator can be defined as:

$$\hat{E}_r(s) = \frac{|H_r(s) - H_{r+1}(s)|}{|H_r(s)|}. \quad (5.32)$$

In fact, for thermal models, it was observed that, for a wide range of frequencies around the expansion point, it is:

$$E_r(s) \sim \hat{E}_r(s). \quad (5.33)$$

Moreover, convergence behaviour is observed when a certain order of the reduced model is reached. This convergence is due to the fact that the machine numerical precision is reached. The

same behaviour holds also for electromechanical models. This has been verified by computing the error indicators for different models at different angular frequencies. Fig. 5.1 shows these curves for an electrostatically actuated clamped-clamped beam. The indicators have been computed at two different frequencies, one before and one after the first resonance peak of the beam. It can be observed that the agreement between the two indicators is very good, also for low values of the reduced model order. Similar results have been observed with other models.

In the time domain, a time-independent quadratic relative step-response error can be defined, with a time integration of a chosen output variable, as:

$$E_r^{av} = \frac{1}{N} \sqrt{\sum_{t_i=0}^{N\Delta t} \left(\frac{y(t_i) - y_r(t_i)}{y(t_i)} \right)^2}$$

where y and y_r are the outputs of the full and the r -dimensional reduced order system, respectively, computed at N time-points t_i spaced by a time Δt . In a similar way, it can be defined a quadratic relative step-response error between two successive reduced order models:

$$\hat{E}_r^{av} = \frac{1}{N} \sqrt{\sum_{t_i=0}^{N\Delta t} \left(\frac{y_r(t_i) - y_{r+1}(t_i)}{y_r(t_i)} \right)^2}.$$

Also in this case, the two errors are very similar to each other and have a convergence behaviour. In this case, however, the computation of the indicator is more expensive and they are more affected by numerical errors, due to the required time integration. The use of frequency domain error indicators is thus more convenient.

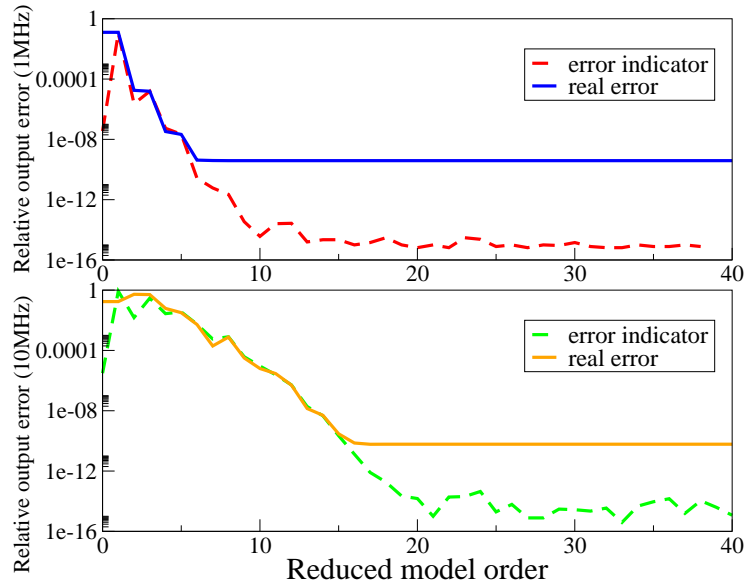


Figure 5.1: Error indicators computed for a clamped-clamped beam with electrostatic actuation at 1 and 10 MHz.

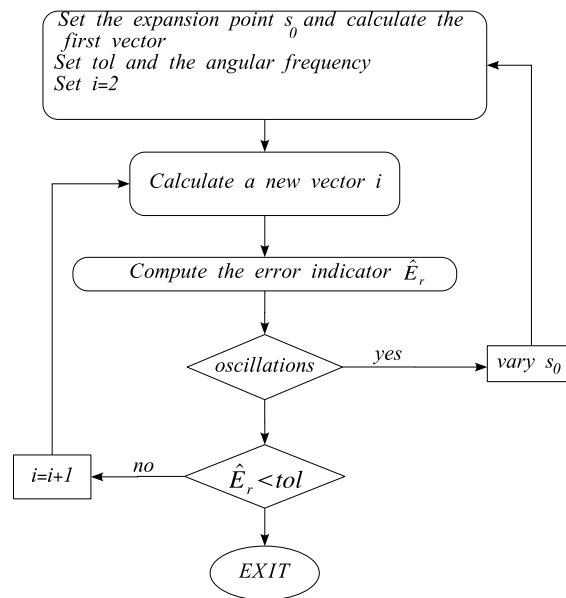


Figure 5.2: Block scheme, which illustrate a possible algorithm for fully-automatic model order reduction using computation of the error indicator in 5.32.

For frequency very far from the expansion point, the convergence behaviour might present fluctuations. The choice of the order of the reduced order model can be done using an iterative scheme, such as the one in Fig. 5.2.

The second possibility is based on the observation that the Hankel singular values of the reduced order model converge to the Hankel singular values of the original system, for increasing value of the reduced model order [179]. The Hankel singular values of the original system define, through equation (5.14), an error bound for the reduced order system obtained with SVD based model order reduction. It is thus possible to proceed as follows:

1. for every new vector computed with the Arnoldi algorithm compute the first k Hankel singular values of the reduced model $\sigma_{k1}, \dots, \sigma_{kk}$, where k is the dimension of the reduced order model;
2. check if the first l Hankel singular values ($l < k$) are converged to the values of the previous iteration step. If not go back to point 1, otherwise continue;
3. using a decay estimate for the Hankel singular values, compute the estimated value of the Hankel singular values of order higher than l ;
4. estimate the global error bound using (5.14). If this value is lower than the absolute value desired, then the reduction process can stop.

This procedure requires to set the maximum acceptable error and the number l of Hankel singular values, which should converge before computing the error bound. If the reduced order model

dimension increases significantly, the computation of the Hankel singular value becomes too expensive and the procedure is not effective anymore [179].

The last idea is the reduction of the order of the original system in two steps, making use of model order reduction for the first step, and a SVD based technique in the second step. In this way, the target reduced order model is generally achieved with a smaller error than using the Arnoldi algorithm only and the computational limitations of SVD based techniques are avoided. The error of the first reduction step can be estimated using one of the previous error indicators, while the one of the second step is given by (5.14). The total error is simply the sum of the two [179].

Expansion point

The choice of the expansion point for the reduced order model is strongly linked to the dynamic range and the kind of analysis of interest for the device to model. However, a general rule for its optimal choice is not available. In this thesis, the following considerations have been adopted.

The reduced order model of a microresonator is mainly used for harmonic analysis in a certain frequency range that contains the resonance frequency of interest of the device. Being one of the main design parameters, this frequency is approximately known in forehand. Hence, the best choice is to expand the system around a frequency, which is close to the device resonance frequency, so that the model accuracy is maximal in the range around it. This is equivalent to approximate with greater accuracy the dominant poles of the system with respect to the others.² The reduced order model tested in this thesis showed that this strategy allows to simulate the harmonic response with good accuracy in a wide range of frequencies around the expansion point. However, this range is difficult to quantify.

For what concerns switches, two typical analysis of interest are static analysis and transient analysis with a square wave applied between its suspended membrane and the actuation electrode. For these kinds of analysis, the expansion point can be simply fixed to zero. The resonance frequency of switching structures is in fact generally low (in the 5 – 50KHz range) and the frequency of the applied signal is even lower so as to avoid oscillation of the membrane after the pull out. Intermodulation analysis is instead performed with high frequency periodic signals applied to the switch. In this case, the expansion point has to be chosen, as for microresonators, according to the frequency of the applied signals.

²Note that if the expansion point is chosen exactly equal to the resonance frequency, the matrix generating the Krylov subspace becomes singular.

Chapter 6

Compact modelling

This chapter presents the capabilities of compact modelling via model order reduction. First, the necessary steps for the creation of the models are briefly summarized. Then, the assumptions intrinsic to the methodology are discussed in order to define its range of validity. Compact models are then extracted for some typical RF MEMS devices and used both in device and circuit simulations. Where possible, results are validated by comparison with full model results and/or experimental data.

6.1 Models extraction

The extraction of a reduced order model starts with the creation of a 3D finite element mechanical model of the device in ANSYS. The description of the electrical part varies depending on the device to model.

If the small signal harmonic behaviour of the device is of interest, the electromechanical coupling is described using TRANS126 elements. For microresonators, fringing effects are generally negligible and a parallel-plate capacitor assumption can be made for the computation of their capacitance/displacement relation. The coupled electromechanical system matrices are then extracted from ANSYS binary files and reduced with MOR for ANSYS, as already described in the previous chapter. The translation of the model into VerilogA language for simulation with a circuit simulator is done using a function created in Mathematica[©] [180].

If the large signal transient or harmonic behaviour is of interest, only the device mechanical system matrices are extracted from ANSYS files and reduced. Distributed electrostatic forces are replaced with concentrated forces, which act on nodes of the movable structure surface and are added to the model at circuit level. This requires two operations. First, a certain number N of nodes of the mechanical structure has to be chosen for concentrated forces application. Afterwards, the entity to assign to these forces has to be calculated, so that the original forces are accurately approximated. In general, it is convenient to choose nodes uniformly distributed over the surface of the structure subjected to electrostatic force. The displacement u_i^k of each of these

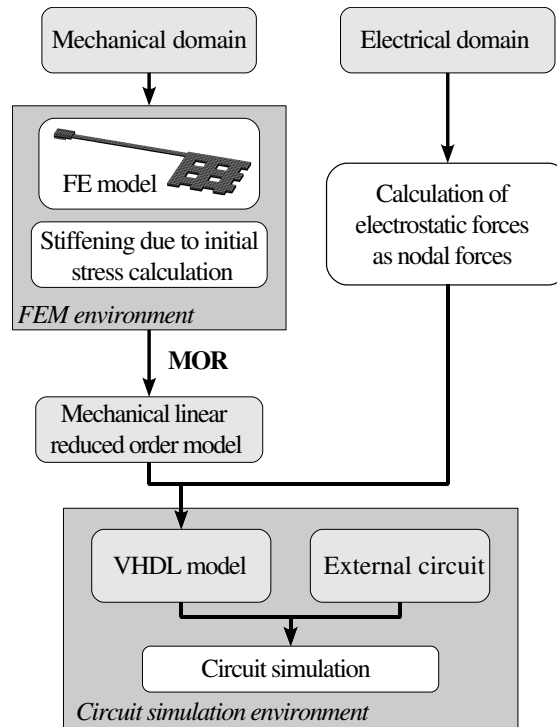


Figure 6.1: 3D finite element model of a vertical free-free resonator.

nodes, along the local preferential direction of movement of the structure, will be included in the output d.o.f. of the mechanical reduced model. In addition, during generation of the mechanical element matrices, a load vector for each of these nodes will be included in the model, describing a lumped force that acts on the node along its direction of movement. If N is large, the description of the electrostatic domain is more accurate, but the time needed for the extraction of the reduced model and its subsequent simulation increases.

Calculation of the entity of the lumped forces can be done in different ways, at different levels of accuracy. A portion of the surface of the structure that is subjected to electrostatic forces can be assigned to each node, depending on its position and on the total number of nodes used. The simplest case is when fringing effects are not important and the variation in shape of each portion, with the deflection of the structure, does not affect significantly its capacitance C_k towards the fixed electrode. In these conditions, the capacitance C_k can be computed using the parallel-plate capacitor formula. The electrostatic force in the local direction of movement x_i is then given by:

$$f_i^k = \frac{\epsilon A_k}{(d + u_i^k)^2} (V_p - V_n)^2 \quad (6.1)$$

where the index k runs on the N chosen nodes, A_k is the area associated to each node, while d and $V_p - V_n$ are the initial gap and the voltage difference between the structure and the fixed electrode, respectively. If fringing effects are not negligible, the capacitance C_k can be calculated with an electrostatic analysis of the undeformed electrical domain. From the computed value, an

effective coupling area can be calculated:

$$A_k^{eff} = dC_k. \quad (6.2)$$

This can be used in (6.1) for electrostatic force computation. If C_k varies considerably with the deformation of the structure, then a series of electrostatic computations for different device deflections in its operation range can be performed. The results can be used for extracting the dependency $C_k(u_i^k)$ and calculating the electrostatic force.

The nodes used for electrostatic force application can be also used for monitoring the distance between the movable structure and the electrode. When this is equal to the transduction gap, the contact condition is reached and contact forces, given by equation (4.24), can be applied to the nodes.

The complete extraction procedure is schematically represented in Fig. 6.1. Stress stiffening due to initial stress or bending of the structure is included in the mechanical stiffness matrix and this, together with the mass matrix, takes part in the computation of the damping matrix according to the Rayleigh formulation. The mechanical FE matrices are reduced and the derived compact model is translated in VerilogA, using mathematica. The approximate expression of the electrostatic forces computed with one of the above described methods, as well as contact forces, are introduced in the VerilogA model, which is then ready for circuit simulation.

Computation of the electrostatic forces adds some complexity to the extraction of the reduced order model, but this is largely compensated by the speed-up of the reduced model simulation, with respect to the simulation of the full model.

6.2 Model validation

As introduced in chapter 4 and 5, the two main approximations introduced in the model are the assumption of linear mechanical behaviour and the lumped description of the electrostatic energy domain. The resulting error and the range of validity of the modelling technique will be here discussed, both for microresonators and switches.

6.2.1 Mechanical linearity

In order to estimate the error introduced by neglecting mechanical nonlinearities, their effect on the deflection of a clamped-clamped beam has been simulated. This structure has been chosen, since it is representative for both flexural resonators and switches. For most of switching devices, only the supporting beams undergo large-deformations. In bulk acoustic wave resonators, nonlinear effects are less relevant [158]. The importance of geometrical nonlinearities strongly depends on the stiffness of the structure and its deformation entity.

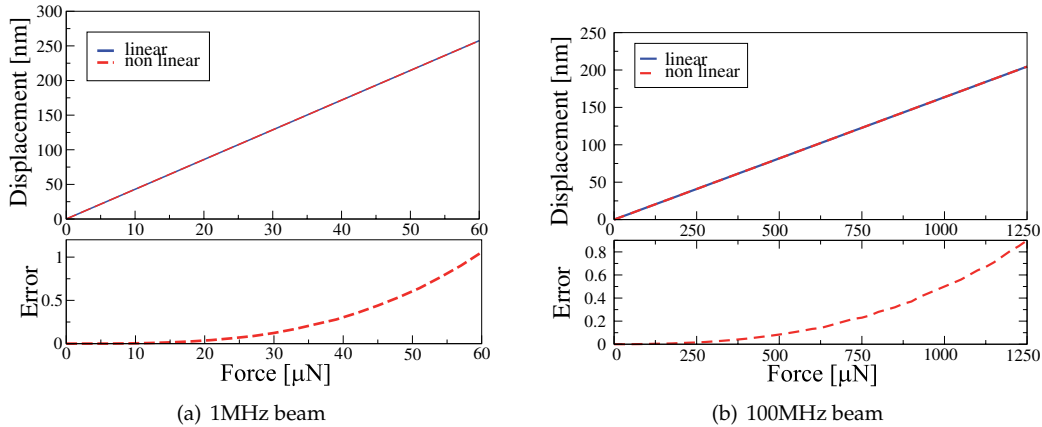


Figure 6.2: Deflection of two beams with different length to a pressure load applied in the center of the beam.

Microresonators

Microresonators have generally a high stiffness and a very small transduction gap. This has been considered in the choice of dimensions for the adopted test beams.

The beams have equal material and geometrical parameters apart for the length (beam A and B in Table 6.1) and first resonance frequencies at 1MHz and at 100MHz. These values roughly correspond respectively to the lowest frequency in the high frequency range and to the maximum frequency, which can be achieved using a flexural beam design, while conserving a high quality factor. The deformations of the beams caused by a vertical force concentrated in its center, in the linear and the nonlinear case, have been evaluated. With this kind of load, the static deflection and linear stiffness coefficient of the beam are very close to the equivalent stiffness of an electrostatically actuated resonator in its first resonant mode (for small actuation electrodes) [80]. The results of the simulation of the two beams are reported in Fig. 6.2, together with the absolute error resulting from the linear assumption. In the considered deflection range, which corresponds to the typical maximum value of a resonator transduction gap, the error is higher for the beam with higher stiffness, at equal values of displacement. However, the absolute error resulting from neglecting mechanical nonlinearity does not allow to quantify the importance of nonlinear effects on device behaviour. The nonlinear curve in Fig. 6.2(b) has therefore been fitted with a third order polynomial curve. The derived stiffness coefficients have been used in equation (2.2.2) to compute the factor κ and thus to evaluate the variation of the resonance frequency of the device

Table 6.1: Geometrical dimensions of the various types of beam used in the simulations.

	Length [μm]	Width [μm]	Height [μm]
Beam A	160	3	10
Beam B	100	12	10
Beam C	100	5	5
Beam D	250	5	5
Beam E	400	5	5

caused by the nonlinear coefficients. The contribution of the quadratic coefficient is much lower than the one of the cubic stiffness and has therefore been neglected. This leads to:

$$\kappa \approx 2.98 \cdot 10^{10} \omega_0,$$

and thus:

$$\frac{\Delta\omega}{\omega_0} \approx 2.98 \cdot 10^{10} X_0^2.$$

The maximum displacement X_0 of the resonator is limited to a fraction of the transduction gap, in order to avoid the dynamic pull-in of the moving structure. Typical values for the maximum displacement are in the 10-100nm range. In the worst case, the variation of the device resonance frequency is therefore around 0.03%.

Switches

Switch supporting beams have generally a lower stiffness than the ones considered in the previous case, while the deformations they are subjected to are larger. They are therefore more affected by geometrical nonlinearities. Here, the influence of mechanical nonlinearity is tested considering three kinds of beams, having equal height and width but different lengths. The chosen values are in the typical range for RF switches. A general treatment of the problem is complicated by the extreme variability of supporting beams and dimensions, which are effectively used.

The beams have been assumed clamped at one end and free to move at the other end, but only in the vertical direction. This boundary condition has been imposed in order to approximately describe the clamping of the supporting beam to a quasi-rigid plate, which is typical of switches. Beam dimensions are listed in Table 6.1 under beam C, D and E and gold is assumed as constitutive material.

A vertical force is applied to the free end of the beam and its displacement is monitored, as a function of the force entity, with a static mechanical analysis. Fig. 6.2.1 shows the relationship between force and displacement for the beams, in the linear and nonlinear case. The displacement has been normalized with respect to the thickness of the beam. It can be seen that the stiffening of

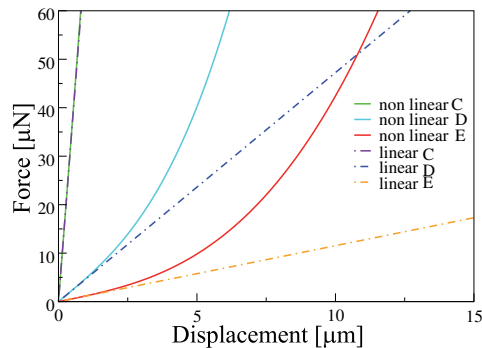


Figure 6.3: Force vs. displacement relationships for the two adopted test structures, with and without the inclusion of mechanical nonlinearities.

Table 6.2: Linear and cubic stiffness coefficient extracted for different beam dimensions.

d/h	Beam C*		Beam D**		Beam E***	
	r	V_p^{nl}/V_p	r	V_p^{dyn}/V_p	r	V_p^{dyn}/V_p
0.2	0.335	1.001	0.335	1.001	0.635	1.001
0.5	0.343	1.010	0.343	1.009	0.342	1.009
1	0.271	1.043	0.271	1.004	0.368	1.039
1.5	0.418	1.106	0.417	1.103	0.412	1.096
2	0.472	1.234	0.468	1.263	0.462	1.185
2.5	0.509	1.332	0.508	1.328	0.502	1.305
3	0.534	1.482	0.533	1.478	0.529	1.447

$$*k_m = 73.47\text{N/m}, k_{m_2} = 2.087\text{N}\mu\text{m}^3$$

$$**k_m = 4.72\text{N/m}, k_{m_2} = 0.1320\text{N}\mu\text{m}^3$$

$$***k_m = 1.15\text{N/m}, k_{m_2} = 0.031\text{N}\mu\text{m}^3$$

the structure due to mechanical nonlinearities depends both on the length of the beam and the ratio between maximum displacement and beam thickness. By polynomial fitting of the curves, the linear and cubic stiffness coefficients of the structures have been extracted. These have been used in the equations (2.52) and (2.51) for evaluating the variation, due to the cubic stiffness, of the pull-in voltage of the structure and of the value of the displacement at which pull-in occurs. Different values of the transduction gap have been considered. This analysis is based on a simple analytical formulas but it gives an idea of the entity of the considered effect and of its dependency on the geometry. The displacement at which pull-in occurs and the nonlinear pull-in voltage, normalized with respect to the transduction gap and the linear pull-in voltage, respectively, are reported in Table 6.2. According to the analytical formulation, the effect of the cubic stiffness on the pull-in voltage is mainly dependent on the ratio d/h and becomes important when values above 2 are reached. In this condition, neglecting mechanical nonlinearity leads to a relative percentage error of around 20%. At constant d/h values, longer beams appear to be slightly less affected by mechanical nonlinearities than short beams.

The influence of the beam nonlinear stiffness on the switching time of the switch is more difficult to quantify. In dynamic conditions, also the electrical stiffness gives a contribution to the total stiffness of the structure.

6.2.2 Electrostatic description

The use of TRANS126 element for the description of the electrostatic forces introduces two error factors: the neglecting of the components of these forces which are tangential to the direction of movement of the structure and the calculation of the parallel component based on the capacitance between the conductors in the model. If methods for an accurate capacitance computation are used, the parallel component can be accurately described. The more relevant source of error is therefore expected to be the first factor.

In microresonators, the gap between moving parts and resonator electrodes is very small, and the device undergoes very small displacement around its rest position. Under these conditions,

Table 6.3: Comparison of the maximum displacement of beams with different geometrical parameters obtained using ANSYS sequential solver and TRANS126 elements. Different values of the applied voltage are considered.

Voltage [V]	Beam A, gap=0.3 μ m			Voltage [V]	Beam A, gap=0.7 μ m		
	Seq. solver	TRANS126	Relative Error %		Seq. solver	TRANS126	Relative Error %
5	-6.37	-6.37	0	12.5	-7.19	-7.19	0.001
10	-28.84	-28.84	0.003	25	-30.32	-30.32	0.003
12.5	-51.60	-51.59	0.003	37.5	-76.15	76.14	0.01
15	-89.6	-89.5	0.03	50	-178.25	-178.38	0.04

electrostatic forces are mainly directed in the beam direction of movement. Hence, TRANS126 elements are not expected to introduce a big error in the description of the electrostatic domain. The validity of this statement has been proven by comparing static analysis results obtained by using these elements and ANSYS sequential solver for a clamped-clamped beam structure and different gap dimensions. Dimensions of the beam are given in Table 6.1 under beam A. The two models used for the analysis differ only in the description of the electrical energy domain. The actuation electrode is assumed to extend for the complete length of the beam and only the portion of air between the beam and the electrode has been considered, so that fringing effects are neglected. In this way, only the contribution to the error introduced by the use of TRANS126 elements, which comes from neglecting horizontal forces is observed. The direct coupled model makes use of automatically layered TRANS126 element, while in the sequentially coupled model the airgap is meshed with second order brick elements (solid122). The obtained numerical results are compared in Table 6.3. For both values of the transduction gap and at all applied voltages the error introduced by the use of TRANS126 elements is very small¹. The error would increase for structure with lower stiffness, subjected to higher deflection. Nevertheless, the beam chosen for the analysis has already a low stiffness, for typical values of RF microresonators.

For what concerns MEMS switches, the accuracy of the approximation introduced in electrostatic forces description has to be proven. The big variety of switches geometry and dimension does not enable a general study of the problem. Hence, this will be done, case by case, for the presented examples.

6.3 Simulation results

This section present the results obtained with the application of compact modelling via model order reduction on different kinds of devices. These have been first modeled and meshed in ANSYS. All the structures considered have a squared and planar geometry. Brick elements, which allow a mapped meshing of the structure, are therefore preferred over tetrahedral elements. In particular, second order brick elements (solid95) are generally used.

Where not specified, reduced order models of the devices are extracted choosing an expansion

¹It should be considered that a value of the gap of 0.7 μ m is already large for microresonators.

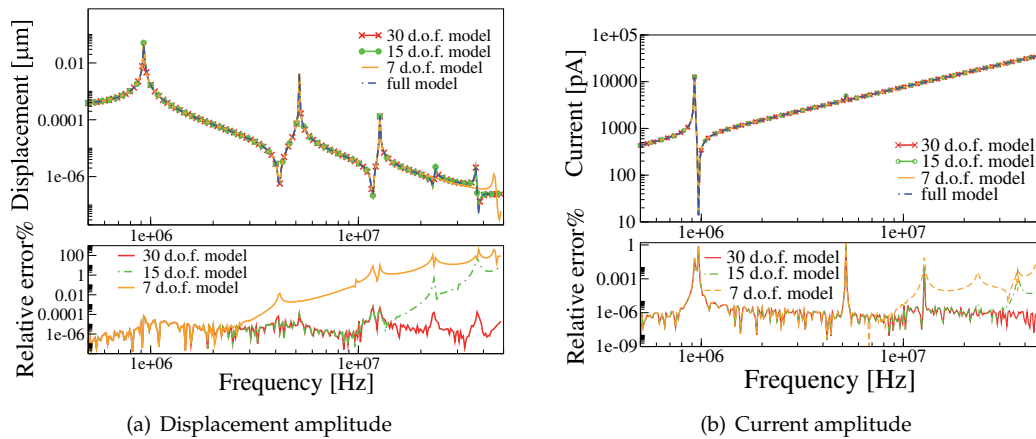


Figure 6.4: Harmonic pre-stressed analysis simulation results obtained with ANSYS full model and compact model of different order extracted using MOR.

point equal to zero.

6.3.1 One port vertical beam resonator

The first device that has been simulated is a vertical flexural polysilicon beam resonator with an actuation electrode centered with respect to the resonator length. The device dimensions (beam A of Table 6.1) correspond to a first resonance frequency of approximately 1MHz. The beam model has been created and meshed using 1200 solid95 elements, for a total of around 15000 d.o.f. 227 TRANS126 elements have been used for the description of the electromechanical coupling. The TRANS126 capacitance vs. displacement relation has been computed using a parallel plate capacitor approximation.

The beam has been considered polarized with a bias voltage of 10 V and a small signal sinusoidal voltage with an amplitude of 100mV has been applied to the device excitation electrode. Damping has been modeled using Rayleigh damping, assuming a quality factor of around 5000 for the first resonant mode. The reduced order models have been simulated in Mathematica, assuming the resonator grounded during the harmonic analysis.

The comparison between 3 extracted reduced order models and ANSYS full model results are presented in Fig. 6.4. The chosen output quantities are the vertical displacement of the central point of the beam and the current flowing in the resonator. It can be seen that the 30 d.o.f. model allows to give a good description of the device harmonic behaviour in the complete frequency range considered. If a narrower frequency range is of interest, also lower order models can be used. The 7 d.o.f. model, for example, reproduces the first 2 resonance peaks of the device with an error, which is lower than 1%. The computational times required to perform the different steps needed for model extraction are reported in Table 6.4. It can be seen that the total extraction time is quite fast, even if the original model has a high number of d.o.f. The simulation time of all considered reduced order models, for 300 frequency steps, is under 1s, while the full model

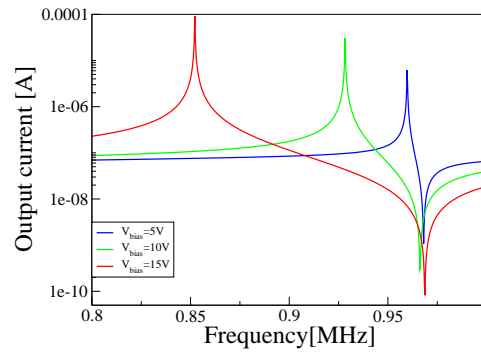


Figure 6.5: Dependency of the vertical beam resonance frequency from the applied bias voltage.

simulation requires around 4200s.

Different models have been extracted for different values of the bias voltage, in order to test the correct modelling of the dependency of the resonance frequency from the applied bias voltage. In Fig. 6.5, it can be seen that, as expected, the device resonance peak migrates towards lower frequencies with increasing applied bias voltages. Results were obtained using a 5 d.o.f. model, which guarantees good accuracy in the frequency range considered.

6.3.2 Lateral beam

Lateral beam resonators are advantageous with respect to vertical beam resonators, since they can be easily fabricated as multiport devices. The simplest example is a two ports device with electrodes centered with respect to the beam length as in Fig. 2.6(b). The electrode of one side of the beam is used for the excitation of one of its odd lateral flexural modes, while the other is used for sensing of the vibration. A FE model for this kind of device has been created assuming a SCS beam with dimensions given in Table 6.1 under beam A and a transduction gap of $0.3\mu\text{m}$. This model corresponds to a fabricated device.

A linearized compact model for the lateral resonator has been extracted, assuming a bias voltage of 10 V, and used for device simulation in Mathematica. For simulation around the first device resonance frequency, 15 d.o.f. proved to be enough to ensure high simulation accuracy. The values of the Rayleigh damping parameters have been computed assuming a quality factor equal to 100 for the first resonance mode. Such a low quality factor has been chosen in order to obtain a worst-case evaluation of the level of the device output current. The model has been imported in

Table 6.4: Computational time for a vertical clamped-clamped beam model extraction.

Computation	Tool	Time
Bias point computation & matrices calculation	ANSYS	31.3 s
Matrices extraction	Mor 4 ANSYS	23.4 s
Matrices reduction	Mor 4 ANSYS	40 s

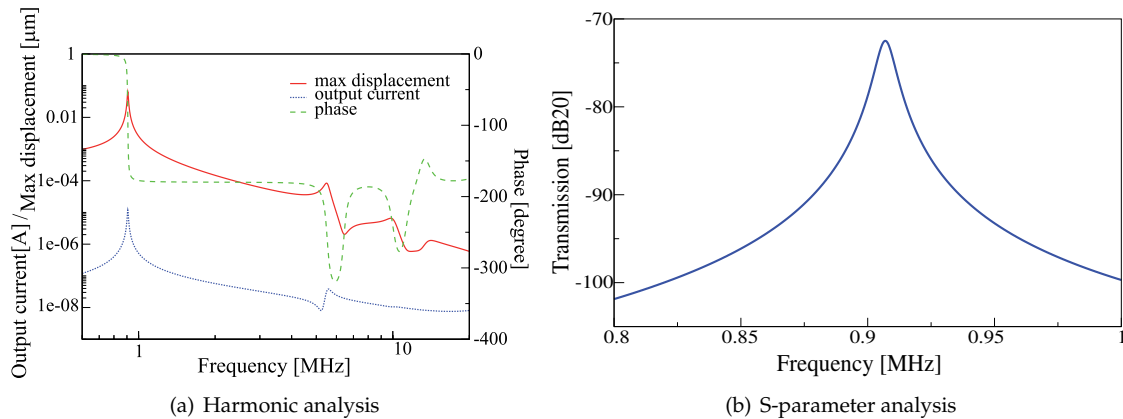


Figure 6.6: Harmonic and S-parameter analysis simulation results of a clamped-clamped beam resonator obtained in Cadence with a 15 d.o.f. reduced order model.

Cadence SpectreTM simulator and used for a harmonic small signal and an S-parameters analysis. The VerilogA model is simply constituted by three voltage terminals, one mechanical terminal and two reference terminals. The voltage terminals represent the input and the output electrode of the device and the contact to the resonator beam. The mechanical terminal allows to observe the displacement of the central part of the beam. The reference terminals, one electrical and one mechanical are used inside the model as reference electrodes for voltages and displacements, respectively, and are usually grounded.

The harmonic analysis has been carried out with a 100mV sinusoidal voltage applied to the input electrode of the resonator and a 50Ω load resistor connected to the output electrode. The harmonic amplitude and the phase of the lateral displacement of the central part of the beam are plotted in Fig. 6.6(a) as a function of the frequency, together with the amplitude of the output current. It can be seen that the two ports excitation ideally allows the complete elimination of the feed-through current at the output of the device. In real devices, a coupling capacitance between the input and output electrode will still be present, but its influence is far less important than in a one port device. At 1MHz and for the chosen quality factor, the level of the output current is sufficient to be detected without amplification.

The S-parameter analysis has been carried out with two ports terminated with a 50Ω impedance connected to the input and the output port of the resonator. The resulting S_{21} transmission parameter is plotted in Fig. 6.6(b).

6.3.3 Free free beam resonator

The high energy dissipation through the anchor, typical of clamped-clamped beam microresonators, can be reduced by adopting a free-free beam design [81]. Both vertical and lateral free-free beam resonators have been considered. Since the resonators are polarized through generally thin and long suspending beams, the value of their resistance could become important and should be taken into account in simulations.

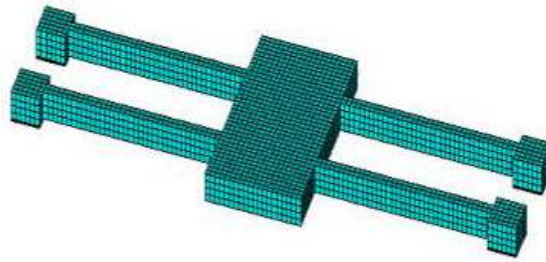


Figure 6.7: 3D finite element model of a vertical free-free resonator.

Vertical design

First, a one port vertical design has been considered, with dimensions and material properties taken from [81]. Its 3D ANSYS model is shown in Fig. 6.7. A central beam is suspended through 4 beams above an actuation/sensing electrode. The beams are located in nodal points of the first mode of vibration of the unconstrained central beam. When this vibrates in such a mode, these points are not moving, but a torsional wave is excited in the supporting beams. In order to minimize the losses towards the substrate, the length of the supporting beams is chosen so to have complete reflection of this wave. The condition is satisfied for a length of the supporting beams equal to a quarter of the wavelength of the torsional wave. In this way, complete isolation of the resonating beam from the substrate is achieved. The resonating beam is quite large, in order to increase the electromechanical coupling area, and thus reduce the device motional resistance.

The model has been used to test the effects of a tensile stress in the polysilicon resonating structure on the device behaviour. At this aim, two compact models of the device with and without a plane constant stress in the polysilicon layer have been extracted and used for device simulation in Mathematica. A 1V signal has been applied to the device excitation electrode, while the res-

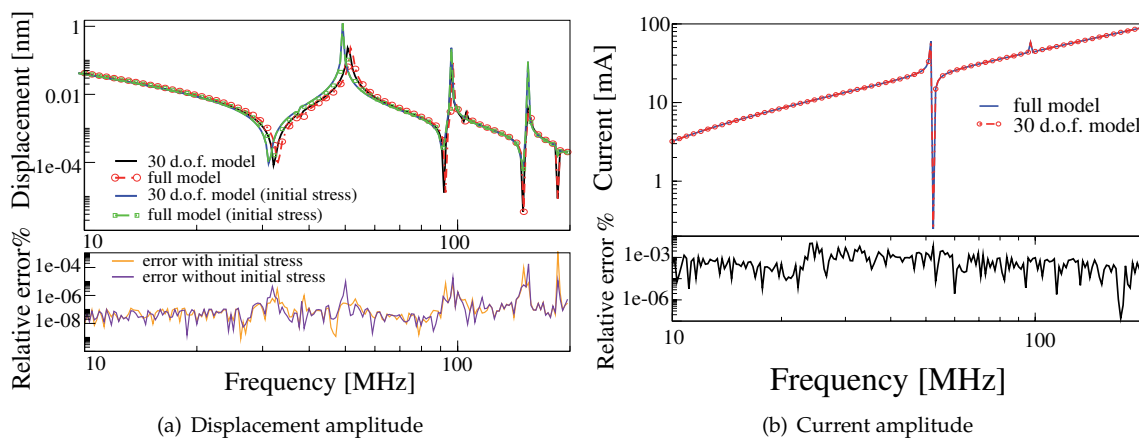


Figure 6.8: Displacement and current amplitude for a one port vertical free-free beam resonator with and without a plane initial stress in the movable structure. Reduced order and full model simulation results are compared.

onator has been considered grounded. Results obtain with a 30 d.o.f. order model are compared with the full model simulation results in ANSYS in Fig. 6.8. In both the stressed and un-stressed case, the maximum displacement and the current in the resonator obtained with the reduced models are in good agreement with ANSYS simulation results.

As expected, the stress in the material leads to a stiffening of the resonating structure. This results in an increase in its resonance frequency and a decrease in its vibration amplitude, at constant quality factor. A high feed-through component is present in the device output current, which render the current resonance peak difficult to detect.

Lateral design

A model for a 10MHz free-free beam two port lateral resonator has been also considered. This corresponds to a device fabricated in SCS, with dimensions of the resonating beam given in Table 6.1 under beam B. For this kind of device, the electromechanical transduction factor is improved adopting a high beam thickness. In addition, in order to isolate the vibrating beam from the anchors, the length of the supporting beam is chosen so that at 10MHz these are vibrating in their second flexural mode, as shown in Fig. 6.9.

A 15 d.o.f. reduced model has been extracted, assuming a Q factor equal to 100 and a bias voltage of 5V. The choice of the quality factor followed the same consideration than for the lateral clamped-clamped beam. The model has been translated into a VerilogA model for circuit level simulation in Cadence. It has three electrical terminals, one for each device electrode, and one mechanical terminal for monitoring the device displacement. Results of harmonic and S-parameter simulation are reported in Fig. 6.10. The harmonic analysis has been done with a 100mV signal applied to one electrode, while the other is terminated with a 50Ω load resistance. It can be seen that the maximum displacement amplitude of the resonating beam, and thus the motional current at the output terminal, are rather small. At this frequency, detection of the resonance requires therefore amplification.

The S-parameter analysis has been conducted by connecting two ports with a 50Ω internal resistance to the device electrodes. In this case, a resistance has also been connected between the resonator terminal and ground, which represents the electrical resistance of the resonator mov-

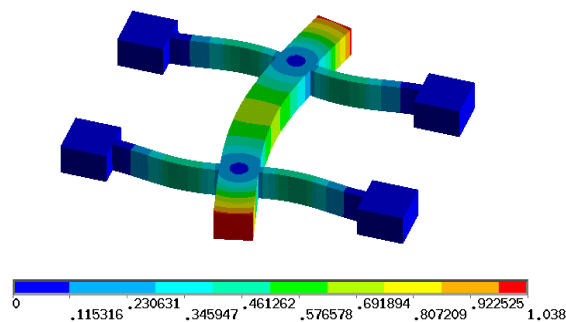


Figure 6.9: First resonant mode of a lateral free-free beam resonator.

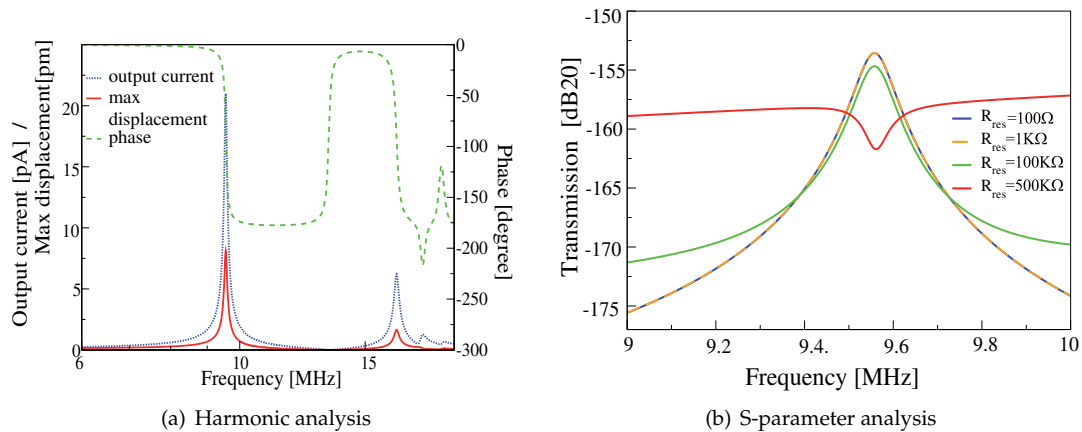


Figure 6.10: Harmonic and S-parameter analysis simulation results of a free-free lateral beam resonator obtained in Cadence with a 15 d.o.f. reduced order model.

able structure, also called series resistance. It can be seen that large series resistances have a detrimental effect on the device behaviour, since they cause an AC current component to arise at the device output terminal. An adequate doping of the resonator, both for polysilicon and single-crystal silicon structures, is therefore very important.

6.3.4 Square resonator

Model order reduction has been used to derive a compact model of a silicon carbide square resonator taken from literature [181], which has been employed for circuit level simulations. Despite its simple structure, the device can be used in various circuit configurations, which have a strong influence on its response. Reduced order modelling can thus be employed for fast circuit design optimization. A square resonator is made of a square suspended plate anchored at its corners through 4 beams. Electrodes facing each side of the plate allow exciting and sensing the in-plane vibration of the plate, which can be biased through the beams. The gap between the electrodes and the plate sides is $0.1 \mu\text{m}$ in order to enhance electrostatic coupling. By applying proper signals on the device terminals, either the Lamé or the extensional mode of the plate can be excited.

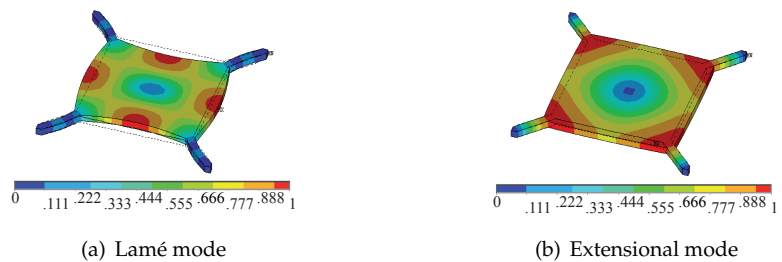


Figure 6.11: Square resonator mode shapes simulated with ANSYS.

Table 6.5: Device dimensions and material properties.

Quantity	Value	Unit
Young modulus	710	GPa
Poisson ratio	0.2	
Density	2.994	kg/m ³
Plate side	40	μm
Plate thickness	2	μm
Beam length	13	μm

The Lamé mode shape is shown in Fig. 6.11(a). The square plate extends along one direction and contracts along the perpendicular one, while conserving the total volume. The extensional mode is characterized by contraction and extension of the plate in all directions, thus conserving the plate shape as in Fig. 6.11(b). For the chosen values of dimensions and material properties, summarized in Table 6.5, the resonance frequencies of the Lamé and the extensional modes are 171 and 177 MHz, respectively.

The 3D device model has a total of 3000 degrees of freedom. A reduced order model has been extracted with MOR for ANSYS for a 5 V bias voltage applied between electrodes and moving structure. Differently from the devices previously considered, this resonator is used in a high frequency mode. An expansion point different from zero has thus been used for the reduced order model extraction. The number of d.o.f. of the reduced order model required for a good modelling accuracy has been deduced by comparing the simulation results obtained with the full model and with low order models of different dimensions. At this purpose the electrode configuration in Fig. 6.12(a) has been adopted with the sensing terminals (i_{out}) grounded.

Results for the full model and the 15 d.o.f. model are shown in Fig. 6.13. In particular, Fig. 6.13(a) shows the variation with frequency of the magnitude of the device currents at the excitation and sensing terminals, while in Fig. 6.13(b) the displacement amplitudes of two points located at the center of two adjacent sides of the plate are plotted. It can be noted that the relative error computed with the 15 d.o.f. model is lower than 1% in a 50MHz range containing the resonance frequency of interest, both for electrical and mechanical quantities. Simulation of the reduced order model has also been used to adjust the value of the damping coefficients so as to achieve an unloaded quality factor for the device equal to 9300.

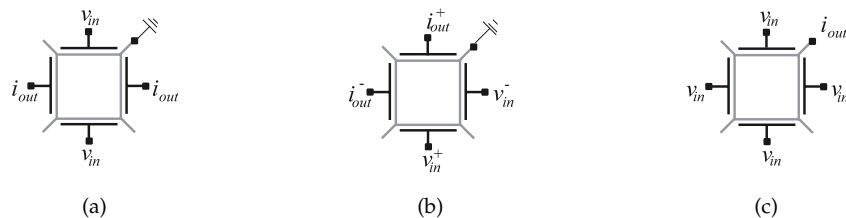
**Figure 6.12:** Two-port single-ended (a), two-port differential (b) and one-port single-ended electrode configuration used for the square resonator in its Lamé (a-b) and extensional (c) modes.

Table 6.6: Computational time comparison.

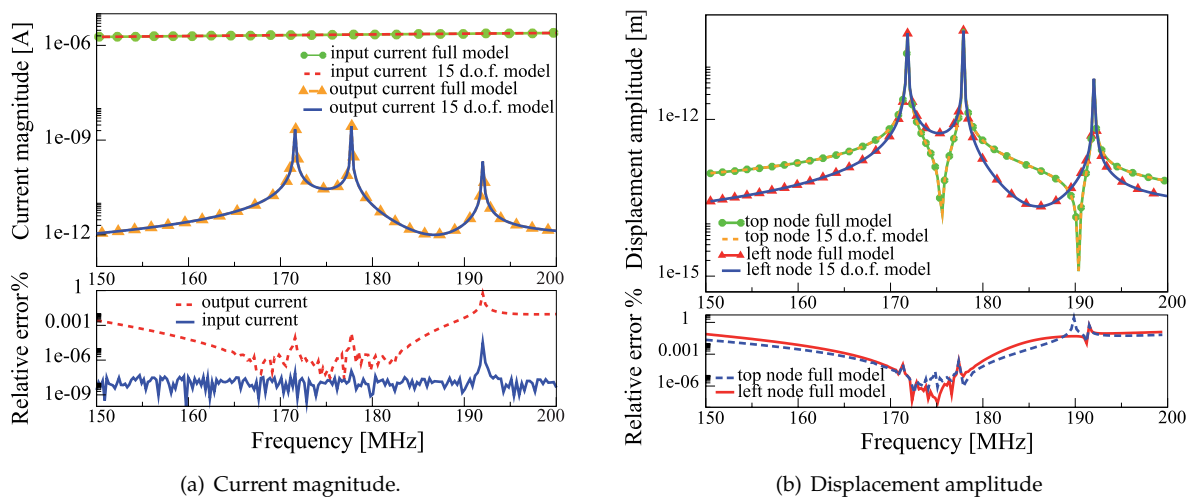
Computation	Tool	Time
Harmonic pre-stressed simulation (full model)	ANSYS	212 s
Bias point computation & matrices calculation	ANSYS	3.3 s
Matrices extraction	MOR 4 ANSYS	1.5 s
Matrices reduction	MOR 4 ANSYS	2.1 s
Harmonic analysis	Mathematica	1 s

The computational time required for all model extraction steps and one harmonic simulation with 200 frequency steps are reported in Table 6.6 both for the full and the reduced order model. A considerable speed up of the simulation time is achieved. Moreover it can be noticed that also in this case the reduced order model can be extracted very fast after computation of the bias point.

Circuit simulation

The 15 d.o.f. model has been translated into a VerilogA behavioural model and has been imported into Cadence Spectre simulator. The model has one input/output electrical terminal for each device electrode, two output mechanical terminals, which allows to monitor the displacement of the middle points of two adjacent device sides and the reference electrodes. Circuit level simulation has been used to study the influence of the series resistance on the device performance for the two resonant modes and the different electrodes configurations described in Fig. 6.12.

In the Lamé mode, each pair of neighboring sides of the square plate vibrates with a 180° phase offset. This mode can therefore be excited using either the single-ended or the differential two-

**Figure 6.13:** Comparison between the full model and the reduced model simulation results.

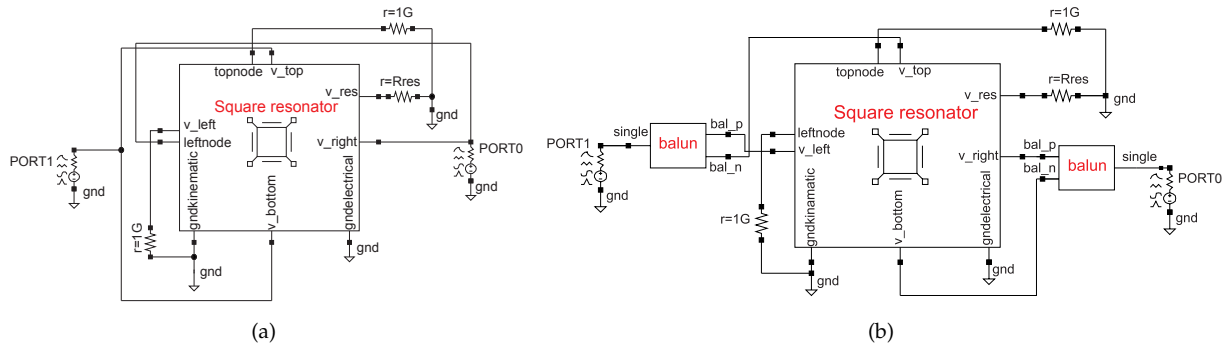


Figure 6.14: Schematic circuits used for the simulations of the square resonator in a two-port single-ended (a) and differential (b) electrode configuration.

port electrode configurations shown in Fig. 6.12(a) and (b) respectively. The single-ended case has been simulated using the small-signal schematic circuit in Fig. 6.14(a). Each pair of facing electrodes is connected to a port with an internal impedance of 50Ω . The resonator terminal is grounded through the resistance R_{res} , representing the resistance of the vibrating plate and beams, which in [181] has been estimated around $200k\Omega$. Silicon carbide has in fact a very high acoustic velocity but also a very low conductivity. The model been simulated for values of R_{res} ranging from 0 to $100K\Omega$ and a fine frequency discretization has been used in order to capture the resonance peak. The device behaviour has been observed through its mechanical outputs (leftnode and topnode) and by computing the electrical scattering parameters matrix. The graph in Fig. 6.15(a) shows the frequency behaviour of device transmission parameter S_{21} in dB. It can be seen that for low values of R_{res} the motional current gives a major contribution to the output current, which shows a resonance peak at 171.3 MHz. For values of R_{res} higher than 100Ω the capacitive feedthrough between excitation and sensing port increases and the sensing current is dominated

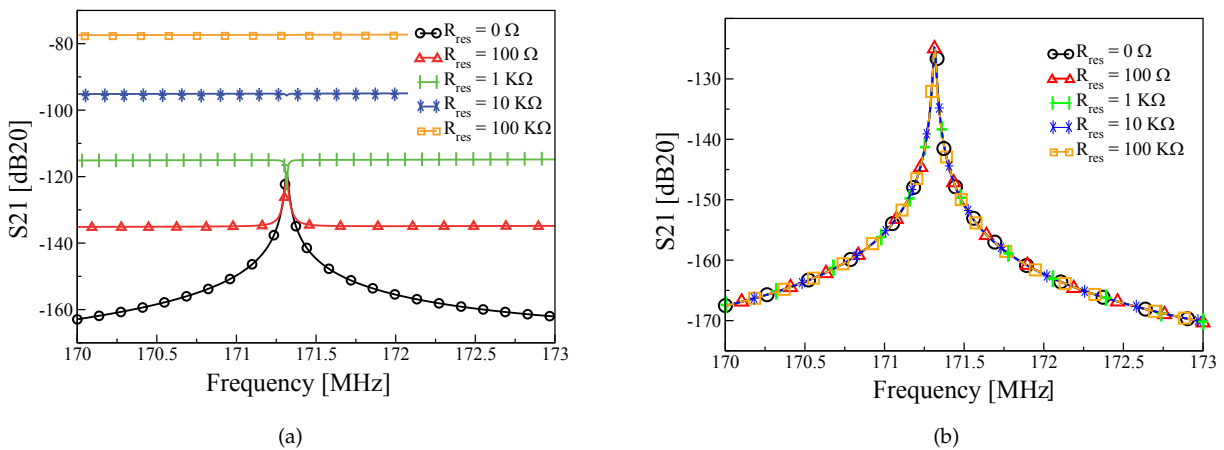


Figure 6.15: Circuit level simulation of the square resonator in its Lamé mode with a single-ended (a) and differential (b) electrode configuration.

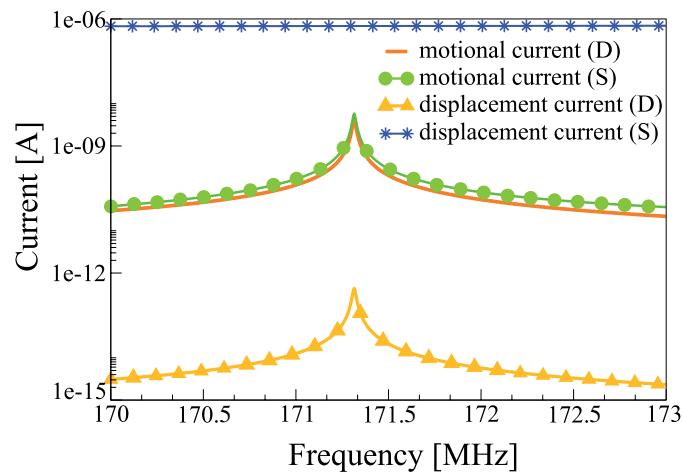


Figure 6.16: Motional and displacement components of the current at the terminal v_{top} for the single-ended (S) and the differential (D) configurations.

by the displacement current term. Thus, the resonance peak becomes more difficult to detect and eventually disappears. With the $200\text{K}\Omega$ resistance of the real device, the resonator Q factor would be impossible to measure.

A different electrode configuration allows to overcome this problem. By using the fully-differential electrode configuration of Fig. 6.12(c), the device behaviour is in fact insensitive to the value of R_{res} . The two pairs of adjacent electrodes are connected to the balanced ports of an ideal balanced-unbalanced transformer (balun), as shown in Fig. 6.14(b). With this setup, the resonator is virtually grounded and no current flows through its suspensions. The Q factor of the device is thus not altered by the presence of the resistance and the displacement current at the unbalanced input terminals of the output of the balun is small. Moreover, this component allows for common mode cancellation so that at the output terminal only the resonator motional current is present and capacitive feed-through is totally eliminated. This can be observe in Fig.

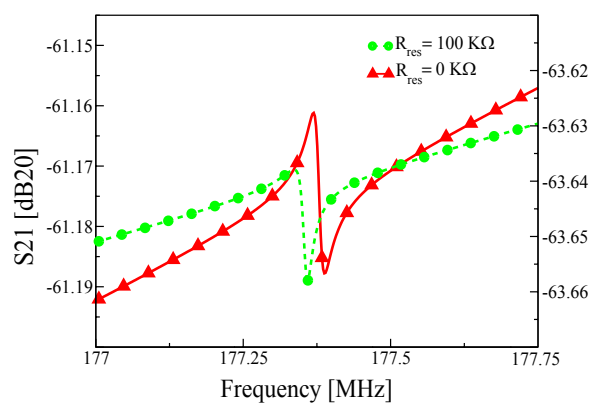


Figure 6.17: Circuit level simulation of the square resonator in its extensional mode.

6.15(b). The motional and displacement components of the current at one of the output electrodes of the resonator (terminal v_top in Fig. 6.14) are shown in Fig. 6.16, both for a single-ended (S) and the differential configuration. The obtained simulation results are in agreement with the experimental results presented in [181] and allow to conclude that the fully-differential electrode configuration is preferable for the excitation of the Lamé mode. The very low values of the transmission parameter is due both to the choice of the standard 50Ω impedance for the source and the load ports, and to the lack of an electrical gain stage that is necessary to amplify the small device motional current.

The use of the device in its higher frequency extensional mode has then been analyzed. The extensional mode is generally excited using the configuration of Fig. 6.12(c), in which four voltage signals with equal magnitude are applied in phase to the electrodes, and the output signal is read from the plate terminal. Simulation results in Fig. 6.17 shows that, independently from the value of the series resistance R_{res} , this configuration setup is characterized by a high capacitive feedthrough between excitation and sensing terminals, typical of one-port measurement setups, which makes the resonance very difficult to detect. The contribution of the displacement current on the output current justifies the values of the transmission parameter, which is much higher than in the fully-differential electrode configuration. With the increase in the value of R_{res} , the device Q factor is also drastically reduced. The use of the device in these conditions leads therefore to poor performance.

6.3.5 Micromechanical filter

Another class of devices having a behaviour strongly affected by the surrounding circuitry are filters. A model for the filter in Fig. 2.13(a) has been created using the dimensions and material properties given in [182]. It presents two beams with resonance frequency around 8.5MHz, linked by a coupling beam. One electrode is placed underneath each beam, centered with respect of the beam length. Two different FE models have been created, corresponding to different positions of the coupling beam.

In the first model, the center of the coupling beam is positioned at a distance from the beams anchors equal to one tenth of their length. The first modal shapes of the resulting structure are shown in Fig. 6.18. In the first one (Fig. 6.18(a)), the beams vibrate in their first modal shape

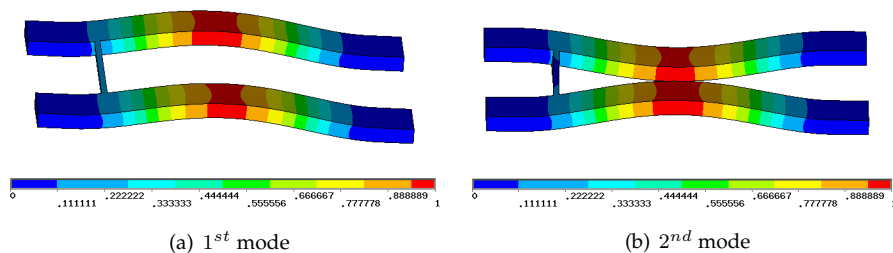


Figure 6.18: Micromechanical filter mode shapes, normalized to unity.

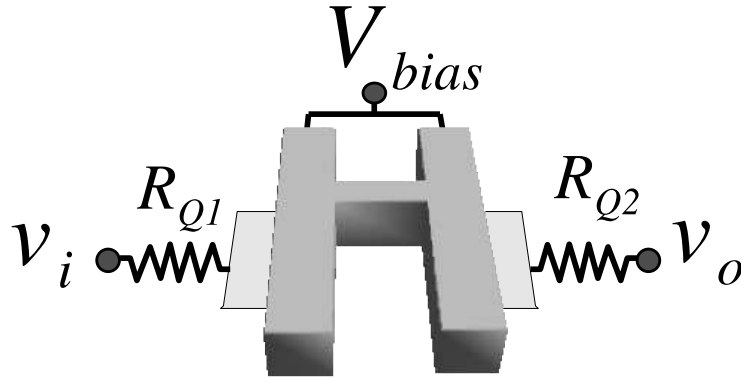


Figure 6.19: Typical measurement setup of a micromechanical filter.

in phase, while in the second (Fig. 6.18(b)) they have a phase offset of 180° . The resonance frequencies of the two modes define the central frequency of the filter f_0 and its bandwidth BW . The low velocity of the coupling point leads to a narrow band filter. In particular, the measured quality factor of the filter, defined as:

$$Q_{filter} = \frac{f_0}{BW},$$

is around 350 [47].

A 15 d.o.f. reduced order model of the device has been extracted for a 15V bias voltage and translated into a VerilogA model for simulation in Cadence. In order to choose damping coefficients, which describe the behaviour of the device reported in literature, a resonator model was first created with the same dimension of the one constituting the filter. The damping coefficients that allowed to reproduce the resonator quality factor measured in [47] have been adopted for the filter model.

Circuit simulations have been performed using the measurement setup suggested in [47] and reported in Fig. 6.19. Key point of this measurement setup is the proper choice of the termination resistances $R_{Q1} = R_{Q2}$, which serve to reduce the quality factor of the input and the output resonators. In this way, the filter characteristic is not marked laterally by high resonance peaks, leading to high in-band ripples of the band-pass filters. The resistance of the resistors that enables to obtain a filter with a flat pass-band is given, according to [47], by:

$$R_{Qi} = \left(\frac{Q_{res}}{q_i Q_{filter}} - 1 \right) R_{m,i}, \quad (6.3)$$

where i refers to the termination resistance in question, Q_{res} is the unloaded quality factor of the resonators constituting the filter, $R_{m,i}$ is the motional resistance of the i th resonators and q_i is a parameter depending on the kind of filter, which, for the case considered, is close to unity.

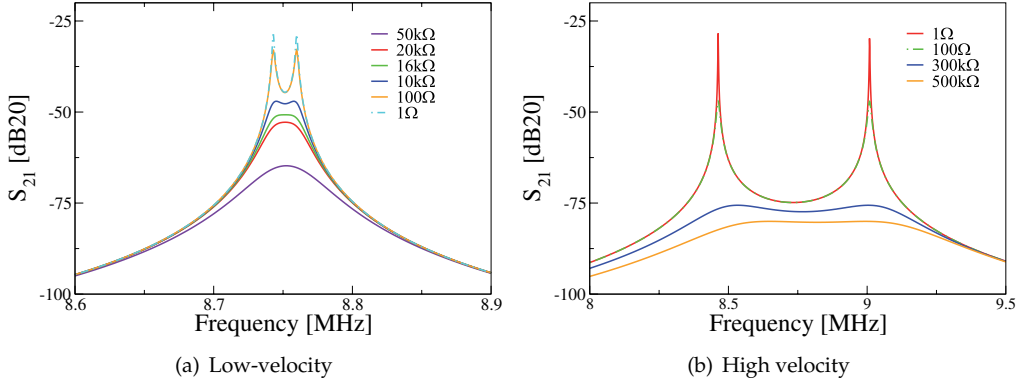


Figure 6.20: Low- and high-velocity coupling filter transmission parameter for different values of the termination resistance.

Considering that $Q_{res} \gg Q_{filter}$, equation (6.3) becomes:

$$R_{Qi} = \frac{Q_{res}}{Q_{filter}} R_{m,i} = \frac{2\pi f_0 m_{eq}}{Q_{filter} \eta^2},$$

with m_{eq} and η equivalent mass and electromechanical transduction factor of the resonator i . Calculating analytically m_{eq} and η and using this expression, a value of the termination resistance of around 20k Ω has been estimated.

An S-parameter analysis has been performed for different values of the loading resistance, including the one calculated, connecting two ports with internal resistance equal to 50 Ω to the terminal v_i and v_o in Fig. 6.19. The transmission parameter S_{21} is plotted in Fig. 6.20(a) as a function of the frequency. It can be seen that the filter flat band is achieved for $R_{Q1} = R_{Q2} = R_{Qlv} = 16\text{k}\Omega$, which is not far from the computed value. For lower resistance, the filter characteristic shows still some ripples, while for higher values the insertion loss of the filter rapidly increases. The filter simulated quality factor for a 16k Ω termination resistance is equal to 348 and is thus in good agreement with the measured value.

A filter model with high-velocity coupling has then been created. In this case, the coupling beam is centered with respect of the resonator length and a higher bandwidth is expected. The calculated quality factor for the filter is in this case 11 [182]. The correct value of the termination resistance can be estimated on the basis of the simulation results of the first model, as:

$$R_{Qhv} = \frac{Q_{filter,lv}}{Q_{filter,hv}} R_{Qlv} = \frac{348}{11} \times 16\text{k}\Omega \approx 500\text{k}\Omega.$$

The S-parameter analysis of the new filter model has been repeated for various values of the resistance around R_{Qhv} . The resulting transmission parameter is plotted in Fig. 6.20(b). It can be noted that the new position of the coupling beam lead to the expected enlargement of the filter bandwidth. The flat-band condition is then achieved with the computed value of R_{Qhv} , at which the filter quality factor is correctly predicted to be equal to 11. Another effect, more evident with respect to the first model, is that for increasing values of the resistance the filter central frequency

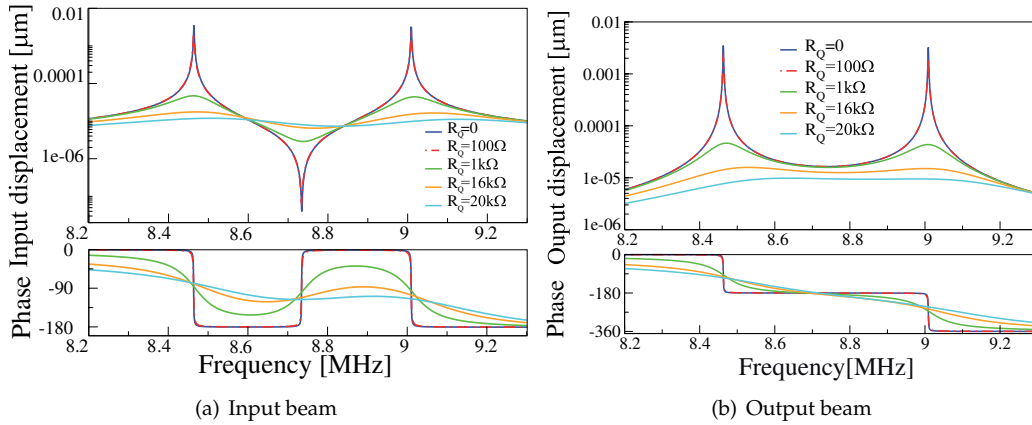


Figure 6.21: Displacement at the center of the filter input and output beam, when a small signal sinusoidal voltage applied to the device input terminal and for increasing values of the termination resistances.

migrates towards the second mechanical resonance frequency of the structure.

Harmonic simulation of the filter model has also been performed applying a small signal sinusoidal voltage to the terminal v_i and grounding v_o . The amplitude and phase behaviour of the displacement of the central points of the beams and of the input and output currents have been observed. They are plotted in Fig. 6.21 and Fig. 6.22 respectively, for increasing values of the termination resistance. The displacement plots show that the displacement of the beams central point is maximal in the first resonance mode. This leads to the asymmetry of the input and output current with respect of the central frequency f_0 , even if resistors with equal resistance are used for filter termination.

Another electrical parameter, which has a strong influence on the filter characteristic, is the parasitic capacitance that the filter excitation/sensing electrodes have towards ground. In Fig. 6.23 the transmission parameter S_{21} has been simulated introducing these capacitors, assuming a termination resistance of $300\text{k}\Omega$ for both termination resistor. Above a value of 100fF , the capacitors

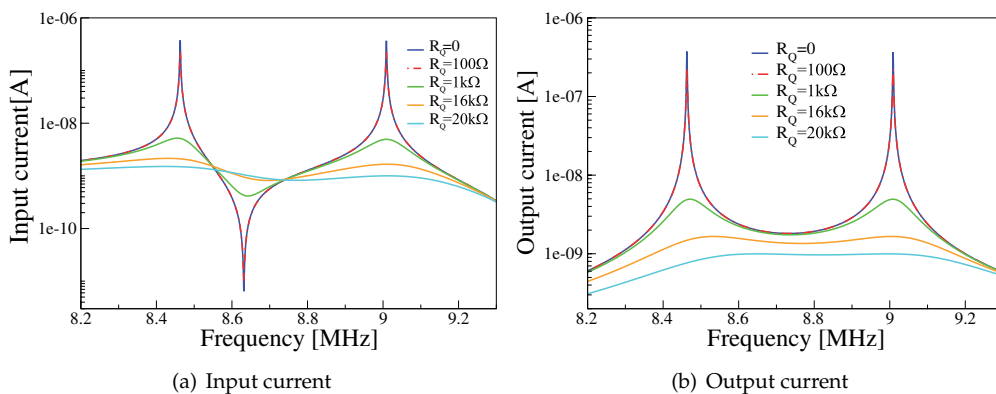


Figure 6.22: Currents at the filters terminals, when a small signal sinusoidal voltage is applied to the device input terminal. Increasing values of termination resistance have been considered.

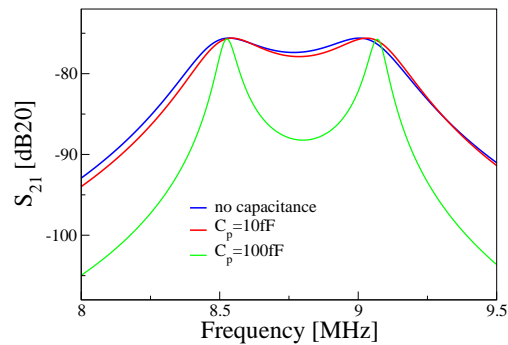


Figure 6.23: Simulated S_{21} parameter for a micromechanical correctly terminated filter in presence of parasitic capacitance at device terminals terminals.

give rise to lateral peaks in the filter characteristic, even if the termination resistance is properly chosen. This effect has therefore to be taken into account in the device design.

6.3.6 IRST capacitive switch

A reduced order model of the RF capacitive switch showed in Fig. 2.18(b) has been extracted and used for circuit simulation. The device has been fabricated at ITC-IRST and characterized optically using an interferometric profilometer (Veeco WYKO NT1100 DMEMS). This allowed to measure the transient mechanical response of the device to different stimuli, which has been used for model validation. Using a stroboscopic LED illumination of the device with a short duty cycle, the profilometer adopted allows to capture the position of the moving device at specific instants in time [183]. At this aim, a periodic signal with the desired waveform is applied to the device. The LED illumination is synchronized with the signal and the device displacement is sampled at a certain phase of the waveform by changing the phase offset between the signal and the light pulse. Since different samples are collected in different periods of the applied signal, condition for a correct measurement is that the device behaviour is perfectly periodic.

The switch consists of a $5\mu\text{m}$ thick gold plate suspended over an electrode through 4 straight beams. The actuation electrode is centered with respect of the switch armature and it is covered

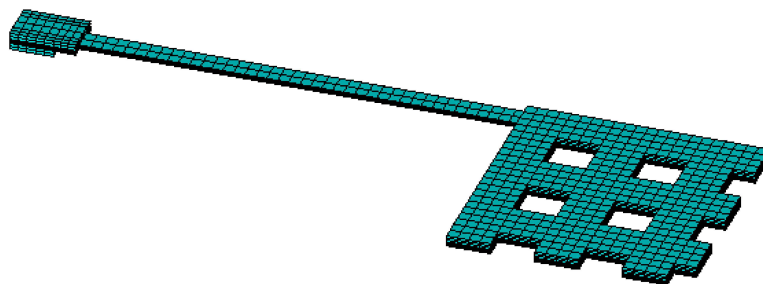


Figure 6.24: Finite element model of the IRST switch. Only one quarter of the geometry has been considered.

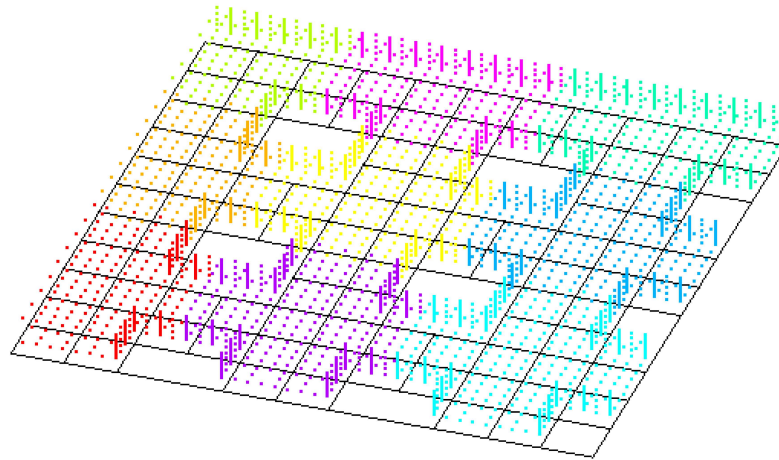


Figure 6.25: Grouping of the external node of the switch armatureswitchconductors for capacitance calculation. Nodes with the same color belong to the same conductor. The bottom area represents the conductor surface.

by a thin layer of silicon dioxide. Exploiting the device symmetry, only one quarter of the switch mechanical structure has been modeled in ANSYS. The mechanical model, shown in Fig. 6.24 has been meshed, for a total of 45000 d.o.f.

Due to the holes in the membrane, fringing effects are not negligible. An electrostatic analysis has thus been used for the computation of electrostatic forces. In particular, the nodes on the external surface of the membrane are grouped into 9 conductors as shown in Fig. 6.25. The capacitance between each conductor and the actuation electrode is computed with an electrostatic analysis. In such a way, also fringing effects due to the finite thickness of the structure and of the electrode are accounted for. However, since the plate behaves basically as a rigid body during the switch actuation, the capacitances are computed only for the undeformed switch and used to derive effective areas for calculation of lumped electrostatic forces. These are applied to the central node of each conductor.

A 15 d.o.f. reduced order model with 9 input/output d.o.f. and load vectors is extracted. The device behaviour resulted affected by a process induced tensile stress in the suspended layer, which has been estimated around 30MPa. Such a stress has been applied as initial stress in the device membrane during the nonlinear analysis preceding full matrices calculation and results thus included in the mechanical reduced model. This has been translated in VerilogA language, maintaining the Rayleigh damping coefficients as parameters, and has been extended with electrostatic forces. The model has then been imported and simulated with Cadence Spectre simulator.

The simulated and measured dynamic response of the device for a square wave actuation voltage is shown in Fig.6.26(a). The square wave has an amplitude of 15V and a frequency of 1kHz. Circuit simulation results are compared with two sets of experimental data, one extending over the full period of the input waveform with $50\mu s$ steps, and the second over the second half period with $5\mu s$ steps. In this first dynamic simulation, the values of the damping parameters are chosen

Table 6.7: Computational time for the extraction and simulation of a switch compact model.

Computation	Tool	Time
Initial stress state & element matrices computation	ANSYS	68.1 s
Reduced order model extraction	<i>MOR for ANSYS</i>	500 s
Electrostatic force computation (with FEM)	ANSYS	59.2 s
Dynamic simulation	Cadence	< 1s

so to obtain the best fit between simulation and experimental data. The agreement achieved is very good, especially in the second semi period of the square wave. The deviation observed in the first semi period can be attributed to the simplified model adopted for damping phenomena. During the first semi period, the switch membrane oscillates close to the actuation electrode and this results in a higher damping with respect to the second semi period. The oscillation frequency of the switch results therefore lower. Such an effect can be captured only if the damping force is dependent from the device position, which is not the case for Rayleigh damping.

The large signal response of the switch to a sinusoidal actuation voltage with 10V amplitude and frequency varying from 5kHz to 15kHz has been simulated. In order to reproduce the measurement conditions, a transient analysis has been performed for each frequency step and the in-phase displacement of the central part of the switch membrane has been measured once the periodic steady state was reached. This time, damping parameters extracted in the previous dynamical simulation have been used. A comparison between experimental measurement and simulation is given in Fig. 6.26(b). It can be noticed that also in this case the agreement is very good, especially for frequency above the switch resonance frequency. It is worth noting that a correct prediction of the device dynamic behaviour would have not been possible without inclusion of initial stress effects.

The times required for the extraction steps and a dynamic simulation are given in Table 6.7. The extraction of the reduced order model requires more time than in the other examples. This is due

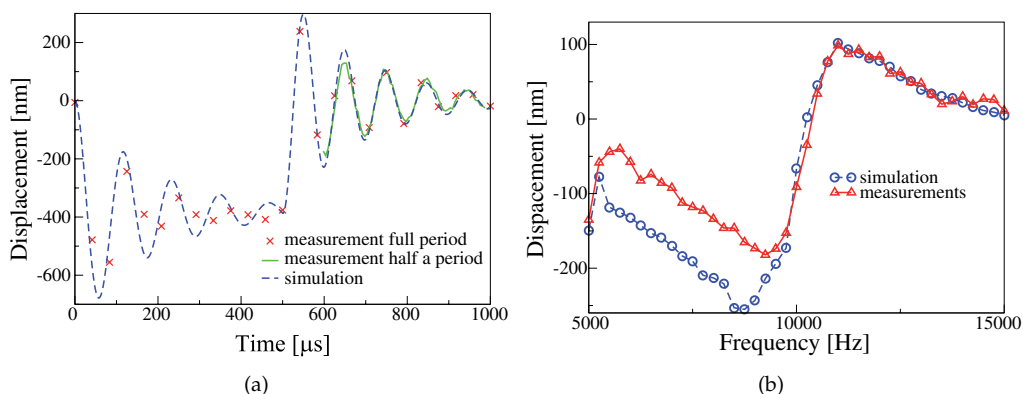


Figure 6.26: Transient (a) and steady-state harmonic response (b) of a capacitive switch to a periodic square wave and sinusoidal signal. Experimental data are compared with compact model simulation results.

both to the high dimension of the original system and to the increased number of system inputs. However, a transient simulation as in Fig. 6.26(a) (2700 time steps) with the reduced model can be performed in less than one second, while a full system transient analysis would require ca. 1000s for each iteration point.

6.3.7 ST capacitive switch

A microswitch model has been created for a capacitive switch, which was fabricated by ST-MicroelectronicsTM [184]. This presents an aluminum rectangular membrane suspended above an electrode, centered with respect of the membrane. The membrane is 3 μm thick and is anchored through 4 beams which form a 30° degree with the membrane longer edges. Since the device has two symmetry axes, only one quarter of the structure have been created and meshed. The created mechanical finite element model of the device is shown in Fig. 6.27.

A compact model has been extracted using a 15 d.o.f. reduced order model with 15 input/output d.o.f. for calculation and application of the electrostatic forces. As in the previous example, the external nodes of the membrane have been regularly grouped into conductors and an electrostatic analysis has been performed in order to compute the capacitances between each conductor and the actuation electrode. These values have been used to compute electrostatic forces. Also in this case, the effects of membrane deformation on the capacitances values have been ignored. Rayleigh damping coefficients have been parametrically included in the model. In order to capture the device pull-in characteristic, contact forces have been also included in the VerilogA model. The contact condition is checked for every output node of the reduced order model. If the absolute value of the node displacement is greater than the transduction gap of the device, than both electrical and contact forces are applied to the node, otherwise only the electrical forces are considered.

The static pull-in behaviour of the device has been simulated at circuit level and compared with the results obtained with a ANSYS full model sequentially coupled electromechanical simulation. The vertical displacements of two of the nodes of the membrane to which forces are applied have

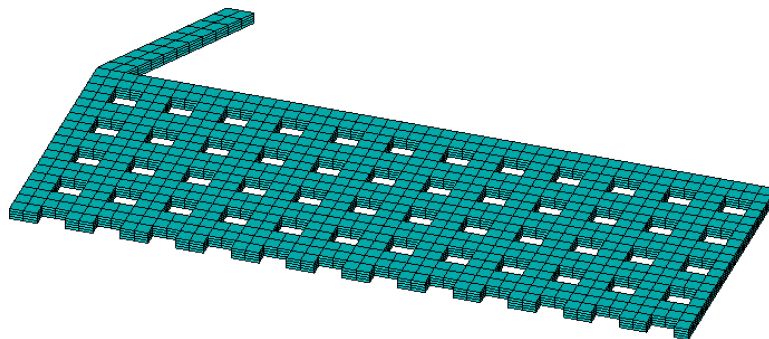


Figure 6.27: Finite element model of the ST switch. Only one quarter of the geometry has been considered.

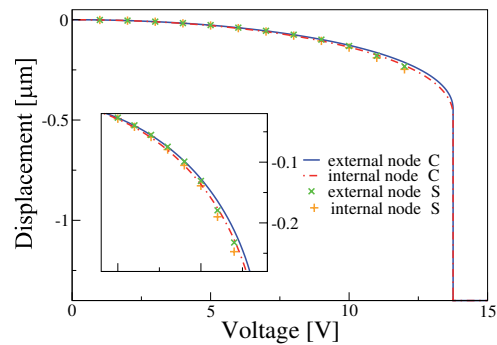


Figure 6.28: Static pull-in behaviour of the ST switch. Full model sequential coupling results are compared with a 15 d.o.f. reduced order model results.

been observed. They correspond to the minimum and the maximum displacement of the area of the membrane above the electrode. Simulation results are plotted in Fig. 6.28. The continuous lines represent the circuit simulation results, while the points represent the sequential solver results. The latter do not describe the complete pull-in curve, because convergence problems are encountered for vertical displacement of the membrane greater than 300nm. It can be seen that for small displacements the agreement between the curves is very good, while at bigger displacement a certain discrepancy between the simulation results arises. As observed for the clamped-clamped beam simulations, the reduced order model underestimates the displacement. This is attributed to the neglect of the horizontal force components arising as the beam deflects. The resulting error on the device pull-in voltage is between 5 and 10 %, which is acceptable especially if the time saving enabled by the compact model enables is considered. While the computation of the electromechanical equilibrium for 12 voltage values requires with around 10100s the sequential solver, the reduced order model simulation in Cadence uses only a few seconds.

A study of the dynamic pull-in voltage of the device has been performed at circuit level. The response of the device to a step voltage of increasing amplitude has been studied, for different values of the Rayleigh damping coefficients. In very low damping conditions, the device shows

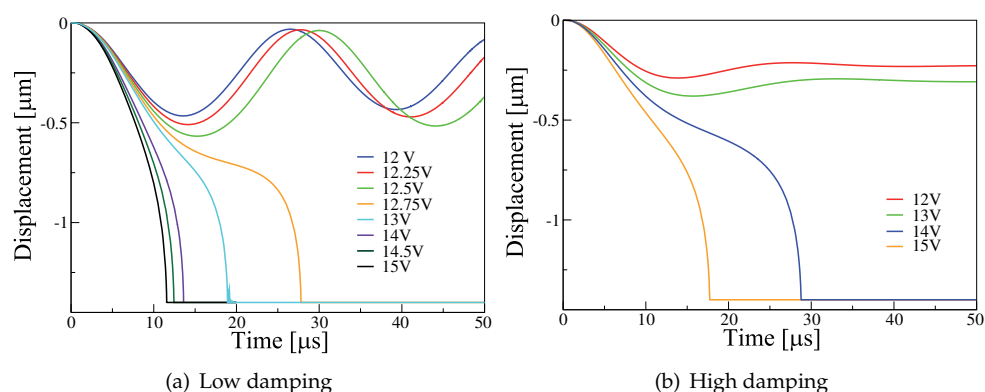


Figure 6.29: Dynamic pull-in behaviour of the ST switch in low and high damping conditions for increasing value of the applied voltage.

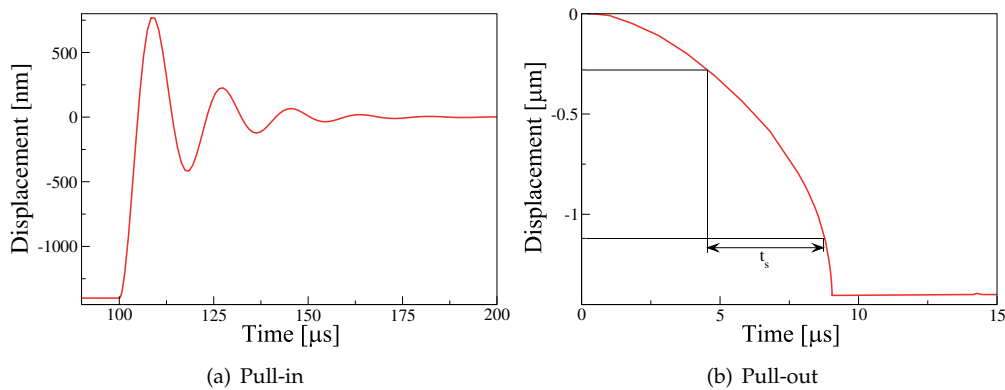


Figure 6.30: Dynamic pull-in (a) and pull-out (b) behaviour of the ST switch for a more realistic stiffness of the structure.

the behaviour of Fig. 6.29(a). For values of the applied voltage lower than 12.75V, the switch oscillates with a frequency decreasing with the applied voltage, as expected due to the spring-softening effect. At 12.75V, the switch reaches in its movement the instability region and collapses on the actuation electrode. This voltage value corresponds to the dynamic pull-in of the switch and it is in good agreement with the expected analytical value. For a static pull-in voltage of 13.75V, the dynamic pull-in voltage predicted by equation (2.49) is in fact equal to 12.78V. In addition, the shortening of the pull-in time with the applied voltage can be observed.

If the damping parameters are incremented to values which represent the typical quality factor for a switch, static and dynamic pull-in cannot be distinguished anymore. In this case, the switch has the behaviour in Fig.6.29(b).

The real switch shows a dynamic value of the pull-in between 15 and 20V, which can be attributed either to a different value of the Young modulus of the Aluminum membrane with respect to the theoretical one or to the presence of stress in the material, or to both factors. Varying the Young modulus of the reduced order model, it has been observed that a Young modulus of 88GPa, instead of the expected 70GPa, would lead to a pull-in voltage above the 15V. This value of Young modulus have been used to derive the expected pull-in and pull-out dynamic characteristics, shown in Fig. 6.30(a) and 6.30(b) respectively, for a 5kHz square wave actuation voltage with a peak value of 20V. The pull-in time, measured as the time needed for the switch to goes from 0% to 80% of the top value is approximately 7.5μ .

6.4 Discussion

The presented results show some of the capabilities that the application of model order reduction to the reduced order modelling of microresonators and microswitches offers. The main features of the proposed approach are:

- Inclusion of pre-stress effect: Electrical and mechanical pre-stress are correctly included in the reduced model. This is very important since it enables the description of effects as

spring-softening or stiffening of the structure due to a initial plane-stress.

- Fast harmonic and transient simulation: Reduced order models, both linearized or nonlinear, allow very fast harmonic and transient simulation, both at device and system level. Harmonic analysis can be quickly performed using fine frequency discretization and/or over wide frequency ranges. This is very useful for high-Q resonating devices, since it allows to correctly capture the device resonance peak and to observe several device resonance modes. The accuracy and convergence rate of transient analysis can be improved adopting small time steps and also long periods of time can be simulated, for example to extract the steady-state behaviour of the device.
- Fast and automatic extraction: Reduced order models can be extracted very fast from the device finite element model and with minimum inputs from the designer. This enables the insertion of model order reduction in an iterative device optimization loop.
- Inclusion in circuit level simulator: Reduced order models can be inserted in a circuit simulator for accurate prediction of the interactions between a microelectromechanical resonator and the surrounding drive and sensing electronic circuitry. The translation in a HDL language and the correct interfacing with external electronics is straightforward and the low complexity of the reduced models allows their use in large numbers and/or in very complex circuits.
- Large application field: The use of a finite element model as a starting point for the reduction process allows the method to be applied to electrostatically actuated structures with any geometrical complexity, without adopting shape simplifications and the two different techniques introduced for dealing with nonlinearities enable the description of the devices for both linear and nonlinear analysis.
- Flexibility in model creation: In the creation of the model, the designer has the possibility to choose the desired output quantities, both from the mechanical and the electrical domains. This is often useful for a better understanding of the device behaviour and can help the interfacing of the model with other kinds of compact models.

The biggest limit of mathematical model order reduction is that the models are device specific. Only parameters that give a linear contribution to the element matrices can be maintained in the reduced order model. This means that material properties such as Young modulus and density can be included in the reduced model, but the model corresponds to specific geometrical dimensions.

Chapter 7

Integrated RF resonators and switches fabrication

This chapter describes a process-flow for the integrated fabrication of RF resonators and switches on a SOI substrate. The process is the result of the combination of two process flows for the separate fabrication of these devices, which will be first introduced. The designed integrated resonator-switch structures are then presented.

7.1 Single processes

7.1.1 Switch process

ITC-IRST developed a process that is optimized for the fabrication of RF MEMS switches on a high resistivity silicon substrate. A cross section of the process is shown in Fig. 7.1 [185]. The process makes use of a photoresist as a sacrificial layer for the creation of the suspended structures. These are defined using electroplating. A thick field oxide is first deposited on the wafer to isolate the devices and minimize the electric loss towards the substrate. A polysilicon layer allows the creation of integrated resistors and the switch actuation electrodes. A multilayer, which is a sandwich of titanium, titanium nitride, aluminum and titanium nitride, can be used as a contact to the polysilicon or as an underpass. Moreover, it can be used to form an integrated capacitor with the subsequent isolation and gold metal layer. Gold suspended structures can be created with three different thicknesses, resulting from the combination of two electroplating steps. The maximum electroplated gold thickness, which is $5\mu\text{m}$, is used also for the definition of the coplanar waveguides. An additional layer of sputtered gold can be used to create floating electrodes. For capacitive switches, a gold layer deposited on top of the dielectric enhances the contact with the armature, when the switch is closed. Moreover, this layer is also required for the realization of gold-gold ohmic contact in metal contact switches.

The IRST switch process makes use of 8 masks and a total of 22 main process steps, listed in Table

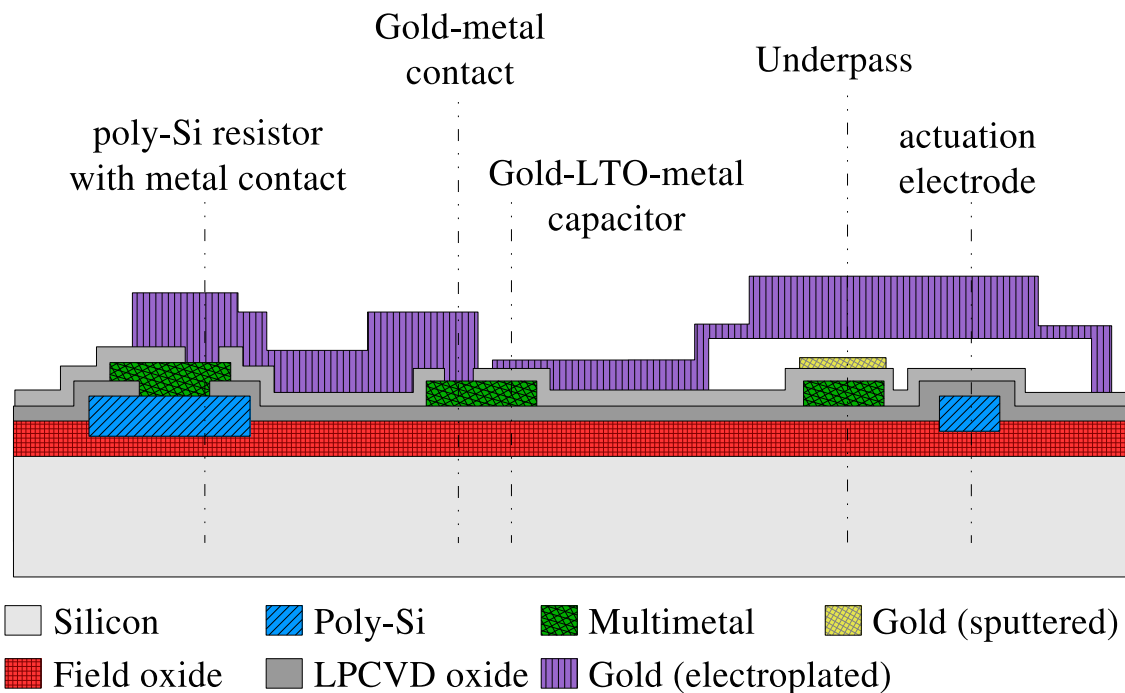


Figure 7.1: Schematic cross section of the IRST switch process.

7.1. The process starts with the growth of the field oxide on the wafer. Then, the polysilicon layer is deposited, doped with boron and covered with a thin TEOS oxide. After opening of the vias to the polysilicon, the multimetal layer is deposited and patterned on the wafer. The metal is covered with a thin low temperature oxide (LTO), which is removed, where necessary, for the realization of electrical contacts. The gold floating metal is deposited and patterned. At this point, a $3\mu\text{m}$ thick photoresist is spin-coated on the surface, which serves as a sacrificial layer for the creation of the suspended structures. The photoresist is post-bake at high temperature, in order to round the edges of the photoresist structures and to avoid further deformation of the spacer photoresist during subsequent high temperature steps. The seed layer for the electroplating of the suspended structures and other thick metal parts is then evaporated on the substrate. Evaporation does not guarantee a good coverage of steep edges. This renders the removal of sharp edges from the wafer surface necessary to ensure a complete coverage of the seed layer and thus electrical continuity during the electroplating steps. Afterwards, gold is electroplated on the wafer in two steps, with different thicknesses: a first layer of $2\mu\text{m}$, called BRIDGE layer, and a second layer of around $3\mu\text{m}$, called CPW layer. Areas on which the gold has to be electroplated are defined with a photoresist masking layer, with a thickness higher than the one of the layer to grow. After the electrodeposition steps, the wafer undergoes a temperature treatment, which serve to improve the adhesion of the gold to the wafer. This is especially important for wire bonding purposes. The suspended structures are then released by dry etching of the spacer with oxygen plasma. The most critical part of the process is the creation of stress-free suspended structures. When thin

films are deposited on a sacrificial layer at a temperature lower than its flow temperature, then intrinsic stresses develop in the film-sacrificial layer stack. Both in-plane stress and stress gradients can arise. These not only modify the mechanical properties of the materials, but can cause out of plane bending of the suspended structures after their release. The entity of the effect depends mainly on the temperature treatment, to which the wafer is subjected and on the materials used [187].

In the presented process, the annealing of the wafer after electroplating leads to in-plane tensile stress in the gold layer. Moreover, the diffusion of the seed layer into the electroplated membrane led in the past to a stress gradient in the thickness of the suspended gold layer. The thicknesses of the layers used in the seed layer were therefore optimized in order to minimize the effects of this phenomenon.

7.1.2 Resonator process

A low-temperature process for the fabrication of in-plane resonators on an SOI substrate has been developed at IMTEK [36,52]. The process uses deep reactive ion etching (DRIE) for creating beam structures in the device layer of the SOI wafer. The etching step reaches the buried oxide of the SOI wafer. Afterward, the etched structures are covered with a few hundreds nanometer low

Table 7.1: IRST switch process: detailed process flow [185,186].

Steps	Details	Mask
1. Growth a thick field oxide	1 μ m @ 975°C	
2. Un-doped polysilicon deposition	LPCVD, 630nm @ 620°C	
3. Polysilicon doping with Boron		
4. Patterning of the polysilicon		POLY
5. TEOS deposition	LPCVD, 300nm @ 780°C	
6. Opening of the contact to the polysilicon	RIE etch	COHNO
7. Deposition of the TiN-Al-TiN	Sputtering, total 630nm @ 780°C	
8. Patterning of the multimetall	Dry etch	TiN
9. LTO deposition	LPCVD, 100nm, @ 430°C	
10. Opening contact to the multimetall	Dry etch	VIA
11. Deposition floating metal (FLOMET)	CVD, Cr 10nm + Au 120nm	
12. Patterning of the FLOMET	Wet etch	FLOMET
13. Deposition sacrificial photoresist (SPACER)	Spin-coating, 3 μ m	
14. Patterning of the SPACER	post-bake @ 200°	SPACER
15. Deposition of the seed layer	CVD, Cr 2.5nm + Au 50nm	
16. Patterning photoresist	Spin-coating, 4 μ m thick	BRIDGE
17. Electroplating	2 μ m Au	
18. Patterning photoresist	Spin-coating 5 μ m thick	CPW
19. Electroplating	3 μ m Au	
20. Removal of the seed layer	Dry etch	
21. Annealing	30m at 190°	
22. Structures release	Oxygen plasma, 200°	

temperature oxide, which serves as a spacer between the beams and their actuation electrodes. The dielectric layer is partially removed to allow for electric contact of the beams. Then, the electrodes of the resonator and the contacts to the beams are electroplated. For this purpose, a seed layer is first deposited on the wafer and the areas to electroplate are defined with a thick patterned photoresist. The seed layer is sputtered, in order to improve the step coverage, and is removed around the beams. In this way, the electrodes can grow laterally very close to the beams, in contact with the oxide sidewalls, but electroplating on top of the beams is avoided. After the electrodes and the contacts are created, the seed layer is removed and the beams are released by wet etch of the LTO and the buried oxide.

The IMTEK process requires only 4 masks. The steps are described in Table 7.2. In order to enhance the electromechanical coupling, high structures are realized, using SOI wafers with a device layer around $10\mu\text{m}$ thick. The critical points of the process are mainly the etching of structures with vertical sidewalls and minimal surface roughness and the patterning of small features after the etching step (photolithography 6 and 7 in Table 7.2), which requires the use of thick resist. These issues were both addressed in [188]. For the etching, the use of the inductive coupled plasma (ICP) BOSCH/ASE[®] process has been proposed [189]. The process allows to achieve nearly vertical sidewalls, it is uniform and very selective against resist and silicon oxide masks. Although the process produces ripples on the sidewalls, their dimensions can be minimized so as to allow the definition of sub-micron transduction gaps. Concerning the photolithography steps, a recipe was developed for the photoresist AZ9260, produced by Clariant[®], which allows deposition of a thick photoresist and its patterning with vertical sidewalls and sub- $10\mu\text{m}$ features. A thickness of $10\mu\text{m}$ is used for patterning of the seed-layer, while $20\mu\text{m}$ are necessary for the patterning of the $10\mu\text{m}$ thick electroplated structures, inside the $10\mu\text{m}$ deep trenches.

The IMTEK process has been demonstrated only for beam shaped resonators, but it can be used for the design of any in-plane flexural or longitudinal resonator.

Table 7.2: IMTEK resonator process: detailed process flow [188].

Steps	Details	Mask
1. SOI wafer doping	$100\Omega\text{sq}$	
2. Oxide deposition	masking layer	
3. Patterning of the oxide		Silicon
4. Device layer etch	ICP dry-etch	
5. Deposition of the LTO	300nm @ 425°	
6. Opening of the contacts to the silicon	$10\mu\text{m}$ photoresist	Plug
7. Deposition of the seed layer	sputtering Cr 50nm + Au 30nm	
8. Patterning of the seed-layer	Wet etch, $10\mu\text{m}$ photoresist	Seed Layer
9. Patterning of photoresist	$20\mu\text{m}$ photoresist	E-plate
10. Electroplating of a gold layer	$10\mu\text{m}$	
11. Removal of the seed	Wet etch	
12. Release of the structure	BHF etch	

7.2 Combined process-flow

The definition of a combined process flow for resonators and switches requires the identification of a common substrate. An SOI substrate, with a device layer of around $10\mu\text{m}$, has been chosen, since it is required by the IMTEK resonator process. The presence and characteristics of a buried oxide has no influence on the behaviour of the switches. The resistivity of the device layer, however, is instead very important for both devices. Electrical isolation of the devices on the wafer and minimization of electrical losses in the substrate require very high resistivity, while resonator performance benefits from very low resistivity. Starting from an SOI wafer with a high resistivity substrate, a local doping is needed of the areas where the resonators will be fabricated.

In addition, an etching step is required to define alignment marks, which can be used for the alignment of the mask used for the doping, with the subsequent masks. The definition of the areas in which the resonators will be fabricated does not require a high resolution lithographic step. Hence, laser-printed masks, which have resolutions of $10\mu\text{m}$ can be used as alternative to the more expensive Chromium masks.

As discussed in section 2.4, two other points have to be considered for the realization of an integrated resonator-switch process flow. These are the topography of the substrate and the maximum temperatures that the different materials on the wafer can stand, without degradation or modification of their properties.

In order to avoid planarity problems, the fabrication of resonators could start after the deposition of the sacrificial layer for the switches. The suspended structures of the switches could be created just before the resonator release, together with the resonator contact. However, the deposition of the sacrificial LTO after a gold deposition (the floating metal) is not desirable due to contamination problems. In addition, temperature-related issues could occur. The deposition temperature, which is around 400°C , might be already too high for the floating gold layer [190]. Moreover, the contacts to the silicon beams could be realized only with the electroplated gold. During the subsequent annealing step, gold and silicon could form an eutectic alloy, thus compromising the functionality of the wafer [191]. Another approach has therefore been defined, which avoids temperature issues by performing the various process steps in order of decreasing temperature.

The process starts with boron doping of the areas of the SOI wafer, where the resonator will be realized. A doping dose is used, such that a resistivity of $26\Omega\text{square}$ for the device layer is achieved (Fig. 7.2(a)). Afterwards, the first steps of the switch process are carried out, as in Fig. 7.2(b-e). The only modification of the original process is that the wet etch of the TEOS is extended in time, so that the complete field oxide is removed, where the contact to the resonators has to be realized (Fig. 7.2(c)). The multimetal layer is then deposited. Electrical contact to the silicon is thus realized through the multimetal (Fig. 7.2(d)). After the deposition of the LTO (Fig. 7.2(e)), the processing of the resonators starts. The LTO serves both as a protection and as a masking layer for the wafer surface during the subsequent DRIE etch of the resonating structures (Fig. 7.2(f)). After etching of the resonator structures, a second LTO layer is deposited on the substrate, which will serve as sacrificial layer for the resonators (Fig. 7.2(g)). The thickness of the LTO that covers

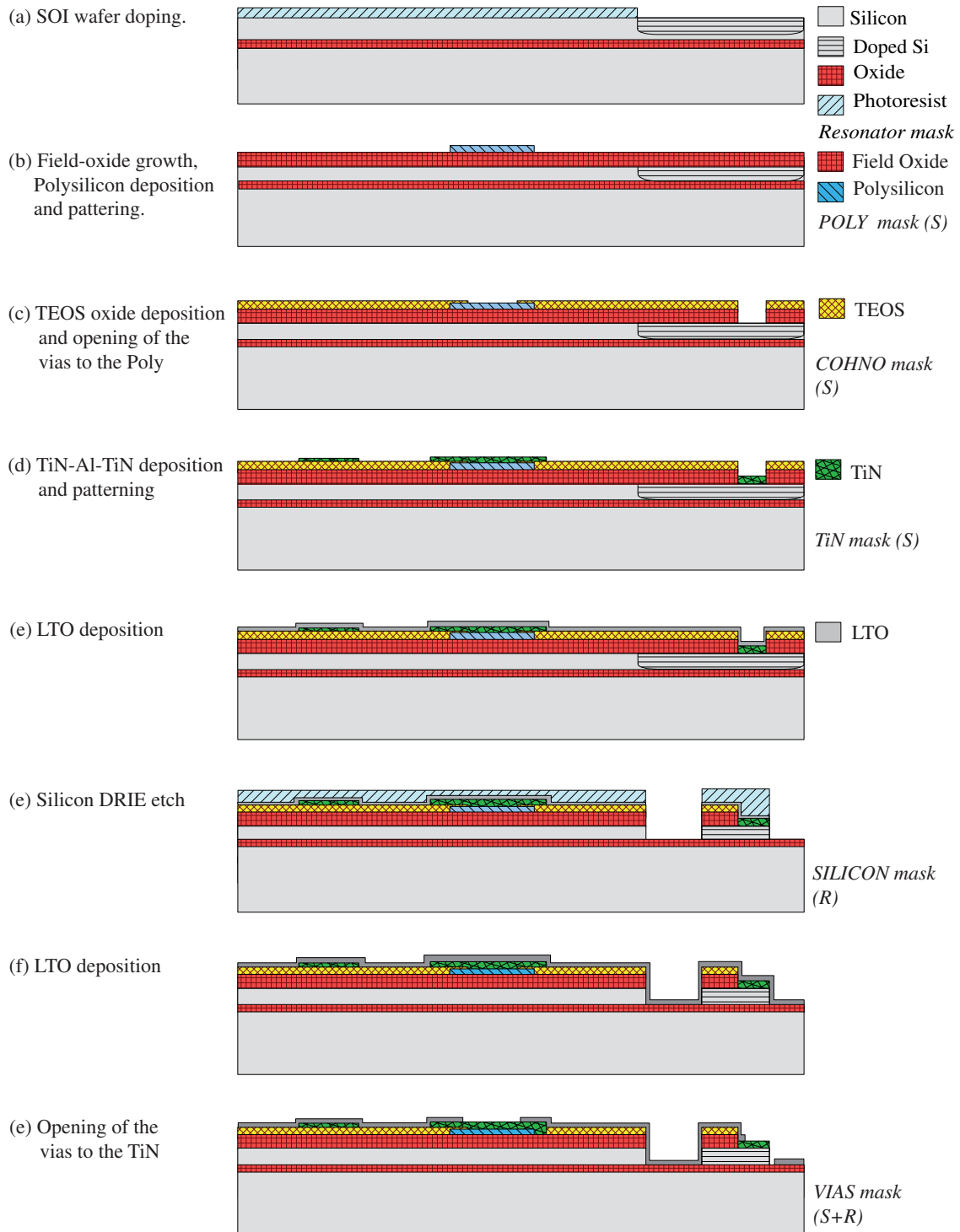


Figure 7.2: Combined process-flow steps (a-g).

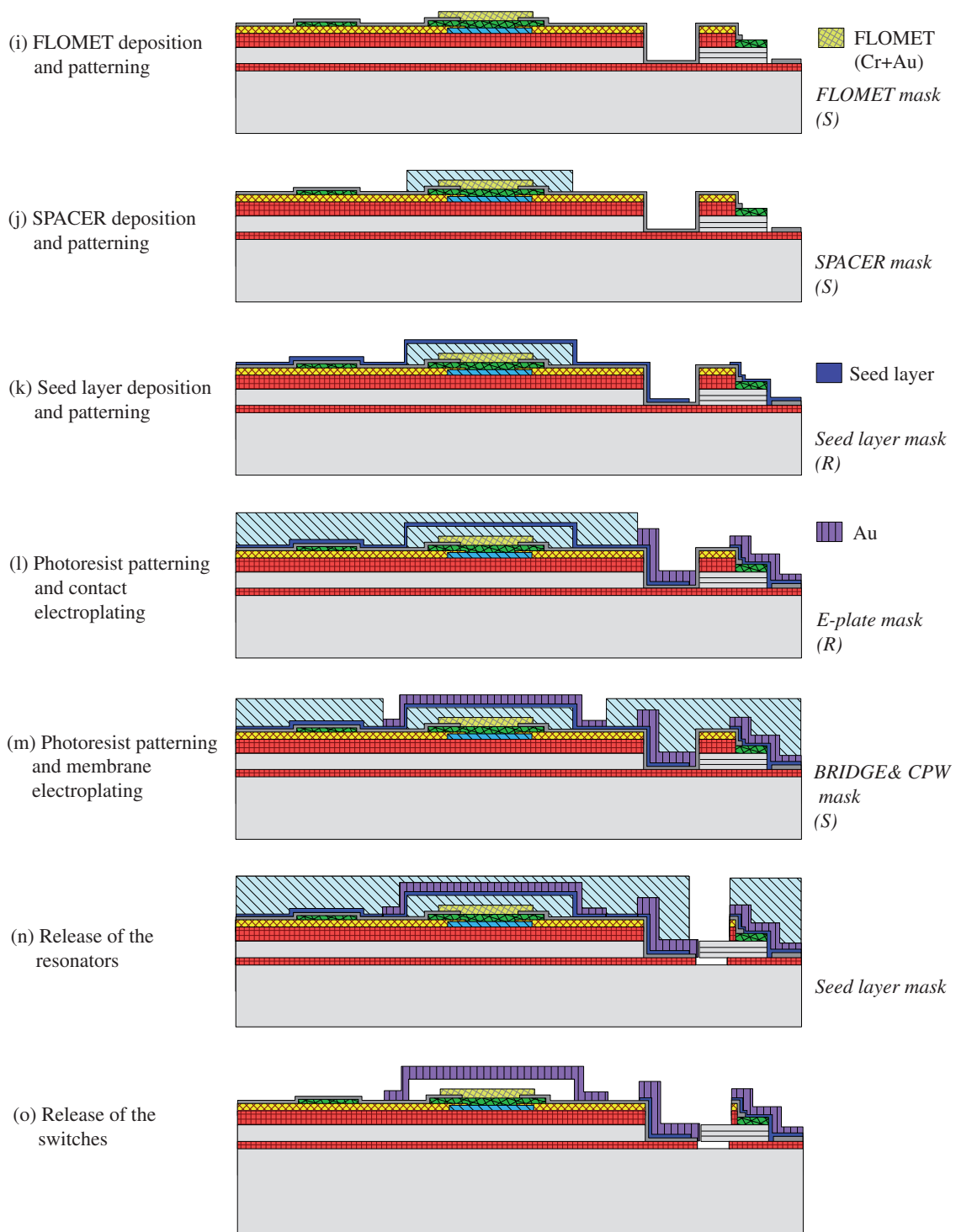


Figure 7.2: (continued) Combined process-flow steps (h-o).

Table 7.3: Combined switch process: detailed process flow. The starting wafer is an SOI wafer with a $10\mu\text{m}$ thick device layer and a resistivity $> 3000\Omega\text{cm}$, both for the device layer and the substrate.

Steps	Details	Mask	S	R
1. Etching of the alignment marks	DRIE etch	Mask 0	✓	✓
2. Patterning of a photoresist mask		Resonator		✓
3. Boron doping of the silicon	Dose $4.5e12$, thermal treatment @ 1150°C			
4. Growth of a thick field oxide	$1\mu\text{m}$ @ 975°C			
5. Un-doped polysilicon deposition	LPCVD, 630nm @ 620°C			
6. Polysilicon doping with Boron				
7. Patterning of the polysilicon		POLY	✓	
8. TEOS deposition	LPCVD, 300nm @ 780°C			
9. Opening of the contact to the polysilicon	Dry etch (time settled to reach the silicon)	COHNO	✓	✓
10. Deposition of the TiN-Al-TiN	Sputtering, total 630nm @ 780°C			
11. Patterning of the multimetall	Dry etch	TiN	✓	✓
12. LTO deposition	LPCVD, 100nm , @ 430°C			
13. Patterning of the oxide		Silicon		✓
14. Device layer etch	ICP dry-etch			
15. Deposition of the LTO	300nm @ 425°			
16. Opening contact to the multimetall	Dry etch	VIA	✓	✓
17. Deposition floating metal (FLOMET)	CVD, Cr 10nm + Au 120nm			
18. Patterning of the FLOMET	Wet etch	FLOMET	✓	
19. Deposition sacrificial photoresist (SPACER)	Spin-coating, $7\mu\text{m}$			
20. Patterning of the SPACER	post-bake @ 200°	SPACER	✓	
21. Spacer thickness reduction	Oxygen plasma, 30W RF power @ 212mTorr			
22. Deposition of the seed layer	Sputtering, Cr 2.5nm + Au 50nm			
23. Patterning of the seed layer	Wet etch	Seed layer		✓
24. Patterning photoresist	Spin-coating, $20\mu\text{m}$ thick	E-Plate		✓
25. Electroplating	$10\mu\text{m}$ Au			
26. Patterning photoresist	Spin-coating $4-7\mu\text{m}$ thick	BRIDGE	✓	
27. Electroplating	$2\mu\text{m}$ Au			
28. Patterning photoresist	Spin-coating $4-7\mu\text{m}$ thick	CPW	✓	
29. Electroplating	$3\mu\text{m}$ Au			
30. Annealing	30m @ 190°			
31. Seed layer removal	Wet etch			
32. Resonators release	Wet BHF etch			
33. Switches release	Oxygen plasma, 200°			

the metal contacts of the switches is thus the sum of the two deposited LTO layers. The LTO is opened to realize the contact to the multimetall layer, both for resonators (original plug mask) and switches (original vias mask), as is shown in Fig. 7.2(h).

After the creation of the vias, the floating metal is deposited and patterned as shown in Fig. 7.2(i). The presence of $10\mu\text{m}$ deep trenches on the wafer requires some caution in the photolithography steps.

At this point, the sacrificial layer of the switches is deposited, patterned and post-baked at high temperature (Fig. 7.2(j)). The seed layer is sputtered and removed from the resonating structures with a wet etch step, as shown in Fig. 7.2(k). It will serve for gold electroplating of the resonator electrodes, the suspended membranes of the switches, the transmission lines and the contact pads. A thick photoresist ($20\mu\text{m}$ according to the resonator process) is then deposited and patterned and the resonators electrodes are electroplated (Fig. 7.2(l)). The same procedure is repeated another two times, for the definition of the BRIDGE and the CPW layers (Fig. 7.2(m)). In this case, a lower resist thickness is sufficient, since the resist is not patterned in the trenches and the thickness of the gold layers to grow is lower. As in the switch process, the gold layer is annealed at 200°C .

After the electroplating steps, the photoresist and the seed layer are removed from the wafer, using acetone stripping and wet etching, respectively. A thick photoresist layer is then deposited on the substrate and patterned with the seed layer mask (Fig. 7.2(n)). This resist serves as a protective mask, during the wet etching of the LTO and the buried oxide for the resonators release. The photoresist is then stripped and the gold suspended structures are released using an oxygen-plasma (Fig. 7.2(o)). The detailed process steps are reported in Table 7.3. The last two columns of the table specify which masks are used for the design of the resonators, of the switches and of both devices.

7.2.1 Critical points

Photolithography on a high topography surface

All the photolithography steps that follow the DRIE etch of the wafer are complicated by the high topography of the substrate. The spin-coat deposition of thin layers of photoresist may result in incomplete or non-uniform coverage of the wafer substrate. The use of thicker resist layers is thus advisable, even if it results in a loss of resolution. The thickness of the photoresist largely depends on the number and dimension of the trenches and also on where the resist has to be patterned. Feature definition on the un-etched wafer surface is less critical than definition in the trenches and can use a thinner resist. A thickness of the photoresist of $3\mu\text{m}$ has been proven to ensure a complete coverage of the surface and a correct exposure and development of the resist, outside from the trenches. Such a value, however, is rather high and could affect the resolution for the definition of the floating metal layer. The resolution of the BRIDGE and CPW layer instead are not affected, since, in any case, a thick resist is used for their definition. As will be discussed in the next section, the spacer layer is deposited and patterned with even higher thickness ($7\mu\text{m}$). This will influence the exact position of the anchors of the suspended structure, with respect to the designed one.

Planarity of the switches sacrificial layer

The planarity of the sacrificial layer of the switches is extremely important. However, if a $3\mu\text{m}$ thick photoresist is spin-coated over a substrate with $10\mu\text{m}$ trenches, the photoresist layer is not

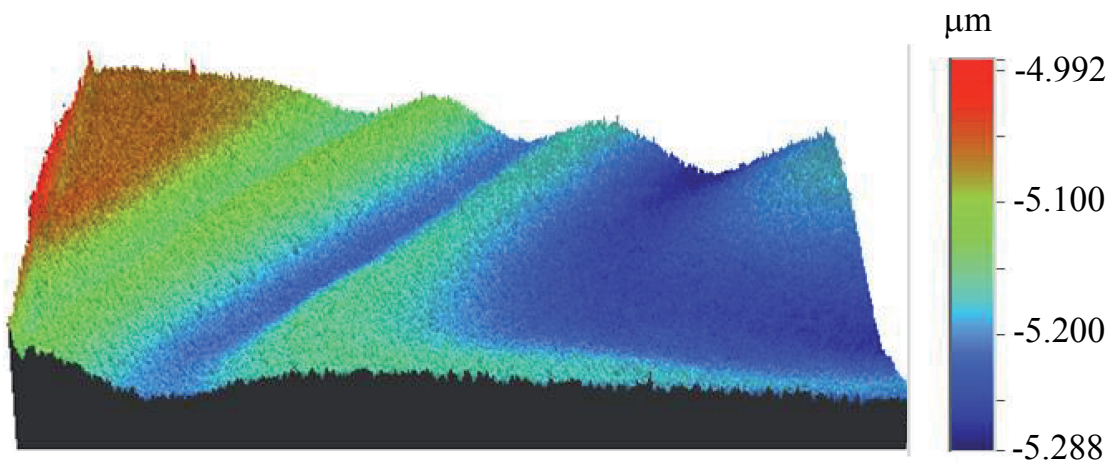


Figure 7.3: Measured 3D profile of the photoresist surface for a $3\mu\text{m}$ resist thickness spin-coated on a substrate with trenches.

expected to be planar. The process step has been studied using some test wafers, in which several trenches have been etched with different dimensions. The planarity and thickness of the photoresist have been measured at different distances from the trenches. It has been observed that “surface waves” are present at the edges of the trenches and propagate from the center to the periphery of the wafer (see Fig. 7.5(a)). A 3D profile of one of this wave has been measured with an optical profilometer and is shown in Fig. 7.3. Fig. 7.4 represents a cross section of an area of the photoresist surface. It can be seen that the amplitude of the wave does not allow to neglect the

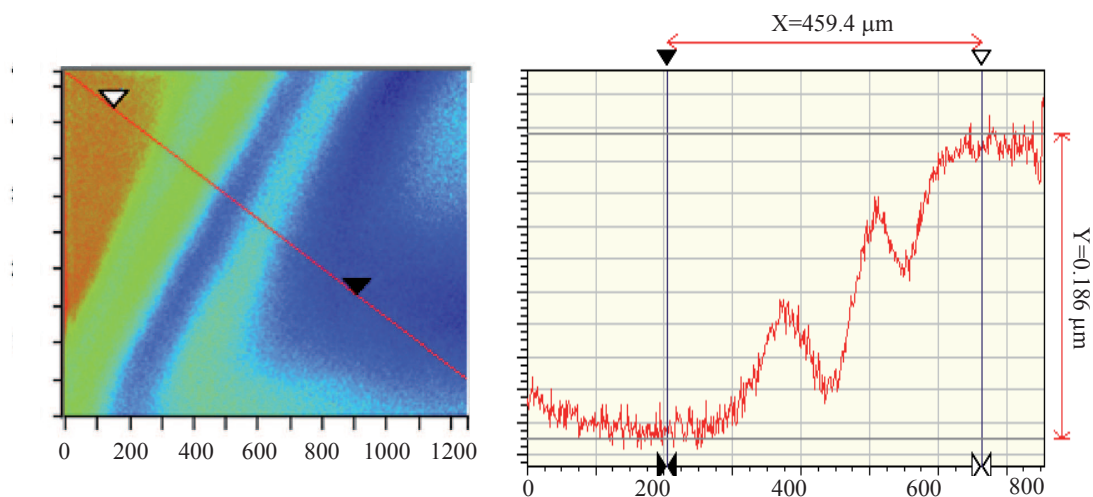


Figure 7.4: Cross section of the wavy area of the photoresist profile.

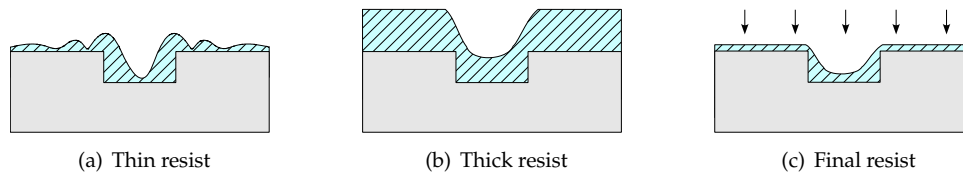


Figure 7.5: Topography of the spin-coated photoresist layer on a wafer with trenches.

phenomenon. The entity of the effect depends on the radial position of the trenches, more than on their dimensions. At the center of the wafer, the resist has a lower tangential and radial velocity, and so surface waves are more attenuated. The propagation length of the perturbation induced by the trenches is very long, so that the photoresist surface cannot be assumed to be planar at a certain distance from the trenches. It is therefore not possible to solve planarity issues by defining a specific set of design rules. Attempts have been done to vary the spinning velocity and/or viscosity, but no big improvement has been achieved.

A planar photoresist deposition, on a wafer with trenches, can be achieved by depositing a photoresist with a thickness close to the depth value of the trenches. Instead of spin-coating the wafer with a photoresist of the desired thickness, it is therefore possible to spin-coat a thicker resist and then to reduce its thickness. In particular, it has been tested that, for $10\mu\text{m}$ deep trenches, a $7\mu\text{m}$ thick photoresist, spin coated on the wafer using standard process parameters, follows the topography of the substrate surface and is planar outside from the trenches (see Fig. 7.5(b)). The thickness of the photoresist can then be reduced as shown in Fig. 7.5(c), with an oxygen-plasma etch. For this purpose, the RIE Multiplex plasma etcher (Surface Technology Systems) has been used, which allows to etch at room temperature. Different trials have been made in order to adjust the process parameters of the plasma-etching step. In particular the pressure and the RF power of the plasma reactor have to be adjusted so that the roughness of the resist surface is low. A high roughness photoresist layer is not suitable to be used as a sacrificial layer for switching devices. The electroplated metal layer on top would reproduce the patterns on the surface and this would negatively affect the contact performance of the switch. Low surface roughness can be achieved by increasing the pressure in the reactor and, at constant pressure, reducing the power [192,193].

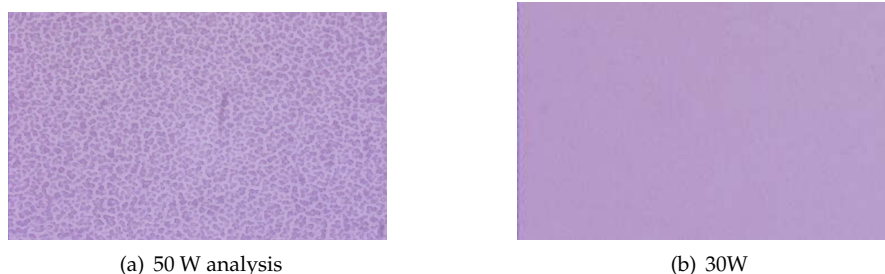


Figure 7.6: Aspect of the resist surface after oxygen plasma etching, for an RF power of 50W 7.6(a) and 30W 7.6(b).

The flow of the oxygen flux in the reactor has therefore been fixed in order to achieve the maximum pressure allowed and the value of the RF power has then been adjusted. For the trials, an etching time of 2 minutes has been used. In Fig. 7.6(a) a picture of the resist surface is shown, after a plasma treatment with a RF power of 50W. It can be seen that the surface presents a very high roughness. The RF power of the plasma reactor has therefore been lowered to 10W. In this case, no modification of the photoresist surface has been observed, but also no thickness reduction. This has been interpreted as an extremely low etching rate of the plasma. The power was increased again to 30W. In this case, $1.2\mu\text{m}$ of photoresist is etched and, as shown in Fig. 7.6(b), the surface of the photoresist is smooth.

Design rules

Together with the definition of a new process-flow, an appropriate set of design rules should be defined. For what concerns the microresonator masks, these rules have been derived based on the experience gained in previous resonator-only process runs. This is logical, since the process maintains all its features in the combined process flow. As in the previous runs, a minimum beam width of $3\mu\text{m}$ has been used. The accurate definition of smaller features via DRIE etching could be problematic. Moreover, the seed layer mask has been designed so to remove $3\mu\text{m}$ of seed layer from etch resonating beam side. In order to ensure a correct patterning of the features inside the trenches, the structures have been kept at a minimum distance of $10\mu\text{m}$ from the trench border. The design rules for the switch masks that are used after the DRIE etch step requires modifications with respect to the switch-only process. This is due to the expected limitation in resolution of these photolithographic steps. Such a new set of rules will be defined on the basis of the first combined process run.

7.2.2 Effects on devices behaviour

The combined process flow aims to maintaining the performance of the switches and resonators fabricated according to their original process. However, for what concerns switching devices, the proposed process flow does not enable to fully fulfil this requirement. This is due to the fact that the LTO layer of the switches is not 100nm thick as in the original process, but around 400nm. This will result in an increase of the pull in voltage of the switch and a 25% reduction of the ratio between the capacitances in the down and the up state. While the first effect is not very important, the second has a strong influence on the performances of capacitive switches. In addition, integrated capacitance will have higher area occupation. In the first process demonstration, these drawbacks have been accepted. A second process run could include an etching step, for the reduction of the oxide thickness on the switch areas.

7.3 Designed structures

The first combined process run includes both resonator-switch structures and single resonators and switches, in order to be able to test the devices separately.

A prototype of a duplexer with integrated filters for channel selection has been designed, using a scheme as in Fig. 7.7. The duplexer is realized by introducing an ohmic series switch in each branch of a CPW T-junction. By closing one of the switches, the signal at the input of the T-junction can be redirected to one of the two outputs of the structure. A resonator, inserted in series with each switch, performs a narrow-band filtering operation on the signal. The switches are broadband, with separate actuation lines and a common ground configuration. An integrated polysilicon resistor is used for the connection of the switch armature to the ground line of the CPW transmission line. In this first design, equal resonators have been used. The signal line of the CPW at the output of each switch is directly connected to the input electrode of the resonators, while the electric terminals of the resonating beam are connected to the ground lines. The resonators can be polarized using an external bias-T connected to the ground line or to the output signal line. They can thus be separately polarized and the bias voltage can be used for the tuning of their resonance frequency. In a real implementation, channel selection will be done by using resonators (or filters) with different central frequencies.

The mask layout of the duplexer with integrated channel selection is shown in Fig. 7.8(a). The structure is perfectly symmetric with respect to the signal line, so only half of the layout is shown. This occupies an area of 1.7mm^2 . This implementation uses free-free beam 1MHz resonators. The beam structures are not directly visible, because of their small dimensions, but are defined under the seed layer mask. In Fig. 7.8(b), a detail of the switch polysilicon and multimetal line is shown. Polysilicon meanders resistors connect the switch armature to the ground line. Polysilicon fingers are also used for the actuation. Multimetal combs transport the signal to the input and the output of the switch. The combs multimetal fingers are deposited on the top of dimples of stacked polysilicon and TEOS, so that, when the switch collapses, it does not get into contact with the actuation lines. Moreover, in the area underneath the switch plate, the LTO on top of the multimetal is removed and the FLOMET is patterned, in order to achieve a gold-gold ohmic contact between the switch plate and the signal line.

This thesis covered only the design of the resonators, which is discussed in the next subsection.

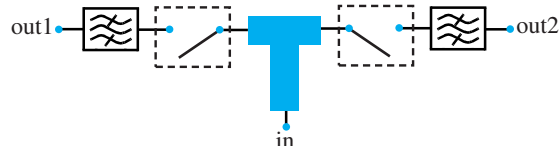


Figure 7.7: Block scheme of the designed duplexer with integrated channel selection.

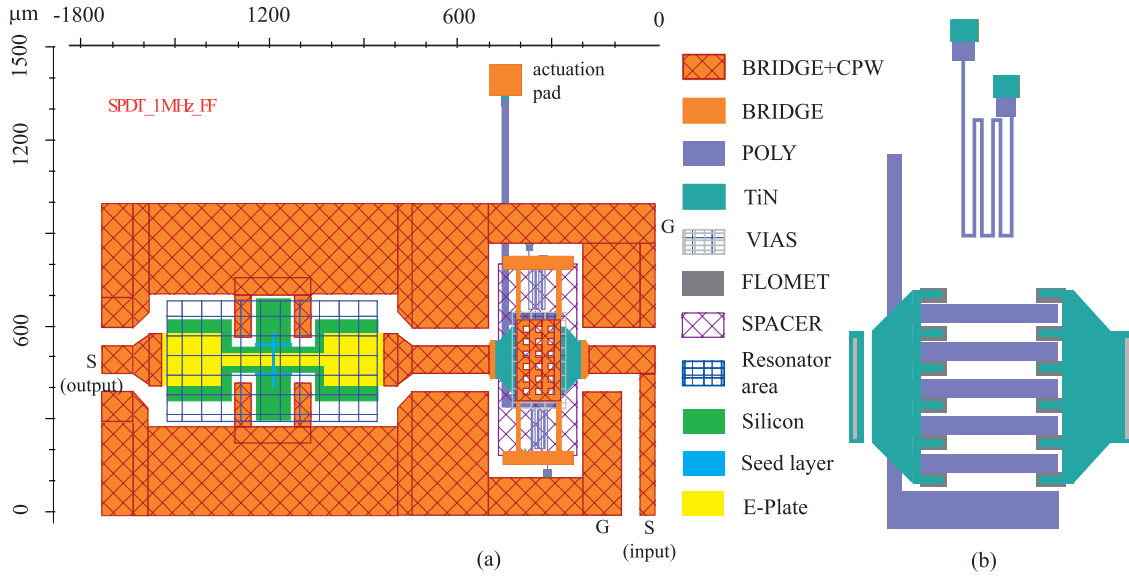


Figure 7.8: Masks layout of the designed duplexer with integrated channel selection (a) and detail on the switch underpass lines.

7.3.1 Resonator design

Clamped-clamped beam and free-free beam lateral resonators have been designed for two values of the resonance frequency (1 and 10MHz). Even though other geometries would have allowed the achievement of higher resonance frequencies, the same geometrical shape of the previous designs has been maintained, in order not to incur in device-specific problems.

The dimensions of the resonators that enable the achievement of the desired resonance frequencies have been chosen as follows. For beams operated in vacuum, the main dissipation phenomena are support damping and thermoelastic damping. Using the equations 2.39 and 2.38 introduced in chapter 2, analytical values of the unloaded quality factor due to these phenomena have been derived as a function of the frequency. These are plotted in Fig. 7.9, for different values of the beam thickness. It can be seen that for clamped-clamped beams vibrating in their first resonance mode, the quality factor Q_{cc} , due to support damping, and the quality factor Q_{TED} , due to thermoelastic damping, have approximately the same entity at 1MHz. At 10MHz, support damping dominates, even for the lowest value of the beam width. In both cases, the minimum beam width has to be chosen in order to minimize damping phenomena. At 1MHz, such a value allows to maximize both quality factors. At 10MHz, only the support quality factor is maximized, which represents the limiting factor of the total device quality factor.

The quality factor Q_{cc} for the free-free beam resonator has been estimated using equation 2.39, but for the second resonance mode of the supporting beams. The resulting quality factor is several orders of magnitude higher, as shown in Fig. 7.9(a). The quality factor Q_{TED} has been assumed to be equal to the one of a clamped-clamped beam resonator. In reality, also the supporting beams vibrate and are therefore subjected to stress in homogeneity. However, their contribution

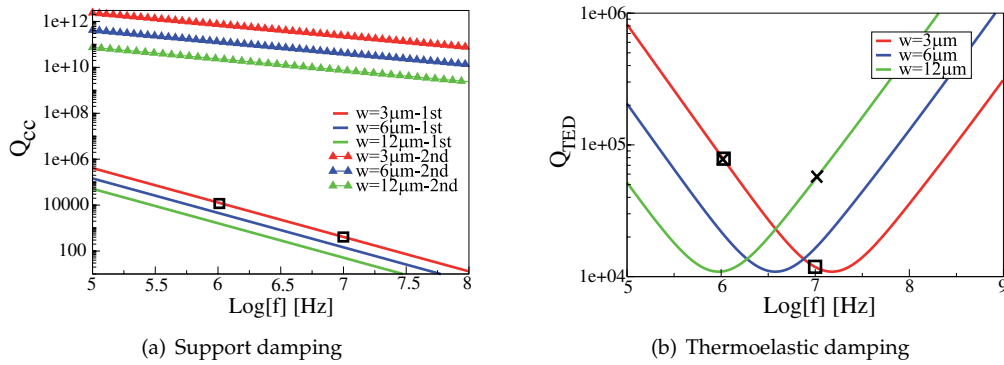


Figure 7.9: Quality factor vs. frequency dependency for various values of the resonator width w , in case of 7.9(a) support damping and 7.9(b) thermoelastic damping. Squares and crosses represent the values corresponding to the designed clamped-clamped and free-free beam resonators, respectively.

to damping phenomena does not influence the choice of the design parameters of the central beam and render dissipative effects due to thermoelastic damping higher. For this kind of device, thermoelastic damping is prevalent with respect to support damping. A $12\mu\text{m}$ beam thickness has been chosen, which allows to reduce the effect of thermoelastic damping, as it can be seen in Fig. 7.9(b).

The quality factors Q_{cc} and Q_{TED} of the designed devices are indicated in Fig. 7.9(a) and 7.9(b) with squares, for the clamped-clamped beam design and with crosses, for the free-free design. After choosing the widths of the beams, their lengths have been computed according to equation 2.6 and have been verified numerically. For the supporting beams of the free-free design the minimum width has been chosen, thus reducing the connecting area between the supporting beam and the central beam. Ideally, the supporting beams should connect only to the central beam nodal points. The length of the supporting beams has been chosen so that when the central beam vibrates in its first mode, the supporting beams are in their second vibration mode.

Design dimensions are tabulated in Table. 7.4. The width of the electrodes is simply the maximum allowed by the previously defined design rules.

Table 7.4: Geometrical dimensions (in μm) of the designed beams. L_r and W_r are the length and the width of the resonator beam, respectively, while L_s and W_s are the length and the width of the supporting beams in the free-free design. W_e is the width of the resonators electrodes.

Frequency [MHz]	Clamped-clamped beam			Free-free beam				
	L_r	W_r	W_e	L_r	W_r	L_s	W_s	W_e
1	160	3	20	160	3	110	2	40
10	50	3	20	100	12	35	2	15

7.4 Conclusions

The combined process flow presented in this chapter enables the simultaneous fabrication of micro-mechanical switches and microresonators, on an SOI substrate. The process has been developed out of two already existing processes for the separate fabrication of resonators and switches. Temperature compatibility issues have been solved by the careful choice of the sequence of the process steps. A new technique for the deposition of a planar spin-coated photoresist layer on a high topography surface has been developed in order to address topography issues.

The interlaced fabrication of the resonators and switches does not require the introduction of extra process steps for protection purposes. Instead, it allows to share of masks and process steps. The defined process flow conserves therefore the cost and complexity of the starting processes. Moreover, it offers a great design freedom and flexibility.

Clamped-clamped and free-free beam resonators have been designed. The resonators have been used to create a first prototype of a duplexer with channel selection, where switches allow separate addressing of two resonators.

Fabrication of the devices is still in progress. Currently, the wafers are ready for the DRIE silicon etch (step 14 in Table 7.3). After completion of the devices, the process design rules will be defined.

Chapter 8

Conclusions

In this thesis, a new approach has been developed for compact modelling of microelectromechanical resonators and switches for radio-frequency applications. The approach is based on the application of mathematical model order reduction to the finite element model of the device, generated with the commercial software ANSYS. Depending on the properties of the devices to model and the analysis of interest, different procedures have been developed for the derivation of linear or nonlinear device models. The extraction of such models makes use of the tool MOR for ANSYS, which has been adapted for application to the electromechanical problems under study. The mathematical basis of this technique enables a quasi-automatic derivation of the reduced models. The compact modelling approach has been applied for the extraction of reduced order models for various types of resonators, filters and switches. These models have been used for simulation both at device and circuit level and their accuracy has been verified by comparison with full-model simulation results and, when available, with experimental data. The reduced models enable a substantial speed-up of the simulation time, especially for nonlinear analysis, while maintaining an excellent modelling accuracy.

At present, the employed technique does not allow the extraction of parametric models. However, since the extraction of the reduced models is very fast, they can still be used for design optimization both at devices and circuit level. Moreover, new methods for parametric model order reduction are currently under development.

The second part of the thesis presents the definition of a new process flow for the combined fabrication of microresonators and microswitches on an SOI substrate. The process has been defined on the basis of previously developed processes that have been optimized for either resonators or switches fabrication. The combination of these processes presents some temperature and topography issues, which have been addressed. The new process flow maintains all the features of the original processes and allows therefore the simultaneous fabrication of microresonators and switches on a same substrate, without degradation of their performance. In addition, also costs and complexity are essentially maintained.

A set of masks has been designed, for the fabrication of clamped-clamped beam and free-free

beam lateral resonators with two different values for the resonance frequency (1MHz and 10MHz). The first process run, which is currently under fabrication, includes amongst other a prototype of a duplexer with integrated filters for channel selection.

Unexpected fabrication issues and limitations on the performances of the devices of the combined process flow will be further investigated at the end of the fabrication run. A second run could include micromechanical filters as well as different type of resonators with higher resonance frequency. Moreover, the possibility of combined resonator-switch fabrication could be maximally exploit for the implementation of a switched filter bank. The successful implementation of such a complex structure is only feasible with the availability of efficient compact modelling tools, such as the one defined and implemented in this thesis.

Publications

L. Del Tin, R. Gaddi, E. B. Rudnyi, A. Gnudi, A. Greiner, J. G. Korvink, "*Compact modeling of RF-MEMS resonators by means of model order reduction*", submitted to IEEE/ASME Journal of Microelectromechanical Systems.

L. Del Tin, R. Gaddi, E. B. Rudnyi, A. Gnudi, A. Greiner, J. G. Korvink, "*Non linear compact modeling of RF-MEMS switches by means of model order reduction*", accepted at The 14th International Conference on Solid-State Sensors, Actuators and Microsystems (Transducer'07), 10-14 June, Lyon (France).

L. Del Tin, R. Gaddi, E. B. Rudnyi, A. Greiner, J. G. Korvink, "*Model Order Reduction for the Extraction of Small Signal Equivalent Circuit Models of RF-MEMS*", Proceedings SCEE 2006, Scientific Computing in Electrical Engineering, Sinaia - Romania, 17-22 September 2006.

L. Del Tin, R. Gaddi, A. Gnudi, E. B. Rudnyi, A. Greiner, J. G. Korvink, "*Efficient pre-stressed harmonic analysis of RF-microresonators by means of model order reduction.*", Thermal, Mechanical and Multiphysics Simulation and Experiments in Micro-Electronics and Micro-Systems, Proceedings of EuroSimE 2006, Como (Milano), Italy, 24-26 April, p. 226-229, 2006.

Kamaljit Rangra, Benno Margesin, Leandro Lorenzelli, Flavio Giacomozzi, Cristian Collini, Mario Zen, Giovanni Soncini, Laura del Tin and Roberto Gaddi, "*Symmetric toggle switch a new type of rf MEMS switch for telecommunication applications: Design and fabrication*", SENSORS AND ACTUATORS A: PHYSICAL, vol.123-124, Issue C.

J. Iannacci, L. Del Tin, M. Bellei, R. Gaddi, A. Gnudi B. Margesin and F. Giacomozzi, "*Radiofrequency Transient Behaviour of Ohmic RF-MEMS Switches*", 10th Italian Conference Sensors and Microsystems (AISEM 2005), Firenze, IT, 15-17 February 2005.

J. Iannacci, L. Del Tin, R. Gaddi, A. Gnudi and K. J. Rangra, "*Compact Modeling of a MEMS Toggle-Switch based on Modified Nodal Analysis*", Symposium on Design, Test, Integration and Packaging of MEMS/MOEMS (DTIP) 2005, Montreux, Switzerland, 01-03 June 2005.

Acknowledgments

I would like to spend the last words of this thesis to thank all the people that, in different ways, rendered this work possible. First of all, I would like to thank Prof. Giorgio Baccarani, who gave me the possibility to start this interesting work at ARCES and to continue it abroad.

Then, I would like to thank Prof. Jan G. Korvink for giving me the opportunity to work in his group at IMTEK.

I also wish to thank Prof. Antonio Gnudi and Dr. Andreas Greiner for their valuable advises and support.

I am grateful to my direct supervisor Dr. Roberto Gaddi, who has introduced me to RF MEMS and has constantly followed and directed my progress during the last three years.

I owe all I know about model order reduction to Dr. Evgenii B. Rudnyi, who patiently supervised my modelling work at IMTEK. Without his help and encouragement I would have not get so far. Several people helped me during the definition and implementation of the first italian-german process run. I would like to thank Dr. Flavio Giacomozzi and Dr. Benno Margesin from ITC-IRST (Trento) and Dr. Patrick Ruther from IMTEK for supporting the project and for their great help in the definition of fabrication details. I also thank Gunter Igel, for his very good advise in fabrication matters, and the technicians of the IMTEK cleanroom that are taking care of my wafers.

I enjoyed very much the collaboration with all these people and I learned a lot from them.

I am grateful to all the people who helped to correct and improve the contents of this thesis and to the committee who took the time to read it.

During my PhD, I had the fortune to be part of nice and cooperative research groups, which always rendered the daily work relaxed and enjoyable, both in Bologna and Freiburg. I wish therefore to thank all the present and the past members of the IMTEK Simulation group. A special thank goes to the secretaries that patiently helped me to fill up all the administrative papers in German.

Un grande ringraziamento va a tutti coloro che, negli ultimi tre anni, hanno lavorato nel laboratorio Ex 3.2. della facoltà di Ingegneria di Bologna. In particolare, vorrei ringraziare Jacopo Iannacci, che ha condiviso con meventure e sventure di questo dottorato, il mio sardo preferito, Lupo, per la sua paziente opera di mediazione tra me e il computer, e Marco Bellei, per la breve ma intensa collaborazione.

Un ultimo ringraziamento, un po' speciale, va a Bologna, alma mater, non solo studiorum, per la calda accoglienza durante i miei anni di studio.

Bibliography

- [1] K. E. Petersen, "Silicon as a mechanical material," in *Proc. IEEE*, vol. 70, no. 5, 1982, pp. 420–457.
 - [2] E. J. J. Krugickl, B. A. warneke, and K. S. J. Pister, "CMOS 3-axis accelerometers with integrated amplifier," in *Pro. of IEEE MEMS Workshop*, 1998, pp. 631–636.
 - [3] E. Eleftheriou, T. Antonakopoulos, G. K. Binnig, G. Cherubini, M. Despont, A. Dholakia, U. Dürig, M. A. Lantz, H. Pozidi, H. E. Rothuizen, and P. Vettiger, "Millipede mems-based scanning-probe data-storage system," *IEEE TRANSACTIONS ON MAGNETICS*, 2003.
 - [4] C.-T. C. Nguyen, "Micromachining technology for miniaturized communication devices," in *Proc. of SPIE: Micromachining and Microfabrication*, 1998, pp. 24–38.
 - [5] ———, "Vibrating MEMS for next generation wireless applications," in *Proc. 2004 IEEE Custom integrated circuits Conf.*, 2004, pp. 257–264.
 - [6] G. M. Rebeiz, *RF MEMS: Theory, Design, and Technology*. John Wiley and Sons, 2002.
 - [7] C. T.-C. Nguyen, L. P. Katehi, and G. M. Rebeiz, "Micromachined devices for wireless communications," in *Proc. IEEE*, vol. 86, no. 8, pp. 1756–1768.
 - [8] B. Razavi, "Architectures and circuits for RF CMOS receiver," in *Proc. IEEE Custom Integrated Circuit Conference*, 1998, pp. 393–400.
 - [9] L. N. Dworsky, "A comparison of band pass filter technologies for communications system applications," in *Proc. IEEE Ultrasonics Symposium*, 1991, pp. 241–250.
 - [10] I. C. Hunter, L. Billonet, B. Jarry, and P. Guillon, "Microwave filters-Application and Technology," *IEEE Transaction on Microwave Theory and Techniques*, vol. 50, no. 3, pp. 794–805, 2002.
 - [11] A. Coon, "Saw filters and competitive technologies: a comparative review," in *Proc. IEEE Ultrasonics Symposium*, 1991, pp. 155–160.
 - [12] K. M. Lakin, "A review of thin-film resonator technology," *IEEE Microwave Magazine*, pp. 61–67, 2003.
-

- [13] R. Weigel, D. O. Morgan, J. M. Owens, A. Ballato, K. M. Lakin, K. Hashimoto, and C. C. W. Ruppel, "Microwave acoustic materials, devices and applications," *IEEE Transaction on Microwave Theory and Techniques*, vol. 50, no. 3, pp. 738–749, 2002.
- [14] S. J. Fiedziuszko, I. C. Hunter, T. Itoh, Y. Kobayashi, T. Nishikawa, S. N. Stitzer, and K. Wakino, "Dielectric materials, devices and circuits," *IEEE Transaction on Microwave Theory and Techniques*, vol. 50, no. 3, pp. 706–718, 2002.
- [15] R. R. Mansour, "Filter technologies for wireless base stations," *IEEE Microwave magazine*, pp. 68–74, 2004.
- [16] C.-T. C. Nguyen, "Transceiver front-end architectures using vibrating micromechanical signal processors," in *Digest of Papers. Silicon Monolithic Integrated Circuits in RF Systems*, 2001, pp. 23–32.
- [17] "RF MEMS market 2005-2009: Analysis, Forecasts and Technology Review," Wicht Consulting Technology, 2005.
- [18] C. T.-C. Nguyen, "Vibrating rf mems overview: applications to wireless communications."
- [19] C.-C. Lo, F. Chen, and G. Fedder, "Integrated HF CMOS-MEMS square-frame resonators with on-chip electronics and electrothermal narrow gap mechanism," in *Digest of Technical Papers, The 13th International Conference on Solid-State Sensors Actuators and Microsystems (Transducers '05)*, 2005, pp. 2074 – 2077.
- [20] G. Fedder, "CMOS-MEMS resonant mixer-filters," in *Technical Digest. IEEE International Electron Devices Meeting (IEDM)*, 2005, pp. 274 – 277.
- [21] H.-M. Hsu, C.-L. Dai, M.-M. Hsieh, M.-C. Tsai, and H.-J. Peng, "Implementation and analysis of microwave switch in CMOS-MEMS technology," in *Proceedings 2006 IEEE International Symposium on Circuits and Systems (ISCAS)*, 2006.
- [22] F. Tejada and A. G. Andreou, "Microelectromechanical systems in 3D SOI-CMOS: sensing electronics embedded in mechanical structures," in *Proceedings IEEE International Symposium on Circuits and Systems (ISCAS 2006)*, 2006.
- [23] S. Ghosh and M. Bayoumi, "An integrated CMOS-MEMS system-on-chip," in *Proc. IEEE 3rd International NEWCAS Conference*, 2005, pp. 31 – 34.
- [24] A. Uranga, J. Teva, J. Verd, J. L. Lopez, F. Torres, J. Esteve, G. Abadal, F. Perez-Murano, and N. Barniol, "Fully CMOS integrated low voltage 100 MHz MEMS resonator," *Electronics Letters*, vol. 41, no. 24, pp. 1327 – 1328, 2005.
- [25] A. Oz and G. K. Fedder, "CMOS-compatible RF-MEMS tunable capacitors," in *IEEE Radio Frequency Integrated Circuits (RFIC) Symposium 2003*.
-

- [26] J.-B. Yoon, Y.-S. Choi, B.-I. Kim, Y. Eo, and E. Yoon, "CMOS-compatible surface-micromachined suspended-spiral inductors for multi-GHz silicon RF ICs," *IEEE Electron Device Letters*, vol. 23, no. 10, pp. 591–593, 2002.
- [27] K. Persson and K. Boustedt, "Fundamental requirements on mems packaging and reliability," in *Proc. 2002 8th International Symposium on Advanced Packaging Materials*, 2002, pp. 1–7.
- [28] S. D. Senturia, "CAD challenges for microsensors, microactuators and microsystem," in *Proc. of IEEE*, vol. 86, no. 2, 1998, pp. 1611–1626.
- [29] A. C. Antoulas, *Approximation of Large-Scale Dynamical Systems*. Society for Industrial and Applied Mathematics, 2005.
- [30] T. Bechtold, "Model order reduction of electro-thermal MEMS," Ph.D. dissertation, Albert-Ludwigs Universität Freiburg im Breisgau, 2005.
- [31] J. Lienemann, "Complexity reduction techniques for advanced mems actuators simulation," Ph.D. dissertation, Albert-Ludwigs Universität Freiburg im Breisgau, 2006.
- [32] Z. Bai, "Krylov subspace techniques for reduced-order modeling of large-scale dynamical systems," *Applied Numerical Mathematics*, vol. 43, pp. 9–44, 2002.
- [33] P. S. Beran, D. J. Lucia, and W. A. Silva, "Reduced-order modeling: new approaches for computational physics," *Prog. Aerosp. Sci.*, vol. 40, no. 1/2, pp. 51–117, 2004.
- [34] E. B. Rudnyi and J. G. Korvink, *Review: Automatic model reduction for transient simulation of mems-based devices*. Wiley-VCH, 2002, vol. 11, ch. 1, pp. 3–33.
- [35] R. Gaddi, M. Bellei, A. Gnudi, B. Margesin, and F. Giacomozzi, "Interdigitated low-loss ohmic RF-MEMS switches," in *Proceedings of NSTI 2004 Nanotechnology Conference and Trade Show, Nanotech 2004*, vol. 2, 2004, pp. 327–330.
- [36] P. Ruther, J. Bartholomeyczik, A. Buhmann, A. Trautmann, K. Steffen, and O. Paul, "Micro-mechanical HF resonators fabricated using a novel SOI-based low-temperature process," *IEEE Sensors J.*, vol. 5, no. 5, pp. 1112–1119, 2005.
- [37] S. D. Senturia, *Microsystem design*. Kluwer, Boston, 2001.
- [38] M. W. Putty, S. C. Chang, R. T. Howe, A. L. Robinson, and K. D. Wise, "One-Port active polysilicon resonant microstructures," 1989, pp. 60–65.
- [39] R.T.Howe and R.S.Muller, "Resonant-microbridge vapor sensor," *IEEE Transaction on Electron Devices*, vol. 33, no. 4, 1986.
- [40] J. van Beek, P. S. and G.J.A.M. Verheijden and J.W. Weekamp, A. den Dekker, M. Giesen, A. de Graauw, J. Koning, F. Theunis, P. van der Wel, B. van Velzen, and P. Wessels, "MEMS
-

- for wireless communication: application, technology, opportunities and issues," in *Proc. IEEE MEMSwave 2006*, 2006.
- [41] V. Kaajakari, "(electrical) equivalent circuits for mems," www.kaajakari.net/ville/.
- [42] S. P. Timoshenko and J. N. Goodier, *Theory of elasticity*, 3rd ed. McGraw-Hill, 1987.
- [43] W. Weaver and S. P. Timoshenko, *Vibration problems in engineering*. Wiley Interscience, 1990.
- [44] R. Johnson, *Mechanical Filters in Electronics*. John Wiley and Sons, 1983.
- [45] H. A. C. Tilmans, D. J. Iitema, and J. H. J. Fluitman, "Single element excitation and detection of (micro-)mechanical resonators," in *Digest of Technical Papers, IEEE Int. Conf. on Solid-State Sensors and Actuators (Transducers'91)*, 1991, pp. 533–537.
- [46] C. T.-C. Nguyen, Ph.D. dissertation, University of Berkely.
- [47] F. D. Bannon, J. R. Clark, and C. C.-T. Nguyen, "High-Q HF microelectromechanical filters," *IEEE J. of Solid-State Circuits*, vol. 35, no. 4, pp. 512–526, 2000.
- [48] V. Kaajakari, "Nonlinearity in micromechanical resonators," www.kaajakari.net/ville/.
- [49] C. T.-C. Nguyen and R. T. Howe, "An integrated CMOS micromechanical resonator high-q oscillator," *IEEE J. Solid-State Circuits*, vol. 34, no. 4, pp. 440–455, April 1999.
- [50] W. T. Hsu, J. R. Clark, and C. T. C. Nguyen, "Q-optimized lateral free-free beam micromechanical resonators," in *Digest of Technical Papers, the 11th IEEE Int. Conf. on Solid-State Sensors and Actuators and Microsystem (Transducers'01)*, 2001, pp. 1110–1113.
- [51] C.-T. C. Nguyen, <http://www.eecs.berkeley.edu/ctnguyen/index.htm>.
- [52] P. Ruther, J. Bartholomeyczik, A. Buhmann, and O. Paul, "Characterization of microelectromechanical HF resonators fabricated using SOI-based low temperature process," in *Proc. IEEE Sensors 2003*, 2003, pp. 820–824.
- [53] Z. Hao, S. Pourkamali, and F. Ayazi, "VHF single-crystal silicon elliptic bulk-mode capacitive disk resonators-part ii: fabrication and characterization," *IEEE J. Microelectromech. S.*, vol. 13, no. 6, pp. 1054–1062, 2004.
- [54] K. B. Lee, S. Ryder, and L. Lin, "Design and fabrication of an annular high frequency resonator," in *Proceedings of IMECE02 2002 ASME International Mechanical Engineering Congress & Exposition*, 2002.
- [55] T. Mattila, J. Kiihamäki, T. Lamminmäki, O. Jaakkola, P. Rantakari, A. Oja, H. Seppä, H. Kattelus, and I. Tittonen, "A 12MHz micromechanical bulk acoustic mode oscillator," *Sensors and Actuators A*, vol. 101, no. 1, pp. 1–9, 2002.
-

- [56] V. Kaajakari, T. Mattila, A. Oja, J. Kiihamäki, and H. Seppä, "Square-extensional mode single-crystal silicon micromechanical resonator for low-phase-noise oscillator applications," *IEEE Electron Device Letters*, vol. 25, no. 4, pp. 173–176, April 2004.
- [57] A. H. Nayfeh and M. I. Younis, "A new approach to the modeling and simulation of flexible microstructures under the effect of squeeze-film damping," *J. Micromech. Microeng.*, vol. 14, pp. 170–181, 2004.
- [58] B. L. Foulgoc, T. Bourouina, O. L. Traon, A. Bosseboeuf, F. Marty, C. Breuzeau, J.-P. Grandchamp, and S. Masson, "Highly decoupled single-crystal silicon resonators: an approach for the intrinsic quality factor," *J. Micromech. Microeng.*, vol. 16, pp. 45–53, 2006.
- [59] C. Zener, "Internal friction in solid II. general theory of thermoelastic internal friction," *Physical Review*, vol. 53, pp. 90–99, August 1939.
- [60] R. Lifshitz and M. L. Roukes, "Thermoelastic damping in micro- and nanomechanical systems," *Physical Review B*, vol. 61, no. 8, pp. 5600–5609, February 2000.
- [61] Y. Jimbo and K. Itao, "Energy loss of a cantilever vibrator," *J. Horological Inst, Jpn.*, vol. 47, pp. 1–15, 1968.
- [62] Y.-H. Park and K. D. Park, "High-fidelity modeling of MEMS resonators-part I: Anchor loss mechanisms through substrate," *IEEE J. Microelectromech. S.*, vol. 13, no. 2, pp. 238–247, 2004.
- [63] ———, "High-fidelity modeling of MEMS resonators-part II: Coupled beam-substrate dynamics and validation," *IEEE J. Microelectromech. S.*, vol. 13, no. 2, pp. 238–247, 2004.
- [64] W. S. Griffin, H. H. Richardson, and S. Yamanami, "A study of squeeze-film damping," *J. Basic Engineering*, pp. 451–455, 1966.
- [65] J. Blech, "On isothermal squeeze films," *J. Lubrification technology*, 1983.
- [66] T. Veijola, H. Kuisma, J. Lahdenperä, and T. Ryhänen, "Equivalent-circuit model of the squeezed gas film in a silicon accelerometer," in *Sensors and Actuators A*, vol. 48, 1995, pp. 239–248.
- [67] T. Veijola, "Compact models for squeezed-film dampers with inertial effects," in *Proc. of DTIP*, 2004, pp. 365–369.
- [68] T. Veijola, A. Pursula, and P. Råback, "Extending the validity of existing squeezed-film damper models with elongations of surface dimensions," in *Proc. of Nanotech 2004*, March 7–11 2004, pp. 235–238.
- [69] T. Veijola, T. Tintunen, H. Nieminen, V. Ermolov, and T. Ryhänen, "Gas damping models for a RF MEMS switch and its dynamic characterization," in *Proc. of IEEE MTT-S Digest*, 2004, pp. 1213–1216.
-

- [70] V. Kaajakari, "RF-MEMS based resonators, filters and oscillators," 2005, MEMS in RF and microwave electronics short course, IMEC.
- [71] M. Koskenvuori, T. Mattila, A. Häärä, J. Kiihamäki, I. Tittonen, A. Oja, and H. Seppä, "Long-term stability of single-crystal silicon microresonators," *Sensors and Actuators A*, vol. 115, pp. 23–27, 2004.
- [72] W.-T. Hsu and C. T.-C. Nguyen, "Geometric stress compensation for enhanced thermal stability in micromechanical resonators," in *Proceedings, 1998 IEEE International Ultrasonics Symposium*, 1998, pp. 945–948.
- [73] —, "Stiffness-compensated temperature-insensitive micromechanical resonators," in *Proc. IEEE International Conference on Micro Electro Mechanical Systems (MEMS'02)*, 2002, pp. 731–734.
- [74] W.-T. H. J. R. Clark and C. T.-C. Nguyen, "Mechanically temperature compensated flexural-mode micromechanical resonators," in *IEEE Int. Electron Device Meeting*, 2000, pp. 493–449.
- [75] S. A. Bhave and R. T. Howe, "Internal electrostatic transduction for bulk-mode MEMS resonators," in *Solid-State Sensor, Actuator, and Microsystems Workshop*, 2004, pp. 59–60.
- [76] —, "Silicon nitride-on-silicon bar resonator using internal electrostatic transduction," *Digest of Technical Papers. The IEEE 13th International Conference on Solid-State Sensors, Actuators and Microsystems (Transducers'05)*, vol. 2, pp. 2139–2142, 2005.
- [77] V. Kaajakari, A. T. Alastalo, and T. Mattila, "Electrostatic transducers for micromechanical resonators: free space and solid dielectric," *IEEE Transactions on Ultrasonics, Ferroelectrics and Frequency Control*, vol. 53, no. 12, pp. 2484 – 2489, 2006.
- [78] M. Demirci and C. T.-C. Nguyen, "Mechanically corner-coupled square microresonator array for reduced series motional resistance," *IEEE J. Microelectromech. Syst.*, vol. 15, no. 6, pp. 1419–1436, Dec 2006.
- [79] S. Lee and C. T.-C. Nguyen, "Mechanically-coupled micromechanical arrays for improved phase noise," in *Proceedings, IEEE Int. Ultrasonics, Ferroelectrics, and Frequency Control 50th Anniv. Joint Conf.*, 2004, pp. 280–286.
- [80] T. Mattila, O. Jaakkola, J. Kiihamäki, J. Karttunen, T. Lamminmäki, P. Rantakari, A. Oja, H. Seppä, H. Kattelus, and I. Tittonen, "14 MHz micromechanical oscillator," *Sensors and Actuators A*, vol. 97-98, pp. 497–502, 2002.
- [81] K. Wang, A.-C. Wong, and C. C.-T. Nguyen, "VHF free-free beam high-q micromechanical resonators," *IEEE J. Microelectromech. S.*, vol. 9, no. 3, pp. 347–360, 2000.
- [82] S. Pourkamali, G. K. Ho, and F. Ayazi, "Vertical capacitive SiBARs," in *Proc. IEEE 18th International Conference on Micro Electro Mechanical Systems (MEMS'05)*, 2005, pp. 211–214.
-

- [83] G. K. Ho, K. Sundaresan, S. Pourkamali, and F. Ayazi, "Low motional impedance highly-tunable i^2 resonators for temperature-compensated reference oscillators," in *Proc. IEEE 18th International Conference on Micro Electro Mechanical Systems (MEMS'05)*, 2005, pp. 116–120.
- [84] V. Kaajakari, T. Mattila, A. Oja, J. Kiihamäki, H. Kattelus, M. Koskenvuori, P. Rantakari, I. Tittonen, and H. Seppä, "Square-extensional mode single-crystal silicon micromechanical RF resonator," in *Digest of Technical Papers, IEEE Int. Conf. on Solid-State Sensors Actuators and Microsystems (Transducers'03)*, 2003, pp. 951–954.
- [85] J. Wang, Z. Ren, and C. C.-T. Nguyen, "1.156ghz self-aligned vibrating micromechanical disk resonator," *IEEE Transaction on Ultrasonic, Ferroelectrics and Frequency Control*, vol. 51, no. 12, pp. 1607–1627, 2004.
- [86] S.-S. Li, Y.-W. Lin, Y. Xie, Z. Ren, and C. T.-C. Nguyen, "Micromechanical hollow-disk ring resonators," in *Proc. IEEE International Conference on Micro Electro Mechanical Systems (MEMS'04)*, 2004, pp. 821–824.
- [87] Y. Xie, S.-S. Lin, Z. Ren, and C. T.-C. Nguyen, "UHF micromechanical extensional wine-glass mode ring resonators," in *Proc. IEEE International Electron Device Meeting*, 2003, pp. 953–956.
- [88] Y.-W. Lin, S. Lee, S.-S.-Li, Y. Xie, Z. Ren, and C. T.-C. Nguyen, "Series-resonant VHF micromechanical resonator reference oscillator," *IEEE J. Solid-State Circuits*, vol. 39, no. 12, pp. 2477–2491, December 2004.
- [89] F. Ayazi, "High-frequency integrated microelectromechanical resonators and filters," in *Advanced Micro and Nanosystems*. Wiley-VCH Verlag, 2004, vol. 1, pp. 165–192.
- [90] S. Pourkamali and F. Ayazi, "Electrically coupled MEMS bandpass filters-part I: with coupling element," *Sensors and Actuators A*, vol. 122, pp. 306–317, 2005.
- [91] —, "Electrically coupled MEMS bandpass filters-part II: without coupling element," *Sensors and Actuators A*, vol. 122, pp. 317–325, 2005.
- [92] M. U. Demirci, M. A. Abdelmoneum, and C. T.-C. Nguyen, "Mechanically corner-coupled square microresonator array for reduced series motional resistance," in *Dig. of Tech. Papers, the 12th Int. Conf. on Solid-State Sensors & Actuators*, 2003, pp. 955–958.
- [93] A.-C. Wong and C. T.-C. Nguyen, "Micromechanical mixer-filters (mixlers)," *IEEE J. Microelectromech. S.*, vol. 13, no. 1, pp. 100–112, 2004.
- [94] W.-T. Hsu, J. R. Clark, and C. C.-T. Nguyen, "A sub-micron capacitive gap process for multiple-metal-electrode lateral micromechanical resonators," 2001, pp. 349–352.
- [95] J. W. Weigold, A.-C. Wong, C. T. C. Nguyen, and S. W. Pang, "A merged process for thick single-crystal Si resonators and biCMOS circuitry," *IEEE J. Microelectromech. S.*, vol. 8, no. 3, pp. 221–228, 1999.
-

- [96] W. Zhang, W. Zhang, K. Turner, and P. G. Hartwell, "Scream'03: A single mask process for high-q single crystal silicon MEMS," in *Proceedings of IMECE04 2004 ASME International Mechanical Engineering Congress and Exposition*, 2004.
- [97] Z. L. Zhang and N. C. MacDonald, "A rie process for submicron, silicon electromechanical structures," *J. Micromech. Microeng.*, vol. 2, 1992.
- [98] E. Quevy, B. Legrand, D. Collard, and L. Buchailot, "Ultimate technology for micromachining of nanometric gap HF micromechanical resonators," in *Proc. IEEE International Conference on Micro Electro Mechanical Systems (MEMS'03)*, 2003, pp. 157–160.
- [99] X. W. Wang, R. M. Lin, Z. Wang, and W. J. Wang, "Development of micromechanical resonators using a new process flow based upon SOI technology," *J. Micromech. Microeng.*, vol. 15, pp. 57–63, 2005.
- [100] F. Ayazi and K. Najafi, "High aspect-ratio combined poly and single-crystal silicon (HARPSS) MEMS technology," *J. Microelectromech. S.*, vol. 9, no. 3, pp. 288–294, 2000.
- [101] S. Pourkamali, A. Hashimura, R. Abdolvand, G. K. Ho, A. Erbil, and F. Ayazi, "High-q single crystal silicon harpss capacitive beam resonators with self-aligned sub-100-nm transduction gaps," *IEEE Journal of Microelectromech. S.*, vol. 12, no. 4, pp. 487–496, 2003.
- [102] S. Pourkamali and F. Ayazi, "Fully single crystal silicon resonators with deep-submicron dry-etched transducer gaps," in *Proc. IEEE International Conference on Micro Elctro Mechanical Systems (MEMS'04)*, 2004, pp. 813–816.
- [103] G. Rebeiz and J. B. Muldavin, "RF MEMS switches and switch circuits," *IEEE Microwave Magazine*, pp. 59–71, December 2001.
- [104] K. E. Petersen, "Micromechanical membrane switches on silicon," *JBM Journal of Research and Development*, vol. 23, pp. 376–385, 1971.
- [105] J. J. Yao, "RF MEMS from a device perspective," *J. Micromech. Microeng.*, vol. 10, pp. R9–R38, 2000.
- [106] H. A. C. Tilmans, "Switches," <http://www.amicom.info/OpenPlatform/index.php/Switches>.
- [107] S. Majumder, J. Lampen, R. Morrison, and J. Maciel, "MEMS switches," *IEEE Instrumentation & Measurement Magazine*, vol. 6, no. 1, pp. 12–15, 2003.
- [108] E. R. Brown, "RF-MEMS switches for reconfigurable integrated circuits," *IEEE Transactions on Microwave Theory and Techniques*, vol. 46, no. 11, pp. 1868–1880, 1998.
- [109] J. B. Muldavin and G. Rebeiz, "Nonlinear electro-mechanical modeling of MEMS switches," in *Digest IEEE MTT-S*, 2001, pp. 2119–2122.
- [110] V. Rochus, "Finite element modeling of strong electromechanical coupling in MEMS," Ph.D. dissertation, University of Liege, 2007.
-

- [111] I. Shiele and B. Hillerich, "Comparison of lateral and vertical switches for application as microrelays." *J. Micromech. Microeng.*, vol. 9, pp. 146–150, 1999.
- [112] C. L. Goldsmith, Z. Yao, S. Eshelman, and D. Denniston, "Performance of low-loss RF MEMS capacitive switches," *IEEE Microwave and Guided Wave Letters*, vol. 8, no. 8, pp. 269 – 271, Aug. 1998.
- [113] Tyndall National Institute, <http://www.tyndall.ie/research/microtechnologies/index.html>.
- [114] B. Scauwecker, K. M. Strohm, W. Simon, J. Mehner, and J.-F. Luy, "Toggle-switch-a new type of RF MEMS switch for power applications," in *IEEE MTT-S. Digest*, 2002, pp. 219–222.
- [115] J. Drake, H. Jerman, B. Lutze, and M. Stuber, "An electrostatically actuated micro-relay," in *Digest of Technical Papers. The IEEE 8th International Conference on Solid-State Sensors and Actuators (Transducers'95)*, 1995, pp. 380–383.
- [116] M. Sakata, Y. Komura, T. Seki, K. Kobayashi, K. Sano, and S. Horiike, "Micromachined relay which utilizes single crystal silicon electrostatic actuator," in *Proc. IEEE International Conference on Micro Electro Mechanical Systems (MEMS'99)*, 1999, pp. 21–24.
- [117] V. G. Kutchoukov, J. R. Mollinger, and A. Bossche, "New photoresist coating method for 3d structured wafers," *Sensors and Actuators A*, vol. 85, pp. 377–383, 2000.
- [118] P. Nga, J. N. Burghartz, and P. M. Sarro, "Spray coating of photoresist for patter transfer on high topography surfaces," *J. Micromech. Microeng.*, vol. 15, pp. 691–697, 2005.
- [119] C. V. Jahnes, J. Cotte, J. L. Lund, H. Deligianni, A. Chinthakindi, L. P. Buchwalter, P. Fryer, J. A. Trnello, N. Hoivik, J. H. Magerlein, and D. Seeger, "Simultaneous fabrication of RF MEMS switches and resonators using copper-based CMOS interconnect manufacturing methods." in *Proc. IEEE International Conference on Micro Electro Mechanical Systems (MEMS'04)*, 2004, pp. 789–792.
- [120] P. C. Andricacos, "Damascene copper electroplating for chip interconnects," *IBM Journal of Research and Development*, vol. 42, no. 5, pp. 567–574, 1998.
- [121] S. D. Senturia, R. M. Harris, B. P. Johnson, S. Kim, K. Nabors, and M. A. S. J. K. White, "A computer-aided design system for microelectromechanical systems (MEMSCAD)," *IEEE J. Microelectromech. S.*, vol. 1, no. 1, pp. 3–13, 1992.
- [122] ANSYS Inc. *Theory Reference Manual*.
- [123] A. Quarteroni, *Modellistica numerica per problemi differenziali*. Springer Verlag, 2003.
- [124] J. White, S. D. Senturia, and N. Aluru, "Simulating the behaviour of MEMS devices: computational methods and needs." *IEEE Computational Science and Engineering*, 1997.
- [125] O. Zienkiewicz, C. Emson, and P. Bettes, "A novel boundary infinite element," *International Journal for Numerical methods in Engineering*, vol. 19, pp. 393–404, 1983.
-

- [126] S. Wuensche, C. Clauss, P. Schwarz, and F. Winkler, "Microsystem design using simulator coupling," in *Proc. European Design and Test Conf.*, 1997, pp. 113–119.
- [127] G. Li and N. R. Aluru, "A lagrangian approach for electrostatic analysis of deformable conductors," *IEEE J. Microelectromech. S.*, vol. 11, no. 3, pp. 245–254, June 2002.
- [128] N. R. Aluru and J. White, "An efficient numerical technique for electromechanical simulation of complicated microelectromechanical structures," *Sensors and Actuators A*, vol. 58, pp. 1–11, 1997.
- [129] V. Rochus, D. J. Rixen, and J. C. Golinval, "Monolithic modelling of electro-mechanical coupling in micro-structures," *Int. J. for Num. Meth. in Eng.*, vol. 65, no. 4, pp. 461–93, 2006.
- [130] K. Sudipto and N. R. Aluru, "Full-lagrangian schemes for dynamic analysis of electrostatic MEMS," *IEEE J. Microelectromech. S.*, vol. 13, no. 5, pp. 737–758, 2004.
- [131] N. R. Aluru and J. White, "A multilevel newton method for mixed-energy domain simulation of MEMS," *IEEE J. Microelectromech. S.*, vol. 8, no. 3, pp. 299–308, 1999.
- [132] S. Przemieniecki, *Theory of Matrix Structural Analysis*. New York: McGraw-Hill, 1968.
- [133] G. Lorenz, A. Morris, and I. Lakkis, "A top-down design flow for MOEMS," in *Proc. Design, Test, Integration, and Pachaging of MEMS/MOEMS (DTIP'01)*, 2001.
- [134] Z. Bai, D. Bindel, J. Clark, J. Demmel, K. S. J. Pister, and N. Zhou, "New numerical techniques and tools in sugar for 3d MEMS simulation," in *Proc. Int. Conf. on Modeling and Simulation of Mycrosystems (MSM'01)*, 2001, pp. 31–34.
- [135] M. H. Zaman, S. F. Bart, and J. R. Gilbert, "An environment for design and modeling of electromechanical micro-system," *J. Modeling and Simulation of Microsystem*, vol. 1, no. 1, pp. 65–67, 1999.
- [136] G. Schrag and G. Wachutka, "Physically based modeling of squeeze film damping by mixed-level system simulation," *Sensors and Actuators A*, vol. 97-98, pp. 193–200, 2002.
- [137] H. A. C. Tilmans, "Equivalent circuit representation of electromechanical transducers: I. lumped-parameter systems," *J. Micromech. Microeng.*, vol. 6, pp. 157–176, 1996.
- [138] T. Veijola, H. Kuisma, and J. Lahdenperä, "Dynamic modelling and simulation of microelectromechanical devices with a circuit simulation program," in *Proc. Int. Conf. on Modeling and Simulation of Mycrosystems (MSM)'98*, 1998, pp. 245–50.
- [139] V. Kaajakari, T. Mattila, A. Oja, J. Kiihamäki, and H. Kattelus, "Square-extensional mode single-crystal silicon micromechanical RF-resonator." in *Digest of Technical Papers, IEEE Int. Conf. on Solid-State Sensors Actuators and Microsystems (Transducers'03)*, 2003, pp. 951–54.
-

- [140] L. D. Gabbay, J. Mehner, and S. D. Senturia, "Computer-aided generation of nonlinear reduced-order dynamic macromodels-I non-stress-stiffened case," *IEEE J. Microelectromech. S.*, vol. 9, no. 2, pp. 262–269, 2000.
- [141] E. S. Hung and S. D. Senturia, "Generating efficient dynamical models for microelectromechanical system from a few finite-element simulation runs," *IEEE J. Microelectromech. S.*, vol. 8, no. 3, pp. 280–289, 1999.
- [142] Y. C. Liang, W. Z. Lin, S. P. Lim, K. H. Lee, and D. P. Feng, "A neural-network-based method of model reduction for the dynamic simulation of MEMS," *J. Micromech. Microeng.*, vol. 11, pp. 226–233, 2001.
- [143] W. Z. Lin, S. P. Lim, and Y. C. Liang, "Proper orthogonal decomposition and component mode synthesis in macromodel generation for the dynamic simulation of a complex MEMS device," *J. Micromech. Microeng.*, vol. 13, pp. 646–654, 2003.
- [144] L. D. Gabbay, J. Mehner, and S. D. Senturia, "Computer-aided generation of nonlinear reduced-order dynamic macromodels-II stress-stiffened case," *IEEE J. Microelectromech. S.*, vol. 9, no. 2, pp. 270–278, 2000.
- [145] M. Schlegel, F. Bennini, J. E. Mehner, G. Herrmann, D. Mueller, and W. Doetzel, "Analyzing and simulation of MEMS in VHDL-AMS based on reduced-order FE models," *IEEE Sensors J.*, vol. 5, no. 5, 2005.
- [146] Y.-J. Yang, M.-A. Gretillat, and S. D. Senturia, "Effect of air damping on the dynamics of nonuniform deformations of microstructures," in *Digest of Technical Papers, IEEE Int. Conf. on Solid-State Sensors Actuators and Microsystems (Transducers'97)*, 1997, pp. 1093–1096.
- [147] E. S. Hung, Y.-J. Yang, and S. D. Senturia, "Low-order models for fast dynamical simulation of MEMS microstructures," in *Digest of Technical Papers, IEEE Int. Conf. on Solid-State Sensors Actuators and Microsystems (Transducers'97)*, 1997, pp. 1101–1104.
- [148] M. I. Younis, E. M. Abdel-Rahman, and A. Nayfeh, "A reduced order model for electrically actuated microbeam-based MEMS," *IEEE J. Microelectromech. S.*, vol. 12, no. 5, pp. 672–680, 2003.
- [149] F. Wang and J. White, "Automatic model order reduction of a microdevice using the arnoldi approach," in *Proc. ASME International Mechanical Engineering Congress and Exposition*, 1998, pp. 527–530.
- [150] Y. Chen and J. White, "A quadratic method for nonlinear model order reduction," in *Proc. Int. Symp. Modeling and Simulation of Microsystem*, 2000.
- [151] J. Chen and S. M. Kang, "An algorithm for automatic model reduction of nonlinear MEMS devices," in *Proc. IEEE Int. Symp. Circuits and Syst.*, 2000, pp. 445–448.
-

-
- [152] M. Riewiński and J. White, "A trajectory piecewise linear approach to model order reduction and fast simulation of nonlinear circuits and micromachined devices," in *Proc. Int. Conf. on Computer-Aided-design*, 2001, pp. 252–257.
- [153] J. Chen, S. M. Kang, J. Zou, C. Liu, and J. E. Schutt-Ainé, "Reduced-order modeling of weakly nonlinear MEMS devices with Taylor-series expansion and Arnoldi approach," *IEEE J. Microelectromech. S.*, vol. 13, no. 3, pp. 441–451, 2002.
- [154] L. H. Feng, "Review of model order reduction methods for numerical simulation of nonlinear circuits," *Appl. Math. Comput.*, vol. 167, no. 1, pp. 576–591, 2005.
- [155] C. Zienkiewicz, *The finite element method*, 3rd ed. McGraw-Hill, 1977.
- [156] R. P. Feynman, R. B. Leighton, and M. Sands, *Lecture on physics: mainly electromagnetism and matter*. Addison-Wesley Publishing company, 1964.
- [157] D. K. Cheng, *Field and Wave electromagnetics*, 2nd ed. Addison-Wiley publishing Company, 1989.
- [158] V. Kaajakari, T. Mattila, J. Kiihamäki, A. Oja, H. Kattelus, and H. Seppä, "Nonlinearities in single-crystal silicon micromechanical resonators," in *Digest of Technical Papers, the Int. IEEE Conf. on Solid-State Sensors Actuators and Microsystem (Transducers'03)*, 2003, pp. 1574–1577.
- [159] M. G. M and G. Ostergaard, "Electro-mechanical transducer for MEMS analysis in Ansys," in *Proc. Int. Conf. on Modeling and Simulation of Microsystems (MSM)'99*, 1999, pp. 270–273.
- [160] I. Avdeev, "New formulation for finite element modeling electrostatically driven microelectromechanical systems," Ph.D. dissertation, University of Pittsburgh, 2003.
- [161] C. W. de Silva, *Vibration: fundamentals and practice*, 2000, ch. Modal Analysis.
- [162] M. E. Mehner, "Simulation of gas film damping on microstructures with nontrivial geometries," 1998.
- [163] B. Moore, "Principal component analysis in linear systems: controllability, observability and model reduction," *IEEE Transaction on Automatic Control*, vol. 26, no. 1, pp. 17–32, 1981.
- [164] B. N. Datta, *Numerical Methods for Linear Control systems*. Elsevier Incorporation, 2004.
- [165] A. Varga, "Enhanced modal approach for model order reduction," *Mathematical Modelling of Systems*, 1995.
- [166] Z. Bai, P. M. Dewilde, and R. W. Freund, "Reduced-order modeling," *Numerical Analysis*, vol. 02, pp. 1–59, 2002.
- [167] G. Obinata and B. D. O. Anderson, *Model Reduction for Control System Design*. Springer, 2004.
-

- [168] R. W. Freund, "Reduced-order modeling techniques based on krylov subspaces and their use in circuit simulation," *Numerical analysis Manuscript*, vol. 98-3-02, 1998.
- [169] —, "Krylov-subspace methods for reduced order modeling in circuit simulation," *Journal of Computational and Applied Mathematics*, vol. 123, no. 1-2, pp. 395–421, 2000.
- [170] J. R. Phillips, "Model reduction of time-varying linear systems using approximate multi-point krylov-subspace projectors," in *Proc. IEEE/ACM ICCAD*, 1998, p. 96102.
- [171] R. J. Guyan, "Reduction of stiffness and mass matrices," *AIAA journal*, vol. 3, no. 2, 1965.
- [172] B. Salimbahrami and B. Lohmann, "Order reduction of large scale second-order systems using krylov subspace methods," *Linear Algebra and its applications*, 2005.
- [173] T.-J. Su, J. Craig, and R. Roy, "Model reduction and control of flexible structures using krylov vectors," *J. Guidance*, vol. 14, no. 2, p. 260267, 1990.
- [174] R. W. Freund, *Dimension Reduction of Large-Scale Systems*, ser. LNCSE, 2005, vol. 45, ch. Pad-Type Model Reduction of Second-Order and Higher-Order Linear Dynamical Systems, p. 192223.
- [175] Z. J. Bai and Y. Su, "SOAR: A second-order arnoldi method for the solution of the quadratic eigenvalue problem," *SIAM J. Matrix Anal. A*, vol. 26, no. 3, p. 640659, 2005.
- [176] J. Chen, S.-M. Kang, J. Zou, C. Liu, and Schutt-Aine, "Reduced-order modeling of weakly nonlinear MEMS devices with taylor-series expansion and arnoldi approach," *IEEE J. Microelectromech. S.*, vol. 13, no. 3, pp. 441–451, 2004.
- [177] M. Rewienski and J. White, "A trajectory piecewise-linear approach to model order reduction and fast simulation of nonlinear circuits and micromachined devices," *IEEE T. Comput. Aid. D.*, vol. 22, p. 155170, 2003.
- [178] E. B. Rudnyi and J. G. Korvink, "Model order reduction for large scale engineering models developed in ansys." *Lect. Notes Comput. Sc.*, vol. 3732, pp. 349–356, 2006.
- [179] T. Bechtold, E. B. Rudnyi, and J. G. Korvink, "Error indicators for fully automatic extraction of heat-transfer macromodels for MEMS," *J. Micromech. Microeng.*, vol. 15, no. 3, pp. 430–440, 2005.
- [180] O. Rübönkonig and J. G. Korvink, "IMS, Imtek Mathematica Supplement," <http://www.imtek.uni-freiburg.de/simulation/mathematica/IMSweb/>.
- [181] S. A. Bhave, D. Gao, R. Maboudian, and R. T. Howe, "Fully-differential poly-SiC lamé mode resonator and checkerboard filter," in *Proc. 18th IEEE Micro Electro Mechanical Systems Conference (MEMS)'05*, 2005, pp. 223–226.
- [182] F. D. B. nad J. R. Clark and C. T.-C. Nguyen, "High frequency microelectromechanical IF filters," in *Proc. IEEE IEDM '96*, 1996, pp. 773–776.
-

-
- [183] *Technical Manual*, Veeco WYKO NT1100 DMEMS.
- [184] G. Cusmai, M. Mazzini, P. Rossi, and C. Combi, "Simple lumped electrical model for an RF MEMS switch considering lossy substrate effects," *Sensors and Actuators A: Physical*, vol. A123-A124, pp. 515–521, 2005.
- [185] B. Marghesin and F. Giacomozzi, "Technical memo," Tech. Rep.
- [186] L. Lorenzelli, K. J. Rangra, C. Collini, F. Giacomozzi, B. Marghesin, and F. Pianegiani, "On-wafer electro-mechanical characterization of silicon mems switches," in *Symposium on Design, Test, Integration and Packaging of MEMS/MOEMS (DTIP'03)*, 2003, pp. 281–285.
- [187] D. Peroulis, S. P. Pacheco, K. Sarabandi, and L. P. B. Katehi, "Electromechanical considerations in developing low-voltage rf mems switches," *IEEE Transation on Microwave Theory and Techniques*, vol. 51, no. 1, pp. 258–270, 2003.
- [188] J. Bartholomeyczik, "Micro-electromechanical resonators- Technology and Design," Master's thesis, IMTEK- Laboratory for Microsystem Materials, Department of Microsystem Engineering, University of Freiburg, 2002.
- [189] J. Bhardwaj, H. Ashraf, and A. McQuarrie, "Dry silicon etching for mems," in *Symposium on Microstructures and Microfabricated Systems at the Annual Meeting of the Electrochemical Society*, 1997.
- [190] P. Ruther, private conversation.
- [191] F. Giacomozzi, private conversation.
- [192] N. Agarwal, S. Ponoth, J. Plawsky, and P. D. Persans, "Optimized oxygen plasma etching of polyimide films for low loss optical waveguides," *J. Vacuum Science and Technology A*, vol. 20, no. 5, pp. 1587–1591, 2002.
- [193] A. Chean, K. Kaviani, A. W. Rempel, S. K. ad W. H. Steier, Y. Shi, Z. Liang, and L. R. Dalton, "Optimized oxygen plasma etching of polyurethane-based electro-optic polymer for low loss optical waveguide fabrication," *J. Electroche. Soc.*, vol. 143, no. 11, 1996.
-